Realization of High Power Diode Lasers with Extremely Narrow Vertical Divergence

Vorgelegt von
Diplom-Ingenieurin
Agnieszka Pietrzak
aus Chorzów, Polen

Vor der Fakultät IV – Elektrotechnik und Informatik
Der Technischen Universität Berlin
Zur Erlangung des akademischen Grades
Doktor der Naturwissenschaften
– Dr. rer. nat. –
genehmigte Dissertation

Promotionsausschuss:

Vorsitzender:	Prof. Dr.-Ing. Heinrich Klar, TU Berlin
Berichter:	Prof. Dr. rer. nat. Günther Tränkle, TU Berlin
	Prof. Dr. Eric Larkins, University of Nottingham

Der Tag der Wissenschaftliche Aussprache: 11.10.2011

Berlin, 2011

D 83

Abstract

The doctoral thesis deals with high power InGaAs/GaAsP/AlGaAs quantum well diode lasers grown on a GaAs substrate with emission wavelengths in the range of 1050 nm – 1150 nm.

The objective of this thesis is the development of diode lasers with extremely narrow vertical laser beam divergence without any resulting decrease in the optical output power compared to current state of the art devices.

The work is focused on the design of the internal laser structure (epitaxial structure), with the goal of optical mode expansion (thus reduction of the beam divergence), and the experimental investigation of the electro-optical properties of the processed laser devices. Diagnosis of the factors limiting the performance is also performed. The optical mode expansion is realized by increasing the thickness of the waveguide layers. Structures with a very thick optical cavity are named in this work as Super Large Optical Cavity structures (SLOC).

The vertical optical mode is modeled by solving the one-dimensional waveguide equation, and the far-field profiles are obtained from the Fourier transform of the electrical field at the laser facet (near-field). Calculations are performed by using the software tool QIP. The electro-optical properties (such as vertical electrical carrier transport and power-voltage-current characteristics, without self-heating effect) are simulated using the WIAS-TeSCA software. Both software tools are described in this thesis.

The lasers chips, grown by means of MOVPE and processed as broad area single emitters, are experimentally tested under three measurement conditions. First, uncoated and unmounted laser chips with various lengths are characterized under pulsed operation (1.5 µs, 5 kHz) in order to obtain the internal parameters of the laser structure. In the second part of the laser characterization, the facet-coated and mounted devices with large (4 - 8 mm long) Fabry-Perot resonators are tested under quasi-continuous wave operation (500 µs, 20 Hz). Finally, these devices are also tested under ‘zero-heat’ conditions (300 ns pulse duration, 1 kHz repetition rate). The ‘zero-heat’ test is performed in order to investigate the factors, other than overheating of the device, that limit the maximum output power. All measurements are performed at a heat-sink temperature of 25°C. The measurement techniques used to characterize the electro-optical properties of the laser and the laser beam properties are also described.

More specifically, the influence of the material composition and the thickness of the waveguide layers on the vertical beam divergence angle (perpendicular to the epitaxial structure) and on the electro-optical properties of the laser is discussed. It is shown that, due to the large cross section of the investigated laser chips, catastrophic optical mirror damage (COMD) is strongly reduced and that one of the major factors limiting the maximum optical power of the discussed diode lasers is weak carrier confinement in the active region leading to enhanced carrier and optical losses due to carrier accumulation in the thick waveguide. The reason for the vertical carrier leakage is a low effective barrier between the quantum well and the GaAs waveguide. Moreover, it is shown that the carrier confinement in the active region can be strengthened in three ways. Firstly, the QW depth is increased for lasers emitting at

longer wavelength (here ~ 1130 nm). Secondly, utilizing a higher number of QWs lowers the threshold carrier density per QW. In this case, the electron Fermi-level shifts towards lower energies for lower threshold currents and thus the effective barrier heights are increased. Thirdly, in lasers emitting especially at wavelengths shorter than 1130 nm (around 1064 nm, a wavelength commercially interesting) the quantum wells are shallower and thus the effective barrier is lower. It is shown that AlGaAs waveguides are required to improve the carrier confinement. The AlGaAs alloys provide higher conduction and lower valence band edge energies of the bulk material. Consequently, the potential barrier against carrier escape from the QW to the waveguide is increased.

Considering the mode expansion in the SLOC structures, it is shown, in simulation and experimentally, that the multi-quantum well active region, due to its high average refractive index, contributes significantly to the guiding of the modes. The optical mode is stronger confined in active regions with a higher number of quantum wells as well as in structures based on AlGaAs waveguides which are characterized by a lower refractive index compared to GaAs material. The increased mode confinement leads to a reduced equivalent vertical spot-size and results in a wider divergence angle of the laser beam. Moreover, by increasing the thickness of the waveguide layers the active region acts more and more as a waveguide itself thus preventing a further narrowing of the vertical far-field. As a new finding, it is presented that the introduction of low-refractive index quantum barriers (LIQB), enclosing the high-refractive index quantum wells, lowers the average refractive index of the multi-quantum well active region and thus reduces the beam divergence (the invention is content of a German Patent Application DEA102009024945).

Through systematic model-based experimental investigations of a series of laser diode structures, the vertical beam divergence was reduced from 19° to 8.6° at full width at half maximum (FWHM) and from 30° to 15°, at 95% power content. The achieved vertical far-field angle is smaller, by a factor of ~3, than state-of-the-art laser devices. The 8 mm long and 200 µm wide single emitters based on the investigated SLOC structures deliver more than 30 W peak-power in quasi-continuous wave mode. The large equivalent spot-size together with the facet passivation prevent COMD failure and the maximum measured power is limited due to the overheating of the device. Moreover, a 4 mm long and 200 µm wide single emitter tested under ‘zero-heat’ condition delivers 124 W power. The maximal measured power was limited by the current supply.

Kurzzusammenfassung

Diese Doktorarbeit handelt von Quantum-Well-Laserdioden höchster Leistung basierend auf einem InGaAs/GaAsP/AlGaAs-Materialsystem auf GaAs-Substrat. Die Laser emittieren in Wellenlängenbereich von 1050 nm bis 1150 nm.

Die Zielstellung dieser Doktorarbeit besteht in der Entwicklung von Laserdioden mit einer extrem geringen vertikalen Strahldivergenz ohne das dadurch die optische Ausgangsleistung gegenüber aktuellen Stand der Technik reduziert wird.

Der Fokus dieser Arbeit liegt auf dem Design der internen Laserstruktur mit dem Ziel, die Feldverteilung der optischen Mode aufzuweiten, um die Strahldivergenz zu reduzieren. Ein weitere Fokus der Arbeit liegt auf der experimentellen Untersuchung der elektro-optischen Eigenschaften der entwickelten Laserprototypen. Außerdem werden die Faktoren bestimmt, welche die maximal mögliche Ausgangsleistung limitieren. Die Ausweitung des optischen Modes wird durch die Verbreiterung des Wellenleiters erreicht. Strukturen mit einem breiten, vertikalen optischen Resonator werden in dieser Arbeit als Super Large Optical Cavity (SLOC) bezeichnet.

Der vertikale optische Mode wird durch die Lösung der eindimensionalen Wellenleitergleichung modelliert. Die Fernfeldprofile werden durch die Fourier-Transformation des elektrischen Felds an der Laserfacette (Nahfeld) bestimmt. Die Rechnungen wurden mit Hilfe der QIP Software durchgeführt. Die elektro-optischen Eigenschaften (wie vertikaler Ladungsträgertransport und Leistungs-Spannungs-Strom-Kennlinien ohne Eigenerwärmung) werden mit Hilfe der WIAS-TeSCA-Software simuliert. Beide Programme werden in der Arbeit näher beschrieben.

Die Laserdioden werden mittels Metal Organic Vapor Phase Epitaxy (MOVPE) hergestellt und als Breit-Streifen Einzelemitter prozessiert. Die Laser werden mit drei verschiedenen Messmethoden untersucht. Als erstes werden unter Pulsstrom Anregung (1.5µs, 5kHz) unbeschichtete Laser mit verschiedenen Resonatorlängen zur Bestimmung der internen Laserparameter untersucht. Folgend werden beschichtete Laser mit langen Fabry-Perot Resonatoren (4 – 8 mm) unter quasi-Dauerstrich (500 µs, 20 Hz) Anregung charakterisiert. Abschließend werden die Diodenlaser unter Verwendung sehr kurzer Stromimpulse (300 ns, 1 kHz) vermessen. Die letztgenannte Messmethode wird verwendet, um die Einflussfaktoren zu ermitteln, welche die Ausgangsleistung der Laserstruktur limitieren. Die Verwendung solch kurzer Pulse ist nötig da es hier zu keiner Eigenerwärmung der Laser kommt, was üblicherweise die Ausgangsleistung limitiert. Alle Messungen werden bei einer Wärmesenkentemperatur von 25°C durchgeführt. Alle Messmethoden für die Untersuchung der elektro-optischen Eigenschaften der Laser und der optischen Eigenschaften des Laserstrahls werden in der Arbeit näher beschrieben.

Insbesondere werden die Auswirkungen der Materialzusammensetzung und der Dicke des Wellenleiters auf die Laserstrahldivergenz in vertikaler Richtung, sowie auf die elektro-optischen Eigenschaften der Laserstruktur diskutiert. Es wird gezeigt, dass durch das große Modenbreite die Gefahr der katastrophalen optischen Facetten-Degradation (Catastrophic Optical Mirror Damage, COMD) reduziert ist. Außerdem wird gezeigt, dass die maximal erreichbare optische Leistung stark durch den schwachen Einschluss der Ladungsträger in der

aktiven Zone, limitiert ist. Dies führt zu erhöhten Ladungsträger- und optischen Verlusten auf Grund von Ladungsträgeransammlung in dem Wellenleiter. Der Grund für die Ladungsträgerverluste ist die niedrige effektive Barrierenhöhe zwischen Quantum Well und Wellenleiter. Es wird gezeigt, dass man den schwachen Ladungsträgereinschluss in der aktiven Zone auf drei Weisen verstärken kann. Erstens, durch Erhöhung der Quantum Well Tiefe. Hier gezeigt für Laser mit einer größeren Wellenlänge von ~ 1130 nm. Zweitens, durch Erhöhung der Anzahl der Quantum Wells dies reduziert die Ladungsträgerdichte pro Quantum Well an der Laserschwelle. Dadurch verschiebt sich das Fermi-Niveau für die Elektronen in Richtung niedrigerer Energien wodurch sich die effektive Barrierenhöhe vergrößert. Als Drittes, bei den Lasern, deren Emissionswellenlänge kleiner als 1130 nm ist (ca. 1064 nm, Wellenlänge kommerziell wichtig). Hier sind die Quantum Wells flacher und die effektive Barriere ist kleiner. Es wird gezeigt, dass um den Ladungsträgereinschluss zu verstärken, ein AlGaAs-Wellenleiter notwendig ist. AlGaAs als Wellenleitermaterial hat eine höhere Leitungsbandkante und niedrige Valenzbandkante im Vergleich zu GaAs al Wellenleiter. Im Resultat ergibt sich eine Barriere gegen vertikale Ladungsträgerverluste und damit wird der Einschluss der Ladungsträger in der aktiven Zone verstärkt.

Es wird sowohl in Simulationen als auch experimentell gezeigt, dass eine aktive Zone bestehend aus mehreren Quantum Wells, durch deren hohe mittlere Brechzahl, einen entscheidenden Einfluss auf die Wellenleitung hat. Der optische Mode ist bei Strukturen mit höherer Quantum Well Anzahl in der aktiven Zone stärker eingeschlossen, vergleichbar zu Strukturen mit einem erhöhtem Al-Anteil im Wellenleiter. Ein höherer Al-Anteil im Wellenleiter führt zu einer kleineren Brechzahl im Vergleich zu einem GaAs-Wellenleiter. Die erhöhte Beschränkung des Modes bewirkt eine geringere vertikale Modenbreite und hat dadurch einen breiteren Divergenzwinkel des emittierten Lichts zur Folge. Außerdem führt die Erhöhung der Wellenleiterdicke dazu, dass die aktive Zone mehr und mehr selbst wie ein Wellenleiter wirkt. Das wiederum verhindert eine weitere Verringerung des vertikalen Divergenzwinkels.

In dieser Arbeit wird erstmalig gezeigt, dass durch die Verwendung von Quantum Barrieren mit einer niedrigen Brechzahl (Low-Refractive Index Quantum Barriers, LIQB) die hohe mittlere Brechzahl der aktiven Zone reduziert wird und dadurch die Strahldivergenz vermindert werden kann. Aus dieser Entwicklung resultierte eine Anmeldung für ein deutsches Patent DEA102009024945.

Durch die systematische, modelgestützte und anschließende experimentelle Untersuchung der Laserdiodenstrukturen konnte die Strahldivergenz von 19° auf 8.6° (full width at half maximum, FWHM) bzw. von 30° auf 16° (95 % optischer Leistungsinhalt) reduziert werden. Die erreichten vertikalen Fernfeldwinkel sind um Faktor 3 kleiner als bei vergleichbaren Laserdioden. Einzelemitter mit einer Länge von 8 mm und einer Streifenbreite von 200 µm erreichten eine optische Leistung von 30 W im quasi-Dauerstrich Betrieb. Die große Modenbreite zusammen mit der Facettenpassivierung verhindern COMD und ermöglichen so höhere optische Leistungen. Dadurch ist die maximale Roll-Leistung hauptsächlich durch thermische Effekte begrenzt. Außerdem, erreichte ein 4 mm langer Einzelemitter mit einer Streifenbreite von 200 µm unter 300 ns Kurzpuls Anregung, eine optische Leistung von 124 W. Hierbei war die maximale Leistung durch die Stromquelle begrenzt.

Acknowledgments

First of all, I would like to express my sincere gratitude to Prof. Dr. Günther Tränkle for having offered me the opportunity to carry out my PhD thesis at the Ferdinand-Braun-Institut, Leibniz Institut für Höchstfrequenztechnik (FBH). No matter what problem, he always gave great advice and assisted finding a solution. The financial support of my work during my stay at the Institute is gratefully acknowledged.

My thanks also go to Prof. Dr. Eric Larkins who dedicated his time as the external reviewer of my PhD thesis.

I am indebted to Dr. Götz Erbert, head of the optoelectronics department at the Ferdinand-Braun-Institut, Leibniz Institut für Höchstfrequenztechnik, for his guidance, his perspective and his unmatched experience in the field which he kindly shared with me.

Because of our invaluable discussions about theoretical levels of this work I consider Dr. Hans Wenzel as one of my mentors during my stay at the FBH. His permanent availability, his advice, and his constructive ideas are truly appreciated. The fruitful debates were essential for the success of this work.

I am deeply grateful to my other mentor Dr. Paul Crump for his encouragement and the countless propositions on how to structure my work. He greatly helped me strengthening arguments and focusing on the important aspects in this thesis. His support introduced a direction and a dynamic into my PhD life at the institute and speeded up the doctoral work.

My warm and sincere gratitude belongs to Sven Schwertfeger, Martin Spreemann and Joe Xiaozhuo Wang for the humorous and helpful atmosphere throughout my time at the Institute. I am particularly grateful to Sven Schwertfeger who has gone out of his way to help me with everything that concerns German language and obstacles encountered in the German system.

I would like to thank Angela Krause for the *Antest* measurements - an essential requirement for my work.

I warmly thank my colleagues at Ferdinand-Braun-Institut for teaching me many aspects of experimental measurement and analysis. Especially Ralf Staske and Martin Spreemann always helped with prompt technical advice and support.

I am sincerely grateful to Dr. Martin Zorn, Dr. Frank Bugge, Dr. Sven Einfeldt, Dr. Jörg Fricke, Dr. Peter Ressel and all other colleagues at Ferdinand-Braun-Institut who have contributed to the epitaxy, processing and mounting of the diode lasers. Without them, this thesis would not have been possible.

The opportunity for me to study in Germany has been made possible by the Deutscher Akademischer Austausch Dienst (DAAD) which generously provided me with a doctoral scholarship.

Where would I be without my family? My parents deserve special mention for all their love and encouragement. I am grateful to them for having supported my ideas and aspirations.

Most of all I would like to thank my loving, encouraging, and patient husband who supported me faithfully during the final stages of this Ph.D.

Publications

Parts of the work have been also presented in the following publications and during conferences:

Journals

[1] ‘High-Power Laser Diodes Emitting Light Above 1100 nm with a Small Vertical Divergence Angle of 13°’, **A. Pietrzak**, H. Wenzel, G. Erbert, and G. Tränkle, Opt. Lett. Vol. 33, No. 19, pp. 2188-90, 2008.

[2] ‘High Brightness Diode Lasers With Very Narrow Vertical Divergence’, G. Erbert, F. Bugge, B. Eppich, J. Fricke, K.H. Hasler, K. Paschke, **A. Pietrzak**, H. Wenzel, and G. Tränkle, Proc. of SPIE Vol. 6909, 69090P, 2008.

[3] ‘Passively Cooled TM Polarised 808-nm Laser Bars with 70% Power Conversion at 80-W and 55-W Peak Power per 100-μm Stripe Width’, P. Crump, H. Wenzel, G. Erbert, P. Ressel, M. Zorn, F. Bugge, S. Einfeldt, R. Staske, U. Zeimer, **A. Pietrzak**, and G. Tränkle, Photon. Tech. Lett., Vol. 20, No. 16, pp. 1378-80, 2008.

[4] ‘55W peak power from 1100 nm wavelength 60 μm broad-area laser diodes enabled by reduced carrier accumulation in the waveguide’, **A. Pietrzak**, P. Crump, H. Wenzel, R. Staske, G. Erbert, and G. Tränkle, Semicond. Sci. Technol. Vol. 24 035020 (5pp), 2009.

[5]‘MOVPE Growth of InGaAs/GaAsP-MQWs for High-Power Laser Diodes Studied by Reflectance Anisotropy Spectroscopy, F. Bugge, M. Zorn, U. Zeimer, **A. Pietrzak**, G. Erbert, and M. Weyers, J. Crys. Growth Vol. 311, pp. 1065–69, 2009.

[6] ‘Assessment of the Limits to Peak Power of 1100 nm Broad Area Single Emitter Diode Lasers under Short Pulse Conditions’, X. Wang, P. Crump, **A. Pietrzak**, C. Schultz, A. Klehr, T. Hoffmann, A. Liero, A. Ginolas, S. Einfeldt, F. Bugge, G. Erbert and G. Tränkle, Proc. of SPIE Vol. 7198-52, 2009

[7] ‘20 W Continuous Wave Reliable Operation of 980 nm Broad-Area Single Emitter Diode Lasers with an Aperture of 96 μm’, P. Crump, G. Blume, K. Paschke, R. Staske, **A. Pietrzak**, U. Zeimer, S. Einfeldt, A. Ginolas, F. Bugge, K. Häusler, P. Ressel, H. Wenzel, and G. Erbert, Proc. of SPIE Vol. 7189-40, 2009.

[8] ‘Limitations to Peak Continuous Wave Power in High Power Broad Area Single Emitter 980 nm Diode Lasers’, P. Crump, C. Roder, R. Staske, **A. Pietrzak**, W. Pittroff, A. Ginolas, J. Fricke, K. Paschke, F. Bugge, P. Ressel, H. Wenzel, and G. Erbert, Proc. CLEO Europe/ EQEQ, CB-P33-TUE, 2009

[9] ‘Advances in Spatial and Spectral Brightness in 800-1100 nm GaAs-Based High Power Broad Area Lasers, P. Crump, H. Wenzel, G. Erbert, and G. Tränkle, Proc. of SPIE Europe Security-Defence, 2009.

[10] ‘975 nm High Power Diode Lasers with High Efficiency and Narrow Vertical Far Field Enabled by Low Index Quantum Barriers’, P. Crump, **A. Pietrzak**, F. Bugge, H. Wenzel, G. Erbert, and G. Tränkle, Appl. Phys. Lett. Vol. 96, pp. 131110-1-3, 2010.

[11] ‘975nm High Power Broad Area Diode Lasers Optimised for Narrow Spectral Linewidth Applications’, P. Crump, C. Schultz, **A. Pietrzak**, M. Spreemann, H. Wenzel, S. Knigge, O. Brox, A. Maaßdorf, F. Bugge, and G. Erbert, Proc. SPIE 7583-22, 2010.

[12] ‘The analysis of factors limiting the maximum output power of broad-area laser diodes’, H. Wenzel, P. Crump, **A. Pietrzak**, C. Roder, X. Wang, and G. Erbert, Opt. Quant. Electron, Vol. 41, No. 9, pp. 645-652, 2009.

[13] ‘Theoretical and experimental investigations of the limits to the maximum output power of laser diodes’, H. Wenzel, P. Crump, **A. Pietrzak**, X. Wang, G. Erbert, and G. Tränkle, New Journal Physics, Vol. 12, 085007, 11pp, 2010.

[14] ‘Finite Element Simulation of the Optical Modes of Semiconductor Lasers’, J. Pomplun, S. Burger, F. Schmidt, A. Schliwa, D. Bimberg, **A. Pietrzak**, H.Wenzel, and G. Erbert, Phys. Status Solidi B, Vol. 247, No. 4, pp. 846–853, 2010.

[15] ‘Root-Cause Analysis of Peak Power Saturation in Pulse-Pumped 1100 nm Broad Area Single Emitter Diode Lasers’, X. Wang, P. Crump, H. Wenzel, A. Liero, T. Hoffmann, **A. Pietrzak**, C. M. Schultz, A. Klehr, A. Ginolas, S. Einfeldt, F. Bugge, G. Erbert, and G. Tränkle, J. Quant. Electron., Vol. 46, No. 5, pp. 658-665, 2010.

[16] ‘Combination of Low Index Quantum Barrier and Super Large Optical Cavity Designs for Ultra Narrow Vertical Far-Fields from High-Power Broad-Area Lasers’, **A. Pietrzak**, P. Crump, H. Wenzel, G. Erbert, F. Bugge, and G. Tränkle, J. Sel. Top. Quant. Electron., Vol. PP, pp. 1-8, 2011.

Patent Application

[1] DEA 102009024945 P.Crump, G.Erbert, **A.Pietrzak**, H.Wenzel: ‘Optoelektronisches Halbleiterbauelement und Verfahren zu dessen Herstellung’, 2009.

International Conferences and Workshops

[1] 'Peak Power from 60-µm Broad Area Single Emitter Limited to 50-W by Carrier Escape', **A. Pietrzak**, P. Crump, R. Staske, H. Wenzel, G. Erbert, and G. Tränkle, (CMN2), CLEO: The Conference on Lasers and Electro-Optics, San Jose, CA, US, 4-9 May 2008.

[2] 'Peak Power and Facet Stability of Broad Area Single Emitters', **A. Pietrzak**, Workshop IEEE LEOS, San Jose, CA, USA, 9th May 2008.

[3] 'Growth of InGaAs MQWs for High Power Laser Diodes with Extremely Low Beam Divergence Monitored by RAS', F. Bugge, M. Zorn, U. Zeimer, **A. Pietrzak**, G. Erbert, and M. Weyers, ICMOVPE - XIV: 14th International Conference of Metalorganic Vapor Phase Epitaxy, Metz, France, 1-6 June 2008.

[4] '1060-nm Multi Quantum Well Diode Lasers With Narrow Vertical Divergence Angle of 8° and High Internal Efficiency', **A. Pietrzak**, P. Crump, F. Bugge, H. Wenzel, G. Erbert, and G. Tränkle, (CWF 2), CLEO: The Conference on Lasers and Electro-Optics, Baltimore, MA, US, 31 May - 5 June 2009.

[5] 'Maximum output power of broad-area laser diodes', H. Wenzel, P. Crump, **A. Pietrzak**, C. Roder, X. Wang, and G. Erbert, NUSOD: 9th International Conference on Numerical Simulation of Optoelectronic Devices, Gwangju, Republic of Korea, 14 – 18 September 2009.

[6] 'High Power 1060 nm Ridge Waveguide Lasers with Low-Index Quantum Barriers for Narrow Divergence Angle', **A. Pietrzak**, P. Crump, H. Wenzel, F. Bugge, G. Erbert, and G. Tränkle, (CWE 2), CLEO: The Conference on Lasers and Electro-Optics, San Jose, CA, US, 16-21 May 2010.

Contents

1

Introduction and motivation

This work concerns high-power semiconductor diode lasers with emission wavelengths in the range of 1050-1150 nm. Diode lasers typically demonstrate high electrical-to-optical conversion efficiencies at relatively high optical power and cover a wide spectral range. These characteristics, together with their compactness, make them very attractive optical sources for commercial applications. Therefore, diode lasers are currently widely applied in industry as pump sources of solid state laser systems, in direct material processing, in fiber and space telecommunications, and in various medical treatments. Currently, significant diode laser research and development is in progress, aiming on achieving the maximum possible optical power and electro-optical efficiency, together with an improved beam quality. In the future, diode lasers will enable high performance optical systems with reduced overall cost. Table 1 shows the best published results of single emitter laser diodes and table 2 the best commercially available products.

The main aim of this work is the realization of diode lasers which emit high optical power within an extremely small vertical divergence angle (direction perpendicular to the active region). High performance diode lasers, which emit a power above 20 W within a far field angle below 10° (defined as full width at half maximum, FWHM) are sought-after. The focus on the reduction of the vertical divergence angle is dictated by application needs such as easier and more efficient beam shaping, which makes optical systems less expensive. A small vertical divergence angle (containing 95% of the optical power) minimizes the power loss and aberrations during the beam collimation process.

The general concept chosen for the reduction of the vertical far field angle are epitaxial structures based on very wide waveguides which are named Super Large Optical Cavity structures (SLOC) in this work. The SLOC concept is considered mainly due to three reasons. Firstly, the beam divergence can be reduced simply by widening the waveguide. The vertical beam profile has a Gaussian shape and the divergence angle containing 95% optical power is stable up to high carrier injection levels.
Secondly, the SLOC design provides a large equivalent vertical spot-size – the high optical field intensity is distributed over a larger area in the vertical direction. This reduces the risk of optical damage of the internal structure and the laser mirrors (catastrophic optical mirror damage, COMD). Consequently, higher output powers can be emitted before the damage occurs. Thirdly, the advantage of this design is the robust tolerance of the growth of the thick waveguides and claddings. Higher order modes are suppressed in a loss discrimination process by varying the thickness of the claddings, whereby good mode suppression with high tolerance of this thickness is achieved.

The emission wavelength of 1050-1150 nm requires an active region consisting of an $In_xGa_{1-x}As$ quantum well with high incorporation of indium content ($x = 0.28$ to $x = 0.37$,

respectively). In structures based on thick waveguides, the overlap of the optical mode with the active region is low. In order to obtain high optical gain, the laser structures comprise a multi-quantum well active region where the quantum wells are separated with $GaAs_{1-y}P_y$ barriers. For structures emitting at wavelengths beyond 1100 nm, the material chosen for the waveguides was GaAs. This choice was made for two reasons. Firstly, for the laser structures emitting at longer wavelengths the GaAs waveguide is expected to build a sufficiently high barrier which confines the electrical carriers in the active region. Secondly, the GaAs material features high electrical and thermal conductivity. Therefore, the thick waveguide layers can be lowly doped. A low free carrier density results in low internal absorption loss making the realization of lasers with a longer gain medium possible. For structures emitting at shorter wavelengths than 1100 nm, an $Al_{0.1}Ga_{0.9}As$ waveguide is utilized in order to strengthen the carrier confinement in the active region. The $Al_xGa_{1-x}As$ alloy, however, is characterized by lower electrical and thermal conductivity (due to higher effective mass of the electrons and thus lower mobility). Therefore, in this case higher doping of the waveguide is required. The thick waveguides are embedded in $Al_xGa_{1-x}As$-cladding layers with aluminum contents between 10% and 25%. The aluminum content in the claddings is chosen in a way to obtain a low refractive index step at the waveguide-cladding interface and thus to reduce the number of higher modes in the vertical cavity.

The laser structures optimized for narrow beam divergence angles are processed as broad area single emitters with long (4 - 8 mm) Fabry-Perot optical resonators in order to reduce the thermal and series resistance of the devices. The long gain medium reduces the out-coupling losses and allows the use of low reflectivities of the front facet. Low reflectivity reduces the optical load on the facet and is expected to reduce the risk of COMD. Consequently, higher overall optical output power is expected to be achieved before a failure of the device occurs.

This work involves a theoretical study of the waveguiding and carrier-transport properties of the laser structures and an experimental part dealing with the electro-optical characterization of processed laser devices, intended in part to diagnose what limits the laser performance.

Wavelength	Vertical divergence angle	Maximum optical power, (CW, 25°C)	Maximum wall-plug efficiency	Single emitter geometry, (stripe × length)	Company
915 nm	35° (FWHM)	23 W	65%	90 µm × ---	Axcel Photonics 2008 [1]
940 nm	---	26 W (15°C)	64%	90 µm × 5 mm	Intense 2009 [2]
980 nm	22° (FWHM) 40° (95%)	25 W (15°C)	54%	96 µm × 4 mm	FBH 2009 [3]
975 nm	15° (FWHM) 28° (95%)	11 W	58%	90 µm × 3 mm	FBH 2009 [4]
1060 nm – 1080 nm	31° (FWHM) ~50° (95%)	16 W	74%	100 µm × 2-3 mm	Ioffe 2004 [5]
1150 nm	20° (FWHM) 34.5° (95%)	13 W	53%	100 µm × 4 mm	FBH 2005 [6]
1060 nm	14° (FWHM)	15 W	52%	100 µm × 4 mm	FBH 2008 [7]
1130 nm	13° (FWHM) 20° (95%)	38 W (QCW)	40%	200 µm × 8 mm	FBH 2008 [8]
1060 nm	*8.6°*(FWHM) *15° (95%)*	*12.5 W* *30 W (QCW)*	*27%*	*200 µm × 8 mm*	*in this thesis*

--- - data not available

Table 1.1. The opto-electrical parameters of single emitter prototypes presented in the years 2001-2009. The laser devices are presented in respect to decreasing vertical divergence angles and the emission wavelength range, first 915-980 nm, second 1060-1150 nm.

Company	Wavelength	Vertical divergence angle	Maximum optical power, (CW, 25°C)	Maximum wall-plug efficiency	Single emitter geometry, (stripe × length)
JDS Uniphase	915 nm – 976 nm	27° (FWHM)	10 W	55%	100 µm × ---
Oclaro	915 nm – 975 nm	23° (FWHM)	9 W 11W	>50% >55%	90 µm × 3.6 mm 90 µm × ---
LUMICS	915 nm – 975 nm	27° (FWHM)	12 W	---	95 µm × ---
	1064 nm	30° (FWHM)	11 W	---	190 µm × ---
AXCEL Photonics	1064 nm	30° (FWHM)	3 W	---	100 µm × ---

--- - data not available

Table 1.2. The electro-optical parameters of the currently (October 2011) commercially available single emitters. Emission wavelength: 915 – 1064 nm.

1.1. Overview of chapter contents

Chapter 2: A literature overview of various approaches of the optical mode expansion targeting the reduction of the vertical far-field angle.

Chapter 3: The basic concept of a diode laser with a Fabry-Perot resonator as well as the phenomenological laser model is presented. The software used to simulate the one-dimensional optical mode propagation in a layered media and the vertical far-field distribution of the emitted light is presented.

Chapter 4: The epitaxy process of high-power, 1050 – 1150 nm, diode lasers based on GaAs substrates as well as the technology and packaging of high-power broad-area diode lasers are presented.

Chapter 5: Measurement techniques and experimental setups for the diode laser characterization utilized within this work are presented.

Chapter 6: The results of the one-dimensional simulations of the basic features of the SLOC design are presented. The first results concern the variation of the near- and far-field profile as a function of the optical transverse cavity width. It is further shown that, in the structures based on extremely wide waveguides, the claddings lose their ability to confine the mode and that the multi-quantum well active region exhibits guiding properties. The influence of the active region design (e.g. quantum well number, quantum well thickness, thickness and composition of the barriers) on the mode properties like the confinement factor and on the beam divergence is presented. The study of the mode confinement by the active region leads to an innovation in the far-field angle reduction. The new concept for far-field reduction based on interpolation of low-refractive-index quantum barriers (LIQB) to separate the quantum wells is presented. Moreover, the dependence of the vertical equivalent spot-size on the waveguide thickness and number of QWs is discussed. The methods used for the suppression of higher order transverse modes in SLOC structures are presented.

Chapter 7: Theoretical and experimental studies of limiting factors to the maximum optical power of the diode lasers based on SLOC design are discussed. The study is focused on structures with 3.4 µm thick symmetric waveguides and MQW active regions emitting at 1100 nm. It is shown that one of the factors reducing the peak optical power is vertical carrier leakage and carrier accumulation in the p-type waveguide. Moreover, it is presented that the carrier confinement in the active region can be strengthened by increasing the number of quantum wells in the gain medium. The result of the study is an increase of the optical power from 45 W to 55 W under ‘zero-heat’ conditions.

Chapter 8: This chapter is focused on the further development of high power diode lasers with the simultaneous reduction of the vertical far-field angle. To assure good carrier confinement in the active region, the tested diode lasers utilize a four QW gain medium emitting at a longer wavelength of 1130nm. The far-field narrowing is obtained by increasing the waveguide thickness from 3.4 µm to 5.0 µm. Based on the experimental data, the influence of the laser geometry on the reduction of the electrical and thermal resistance (and thus a further increase of the optical output power) is discussed. The experimental results of diode lasers based on the design with reduced divergence angle

from 18° to 13° (FWHM) and simultaneously maintained high optical output power of more than 35 W are presented.

Chapter 9: This chapter deals with the theoretical and experimental study of high power diode lasers emitting at 1065 nm. Factors deteriorating the internal efficiency and factors limiting the reduction of the vertical divergence angle are discussed. More exactly, the influence of the composition of the $Al_xGa_{1-x}As$ waveguide on the effective barrier depth and on the optical mode distribution is discussed. The reduction of the far-field angle (13° to 10° at FWHM) is realized by widening the $Al_{0.1}Ga_{0.9}As$ waveguide from 6.0 µm to 8.6 µm. The further reduction of the divergence angle, especially the angle containing 95% of the optical power, by widening the waveguide was not successful. The limit to the minimum far-field angle is caused by the high average refractive index of the multi-QW active region.

Chapter 10: In this chapter, it is shown that the use of low refractive index quantum barriers (LIQB) reduces the high average refractive index of the active region and results in a lower divergence angle of the laser beam. Structures based on 8.6 µm thick $Al_{0.1}Ga_{0.9}As$-waveguides with LIQB are considered. Furthermore, the limits of the LIQB design are investigated. High power devices delivering 30 W of quasi-CW optical power enclosed in a beam divergence reduced to 8.6° (FWHM) and 15.4° (95% power content) are demonstrated. Moreover, the lateral beam profiles of the LIQB design are presented in comparison to the SLOC design.

2

Overview of general concepts for vertical mode expansion

The vertical far-field profile is obtained from the Fourier transform of the electric field distribution at the laser surface (near-field) perpendicular to the active region. Therefore, the reduction of the vertical divergence angle of the laser beam is mainly based on the extent of the optical transverse mode. The optical mode is tailored by the refractive indices of the particular epitaxial layers and their thicknesses [1]. In the literature one can find various approaches for the optical mode expansion and, consequently, for the reduction of the vertical far-field angle. Some of them are briefly described below.

2.1. Thin Active Layer (TAL) lasers

The design concerns double heterostructure lasers, i.e. the active layer with low energy band-gap is sandwiched between two high band-gap layers (Figure 2.1.a).The key concept of the TAL structure is a significant reduction of the active region thickness (from e.g. 140 nm to 25 nm) so that most of the optical mode penetrates into the adjacent cladding layers, resulting in a narrower vertical divergence angle (Figure 2.1.b). The drawback of this design is the high threshold current density due to a low confinement factor and the high free-carrier absorption loss caused by the light propagation in the highly doped claddings.
To satisfy the requirements of low divergence and low threshold current a '*thin tapered-thickness active layer*' (*T^3 laser*) is proposed [2]. The very thin active layer (showing quantum properties) is placed near the mirror in order to obtain the narrow vertical divergence angle and is widened in the inner part of the laser (showing bulk material properties) for maintaining high optical mode confinement and thus low threshold current density (Figure 2.1.c.).

The design performance may degrade due to the optical mode instability with increasing injection current caused by induced carrier refractive index change.

The vertical far-field angle of 10° and the optical power of 120 mW are presented in [2] from a 65 µm long laser at a wavelength of 780 nm).

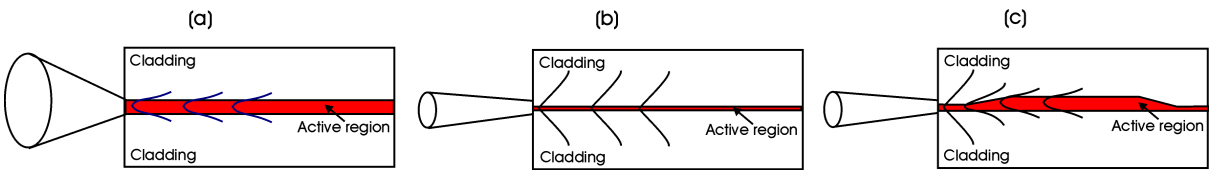

Figure 2.1. The basic concepts of the (a) DH structure, (b) TAL design and (c) T^3 design, redrawn from [2].

H. Kobayashi et al. [3] presented an improved design called '*Tapered thickness MQW waveguide*'. Here, the multi-QW active region is embedded in a tapered shape waveguide. The waveguide helps to confine light in the active region and plays a role of a tapered active layer in the T^3 design where the light is guided. A vertical far-field of 11.8° is reported. The additional waveguide layers, generally low doped, eliminate the free-carrier absorption losses. The main disadvantage of this design is the growth method. The so called Selective Area Growth technique (SAG) has to be used, which is more challenging than the one-step epitaxy.

2.2. Separate Confinement Heterostructure (SCH)

The quantum well (QW) layer is too small to effectively confine the light. To compensate this effect, the active region is embedded between two additional low doped layers (called waveguide or confinement layer) with a lower refractive index than that of the QW and higher than that of the cladding layers. The optical mode is confined in the waveguide by the low refractive index claddings with its maximum intensity in the active region.

SCH with low-index layers

In [1, 4 - 7] a single-QW InGaAs/GaAs/AlGaAs graded-index-SCH structure (GRINSCH) is considered. The reduction of the vertical far-field angle is achieved by the implementation of two low-index layers on both sides of the graded waveguide. The low-index layers strongly confine the optical field in the active region (index guiding effect). The optical mode effective index is simultaneously reduced by the low-refractive index layers to the value close to the refractive index of the claddings. Consequently, due to the index anti-guiding effect, the optical mode spreads into the cladding layers resulting in a strong reduction of the divergence angle.

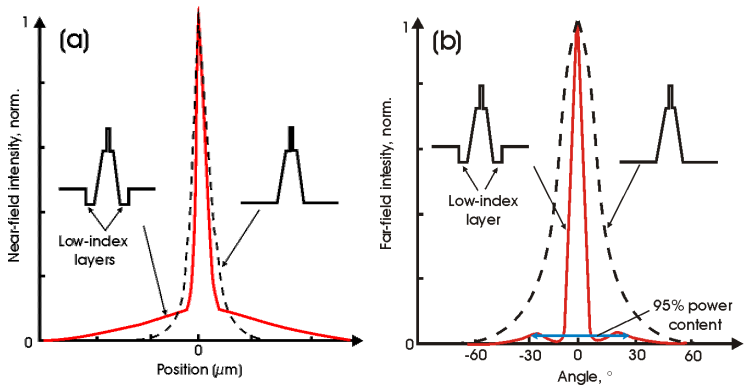

Figure 2.2. The vertical near-field (a) and far-field (b) profiles of the structure with and without low-index layers, redrawn from [4].

Using this design, a vertical far-field angle of 13° (FWHM) and 250 mW of optical power with a slope efficiency of 0.9 W/A from a 2.5 µm-ridge waveguide laser (0.5 mm long) is reported [4]. A. Maląg et al. [8] report 2.4 W optical power emitted into a 13°-14° (FWHM) vertical angle from a 100 µm wide, 1 mm long single-QW laser device (emission wavelength 800 nm).

Although the vertical angle at full width at half maximum is reduced, the design exhibits a far-field with side lobes leading to a wide angle containing 95% of the optical power that is disadvantageous for practical applications.

In order to minimize the optical losses originating from the light propagating in the highly doped p-cladding layer, a structure with only one low index layer at the n-doped waveguide-cladding interface is proposed by Z. Xu et al. [9]. A vertical far-field angle of 12° is reported for this case. An optical power of 500 mW with a slope of 1.0 W/A for a 5 µm-RW laser with cavity length of 1.5 mm is presented in [9] (emission wavelength 808nm).

The same concept is utilized for MQW structures, e.g. [10], where the optical confinement, achieved by the competition of the index guiding and anti-guiding effects, is controlled by the thickness and composition of the low-index layers.

The theoretical analysis of such low-index layer designs emitting at 980 nm results in a predicted vertical far-field angle of 11° (FWHM) [10].

SCH with high-index mode expansion layers – passive waveguide structures

In this design, additional high-index layers (called passive waveguide) in the otherwise low index cladding layers are implemented. The composition and the thickness of the mode expansion layers as well as the distance from the active region are chosen in such way that the optical mode spreads into the cladding layers consistently with a minimum reduction of the light overlap with the active region [11-13]. The idea is presented in the figure 2.3.

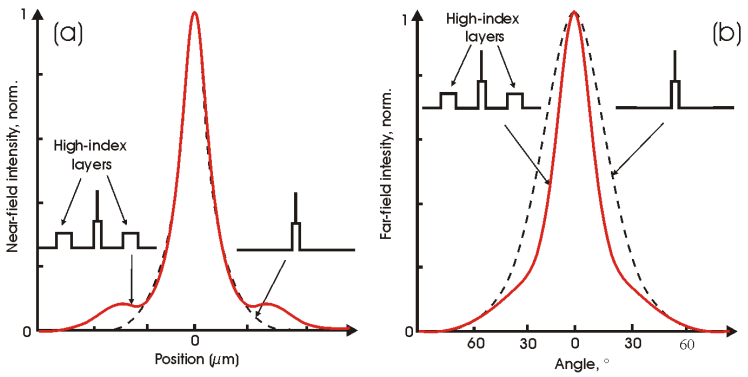

Figure 2.3. The comparison of the calculated (a) near-field and (b) far-field profiles between the SCH structure (black dashed line) and SCH with high-index mode expansion layers (red solid line) [12].

P. M. Smowton et al. [12] report a far-field reduction from 37° to 23° (FWHM) using this structure.

The drawback of this design is the requirement of higher accuracy in the growth process due to very small tolerance regarding the mode-extension layer thickness and composition of the high index layers [12]. In order to improve the growth tolerance B. Qiu et al. [11] propose a structure with a V-profiled (graded) mode-extension layer. Another drawback is that this design does not improve the emission angle containing 95% of optical power. B. Qiu et al. [11] present a reduction of the vertical divergence angle (FWHM) from 26° to 18°. The V-profiled mode-extension is implemented only in the n-type cladding layer in order to avoid the light propagation in the p-doped layer and thus to reduce the optical loss. Using this technology, 380 mW optical power from a ridge waveguide laser is reported. Vakhshoori et al. [14] present a structure (980 nm, InGaAs/GaAsP/InGaP) with 17° vertical divergence angle and 700 mW optical power with a slope of 0.9 W/A from a ridge waveguide laser (3 µm x 750 µm).

The number of high-index layers (or passive waveguides) can be increased. For example, in the work of Y. C. Chen [15] four passive waveguides are symmetrically inserted around the active region, in the cladding layers. The FWHM-vertical divergence is reduced by a factor of four, from 44° (standard SQW GRINSCH) to 11.2°. M. C. Wu et al. [16] present a structure with 16 additional passive waveguides. The 5 µm x 750 µm RW laser emits 620 mW optical power into a vertical far field of 20° (FWHM).

Antiresonant Reflecting Optical Waveguide (ARROW)

The ARROW has its origin in the passive waveguide structures. Choosing the thickness of the high-index layer as odd multiples of $\lambda_1/4$, the antiresonant condition is provided and the layers become highly reflecting (λ_1 is the vertical wavelength in the high-index layer, see the wave-front in figure 2.4, incident under angle Θ) [17-18]. Under such conditions the optical mode is strongly confined and propagates in the low-index layer (in contrast to the conventional waveguides) with embedded active area. To maximize the net reflection, the spacing to the next reflector should also be antiresonant. Therefore, it is chosen as odd multiples of half width of the low index waveguide core [18]. For higher order modes the antiresonant condition is not valid. The high-index layers are transparent for the higher modes and thus they experience large leakage loss. The schematic ARROW structure is presented in figure 2.4 together with mode intensity propagation.
A vertical far-field angle of 18° (FWHM) is reported in [18].

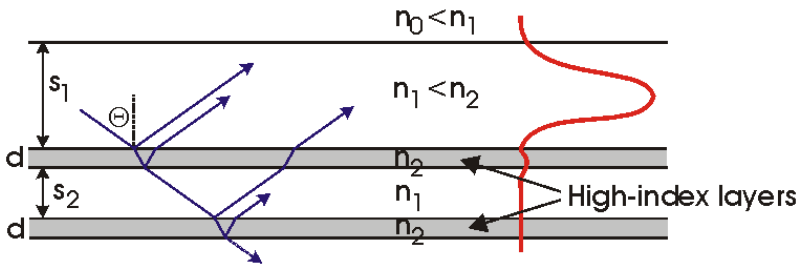

Figure 2.4. The concept of the ARROW structure with the optical mode profile. In the slab s_1 the active region is embedded. Redrawn from [19].

2.3. Photonic Band Crystals Lasers (PBC)

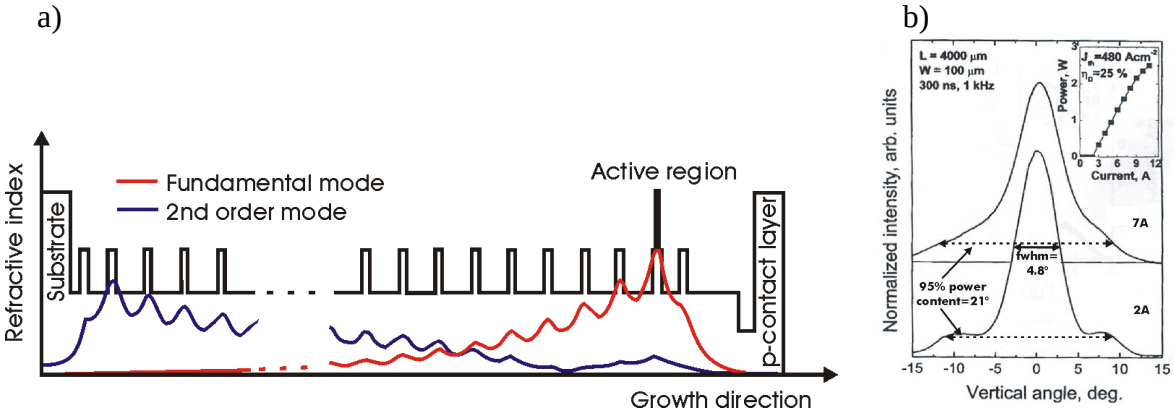

Figure 2.5. (a) The refractive index distribution of the PBC structure with the fundamental and second order mode patterns. (b) Vertical far-field profiles measured at different current levels. Redrawn from [20-21].

This type of structures has its origin in the passive waveguide structures. Lasers based on the photonic band crystal concept utilize very wide (10 µm – 30 µm) waveguides with a periodic modulation of the refractive index and a localized optical defect – a feature that violates the index periodicity. By an optical defect one understands a high refractive index layer that is wider or higher than the corresponding layers of the rest of the periods (Bragg reflector concept).

The 'localized optical defect' with an embedded active region causes fundamental mode localization with a strong overlap with the active region. At the same time, the mode is widely expanded through the periodic waveguide with a decaying tail. Simultaneously, the higher order modes are expanded over the entire PBC structure, with a low confinement in the active region, and are effectively channeled into the substrate or absorbed. Examples of the refractive index distribution and the profiles of the fundamental and second order modes are presented in figure 2.5.

Shchukin et al. [22] present a design that exhibits a vertical far-field of 8° (FWHM) and an optical power of 20 W (under short 300 ns-pulse operation) from a 100 µm stripe device that is 1.5 mm long. Gordeev et al. [21] also present a PBC laser with 8° vertical divergence (emission wavelength 660 nm). The design realized as 4 µm ridge waveguide laser with a cavity length of 1.5 mm exhibits 115 mW in CW operation mode and 20 W under short pulse operation. A 980 nm PBC design, processed as 100 µm wide, 2 mm long device, emits 17 W in pulsed operation into a 4.8° vertical far-field angle. A 10 µm ridge device with a cavity length of 1.5 mm delivers 1.3 W optical (however, not kink-free) power in CW operation mode.

Although the lasers based on PBC design exhibit a very narrow vertical angle at FWHM, the angle containing 95% of the optical power is very wide due to side lobes (figure 2.5.b). The vertical far-field pattern is also unstable at higher current levels.

2.4. Tilted Wave Laser (TWL)

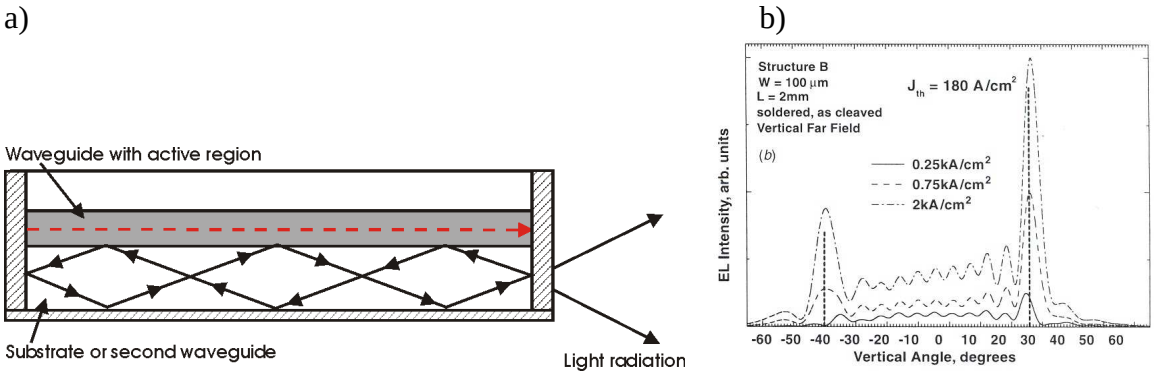

Figure 2.6. (a) Concept of the TWL with light wave propagating in the narrow waveguide and leaky waves in the second large cavity or substrate. (b) The vertical far-field profile at different current levels. Redrawn from [23].

TWL designs are MQW SCH structures that are based on antiguiding and the resonant optical wave coupling phenomenon. The light emitted from the active region is weakly guided into the waveguide and leaks into a second very thick waveguide (10 µm – 30 µm) or into a substrate. The bottom surface of the second vertical optical cavity is usually polished or coated with a highly reflective layer. The structure is designed so that the back-reflected light undergoes constructive (in the case of the fundamental mode) or destructive (for higher

modes) interference with the light propagating in the waveguide. The gain in these structures is not sufficient to enable lasing without this feedback mechanism [23].

The mode expansion into the second vertical cavity results in a wide equivalent vertical spot-size and in a vertical far-field pattern with two narrow-peaks (Figure 2.6.b). However, the design exhibits a very wide angle containing 95% of the optical power.

2.5. Super Large Optical Cavity (SLOC)

SLOC laser designs utilize very thick optical confinement layers (also called waveguides) for which, due to their superior thickness, the ability to confine the light in the active region decreases and which mainly serve to expand the optical mode. The advantageous result of the vertical mode expansion is the Gaussian shaped far-field profile with a small divergence angle defined at both, FWHM and an angle containing 95% optical power. On the other hand, wide expansion of the mode leads to a small overlap of the optical field with the active region (a small confinement factor, Γ) and hence increased threshold current. The confinement factor and, thus, the optical gain can be increased by implementing a multi-quantum well active region (MQW).

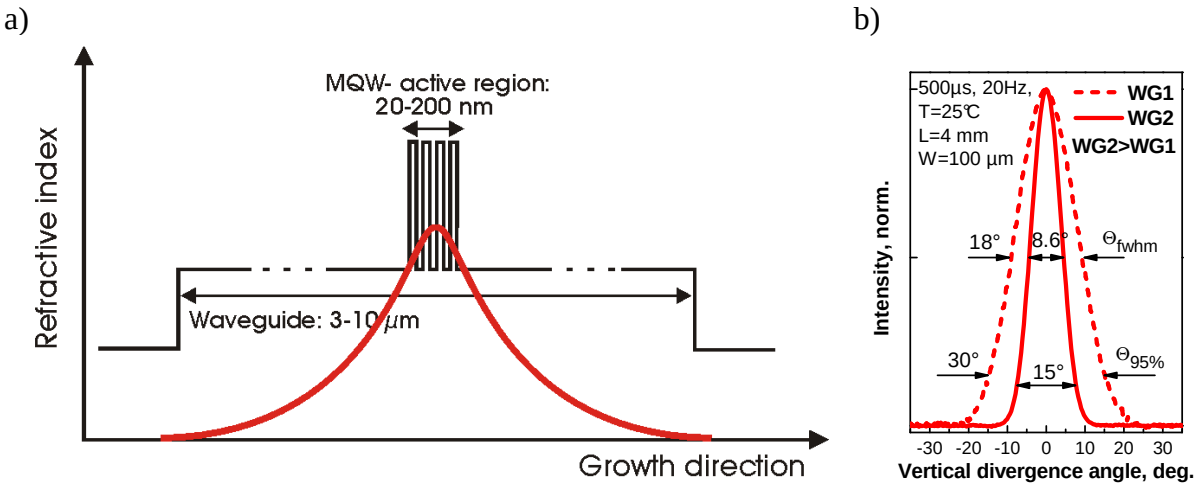

Figure 2.7. (a) The refractive index of the SLOC design and the optical mode distribution. (b) Vertical far-field profiles, measured at 7.5 A, of a SLOC with thinner (3.6 μm) and wide (8.6 μm) waveguide [24-25].

The wide optical mode distribution in the optical cavity leads to a reduced optical density in the gain region and at the laser facet (also called large equivalent vertical spot-size). The reduced optical facet load increases the threshold of the laser mirror damage (COMD). Consequently, the design has the potential to deliver high optical output power before the failure occurs.

Another positive feature is the small fraction of the optical mode overlapping with the cladding layers which are usually highly doped. This results in lower internal optical losses and allows the manufacturing of devices with long optical resonators.

Moreover, the advantage of this design is the tolerance regarding the thickness of waveguides and claddings. Higher order modes are suppressed in a loss discrimination process by varying the thickness of the claddings, whereby good mode suppression is achieved with a high tolerance of this thickness. Therefore, the design offers stable fundamental mode operation even up to high carrier injection levels.

Due to the above mentioned features, the SLOC was the design chosen for this thesis. The final, optimized structure delivers a quasi-CW optical power of 30 W into vertical far-

field angles of 8.6° (FWHM) and 15° (95% power content) [25]. The vertical far-field profile is free from side lobes and has a Gaussian shape even for high injection current levels. Until now, structures with vertical divergence angles of 13° (FWHM) and 21° (95% power content) for an output power of 38 W from a 200 µm wide, 8 mm long laser device are reported in [24]. The detailed discussion considering SLOC design is presented in the following chapters.

3

Semiconductor laser model with Fabry-Perot resonator

This chapter deals with the electro-optical features of diode lasers. The basic concept of a diode laser is presented in section 3.1. Section 3.2 describes the one-dimensional optical mode propagation in a layered media and the vertical far-field distribution of the emitted light. Furthermore, the software used for waveguide simulations is described. Section 3.3 deals with basic relations describing carrier injection and stimulated photon generation. The optical gain and the threshold conditions for a quantum well diode laser with a Fabry-Perot resonator are presented followed by relations describing power-current characteristics in steady-state conditions above threshold. The thermal mechanisms influencing the diode laser performance are discussed as well.

3.1. Basic diode laser concept

A diode laser is a stack of semiconductor epitaxial layers, with an active region embedded in a p-n or a p-i-n junction and is typically grown on an n-type substrate. There are several features making diode lasers more advantageous than other types of lasers. Diode lasers, in contrast to other types of lasers, can be pumped electrically, which means that no external light source is required. The optical gain is obtained by stimulated recombination processes of electrons and holes in the active region that amplify the present light reflected by the mirrors. In the stimulated recombination and light amplification process in semiconductors, the energy bands of the active region are essential and not electronic transitions of excited single atoms, ions or molecules like in plasma lasers. Due to a considerably higher density of states in the energy bands, semiconductor lasers provide much higher gain and electro-optical efficiency than other solid-state or gas lasers. Diode lasers emit light at a wavelength related to the direct band-gap of the semiconductor utilized as the active region. This way, lasers over a wide wavelength range can be realized. The semiconductor crystal is embedded between two parallel mirrors in order to initiate and to sustain the lasing process. The optical cavity is called a Fabry-Perot resonator. In modern diode laser technology, additional lateral carrier and/or light confinement is provided. The lateral confinement is achieved by the utilization of

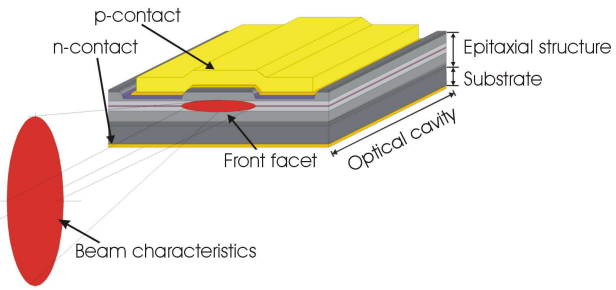

Figure 3.1. Schematic diagram of a broad area diode laser.

various designs like broad area (BA), ridge waveguide (RW) or buried heterostructures (BH). The schematic drawing of a laser diode manufactured as a broad area device is presented in figure 3.1.

There are several basic requirements to realize a diode laser; some of them are described below.

Requirements for light emission. A direct band-gap semiconductor has to be utilized as an active medium (the p-n or p-i-n junction) in order to obtain an efficient light emission. Most III-V and II-VI compound semiconductors have a direct transition gap and can therefore be suitable materials for the realization of diode lasers. The chosen semiconductor materials have to be lattice matched to the substrate crystal on which they are grown in order to avoid mechanical defects. The maximum tolerable lattice mismatch is typically 0.1% or less for bulk layers [1]. The band-gap energy and the lattice constant of some III-V semiconductors are presented in figure 3.2. The relation between the emitted wavelength and the direct band-gap energy of the semiconductor is [2]:

$$\lambda = \frac{h \cdot c}{E_g} \approx \frac{1.24}{E_g[eV]} \qquad (3.1.1)$$

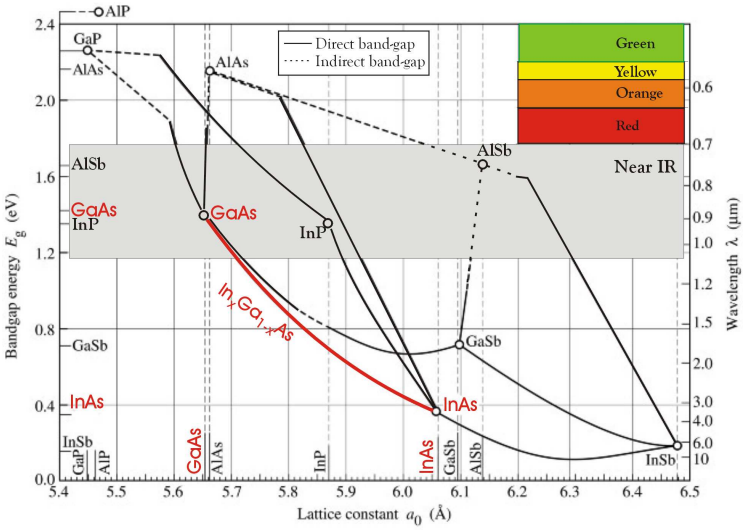

Figure 3.2. Band-gap energy and corresponding wavelength versus lattice constant of some III-V semiconductors.

The modern semiconductor lasers are realized through vapor-phase growth techniques like metal-organic vapor-phase epitaxy (MOVPE) and molecular-beam epitaxy (MBE). These techniques enable the growth of layers with precisely controlled composition and thickness at the atomic layer level. Therefore, ternary and quaternary components can be grown by varying the mole fraction of a particular element within a wide range (from 0 to 1), e.g. indium in $In_xGa_{1-x}As$ material. By mixing elements, the band-gap of the layer can be tuned, enabling lasing operation in a wide wavelength spectrum. Moreover, these techniques enable the fabrication of matched or strained quantum well (QW) structures by carefully selecting the composition of adjacent layers.

Requirements for carrier transport. A p-i-n junction has to be created through appropriate doping of the different layers in order to ensure electrical transport through the structure. The n-type and p-type semiconductors are realized by embedding impurity atoms with a higher and lower number of electrons in the outer shell, respectively. The atomic impurities create new states within the band gap called the donor and acceptor states. Donor states are located in the vicinity of the conduction band edge. Thus, at 300 K practically all of their excess electrons are thermally excited to the conduction band. Acceptor states are located near the valence band. Hence, an electron from the valence band occupies the

acceptor state, leaving a hole in the valance band. The chemical potential where the probability that a state is occupied by an electron is 1/2 is called the Fermi-level. In the absence of an external voltage, this level is flat throughout the entire structure, and the carrier flow is absent (figure 3.3a). Free charge-carriers (electrons and holes) carry current through the p-n junction if a forward bias (positive potential difference from p to n) is applied. The population inversion, required for the stimulated recombination process, is obtained in the region containing both electrons in the conduction band and holes in the valance band. When the applied external voltage V is higher than the potential given by the junction gap ($eV > E_g = h\nu$), the voltage drop across the junction is sufficiently reduced allowing free carriers to flow through the p-n junction. Hence, the intrinsic zone between the n- and p-regions is fed with carriers of both types. The high density of electrons and holes allows treating them separately as two fermions statistics with the help of two quasi-Fermi levels (figure 3.3).

Requirements for vertical carrier confinement in the active region. If the active zone has a lower energy gap than the neighboring p or n layers and the interface electric dipoles are such that the band offsets for conduction and valence band are toward the chemical potential (type one alignment) then electrons and holes are both confined in the potential well of the active zone. These neighboring layers, creating the potential barriers, are called confinement layers. In typical modern diode lasers the confinement layers are embedded between two cladding layers forming a waveguide for the optical mode. The energy gap of the confinement layers is smaller than that of the cladding layer in order to improve the carrier confinement in the active region. The distribution of the band-gaps of a typical diode laser is presented in figure 3.3. The active region in modern diode lasers is a thin layer (3-20 nm) exhibiting quantum size effects. Therefore, the layer is called a quantum well (QW). Often the active region is spread over several quantum wells. In this case, the structure is called a multi quantum well. The use of QWs as an active region has the following advantages. Firstly, due to the small volume, the necessary injection current density to reach threshold is reduced by over three orders of magnitude in comparison to a bulk layer [3].

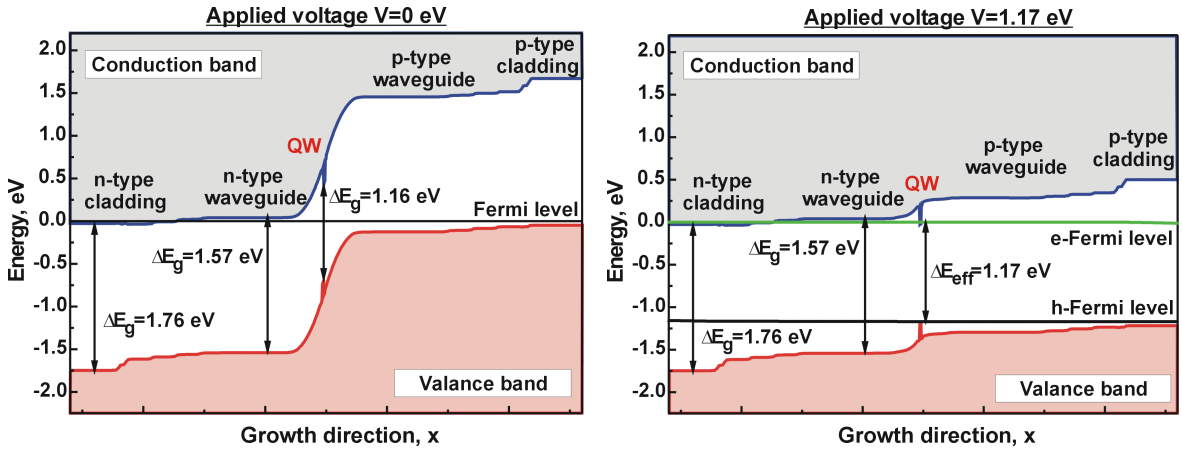

Figure 3.3. Energy band diagram of an InGaAs-SQW diode laser based on GaAs substrate (a) without an applied voltage and (b) with a forward biased applied voltage. (Emission wavelength: 1.06 µm. Energy band diagram calculated be means of Wias-TeSCA software.)

Secondly, the small thickness of QWs allows the use of materials with different compositions that do not always fully match the lattice constant of the substrate. The lattice mismatch to the substrate contributes to compressive or tensile strain in the QW. Compressive strain is introduced when a layer is grown with a larger native lattice constant than the substrate (e.g.

InGaAs on GaAs substrate). On the contrary, tensile strain is introduced when a layer with smaller native lattice constant than the substrate is grown (e.g. GaAsP on GaAs). The compressive strain increases the energy band-gap and the tensile strain reduces it. The second effect of the introduced strain is the splitting of the heavy hole (*hh*) and light hole (*lh*) bands, each being pushed in opposite directions from the center at the Γ point. In compressively strained layers, the *hh* band shifts upwards and *lh* band shifts downwards, while in tensile strained layers the opposite variation occurs [4]. This process modifies the distribution of the density of states in the active quantum well layer leading to a lower threshold current density. Moreover, the polarization-dependent gain is changed by the introduced strain. The optical gain is mainly TE polarized (transverse electric wave - electric field vector parallel to the active layer) for the transition between the electron and the heavy-hole bands but can also be TM polarized (transverse magnetic wave, electric field vector perpendicular to the active layer) for the transition between the electron and the light-hole bands [2, 4].

Requirements for the light confinement in the gain medium and the light waveguiding. The carrier confinement layers having a larger band-gap energy than the active region are almost transparent for the light produced in the stimulated emission process. Simultaneously, the confinement layers should have a larger refractive index than the cladding layers, so that the optical wave can be confined within the high index region due to total internal reflection at the interfaces with the cladding layers. Often the refractive index of the consecutive layers is tailored in such a way that the maximum intensity of the optical mode overlaps with the active region for maximum gain. Light propagation takes place along the plane of the active region. The layers that confine the light build up the waveguide. The distribution of the refractive index of a single-QW diode laser and the optical mode distribution are presented in figure 3.4.

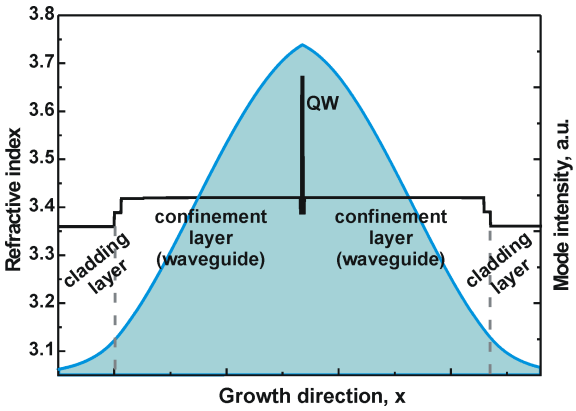

Figure 3.4. Refractive index distribution of a single-QW diode laser (left axis). Distribution of the fundamental optical mode (right axis). Calculated using QIP software.

In order to initiate and to sustain the lasing process, a positive feedback situation has to be created. The resonator is realized by cleaving the laser crystal on two planes perpendicular to the active region. The cleaved facets themselves create mirrors between which the optical wave propagates and thus defines the longitudinal plane of the diode laser. The optical wave undergoes amplification while traveling back and forth along this plane (gain medium) between the two mirrors. The light intensity at the facet is partly transmitted to the air and partly reflected back into the cavity. Lasing conditions are fulfilled if the optical gain exceeds the absorption and reflection losses (appendix 3):

$$R_f R_b \cdot \exp\left[2L\left(g_{\mathrm{mod}\,al} - \alpha_i\right)\right] = 1 \qquad (3.1.2)$$

where L denotes the distance between the front and the rear laser facets with reflectivities R_f and R_b, respectively. The traveling wave in the cavity experiences a modal gain g_m and

internal losses α_i due to absorption and scattering on crystal imperfections. The condition described by (3.1.2) is best fulfilled in the resonance case:

$$2L = m\lambda\,, \qquad (3.1.3)$$

where λ is the optical wavelength in the laser crystal and m is an integer that corresponds to the longitudinal mode number.

3.2. Simulation of an optical mode in a layered media

3.2.1 The Quasi–2Dimensional Semiconductor Laser Simulation Program (QIP)*

The program QIP* solves the quasi-two dimensional waveguide equations in the effective index approximation. However, for the purposes of this work only the one-dimensional (vertical) Helmholtz equation is solved and only transverse electric modes are considered. Based on a given set of refractive indices, the software calculates the fundamental and higher mode distributions in the waveguide and, consequently, the shape of the far-field pattern. The effective indices of the propagated modes and their confinement factors are also calculated. Moreover, this program is used to create input data for more sophisticated WIAS-TeSCA software, which is described later in appendix 4.
(*The software QIP is a non-commercial program written by Dr. H. Wenzel (Ferdinand Braun Institute) and Dr. H. J. Wünsche (Humbolt University Berlin).)

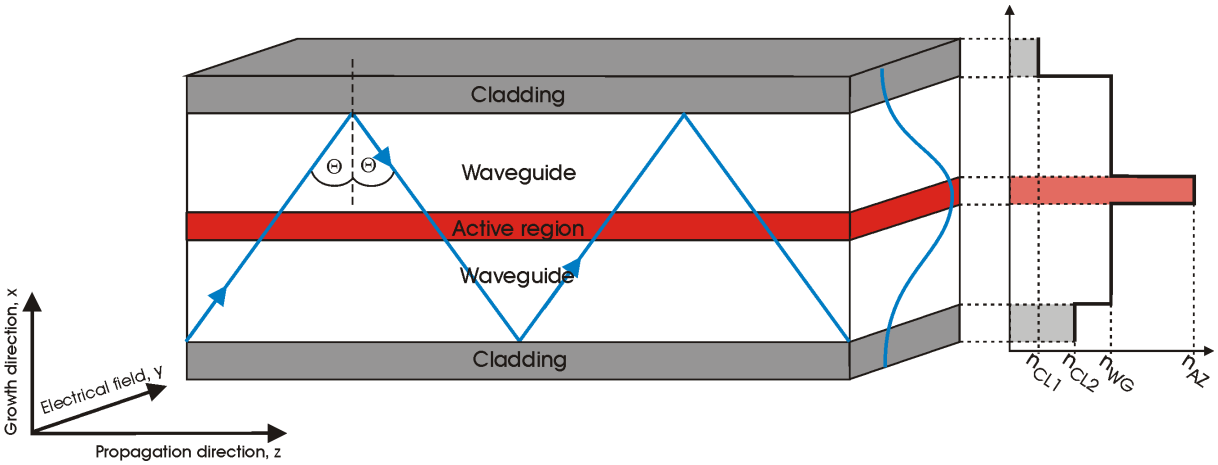

Figure 3.5. Model of a plane waveguide with a vertical refractive index distribution. The illustrated coordinator system is utilized during optical waveguide modeling.

3.2.2. Calculation of the index of refraction

The optical mode in a layered medium is tailored by the refractive indices of the particular epitaxial layers and their thicknesses [6]. The refractive index as a function of photon energy at room temperature is calculated using the Afromowitz model (the modified single oscillator model) [7]. The oscillator model reflects the fact that the optical wave interacts with charged particles that behave like mechanical oscillators. The inclusion of a variation of the imaginary part of the dielectric constant ε_2 (the absorption at the band gap)

gives results that are in good agreement with measurements on AlGaAs, GaAsP and GaInAsP for the photon energy (E) range below and close to the energy gap (E_g) of the material.

The expression for the refractive index in this model is [8]:

$$n^2 - 1 = \frac{E_d}{E_0} + \frac{E_d}{E_0^3}E^2 + \frac{\eta}{\pi}E^4 \ln\left(\frac{2E_0^2 - E_g^2 - E^2}{E_g^2 - E^2}\right), \qquad (3.2.1)$$

where

$$\eta = \frac{\pi E_d}{2E_0^3\left(E_0^2 - E_g^2\right)}, \qquad (3.2.2)$$

with E_0, E_d denoting the energy parameters of the oscillator.
A small imaginary part of 5 meV is added to the photon energy E and it starts to matter when the photon energy equals the band gap energy $E = E_g$.

The parameters E_0, E_d and E_g are known for many binary semiconductors and may be calculated for ternary and quaternary materials by interpolation and by considering appropriate bowing coefficients for better agreement with measurements.

In this work ternary materials like $Al_xGa_{1-x}As$, $In_xGa_{1-x}As$ and $GaAs_yP_{1-y}$ are used. The interpolation scheme for the parameters E_0, E_d and E_g is as follows:

$$P(x) = (1-x)\cdot P(x=0) + x\cdot P(x=1) - x\cdot(1-x)\cdot bowing\,. \qquad (3.2.3)$$

In the above equation, P stands for the parameter that is interpolated (i.e. E_0, E_d or E_d), and x is the mole fraction. In table 3.1, the fit parameters for the utilized ternary components are presented.

$Al_xGa_{1-x}As$	$In_xGa_{1-x}As$	$GaAs_yP_{1-y}$
$E_0 = 3.65 + 0.871\cdot x + 0.179\cdot x^2$	$E_0 = 3.65 + 2.8\cdot x$	$E_0 = 4.72 - 1.07\cdot y$
$E_d = 36.1 - 2.45\cdot x$	$E_d = 36.1 - 26.8\cdot x$	$E_d = 38.4 - 2.3\cdot y$
$E_g = 1.425 + 1.705\cdot x$ $+ 1.44\cdot x^2 + 1.31\cdot x^3$	$E_g = 1.424 - 1.514\cdot x + 0.45\cdot x^2$	$E_g = 2.778 - 1.566\cdot y + 0.21\cdot y^2$

Table 3.1. The fit parameters for $Al_xGa_{1-x}As$ [7], $In_xGa_{1-x}As$ and $GaAs_yP_{1-y}$ [9] materials. The expressions given for E_g are for the direct band gap.

The above interpolation scheme for the energy gap value is utilized only for bulk materials. In this work, the InGaAs and GaAsP materials are used only as thin strained layers (quantum wells or quantum barriers, respectively). The calculated energy gap for a strained layer corresponds to the distance between the conduction band and the heavy-hole valance band. The value of the energy gap is calculated using a model that considers strain and quantization effects described in [4].

3.2.3. The one-dimensional (vertical) optical waveguide model

The propagation of an electromagnetic field in one dimension (vertical direction *x*) is considered. The boundary conditions, imposed by the waveguide geometry, force the electromagnetic radiation to propagate as Transversal Electric (TE) modes with a zero E_z longitudinal component or as Transversal Magnetic (TM) modes – modes with a zero H_z longitudinal component. As the electric field is orthogonal to the wave propagation vector $\vec{E} \perp \vec{k}$, the x component of the electric field also equals zero ($E_x = 0$). This is similar for the magnetic field of TM modes. Structures utilizing highly compressive strained active regions that result in nearly 100% TE polarized light [1-2] are studied. Therefore, only TE modes are considered in further discussions. The coordinate system is presented in figure 3.5

A wave propagating in the plane perpendicular to $x = const$ in direction z is considered:

$$E_y(x,z,t) = E(x) \cdot \exp\left(i\omega t - i\tilde{\beta} z\right), \tag{3.2.4}$$

with ω denoting the angular frequency of the propagating wave and $\tilde{\beta}$ representing the complex propagation constant in the z-direction. The guided wave obeys the time-independent wave equation (1D Helmholtz wave equation):

$$\frac{d^2 E(x)}{dx^2} + \left(k_0^2 \tilde{\varepsilon}_r(x) - \tilde{\beta}^2\right) \cdot E(x) = 0, \tag{3.2.5}$$

where $k_0 = \frac{\omega}{c}$ is the wave vector in vacuum (c – vacuum speed of light) and $\tilde{\varepsilon}_r = \tilde{n}^2$ denotes the relative permittivity as a complex dielectric function. The term $\Im m\tilde{\varepsilon}$ describes the optical gain or losses and $\tilde{n}$ denotes the complex index of refraction [4].

During waveguide simulations the software QIP finds the solution of the Helmholtz equation using the Transfer Matrix Method (step-wise constant) and treats it as a *real* or *complex* vertical waveguide equation by utilizing appropriate boundary conditions.

1. Dirichlet boundary conditions. There are hard boundary conditions imposed for a TE mode (tangential E-field vanishes at the boundary $E_y(x) = 0$). On the internal layer interfaces the continuity of the tangential E and H fields is employed. The *real* waveguide equation is solved considering only a real dielectric function ε_r and a propagation constant β. In this case, the equation (3.2.5) has non-trivial solutions for certain values of β fulfilling the condition:

$$\max(n_{CL1}, n_{CL2}) < \frac{\beta}{k_0} < n_{\max}, \tag{3.2.6}$$

with the modal cut-off condition:

$$\beta = k_0 \cdot \max(n_{CL1}, n_{CL2}). \tag{3.2.7}$$

The n_{max} represents the highest refractive index of a semiconductor layer confined between the claddings with refractive indices n_{CL1} and n_{CL2} (presented in figure 3.5), however, throughout the work symmetric claddings are considered, i.e. $n_{CL1} = n_{CL2}$.

The solutions have a harmonic form in the waveguide. The transversal distribution is

$$E_y(x) = A \cdot \cos(\kappa \cdot x) + B \cdot \sin(\kappa \cdot x) \text{ and } \kappa^2 = k_0^2 n^2 - \beta^2 > 0, \qquad (3.2.8)$$

where $\kappa = \pi / \textit{confinement layer thickness}$. The number of extremes corresponds to the index of the guided mode.

2. Outgoing-wave boundary conditions. The *complex* waveguide equation is solved. Outside the waveguide [10]:

$$k_0^2 n_{substrate}^2 - \tilde{\beta}^2 = \kappa_{Substrate}^2 > 0 \qquad (3.2.10)$$

leading to an exponential solution with an asymptotic form at $|x| \to \infty$:

$$E_y(x) \sim \exp(-i\kappa|x|). \qquad (3.2.11)$$

The solution of the wave-equation utilizing outgoing-wave boundary conditions results in leaky modes [10]. For the structures discussed in this work, the propagating mode in the waveguide is intentionally leaky for higher order modes. This is fulfilled when the real part of the propagation constant (effective index) for a considered m-mode ($\Re e\tilde{\beta}_m$) is smaller than the refractive index of the GaAs-substrate. The substrate is assumed to be infinitely thick.

$$\Re e\tilde{\beta}_m < k_0 \cdot n_{substrate}. \qquad (3.2.12)$$

The losses of the m-mode due to leakage are:

$$\alpha_{leak,m} = 2 \cdot \Im m\tilde{\beta}_m.$$

The effective refractive index quantifies the phase delay per unit length in a waveguide relative to the phase delay in vacuum and is given for an m-mode by [4]:

$$n_{eff,m} = \frac{\Re e\tilde{\beta}_m}{k_0}. \qquad (3.2.13)$$

The fundamental mode, having the largest propagation constant (lower frequency and larger incident angle than higher order modes), experiences higher phase shift per unit length and exhibits the highest value of the effective refractive index.

The optical mode distribution is graphically presented by the software as the distribution of the mode intensity on the x-direction:

$$I_m(x) = |E_{y,m}(x)|^2. \qquad (3.2.14)$$

3.2.4. Vertical divergence angle

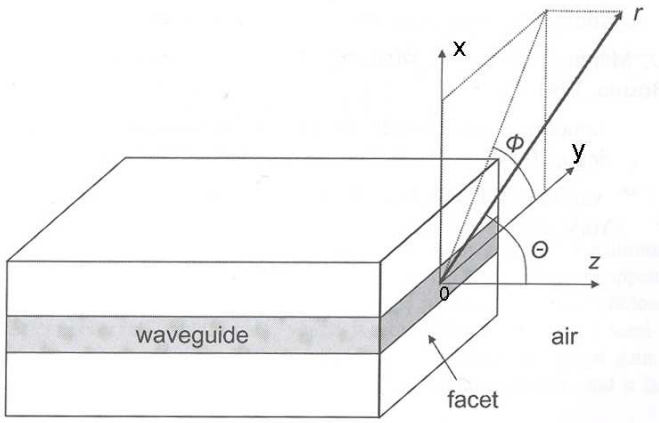

Figure 3.6. The Cartesian and spherical coordinator system of the far-field. (Figure reprinted from [4].)

The emitted optical field is obtained by solving the homogeneous Helmholtz equation for the free-space region [11].
The assumptions for the calculation of the vertical far-field intensity are as follows [4]:

a) The facet is placed at the z = 0 position ;
b) The far-field is expressed in spherical coordinators: generally (r, Θ, Φ) and in case of a vertical far-field $\Phi = 90°$, see figure 3.6.
c) The electric field distribution (near-field) E^{NF} in the vicinity of both sides of the facet is, due to continuity the same. The reflection into other modes is neglected.
d) For large values of r ($r > 5\lambda_0$) the vertical far-field is approximated by [4]:

$$E^{VFF}(r,\Theta) = -\frac{i\exp(-ik_0 r)}{k_0 r}\cos\Theta\vec{E}_{FT}^{NF}(k_0\sin\Theta), \qquad (3.2.15)$$

where $\vec{E}_{FT}^{NF}$ is the Fourier transform of the near-field.

The vertical far-field intensity (for TE modes; E_x=0) at a fixed distance r = r_0 is expressed as:

$$I^{VFF}(\Theta) = \left|\vec{E}^{VFF}(r_0,\Theta)\right|^2 \propto \cos^2\Theta\cdot\left|E_{FT}^{NF}(k_0\sin\Theta)\right|^2 . \qquad (3.2.16)$$

3.3. Phenomenological laser model – Basic relations describing the quantum well diode lasers

3.3.1. Carrier injection and photon generation

The concentration of the carriers injected into the active region (where they take part in the stimulated photon emission process) is determined by the rate equation for the carrier density:

$$\frac{dN}{dt} = \frac{J}{e\cdot d_{AZ}} - \frac{N}{\tau} - R_{Stim} . \qquad (3.3.1)$$

The first term on the right-hand side of the above equation accounts for the carrier generation rate described by the injection current density *J*, where *e* is the elementary charge and d_{AZ} the

active layer thickness [1]. The second term denotes the loss rate for all carriers with the density N having an effective life time τ involved in recombination mechanisms other than stimulated emission. The carrier loss rate is usually presented in the form [1]:

$$R(N) = A_{nr}N + BN^2 + CN^3 = \frac{N}{\tau(N)}, \tag{3.3.2}$$

where the first term, $A_{nr}N$, accounts for nonradiative processes (e.g. lateral, vertical leakage or Shockley-Read-Hall (SRH) recombination). The term BN^2 accounts for the spontaneous radiative recombination rate, and the term CN^3 accounts for nonradiative Auger recombination. The third term of the equation (3.3.1) is the stimulated recombination rate describing the density of generated photons per unit time in the stimulated electron-hole recombination process [12] (the process takes place in the active region).

$$R_{stim} = \frac{dN_{ph}}{dt} = g_m \cdot v_{gr} \cdot N_{ph} \tag{3.3.3}$$

where g_m denotes the material gain, N_{ph} and v_{gr} represent the density and group velocity of stimulated photons, respectively.

The stimulated emission rate can be expressed by the modal gain $g_{\mathrm{mod}\,al}$ and the average internal optical power $\overline{P}(z)$ along the gain medium in the z direction (see appendix 2):

$$R_{Stim} = \frac{g_{\mathrm{mod}\,al}}{d_{AZ} \cdot W} \cdot \frac{\overline{P}(z)}{\hbar\omega} \tag{3.3.4}$$

The gain medium area is described by the vertical active region thickness d_{AZ} and the lateral active width W. The stimulated photons are also a loss mechanism for carriers.

3.3.2. Optical loss, gain and threshold conditions

Implementing a quantum well gain region into a waveguide introduces a perturbation of the dielectric constant $\Delta\varepsilon_r$ as well as a perturbation of the propagation constant $\Delta\beta$. Solving the transverse Helmholtz equation (3.2.5) with the introduced perturbations similar to [12], the modification of the propagation constant can by expressed in the form:

$$\Im m\beta^2 = \frac{k_0^2 \int_{-\infty}^{+\infty} \Im m\varepsilon \cdot \left|E_y(x)\right|^2 dx}{\int_{-\infty}^{+\infty} \left|E_y(x)\right|^2 dx}. \tag{3.3.5}$$

Since

$$\Im m\varepsilon = \begin{cases} \dfrac{n_{AZ}\cdot g_m}{k_0} = const, & |x| \le \dfrac{d_{AZ}}{2} \\ 0, & |x| > \dfrac{d_{AZ}}{2} \end{cases}, \qquad (3.3.6)$$

the integration is limited to the active area (n_{AZ}, d_{AZ} denote the refractive index and thickness of the active region, g_m is the material gain), and considering [4]:

$$\Im m\beta^2 = 2\cdot\Im m\beta\cdot\Re e\beta = g_{\mathrm{mod}al}\cdot k_0 n_{eff}, \qquad (3.3.7)$$

one can obtain the following expression for the modal gain:

$$g_{\mathrm{mod}al} = \frac{n_{AZ}}{n_{eff}}\cdot\frac{\int_{-d/2}^{+d/2}\left|E_y(x)\right|^2 dx}{\int_{-\infty}^{+\infty}\left|E_y(x)\right|^2 dx}\cdot g_m = \frac{n_{AZ}}{n_{eff}}\cdot\Gamma\cdot g_m \qquad (3.3.8)$$

The confinement factor $\Gamma < 1$ exhibits the overlap of the optical transverse mode with the active area and is in the range of 0.01-0.04 for multi-QW diode lasers.

The maximal material gain in quantum well lasers can be empirically expressed by a logarithmic dependence on the injected carrier density [2]:

$$g_m = g_a \ln\left(\frac{N}{N_{Tr}}\right) \qquad (3.3.9)$$

with g_a as empirical gain parameter and N_{Tr} denoting the transparency carrier density. This density corresponds to the case for which the absorption equals generation and thus the material gain equals zero.

The minimum modal gain required to compensate the internal modal losses α_i and the mirror losses α_m, and to initiate the lasing process is called the *threshold gain* g_{th}, which is defined as:

$$\frac{n_{AZ}}{n_{eff}}\cdot\Gamma g_{th} = \alpha_i + \alpha_m \qquad (3.3.10)$$

There are several mechanisms of modal losses α_i decreasing the intensity of the vertical mode. Typically these are losses due to free-carrier absorption, leakage losses of the optical mode, and losses due to scattering of the optical mode on defects or rough interfaces. The last mechanism can be neglected due to high quality diode laser technology that is used nowadays. The general relation for the modal losses can be presented as follows [4, 13]:

$$\alpha_i = \sum_j \frac{n_{AZ}}{n_{eff}}\cdot\Gamma_{j,m}\alpha_j^{fc} + \alpha^{leak} + \left(\alpha^{scat}\right), \qquad (3.3.11.a)$$

where $\alpha_j^{fc} = \sigma_n n_j + \sigma_p p_j$. (3.3.11.b)

The first element of the equation (3.3.11.a) represents losses of the light in the j-layer due to free-carrier absorption. These losses depend on the overlap of the m-light mode with the considered j-layer $\Gamma_{j,m}$; n and p in (3.3.11.b) are the 3D-densities of electrons and holes, σ_n and σ_p are the free-electron and hole absorption cross-sections, respectively. The carrier cross-sections are defined experimentally and are of the magnitude of 10^{-18} cm^2. During loss calculation, both parameters are provided manually to the software.

Losses due to leakage of the optical mode. The optical mode undergoes absorption in the GaAs-substrate and the p-type contact layer and is described by radiation loss assuming an infinitely thick substrate and boundary conditions for the outgoing wave.

The mirror losses for a Fabry-Perot resonator depend on the resonator length L, the front and rear mirrors reflectivities R_f and R_b, respectively, and are described as follows (appendix 3):

$$\alpha_m = \frac{1}{2L}\ln\left(\frac{1}{R_f \cdot R_b}\right). \qquad (3.3.12)$$

The mirror losses equal zero for an infinite length of the optical resonator. In such a case, the modal gain equals the modal loss only.

3.3.3. Optical power-current characteristic

Under steady state conditions corresponding to a continuous carrier injection mode ($t \to \infty$; continues wave (CW) operation) it holds:

$$\frac{dN}{dt} = \frac{I}{e \cdot d_{AZ} \cdot W \cdot L} - R(N) - \frac{g_{\mathrm{mod}\,al}}{d_{AZ} \cdot W} \cdot \frac{\overline{P}}{\hbar\omega} = 0, \qquad (3.3.13)$$

Below or near the threshold the averaged power along the gain medium is $\overline{P} = 0$ ($R_{Stim} = 0$), since the photon density is small. The threshold current can be estimated through:

$$I_{th} = e \cdot d_{AZ} \cdot W \cdot L \cdot R(N_{th}), \qquad (3.3.14)$$

where N_{th} depends on the applied model for the gain $g(N)$ (linear or logarithmic dependence on carrier concentration [1]).

Injection of carriers for currents higher than the threshold ($I = I_{th} + \Delta I$) leads to stimulated light emission ($R_{Stim} > 0$ and $\overline{P} > 0$) and (3.3.13) takes the form:

$$\frac{\overline{P}}{\hbar\omega} = \frac{\dfrac{I_{th} + \Delta I}{e \cdot d_{AZ} \cdot W \cdot L} - R(N_{th})}{\dfrac{g_{\mathrm{mod}\,al}}{d_{AZ} \cdot W}} \qquad (3.3.15)$$

Substituting expression (3.3.14) into (3.3.15) this yields:

$$\overline{P} = \frac{\hbar\omega}{e} \cdot \frac{I - I_{th}}{g_{modal} \cdot L}. \qquad (3.3.16)$$

Since the output power is the energy leaving the laser facet in a time interval, the relation between the output optical power and the internal averaged power can be presented in the form [2]:

$$P_{out}\left(\overline{P}\right) = L \cdot \alpha_m \cdot \overline{P}. \qquad (3.3.17)$$

Substituting (3.3.16) into (3.3.17) and considering (3.3.10) this yields an expression for the optical power in the linear range above threshold:

$$P_{out} = \frac{\hbar\omega}{e} \cdot \frac{\alpha_m}{\alpha_i + \alpha_m} \cdot \left(I - I_{th}\right) \qquad (3.3.18)$$

In real laser devices, the number of carriers that are involved in the stimulated recombination process is less than the number of total injected carriers. The ratio between these two types of carriers is defined as the internal quantum efficiency $\eta_i^{st} < 1$. Therefore, the equation (3.3.18) has to be modified:

$$P_{out} = \eta_i^{st} \cdot \frac{\hbar\omega}{e} \cdot \frac{\alpha_m}{\alpha_i + \alpha_m} \cdot \left(I - I_{th}\right) \qquad (3.3.19)$$

The internal efficiency (η_i^{st}) is one of the most important parameters for a high power laser. It influences the external efficiency and the optical output power. The internal efficiency parameter is governed by several mechanisms like lateral carrier spreading and nonradiative recombination processes [14]. In the lateral carrier leakage process, a part of the supplied current does not enter the active geometrical area. Therefore, these carriers do not take part in the stimulated recombination process. Other mechanisms reducing the internal efficiency are thermionic carrier escape and vertical carrier leakage if the potential barriers of the active region are too low. The non-confined carriers take part in non-stimulated recombination processes in the barriers or confinement layers (waveguide, cladding). The non-stimulated recombination process can involve electron-hole recombination in the confinement layer, nonradiative recombination of free-carriers on defects (Shockley-Read-Hall) or Auger recombination.

The diode laser performance is also characterized by the differential external efficiency (η_{ext}^{d}) and the conversion efficiency (η_C).

The differential external efficiency (η_{ext}^{d}) is defined as the ratio between the number of emitted photons (N_{ph}) (per time unit) through a laser facet and the number of injected charged-carriers (N_{el}) (per time unit):

$$\eta_{ext}^{d} = \frac{dN_{ph}}{dN} = \frac{dP/dI}{\hbar\omega/e}. \qquad (3.3.20)$$

Combining (3.3.19) and (3.3.20), the η_{ext}^{d} parameter can be expressed as a function of the internal efficiency and the internal optical and mirror losses:

$$\eta_{ext}^{d} = \eta_{i}^{st} \frac{\alpha_m(L)}{\alpha_m(L)+\alpha_i}. \tag{3.3.21}$$

To show its dependency on the laser cavity length, the η_{ext}^{d} parameter is often presented in the form:

$$\eta_{ext}^{d} = \frac{\eta_{i}^{st}}{1+\frac{2\alpha_i L}{\ln\left(\frac{1}{R_f R_r}\right)}}. \tag{3.3.22}$$

The conversion efficiency (η_C) shows how efficiently the electric power injected into the laser (P_{el}) is converted to optical output power (P_{opt}) and is described by a ratio of the two powers:

$$\eta_C = \frac{P_{opt}}{P_{el}} = \frac{P_{opt}}{I \cdot U(I)} = \frac{\eta_{ext}^{d} \frac{\hbar\omega}{e}(I - I_{th})}{I(U_0 + IR_s)}, \tag{3.3.23}$$

where $U(I)$ is the current-voltage characteristic of the diode, U_0 is the 'turn-on voltage' of the diode and R_s is the series resistivity given by:

$$R_s = \frac{\sum_j d_j \rho_{s_j}}{LW}. \tag{3.3.24}$$

The terms d_j and ρ_{s_j} denote the thickness and the sheet resistivity of the j epitaxial-layer, respectively. The term U_0 is the voltage drop across the band gap and $I^2 R_s$ is the dissipated power due to Ohmic heating.

3.3.4. Thermal parameters influencing the semiconductor laser performance

3.3.4.1. The characteristic temperatures T_0, T_1

The parameters T_0 and T_1 characterize the sensitivity of the laser threshold current and the external efficiency, respectively, on the temperature of the laser active region. From the experimental observation, it has been empirically determined that the temperature dependence of the threshold current density and the temperature dependence of the external efficiency are usually well approximated by:

$$J(T) = J(T_{ref}) \exp\left(\frac{T - T_{ref}}{T_0}\right) \quad \text{or} \quad \ln J(T) = \ln J(T_{ref}) + \frac{T - T_{ref}}{T_0}, \qquad (3.3.25)$$

$$\eta_{ext}^{d}(T) = \eta_{ext}^{d}(T_{ref}) \exp\left(\frac{T_{ref} - T}{T_1}\right) \quad \text{or} \quad \ln \eta_{ext}^{d}(T) = \ln \eta_{ext}^{d}(T_{ref}) - \frac{T - T_{ref}}{T_1}. \qquad (3.3.26)$$

The reason for laser performance deterioration is the optical gain (g_m) reduction with increasing temperature [4, 12]. In order to compensate for the decreased optical gain, higher carrier densities are required. An increased carrier density, however, implies increased nonradiative recombination ($\sim A_{nr} N$) leading to further heating of the laser crystal. Additionally, the increased temperature gives rise to thermionic carrier emission out of the active region. These processes consequently lead to an increment in the threshold current as well as to a reduction of the injection efficiency, observed as reduction of the external efficiency of the laser structure. From the above equations, one can see that laser structures, which are more sensitive to the temperature, exhibit lower characteristic temperatures T_0 and T_1. The improved vertical carrier confinement (obtained for example by high quantum barriers) is expected to result in a more temperature stable threshold current and external efficiency of the laser. Moreover, laser devices with a high optical overlap within the gain region (high confinement factor Γ) and a long resonator (low mirror loss, low threshold current density) should exhibit a higher characteristic temperature T_0.

The experimental temperature dependences of the threshold current and the external efficiency of a MQW diode laser are presented in figure 3.7.

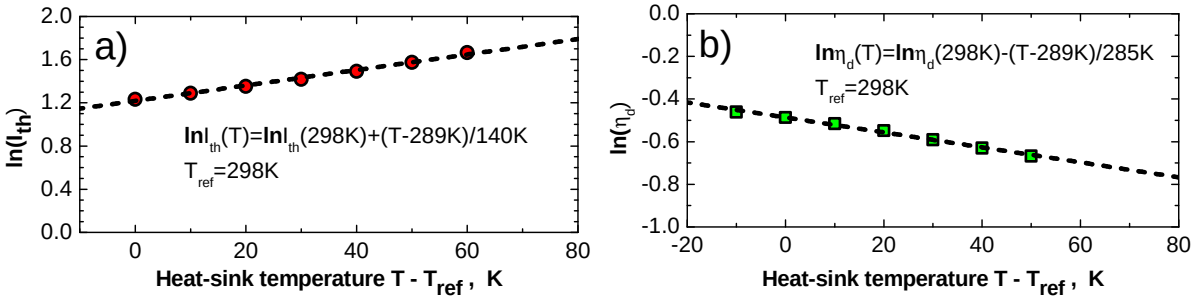

Figure 3.7. The experimental temperature dependences of the threshold current (a) and the external efficiency (b) of a multi-QW InGaAs/AlGaAs broad area device on the heat-sink temperature from 15°C to 85°C. (Device geometry: electrical stripe width W = 100 μm, cavity length L = 8 mm; Structure C1690-6)

However, the threshold and slope of the QW lasers (broad area devices) often show a deviation from the exponential thermal behavior mainly at high temperatures. Examples of the T_0, T_1 thermal behavior of a 1060 nm laser are presented in figure 9.4. The significant deterioration of T_0, T_1 parameters is likely to be caused by vertical carrier leakage and additional or increased non-radiative processes that often happen in long-wavelength lasers, i.e. Auger recombination [15].

3.3.4.2. The thermal resistance

The thermal resistance R_{th} [K/W] defines the temperature rise of the laser active region compared to an ambient temperature (ΔT_j) during laser operation and is described as:

$$R_{th} = \frac{\Delta T_j}{P_{waste}} = \frac{T_{AZ} - T_{ref}}{\left(P_{el} - P_{opt}\right)}, \qquad (3.3.27)$$

where T_{AZ} refers to the active region temperature and T_{ref} refers to the heat sink temperature - usually set to 300 K. The wasted power $P_{waste} = P_{el} - P_{out}$ is the difference between the supplied electrical power and the produced optical power (the fraction of injected electrical power which was not converted to optical power) and is the reason for laser heating.

Through good management of the heat dissipation, the thermal resistance can be reduced. By mounting a laser chip with the epitaxial-junction down to the heat-sink, for example, the flow of the generated heat through the thick substrate is strongly reduced and the thermal conductivity is improved (see figure 3.8).

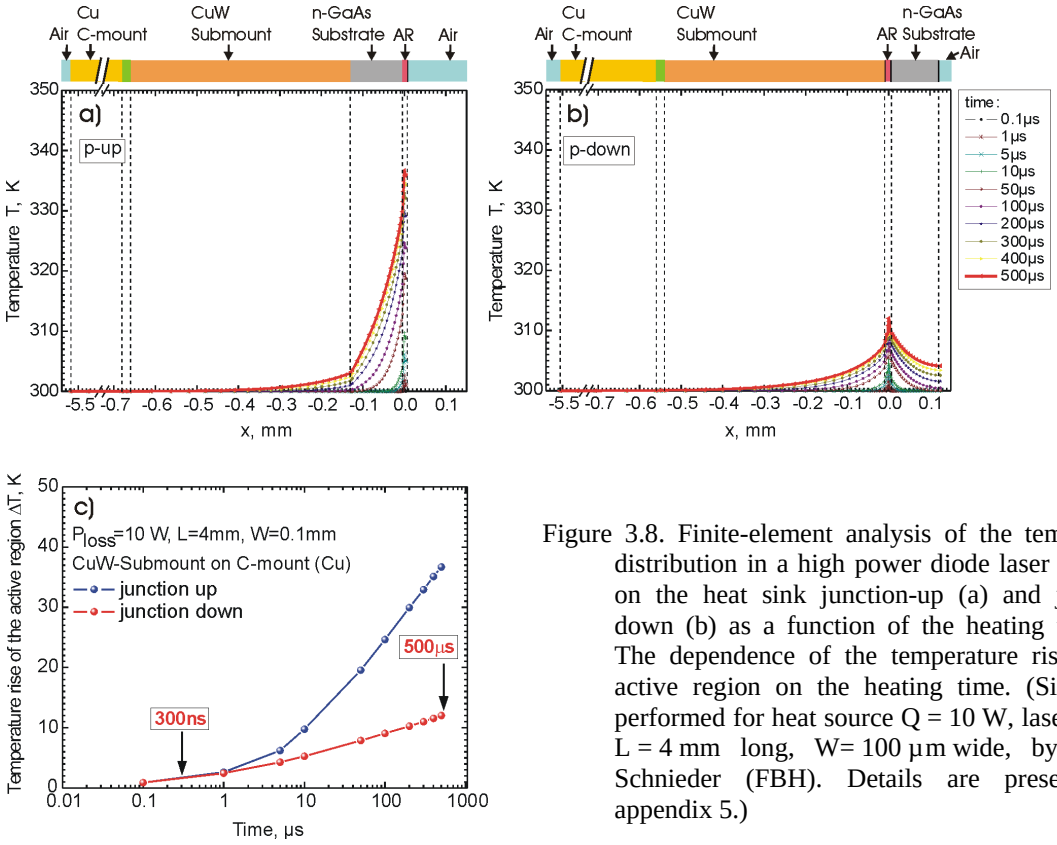

Figure 3.8. Finite-element analysis of the temperature distribution in a high power diode laser mounted on the heat sink junction-up (a) and junction-down (b) as a function of the heating time. (c) The dependence of the temperature rise of the active region on the heating time. (Simulation performed for heat source Q = 10 W, laser cavity: L = 4 mm long, W= 100 µm wide, by Dr. F. Schnieder (FBH). Details are presented in appendix 5.)

Altogether, the optical power can be described as:

$$P_{opt} = \eta_d \cdot \exp\left(-\frac{\Delta T_j(R_{th})}{T_1}\right) \cdot \left(I - I_{th} \cdot \exp\left(\frac{\Delta T_j(R_{th})}{T_0}\right)\right), \qquad (3.3.28)$$

with $\Delta T_j = R_{th}\left(I \cdot \left(U_0 + IR_s\right) - P_{out}\right)$ and the external efficiency and threshold current being a function of temperature (see equations (3.3.25-26)).

Equation (3.3.28) is usually used as an empirical tool for the extrapolation of the power-current characteristic. However, this equation does not apply when the T_0, T_1 parameters decrease above a certain temperature of the active region (e.g. sample C1357-6,

chapter 9) and when considering the temperature dependence of the thermal resistance like in [16].

3.3.4.3. Catastrophic Optical Mirror Damage (COMD)

The catastrophic optical mirror damage (COMD) is one of the most common power limitations of the high power diode-lasers leading to irreversible damage of the laser chip. The COMD is a sudden facet degradation due to increased facet temperature caused by nonradiative surface recombination processes in the vicinity of the facet surface.

The power leading to COMD is proportional to the internal power density $\overline{p}_{\text{int}}$ (often indicated as $\overline{p}_{COMD}$, i.e. the internal power density which is reached at the moment of COMD failure). For a given output power P_{out}, the internal power is given by [17]:

$$\overline{p}_{\text{int}} = P_{out} \cdot \frac{1+R_f}{1-R_f} \cdot \frac{1}{\frac{d}{\Gamma} \cdot W}, \qquad (3.3.29)$$

where R_f denotes the reflectivity of a front facet, d is the quantum well thickness and Γ is the optical confinement factor. From the above equation, one can see that the facet heating, leading to its failure, depends on the modal cross-section (i.e. equivalent vertical spot-size (d/Γ) and lateral stripe width) as well as on the reflectivity of the front facet. Reducing the optical mode intensity (and thereby increasing the COMD threshold) by increasing the modal cross section leads to a higher output power before catastrophic optical damage (COD) occurs (chapter 8, figure 8.3).

4

Process technology and packaging of high power diode lasers

4.1. Epitaxy of high power 1050 – 1150 nm diode laser structures based on GaAs substrates

The epitaxial structures are grown on an n-GaAs (100) substrate [1] by means of metal organic vapor phase epitaxy (MOVPE).

The emission wavelength range of the diode lasers characterized in the framework of this thesis is 1050 nm to 1130 nm. This wavelength range is obtained utilizing InGaAs as the active region material. The active region is embedded in $Al_xGa_{1-x}As$ waveguides and cladding layers that are lattice matched to the GaAs substrate. (The lattice mismatch between AlAs and GaAs is only $1.3 \cdot 10^{-3}$ [1])

Long wavelength emission requires the incorporation of a high indium content ($x \approx 28\%$ for 1050 nm to $x \approx 37\%$ for 1150 nm) in the $In_xGa_{1-x}As$ quantum well. This leads to high compressive strain of the layer. To avoid strain relaxation and the formation of defects, three designs of the active region are proposed.

1) Utilization of thick (50-100 nm) GaAs barriers between quantum wells. The stress from a high compressively strained quantum well is relaxed during the barrier growth and does not influence the neighboring quantum well [2-3]. This design works especially well when a GaAs waveguide is utilized.
2) Utilization of an additional strain compensating GaAsP layer (~20 nm thick) sandwiched between GaAs barriers (~15 nm thick) [2]. For a fully compensated active region, the condition $\left|2 \cdot \varepsilon_{InGaAs} \cdot d_{InGaAs}\right| \approx \left|\varepsilon_{GaAsP} \cdot d_{GaAsP}\right|$ has to be fulfilled. The terms ε and d denote the strain and the thickness, respectively, of the particular layer [3].
3) Utilization of tensely strained GaAsP layers as a quantum barrier (~7 nm thick) [4]. The use of oppositely strained barrier layers to those produced by the QW compensates the misfit stress appearing in the active region. This design can be used for any composition of $Al_xGa_{1-x}As$ waveguide layers. Here, an additional thin GaAsP layer (a so called spacer) at the interface of the QW and the waveguide should be introduced [4-5]. Moreover, V. Duraev [6] notes that the height of the quantum barrier (related to the GaP mole fraction) should not be much higher than the waveguide potential level (in both the conduction and the valence bands) to avoid inhomogeneous pumping of the quantum well.

The schemes of the active region designs are presented in figure 4.1.

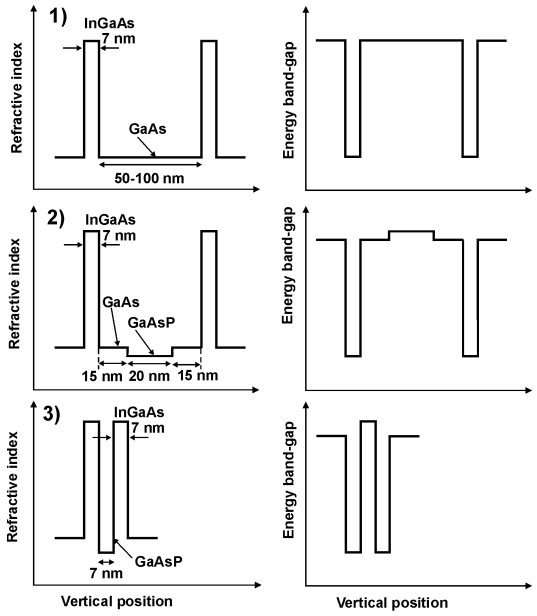

During the growth of the structures presented in this work the first and the third active region design was utilized (GaAs or GaAsP barriers).

The epitaxial growth requires an optimal growth temperature, which is different for the active region and the other epitaxial layers. The growth temperature of the active region for emission wavelengths of 1100-1200 nm is examined by Bugge et al. [4, 7]. The active regions of the presented structures in this work were grown at the temperatures of 650°C and 530°C for emission wavelengths of 1060 nm and 1130 nm, respectively. The $Al_xGa_{1-x}As$ waveguide and cladding layers were grown at 770°C. The growth details are presented in [2, 4-5].

The waveguide, the cladding, and the contact epitaxial layers are doped during growth. The impurity atoms of zinc and carbon were introduced to obtain p-type material and atoms of silicon were introduced to obtain n-type material. The active region stays intentionally un-doped. GaAs is a material with a high carrier mobility and therefore, when used as a waveguide, the thick region facing towards the active region is intentionally undoped and lowly doped ($<5\cdot10^{17}$ cm^{-3}) towards the cladding layers. The low doping of the waveguide ensures low optical losses. The undoped GaAs material exhibits intrinsic n-type character ($n\sim5\cdot10^{15}$ cm^{-3}). In order to place the p-i-n junction at the active region, the first 100 nm of the p-waveguide is lowly doped ($p<5\cdot10^{16}$ cm^{-3}) with carbon atoms (carbon has a negligible diffusion coefficient [8], so it does not influence the active region which should stay free from undesired impurity atoms). In the case of AlGaAs material, a higher doping level is introduced in order to compensate for the lower carrier mobility of the material and to ensure higher conductivity. For the waveguides a doping level of around $1\cdot10^{17}$ - $1\cdot10^{18}$ cm^{-3} is utilized, whereas for the cladding layers a higher doping level ($\sim2\cdot10^{18}$ cm^{-3}) is introduced. Because in SLOC structures only a small fraction of the optical mode propagates in the cladding, the high doping will not increase the optical losses dramatically.

The epitaxial structures discussed in this work consist of highly compressively strained multi-QW active regions that are embedded in $Al_xGa_{1-x}As$ waveguides and cladding layers. On top of the p-cladding layers, a highly p-doped 100 nm thick GaAs contact layer is grown. The structures discussed in this work differ in the number of quantum wells (two or four quantum wells (DQW, QQW)), each being 7 nm thick, the emission wavelength (1130 nm, 1100 nm and 1060 nm), the waveguide and cladding layer thicknesses and the aluminum content. The calculated (using QIP software) energy bands and refractive index profiles of each epitaxial design are presented in appendix 1.

The epitaxial structures are grown on ~ 350 – 450 µm thick n-GaAs substrates. After the growth process, the substrate is polished to a thickness of ~ 130 µm for better cleaving during the technology process. The sizes of the wafers used are 2” or 3”.

4.2. Processing of edge emitting broad area diode lasers

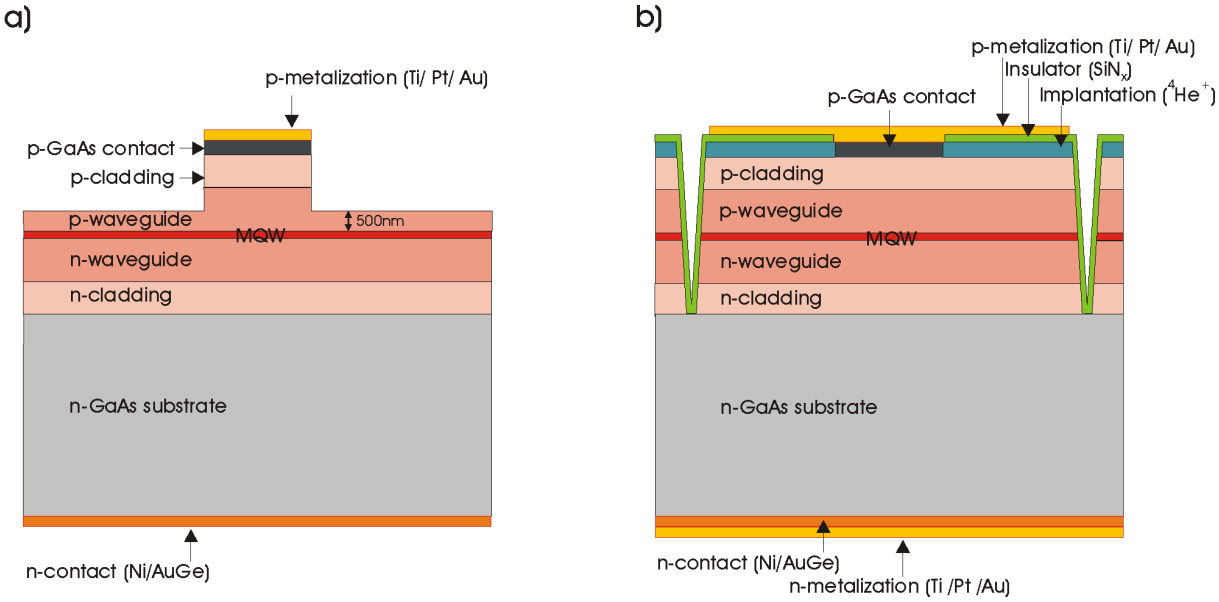

Figure 4.6. (a) Schematic structure of an edge emitter processed particularly for ‘pre-test’ measurements. (b) A fully processed gain-guided broad area single emitter.

4.2.1. Technology of diode lasers for ‘Pre-test’

The ‘pre-test’ is a quick test process of uncoated and unmounted laser chips in order to obtain material information. During the ‘pre-test’ measurement process, the laser chip is characterized under short current pulse operation (1500 ns, 1 kHz) as well as at low current injection levels (max. 2 A). The produced heat during the laser assessment is minimal and therefore the laser chips are neither soldered to the heat-sink nor are metal bound wires soldered to the laser chip. The electrical potential is applied to the diode laser through two thin metal needles contacted to the p-ohmic metal contact (two needles are used to ensure homogeneous current injection along the whole laser chip) and to the measurement holder on which the laser chip, with its n-contact facing the holder, is placed.

The laser chips for the ‘pre-test’ measurement are index-guided structures and are prepared in the following way.

In the first step, a photo-resist mask for metallization with a 100 µm (or 200 µm) wide window is applied on top of the epitaxial structure (p-side). Next, the 445 nm thick ohmic contact is evaporated on top of the highly doped p-GaAs epitaxial contact layer. The metallization system used is Ti(30 nm)/Pt(40 nm)/Au(375 nm), where Pt is used to prevent gold diffusion into the GaAs layer and Ti is an adhesion promoter material. The resist mask is removed in the lift-off process. In the following step, the mesa (the lateral confinement region) is realized during the wet chemical etching process with the p-contact acting as a mask. The residual thickness (the distance from the active region to the last epitaxial layer in the etched -passive- region) is 500 nm. The so created mesa provides a good electrical

confinement without the utilization of additional dielectric barriers outside. The calculated current spreading [9] is around 5% for a device with a 100 µm wide stripe and 3% for a 200 µm stripe. In the next step, the 450 µm thick n-GaAs substrate is polished down to a thickness of 130 µm via mechanical polishing. Finally, the 250 nm thick n-contact is evaporated. The metallization system used is Ni/AuGe/Ni/AuGe, where the first Ni(5 nm)/AuGe(110 nm) layer is used to create the ohmic contact while the second layer of Ni(25 nm)/AuGe(110 nm) is used to mechanically consolidate the contact surface. A schematic drawing of the cross-section of the 'pre-test' laser chip is presented in figure 4.6a.

Such processed laser chips can be easily cleaved along cleavage planes ([110] direction) to any cavity length. The laser facets are neither passivated nor coated. The natural reflectivity of the GaAs material system for the optical fundamental mode is ~ 31%.

4.2.2. Technology of high power broad area single emitters

The broad area emitters tested in the frame of this work are gain-guided laser diodes (figure 4.6b). The ion-implantation ($^4He^+$) of the highly doped p-GaAs semiconductor layer compensates the predominant doping and transforms the layer characteristics to that of an isolator. This compensated GaAs as well as dielectric current barriers (SiN_x) are used to define the contact window of the devices. The contact window (60 µm, 100 µm and 200 µm) is defined on top of the epitaxial structure to minimize lateral current spreading or pumping of regions outside the contacts. The electrical contact on the p-side is created by using the common metallization system of Ti/Pt/Au (445 nm). On the n-side, in order to achieve good ohmic contact, an additional 250 nm thick Ni/AuGe alloy is utilized between the n-GaAs substrate and the 300 nm thick metallization (the substrate is polished down to 130 µm before the n-contact is evaporated). For easier wire bonding and soldering to the heat sink the metal contacts are strengthened by a 3-6 µm thick plated Au layer.

In order to avoid lasing perpendicular to the intended direction (so called ring modes), V-shaped trenches are etched on both sides of the window contact. In figure 4.6b, the schematic structure of the gain-guided edge emitter is illustrated.

Next, the processed laser bars on the wafer are cleaved. The cleaved facets are cleaned in vacuum with atomic hydrogen and next passivated with ZnSe [10-11]. The passivation process minimizes defect formation and inhibits failure due to catastrophic optical mirror damage (COMD). The ZnSe layer prevents the oxygen in the dielectric mirrors from penetrating into the active region and also minimizes the surface recombination processes being the factors leading to facet degradation. The laser facets are subsequently coated with dielectric layers to achieve various reflectivities on the front (R_f) and back (R_b) facets. During this process a pair of TiO_2/Al_2O_3 dielectric layers is sputtered, in order to obtain a low reflection coefficient (on the front facet R_f = 0.1% - 2%). If a high reflection coefficient is desired, (on the back facet R_b ~95%) several pairs of Si/Al_2O_3 dielectric layers are used.

4.3. Mounting of high power diode lasers

The processed broad area laser chips are mounted junction side down (p-down) on the CuW submounts for better heat transport [12] using the hard solder medium AuSn (melting temperature 280°C). $Cu_{0.1}W_{0.9}$ material is used in this step mainly because it has a similar coefficient of linear thermal expansion ($CTE_{CuW} = 6.5 \cdot 10^{-6} / K$) to that of the diode laser crystal (GaAs $CTE_{GaAs} = 6.4 \cdot 10^{-6} / K$). This way the laser chip is protected from mechanical stress during its operation (for comparison Cu: $CTE_{Cu} = (16-17) \cdot 10^{-6} / K$ [13]). Another

advantage of the CuW material is its high thermal conductivity (180 W/mK) [13, 14], though still lower than that of pure Cu. The coefficient of thermal expansion and the thermal conductivity of materials for heat spreaders are illustrated in figure 4.7.

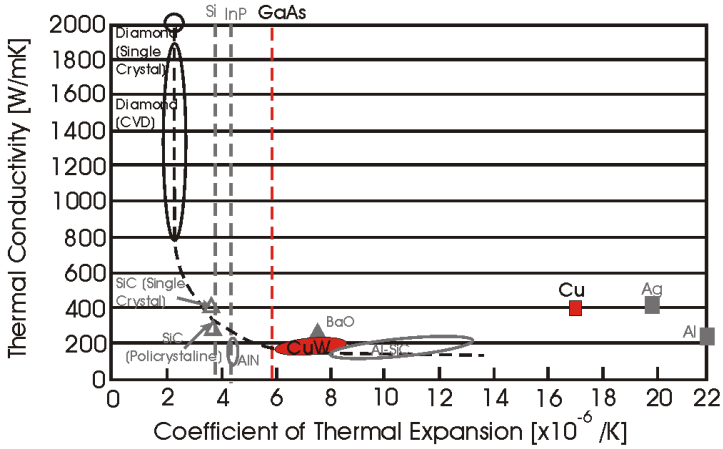

Figure 4.7. Coefficient of thermal expansion (CTE) and thermal conductivity of materials used as heat spreaders. The materials of main interest: Cu and CuW are compared with GaAs. (Redrawn from [15].)

Subsequently, the laser chip on the CuW submount (heat spreader) is soldered onto a commercially available Cu-block heat sink like an open heat sink (c-mount) or a conduction cooled package (CCP), both depicted in figure 4.8. Here, soft solder (PbSn) is used due to its lower melting temperature (~183°C) in order to prevent the hard solder from melting. The gold wires are bonded to the n-contact employing an ultrasonic bonding process. More details about the mounting processes, particularly concerning the techniques and materials used, are given in [14]. Figure 4.8 shows the schematic picture of a mounted laser chip on a heat-sink.

Such prepared devices are ready for further characterization. Lasers mounted on c-mounts are typically characterized under the quasi continuous wave (quasi-CW) operation mode. Since the larger CCP copper blocks remove the heat from the laser chip more efficiently (than c-mounts), the laser devices mounted on this type of heat-sink can also be characterized under the CW mode.

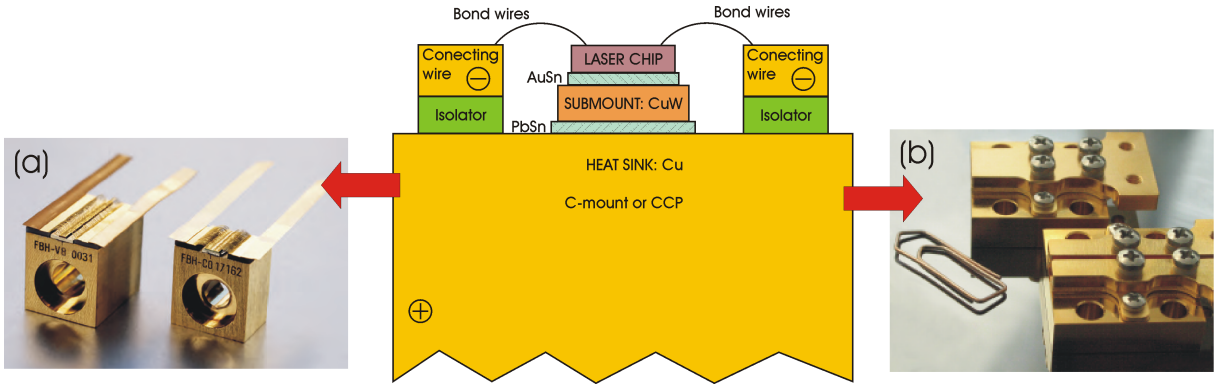

Figure 4.8. The diagram of mounted laser chip on a Cu-heat-sink. Standard heat-sinks used during laser characterization: (a) open heat-sink (c-mount) and (b) conduction cooled package (CCP).

5

Measurement techniques and experimental setups for diode laser characterization

Within this work, diode lasers were generally characterized in two steps. First, the length-dependence measurement of uncoated and unmounted laser chips is performed. Here, intrinsic parameters like internal loss α_i, internal efficiency η_i^{st}, modal gain Γg_0 and transparency current density J_{Tr} are determined. Second, after the previously explained laser facet coating and laser mounting process, the laser devices are characterized to determine:

a) the external electro-optical parameters like: threshold current I_{th}, optical power at an operation current P_{Iop}, slope efficiency S, maximum conversion efficiency $\eta_{C,\max}$ and series resistance R_s;

b) thermal parameters like: characteristic temperatures T_0, T_1 and thermal resistance R_{th};

c) laser beam parameters like: beam propagation factor M^2 and vertical and lateral near-field and far-field profiles.

5.1. Characterization of uncoated and unmounted laser chip

5.1.1. Length-dependence measurement, called 'Pre-test'

The intrinsic parameters of a laser structure are extracted from power-current characteristics for different cavity lengths. The measurements are performed under a short current pulse duration of 1500 ns with a repetition rate of 5 kHz at a temperature of 20°C.

The main assumptions of this experiment are:

- the logarithmic dependence of the material gain on the injected current density:

$$g_m = g_0 \ln\left(\frac{J}{J_{Tr}}\right), \qquad (5.1.1)$$

- the internal losses (α_i), and internal efficiency (η_i^{st}) do not depend on the laser cavity length.

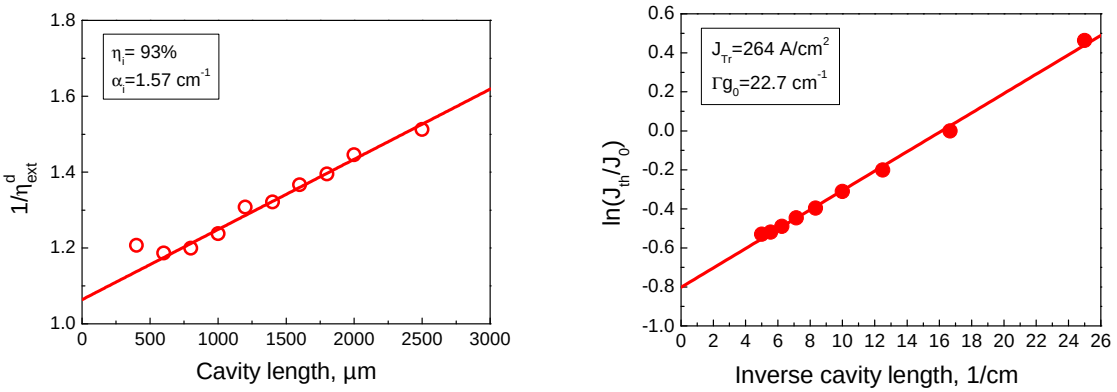

Figure 6.1. The experimental 'pre-test' results (points) and the performed linear fit (solid line) of a 1060 nm multi-QW SLOC structure (C1625-6).

Plotting the inverse differential external efficiency versus cavity length:

$$\frac{1}{\eta_{ext}^{d}} = \frac{1}{\eta_{i}^{st}} + \frac{\alpha_i}{\ln\frac{1}{R}} \cdot L \tag{5.1.2}$$

and performing a linear fit delivers intrinsic parameters like: internal efficiency and internal losses. The above mentioned relation is a product of a modification of (3.3.31) with the assumption of equal facet reflectivities (R).

From the threshold conditions (3.3.10) and the logarithmic dependence of the maximum material gain on the current density (6.1.1), one can express the threshold current density [1] in the following form [2]:

$$J_{th} = J_{Tr} \exp\left(\frac{\alpha_i + \alpha_m(L)}{\frac{n_{AZ}}{n_{eff}} \cdot \Gamma g_0} \right), \tag{5.1.3}$$

where α_m is the resonator length dependent mirror loss (known also as the resonator loss) (3.3.12). Plotting the natural logarithm of the threshold current density versus the inverse cavity length:

$$\ln J_{th} = \ln J_{\infty} + \frac{\ln\frac{1}{R}}{\frac{n_{AZ}}{n_{eff}} \cdot \Gamma g_0} \cdot \frac{1}{L}, \tag{5.1.4}$$

$$\text{where } \ln J_{\infty}(\alpha_m = 0) = \frac{\alpha_i}{\frac{n_{AZ}}{n_{eff}} \cdot \Gamma g_0} + \ln J_{Tr} \tag{5.1.5}$$

and performing a linear fit delivers the transparency current density J_{Tr} and the modal gain parameter Γg_0. The parameter J_{∞} is an extrapolation of the threshold current density for a

laser with infinite cavity length. In the experiment, the threshold current density is normalized to the threshold current density of the shortest laser (with the highest threshold). An example pre-test result of a 1060 nm laser structure is shown in figure 5.1.

5.2. Characterization of mounted laser devices

5.2.1 Power-Voltage-Current characteristics and optical spectrum

High power diode lasers are generally characterized at 25°C heat-sink temperature under three operation modes:

a) *continues wave (CW) operation* – the laser diode is continuously pumped with an electrical current and thus continuously emits light. The CW regime leads to a strong heating of the active region.

b) *quasi-continuous wave (quasi-CW) operation* – the electrical current source supplying the electrical power to the laser diode is switched on for short time intervals. The 'switch-on' time is typically hundreds of µs to several ms long, and the 'switch-off' time is 10 ms to 0.1 s. The duty-cycle (d-c = pulse duration (t)*repetition rate (f)) is in the range of a few percent. This leads to a reduction of the heating of the active region (figure 5.2). The current pulse duration (time of current density injection) is ~ 10^5-10^6 longer than the temporal variation of the carriers (ns) (and photons (ps)) densities in the laser. Therefore, the laser process is considered as to be close to the steady state conditions – the laser is optically in the state of CW operation. The quasi-CW conditions for lasers tested during this work are: t = 500 µs, f = 20 Hz (50 ms) repetition rate (d-c = 1%).

c) *short pulse operation* ('zero heat' conditions) – the electrical current is supplied to the laser diode in a time duration of several hundreds of ns. In this work, lasers were tested under a 300 ns current pulse duration with a 1.67 kHz repetition rate, corresponding to 0.05% duty-cycle. Under such operating conditions, the laser is optically in the state of CW operation. However, the temperature of the active region is significantly reduced (figure 5.2). The great reduction of the crystal heating strongly increases the threshold for damage due to overheating. It therefore enables the operation with high peak output powers.

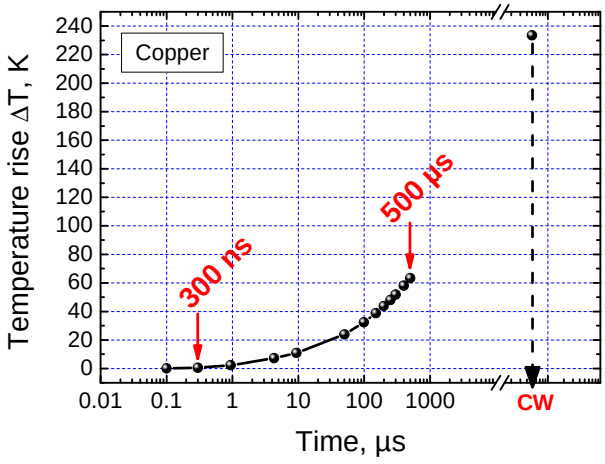

Figure 6.2. Finite-element analysis of transient temperature of the active layer. Simulation performed for a heat source Q = 70 W, laser cavity: L=4 mm long, W = 200 µm wide. (Simulated by Dr. F. Schnieder at FBH; details are given in appendix 5).

From the power-voltage-current (P-U-I) characteristics the main electro-optical parameters are determined. The threshold current I_{th} is determined from a Gaussian fit of the second derivative of the power-current characteristic. The slope efficiency S is a ratio of the optical power to the supplied electrical current above threshold in the linear range:

$$S = \frac{\Delta P_{opt}}{\Delta I} \qquad (5.2.1)$$

and is usually determined from the linear fit to the P-I characteristic.

From the voltage–current characteristic $U(I)$ the 'turn-on voltage' of the diode U_0 and the series resistance R_s are determined. The 'turn-on voltage' is determined by an extrapolation of U(I) measured above the threshold (in linear range) back to I = 0. The series resistance is determined by linear fit to U(I) above the threshold.

From the power-current P(I) and the voltage-current characteristics, the dependence of the conversion efficiency η_C (discussed in chapter 3) on the injected current can be plotted.

$$\eta_C(I) = \frac{P_{out}(I)}{I \cdot U(I)} \qquad (5.2.2)$$

In practice, the measured conversion efficiency, presented later on in this work, is actually a wall-plug efficiency $\eta_{W\text{-}P}$, where the series resistance of the laser package is additionally taken into account. Therefore, the wall-plug efficiency is smaller than the conversion efficiency.

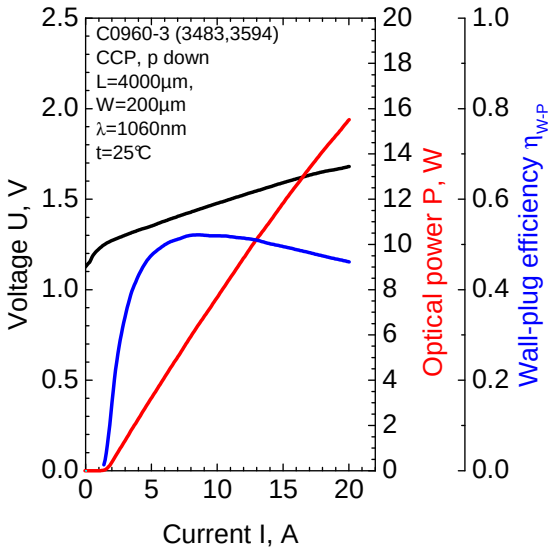

Figure 5.3. An example P-V-I characteristic of a high power broad area single emitter diode laser (W=200µm, L=4000µm, CW operation mode).

Thermal resistance measurement

The thermal resistance R_{th} [K/W] of a laser diode, defined in chapter 3, is measured in the following way.

First, the measurement of the temperature dependence of the photoluminescence peak energy is performed. This measurement delivers the thermal band-gap shrinkage parameter dE_g/dT. This is a characteristic parameter for the active region material. For structures based on the InGaAs material, $\frac{dE_g}{dT} \approx -0.5 \frac{meV}{K}$ [3]. This relation can also be presented as a function of the wavelength:

$$\left|\frac{d\lambda}{dT}\right| = 0.4 \cdot \left(\frac{\lambda}{\mu m}\right)^2 \left[\frac{nm}{K}\right] \qquad (5.2.4)$$

(from a fit to an experimental set of data $\Delta\lambda/\Delta T = f(\lambda(T_{ref}))$).

Second, the optical spectrum is measured as a function of increasing electrical power ($I \cdot U$) at a fixed heat-sink temperature of 298 K. The lasing wavelength shift $\Delta\lambda$ plotted versus the wasted power P_{waste} typically exhibits a linear behavior, from which a coefficient $\Delta\lambda / \Delta P_{waste}$ can be determined. Converting the wavelength change into a temperature rise using the $d\lambda / dT$ relation (eq. 5.2.4), the thermal resistance of the laser chip together with the mounting package (when characterized in the CW regime) is estimated.

Characteristic temperatures T_0 and T_1

The temperature dependence of the threshold current and the slope efficiency are defined by the characteristic temperatures T_0 (eq. 3.3.25) and T_1 (eq. 3.3.26), respectively.

The threshold current and the slope efficiency are determined from pulsed power-current characteristics at different heat-sink temperatures, usually 15°C to 105°C. The laser characterization is realized under short pulse conditions (300 ns) in order to avoid additional overheating of the active region during its operation, so that the active region temperature (T_{AZ}) is the same as the reference heat-sink temperature (T_{ref}) and the T_0, T_1 parameters can be accurately determined.

5.2.1.1. Experimental setup for diode laser characterization under quasi-CW and CW operation mode. Measurement of power-voltage-current characteristics and optical spectrum

The diode laser is driven by the current source ILX Lightwave LDX-3690 from 0 to a maximum of 120 A with a minimum step of 0.1 A in CW or quasi-CW mode. The pulse duration (quasi-CW mode) can be adjusted from 40 µs to 10 ms with a duty cycles from 0.1% to 20%. The inaccuracy of the applied current above 1 A is less then 5%.

In order to measure the optical power, the laser output light is collected in two ways.

1. Testing the diode laser under CW mode, the laser beam is directly collected by laser power meter (a thermopile). There are two thermopiles in use: Gentec UP19K-15S-W5 for detection of a maximum optical power of 15 W (noise level 1 mW,) and Gentec UP25N-300W-H9-D0 for measurements of optical power up to 300 W (noise level 3 mW). The latter device is water cooled. The diameters of the active areas are 17 mm and 25 mm diameter, respectively. Due to the large diameter, the laser beam does not have to be collimated. The spectral range is 0.19 – 10 µm. The output power is obtained in Watts directly from the Gentec-SOLO monitor. Both power meters are calibrated to ± 2.5% of national standards.

2. Testing the diode laser under quasi-CW mode, the laser output is collected with an integrating sphere (Ulbrichtkugel S19-OPT-04 SL-CM-DL), where it is scattered by a highly reflective diffuse surface. This spatially integrated laser light is collected by an InGaAs photodetector (Newport 818-SL). The signal from the photodiode is transferred via the optical power meter Newport Model 1830-C that works as a photocurrent-to-voltage converter (this element provides a linear response in a wide range of the photocurrent). The voltage signal (U_{PH}) is registered with the oscilloscope (Tektronix TDS 5045). To find the corresponding value in Watts of the laser output power (P_{opt}), the laser is tested in CW mode at a low current range where the power-current characteristic is linear. Next, via linear fitting of the voltage signal from the photodetector to the optical signal from the thermopile, a parameter (f) with the unit W/V is found. Finally, the measured laser output is presented as $P[W] = f[W/V] \cdot U_{PH}[V]$. The measurement inaccuracy is enclosed in a range of $\pm 5\%$.

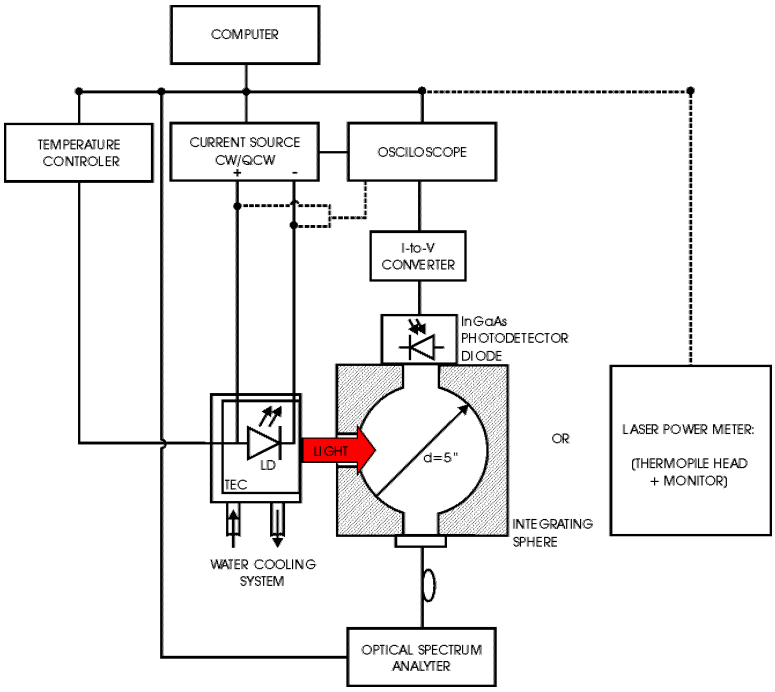

Figure 5.4. Experimental setup for diode lasers characterization (PUI characteristics, optical spectrum) in quasi-CW and CW operation mode.

In order to measure the optical spectrum, the light is directed into the integrated sphere first and then collected by an optical multimode fiber (62.5 µm) and registered by means of the optical spectrum analyzer (Option 1: Hewlett Packard 70951A, spectral range 600 nm – 1700 nm, minimum resolution 0.08 nm. Option 2: Ocean Optics HR4000 (HR4C2337), spectral range 950 nm – 1090 nm, minimum resolution 0.04°nm).

The measurement of the voltage over a diode laser is done by means of the oscilloscope (during quasi-CW operation) or by the multimeter Keithley 2000 (during CW operation).

The actual temperature of the laser mount is measured by means of the thermoelectric sensor PT100 and controlled by the temperature controller Newport Model 3150. The temperature of the laser heat-sink can be reduced down to 15°C and heated up to 80°C by means of a Peltier element. Additionally, for more efficient heat removal from the laser mount, the device is placed on a water cooled heat spreader.

All of the electronic test equipment is controlled by a PC.

5.2.1.2. Experimental setup for diode laser characterization under short pulse operation mode. Measurements of power-voltage-current characteristics and optical spectrum

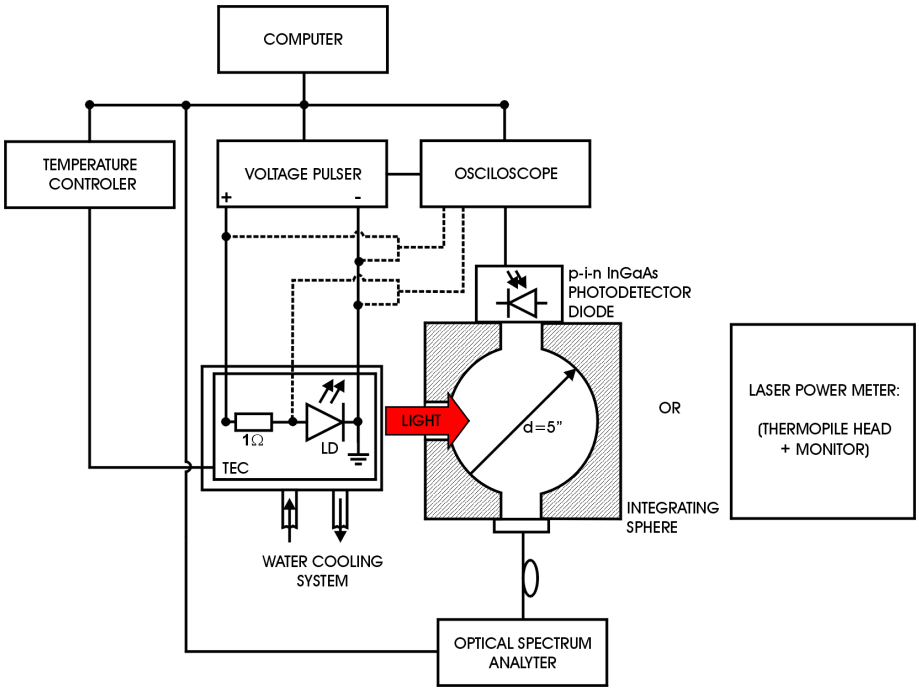

Figure 5.5. Experimental setup for mounted diode lasers characterization (PUI characteristics, optical spectrum) in short current pulses operation mode.

The diode laser in series with a 1 Ω resistor is driven by the voltage pulser (AVTECH AVOZ-A3-B) from 0 V to a maximum of 110 V with a minimum step of 0.1 mV. The 1 Ω resistor is required for the measurement of the output current (I) that is related to the output voltage (U) and the diode forward voltage drop (U_D) through $I = (U - U_D)/1\Omega$. The voltage drop over the diode itself and the combination of the diode with the 1 Ω resistor in series is registered by the oscilloscope (Tektronix TDS 754D 500MHz, 2GS/s). The electrical circuit is optimized to reduce the stray capacitance and the load impedance mismatch. However, the waveforms still show ringing. There is a plateau region of the waveform usable to perform reliable measurements (see figure 5.6). AVTECH voltage pulser offers pulse widths from 50 ns to 2 µs with 30 ns rise time and a maximum repetition rate of 20 kHz.

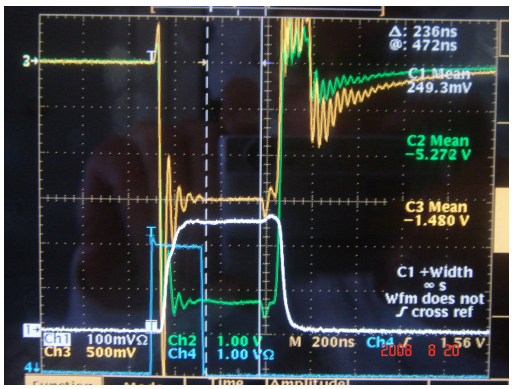

Figure 5.6. An oscilloscope record of the waveforms of the voltage drop on a diode laser (orange), diode laser with 1 Ω resistor in series (green) and the laser light signal from the photodetector (white). The vertical white lines represent the plateau range in which measurements are performed.

The laser output signal can be detected in two ways. First, by using the integration sphere and the high speed PIN InGaAs photodetector. The light waveform in a plateau region is registered with the oscilloscope (presented in figure 5.6). The electrical signal is converted to optical power using a similar calibration process as described above in chapter 5.2.1.1. The second method is the direct laser light detection using a high sensitive laser power meter with an absorptive filter (Gentec XLP12F-1S-H2). It is a thermopile that offers (together with the absorptive filter) a measurement in the spectral range of 0.28 – 1.36 µm. The device measures the average optical power signals from 1 µW to 2 W. The geometry of the active area allows for power-loss-free detection (without previous beam collimation) of a laser beam with a maximum divergence angle of 46° (95% optical power). Using the absorptive filter the thermal drift is reduced to 6 µW/°C, leading to a negligible background noise level. The calibration uncertainty is ± 2.5%. This device has a response time of 2.5 s, which means it integrates the average power over many pulses. The peak power is calculated by dividing the measured average power by the duty cycle.

The optical spectrum is measured simultaneously with the PUI characteristic. The spectral intensity distribution is measured in the same way as described in chapter 5.2.1.1.

All electronic test equipments, except the power meter, are remotely controlled by a PC.

5.2.2. Measurement of the spontaneous emission from the waveguide

This measurement method is used to assess the laser vertical carrier confinement and the loss factor to the maximum optical power. During the laser operation, especially at high carrier injection levels, as well as at high temperatures, vertical carrier leakage into the waveguides or/and cladding layers may occur. The carriers accumulate and recombine in the confinement layers, being a loss to the output power. As long as the waveguide or cladding layers are direct materials, the recombination process results in spontaneous radiative emission at a wavelength related to the direct energy gap of the particular bulk epitaxial-layer. Furthermore, the spontaneous emission light is collected with a fiber and the wavelength is registered by an optical spectrum analyzer.

5.2.2.1. Experimental setup for collection of spontaneous emission of light

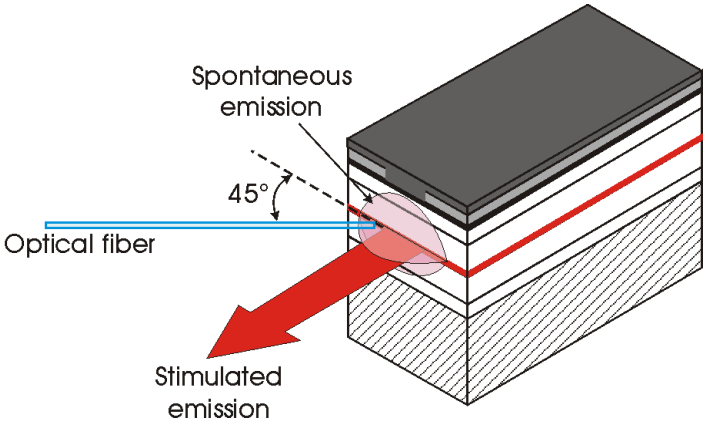

Figure 5.7. The principle of the spontaneous emission light collection.

The laser diode is placed on the holder described in chapter 5.2.1.1, or -2 in order to be tested under short pulse as well as (quasi-)CW operation mode and also at various temperatures. The spontaneous emission is collected by a bare optical fiber fixed on a six axis

translation stage, which allows precise adjustment of its position. The fiber is placed in the vicinity of the laser facet and is aligned at an optimum angle greater than the laser emission angle (~45°). Such fiber adjustment allows for collection of the spontaneous emission component alone and examination of its changes with increasing current or temperature. The optical signal is transferred to a spectrometer (Ocean Optics HR2000, HR4000).

This method only gives the relative changes in spontaneous emission intensity and is not a quantitative method.

5.3. Characterization of the laser beam (mounted devices)

An ideal laser beam takes the form of a Gaussian beam. The Gaussian beam travelling in the space in the z -direction has the following properties:

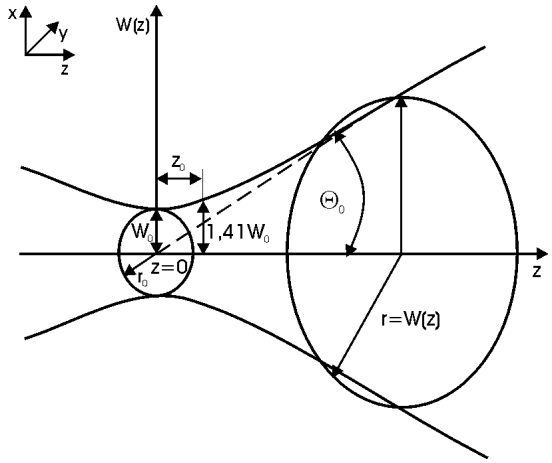

Figure 5.8. Gaussian beam radius.

1. The optical intensity distribution I of the beam in the transverse plane (X,Y) is the circularly Gaussian function:

$$I(r,z) = I_0\left[\frac{W_0}{W(z)}\right]^2 \exp\left[-\frac{2r^2}{W^2(z)}\right], \text{ and } r = \sqrt{x^2+y^2}, \qquad (5.3.1)$$

   where r is the radial coordinator and x, y are Cartesian coordinates, lying in the transverse plane. W_0 at $z = 0$ denotes the beam radius of the beam waist and $W(z)$ denotes the beam radius at a distance z. The beam exhibits its maximum intensity I_0 in the center of the beam $(r = 0, z = 0)$. The peak value lies on the beam axis and decreases with increasing distance from this axis. While propagating in the z-direction, the beam intensity drops gradually with increasing z. The maximum intensity drops to $0.5I_0$ at the distance of $z = z_0$.
2. The total optical power carried by the beam is independent of the distance z and equals:

$$P = \frac{1}{2} I_0\left(\pi W_0^2\right) \qquad (5.3.2)$$

The power contained in a circle of radius $r = W(z)$, for which the optical intensity drops by a factor of $1/e^2$, is approximately 86% of the total power.

3. The beam radius increases with the distance z as:

$$W(z) = W_0\sqrt{1+\left(\frac{z}{z_0}\right)^2}\ , \text{ and } \ z_0 = \frac{\pi \cdot d_0^2}{4\lambda}, \qquad (5.3.3)$$

where z_0 is a Rayleigh length which represents the distance from the beam waist in which the beam radius is increased by a factor of $\sqrt{2}$. The term d_0 denotes the beam diameter at the beam waist ($d_0 = 2W_0$) and λ the wavelength.

4. In the far-field (at a distance $z >> z_0$), where the beam radius r increases linearly with z, the full divergence angle of the beam Θ can be written as:

$$\Theta = \frac{d_0}{z_0} = \frac{4\lambda}{\pi d_0}. \qquad (5.3.4)$$

The beam divergence is directly proportional to the wavelength and inversely proportional to the beam-waist diameter. The bigger the beam waist the weaker is the beam divergence.

5. The focus depth is twice the Rayleigh length

$$2z_0 = \frac{2\pi W_0^2}{\lambda} \qquad (5.3.5)$$

and is proportional to the area of the beam at its waist and inversely proportional to the wavelength.

6. The wavefronts are approximately planar at the beam-waist $R(z=0) = \infty$ (near-field). Their curvature decreases with the distance z to reach its minimum value of $2z_0$ at $z = z_0$ and slowly increases again so that in the far distance ($z >> z_0$) the wavefronts become approximately spherical (far-field).

The real laser beam is not an ideal Gaussian beam and thus its spatial quality is often quantified via the diffraction parameter M^2. This parameter says how the laser beam, under test, compares to a purely Gaussian beam for which M^2 takes a value of 1. A beam of higher order or beam of mixed modes often exhibits a larger beam waist and/or has a faster divergence. Therefore, it holds:

$$\Theta = M^2 \frac{4\lambda}{\pi d_0} \qquad (5.3.6)$$

Here, Θ represents the full divergence angle. The real laser beam has an M^2 value greater than 1. M^2 is also called Times-Diffraction-Limit-Factor. Thus, it gives information about the spot-size of a focused beam. The ideal beam, when focused, has the minimum spot

diameter ($2W_0$), while a focused real beam has a spot width M^2 times larger than expected for a Gaussian beam. Moreover, the energy intensity is M^4 times less than for an ideal beam.

The diode laser, due to its asymmetric light emission area, produces a beam with a simple astigmatism [4] (or orthogonal astigmatic beam [5]). Such a beam exhibits different divergence angles, different beam waist thicknesses, as well as different beam waist positions in two transverse planes on the propagation axis (also called longitudinal astigmatism [5]). The evolution of the beam along these two planes is described independently. Therefore, by the diode laser characterization, all beam parameters can be determined independently in both, lateral and vertical, planes. It should also be noted, that in the broad area diode lasers both transverse planes describing a Gaussian evolution produce the waist at the same plane, namely at the laser facet.

5.3.1. Measurement techniques

During beam characterization of a broad-area diode laser, two beam parameters are measured:

- the width of the beam waist (near field (NF)) in the lateral $d_{0,y}$ (LNF) and in the vertical $d_{0,x}$ (VNF) directions;
- the beam divergence in the far-field (FF) in the lateral Θ_y (LFF) and in the vertical Θ_x (VFF) directions.

With these two values the diffraction parameter M^2 can be calculated from eq. (5.3.6).
The beam width z_0 for broad area lasers is placed at the emitting laser facet ($z_0 = 0$).

There are two methods utilized during this work for the laser beam characterization. To measure the vertical divergence angle (far-field), a goniometric method was utilized. This method allows for the measurement of very wide as well as narrow divergence angles. The vertical near-field and the lateral beam properties (near- and far-field) are assessed utilizing a method known as ‘moving slit’. The ‘moving slit’ method can be optionally used for the measurement of vertical far-field profiles, but only in the case of lasers with narrow (<22°) beam divergence. This limitation comes from the utilized lens system described below.

5.3.2. Experimental setup for laser beam characterization in the vertical plane

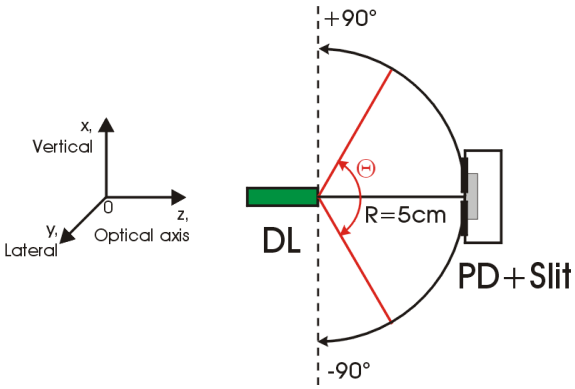

Figure 5.9. Principle of the vertical far-field measurement by means of a goniometer. (View from the side.)

A photodiode with a rectangular slit (d_s = 100 μm) is placed on a motorized rotating arm (a goniometer). The output of the laser diode is placed exactly in the central point (0,0,0) of the circle (5 cm radius) drawn by the moving detector. The rotation takes place in the XZ plane (perpendicular to the laser epitaxial structure x). The maximum angle of rotation is 180°. The measurement of the beam intensity profile is realized in 300 measurement steps.

The angle is measured with the resolution $\Delta\Theta$ that is given by the ratio between the slit thickness and its distance from the laser facet R:

$\Delta\Theta_1 = \frac{0.5 \cdot d_S}{R}$ (in radian) and equals 0.057°. This leads to a measurement uncertainty of less than 1%. An additional factor that influences the accuracy of the measurement is the fixed number of measurement steps (300):

$\Delta\Theta_2 = \frac{measurement\ angle\ range}{300\ steps}$ (in deg.) and in the case of maximum measurement angle range (180°) this leads to a minimal measurement precision of 0.6°. For a measurement angle range of e.g. 30° the precision increases to 0.17°. Also, a misalignment of the laser facet from the central point of the measurement path (in figure 5.9 (0,0,0) point) leads to a deviation from the real angle value. The error linearly depends on the misalignment on the z-direction ΔR_z: $\Delta\Theta_3 = \Theta \cdot \frac{\Delta R_z}{R}$. Measurement of a real divergence angle Θ = 10° with a misalignment of the laser of $\Delta R_z = 1\,mm$ leads to an error of 0.2° that corresponds to an error of 2% (misalignment on x leads to a deformation of the detection path in relation with the beam divergence angle and will result in an asymmetric far-field profile). The total inaccuracy $(\Delta\Theta_1 + \Delta\Theta_2 + \Delta\Theta_3)$ of the vertical angle ranges from 0.6° to 0.25°. For small angles (10°) this leads to a measurement error between 6% and 2.5%.

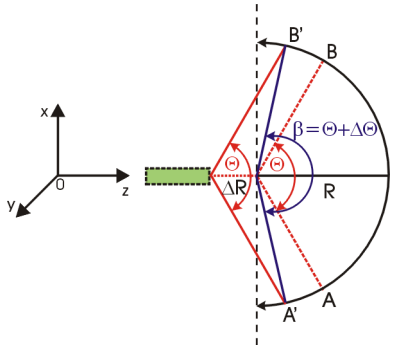

Figure 5.10. Schematic presentation of the misalignment on the optical axis.

5.3.3. Experimental setup for laser beam characterization in the lateral plane

Measurement of the lateral near-field.

Figure 5.11 presents the optical bench used for the measurement of the lateral near-field distribution. Two optical lenses are placed on the optical axis z, between the laser facet and the photodetector. In order to transform the near-field (beam waist) onto the photodetector a telescope is built consisting of an aspheric lens L_1 with an aperture NA= 0.5 (Thorlabs C240T-B with special coating) and a focusing lens L_2. The focal lengths are f_1 = 8 mm and f_2 = 500 mm, respectively. The magnification of the telescope corresponds to:

$$m = \frac{f_2}{f_1} = 62.5 \qquad (5.3.7)$$

and is later subtracted during the measurement setup calibration process.

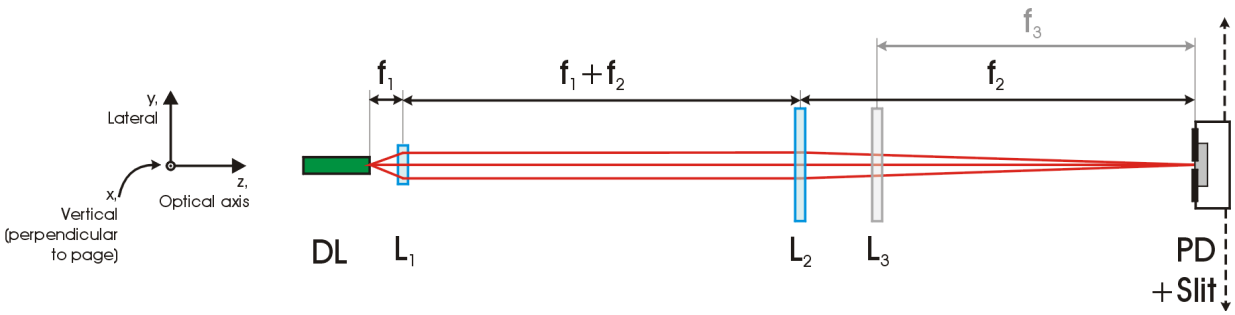

Figure 5.11. The optical bench for the measurement of the lateral beam profiles. Propagation of light rays through the lens system (L_1 and L_2) for the near-field imaging is depicted. (View from the top.)

The near-field spatial resolution (on the basis of Rayleigh's criterion [6]) is:

$$\Delta NF = 0.61 \cdot \frac{\lambda}{NA} \qquad (5.3.8)$$

The spatial resolution of the near-field depends on the wavelength and is in the range of 1.16 µm to 1.25 µm for wavelengths of 1050 nm to 1130 nm, respectively. It leads to a measurement uncertainty of 1.16 % for a 100 µm broad emitter emitting at the wavelength of 1050 nm.

Measurement of the lateral far-field angle.

When a laser beam profile in the far-field is characterized, an additional focusing lens L_3 is placed on the optical axis, as shown in figure 5.11. The lens is placed in the far-field of the beam (with its beam waist on the detector) at a focus length of $f_3 = 400$ mm. The lens performs a Fourier transform of the beam divergence angle Θ in the observation 'point' y on the detector, which has a 10 µm wide slit (the photodetector with a slit moves in the plane YZ). The divergence angle is then calculated as $\Theta = \frac{y}{f_3}$ and the resolution is $\Delta\Theta = 0.001°$.

The measurement uncertainty is less than 1%.

The aspheric lens aperture of NA = 0.5 corresponds to a full acceptance angle of 60°. Following the ISO standards, the measurement range should be three times the beam waist W (for which the intensity drops by factor $1/e^2$). Thus, the maximum divergence angle that can be measured with this measurement setup is $\Theta_{max} = 20°$.

The uncertainty of the beam propagation factor M^2 (lateral) is calculated using the law of error propagation (the "root-sum-of-squares" method) and results in an uncertainty of 0.6%.

6

Basic features of the SLOC design – simulation results

6.1. Introduction

In this chapter, the results of the one dimensional simulations of the basic features of the SLOC design are presented. The simulations concern a variation of the near- and far-field profiles as well as the optical confinement factor and equivalent vertical spot-size with the optical cavity width, and the refractive index step at the waveguide-cladding interface, as well as the QW-waveguide interface. Moreover, the number of higher modes is presented as a function of the waveguide widths and the refractive index step at the waveguide-cladding interface. The methods of higher order modes suppression are also discussed. The calculations are performed using the QIP software for each structure developed during the work. The results presented here consider the B1110-3 design (double-QW, GaAs-WG, $Al_{0.25}Ga_{0.75}As$-CL) that is properly modified to show the principle of the large optical cavity design. The emission wavelength considered during the calculations is 1120 nm. This work is focused on the reduction of the divergence angle of the laser beam. Therefore, the main subject of the study is the optical mode distribution and its confinement in the vertical cavity.

6.2. The optical cavity size and the optical mode distribution

Waveguides for which the thickness is varied from 0.5 µm to 10 µm are considered. A double, triple or quadruple QW (DQW, TQW or QQW) active region is enclosed in the middle of the optical waveguide. The waveguide is embedded between 'infinitely' thick cladding layers. By 'infinitely' thick claddings one understands a thickness for which the distribution of the optical mode is independent of the cladding thickness. In this case, the cladding layer thickness is set to 2 µm on both sides of the waveguide. The substrate and the p-contact layers are not taken into consideration. The TE mode intensity ($\sim |E(x)|^2$) is obtained by solving the *real* waveguide equation. The vertical far-field profile is obtained from the Fourier transform of the electrical field distribution and is usually described by several parameters: (1) the angle at the full width at half maximum intensity (FWHM), (2) the full angle at $1/e^2$ optical intensity drop, and (3) the angle containing 95% of the optical power (95% power content), see figure 6.1.

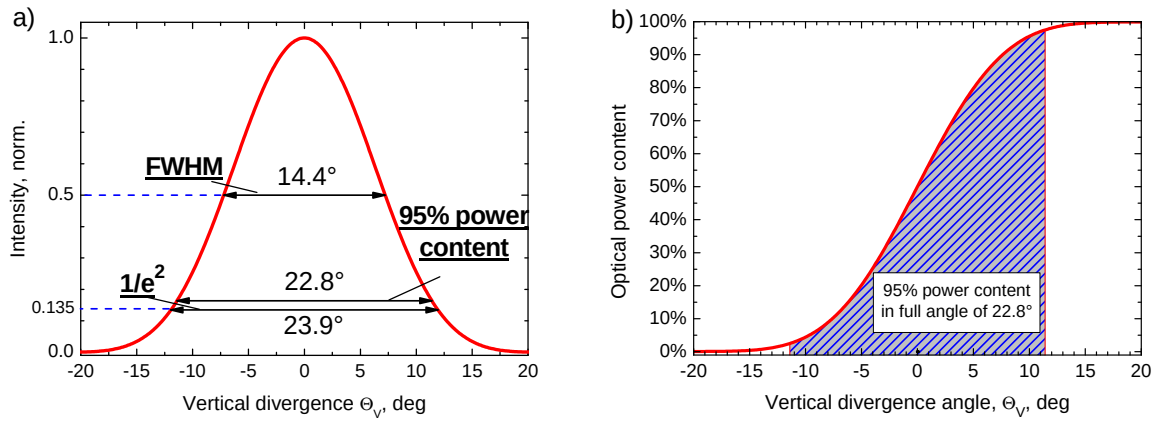

Figure 6.1. (a) Calculated vertical far-field with indicated full angles: at FWHM, at $1/e^2$ and an angle containing 95% of optical power. (b) Integral of the vertical far-field profile indicating the full angle containing 95% of the optical power.

Figure 6.2 shows how the optical mode distribution and the corresponding vertical beam profiles change with increasing thickness of the waveguide. The important result here is that widening the optical cavity (waveguide) changes the optical mode profile and also leads to its wider distribution. The wide optical mode distribution (e.g. for WG = 5 µm) further results in small divergence angle of the beam. During calculations, the refractive index step at the cladding-waveguide interface remains unchanged. The active region is placed at position x = 0. The 'real' waveguide equation is solved.

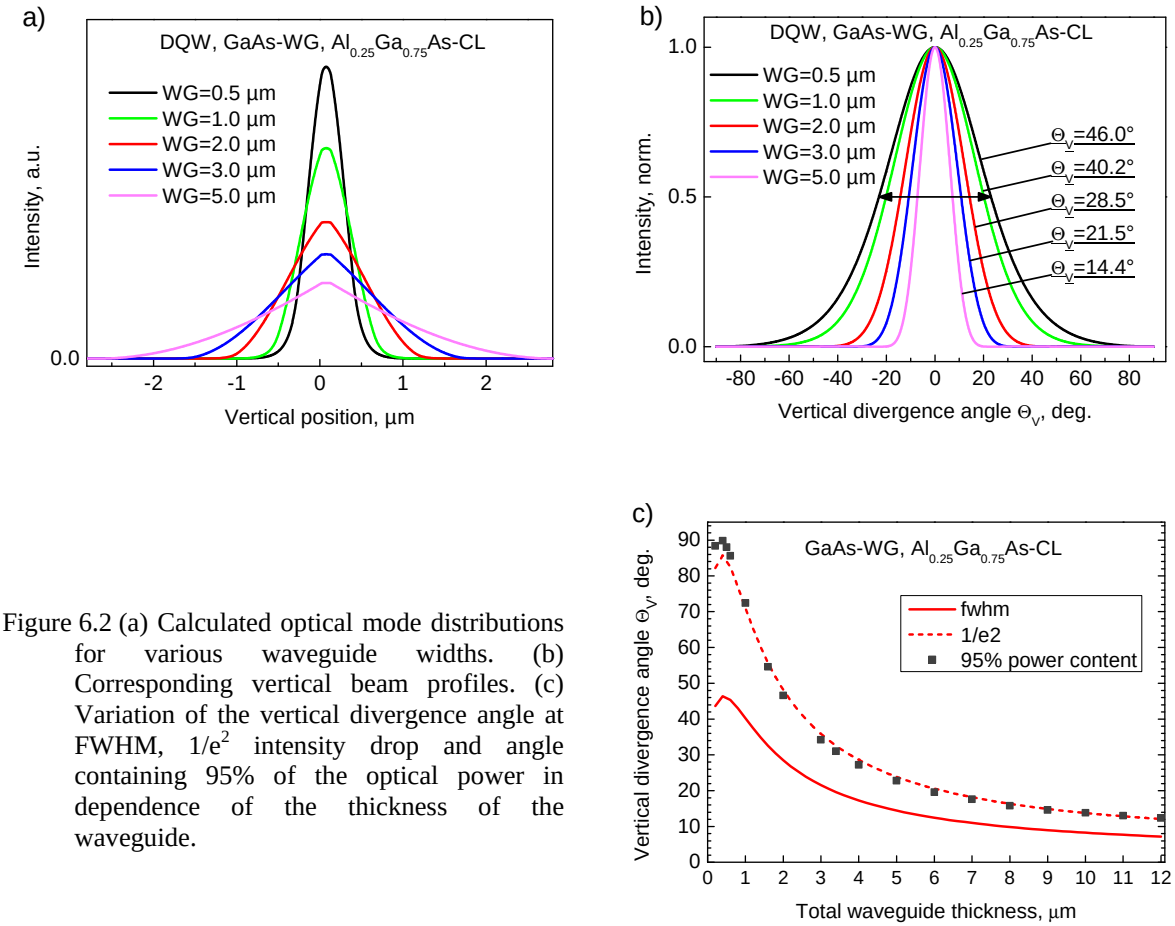

Figure 6.2 (a) Calculated optical mode distributions for various waveguide widths. (b) Corresponding vertical beam profiles. (c) Variation of the vertical divergence angle at FWHM, $1/e^2$ intensity drop and angle containing 95% of the optical power in dependence of the thickness of the waveguide.

The simulations pointed out a new aspect: the mode profile in the waveguide is strongly influenced by the refractive index of the claddings when the waveguide is *narrow*. On the contrary in extremely *wide* waveguides the mode profile is dominated by the guiding of the multi-QW-active region. For waveguides thicker than 3 µm the claddings have no influence on the mode profile, see figure 6.3. Figure 6.4 illustrates the dependence of the confinement factor and the vertical divergence angle on the waveguide thickness, with the refractive index step at the active region-waveguide interface being the parameter (in the calculations the refractive index step at the waveguide-cladding interface is constant; the active region design was unchanged). The calculations show, that independent from the waveguide thickness, an increase of the refractive index step at the active region-waveguide interface results in a higher confinement of the optical mode in the active region and a higher vertical divergence angle. The changes are clearly to be seen for waveguides thicker than 3 µm. Moreover, the higher the refractive index of the active region, compared to that of the waveguide, the more difficult it is to change the optical mode profile and its overlap with the active region by widening the waveguide layers. Concluding, the multi-QW-active region shows guiding properties for any waveguide thickness, that, however, start to dominate for waveguides thicker than 3 µm.

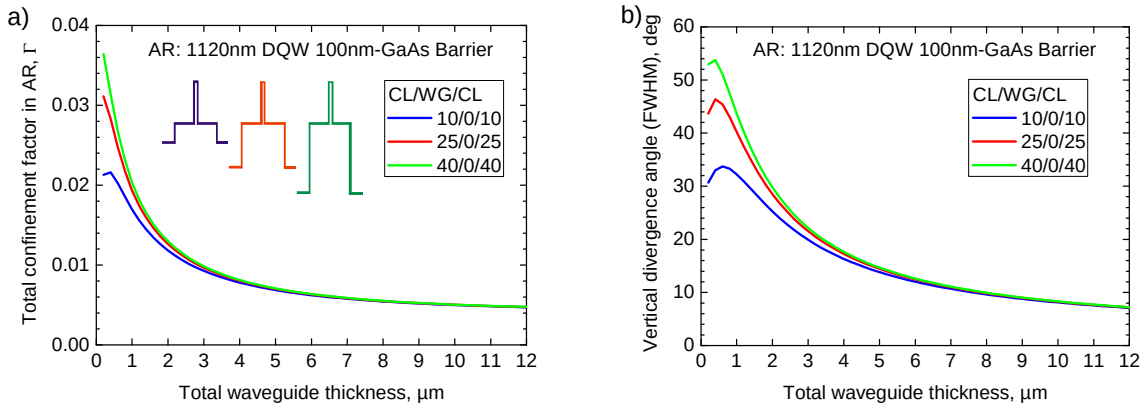

Figure 6.3. The dependence of the confinement factor Γ and the vertical divergence angle on the waveguide thickness for different refractive index steps (correlating with Al content) at the cladding-waveguide interface. '0' denotes GaAs-waveguide, '10', '25', '40' denote 10%, 25% and 40% Al content in n- and p-doped claddings, respectively. Calculations performed by means of the QIP software.

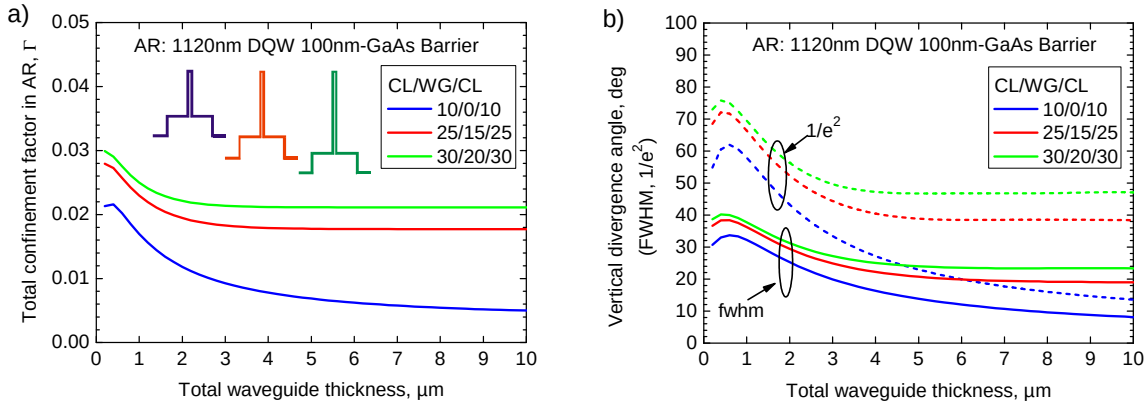

Figure 6.4. The dependence of the confinement factor Γ (a) and of the vertical divergence angle (b) on the waveguide thickness for different refractive index steps (correlating with Al content) at the waveguide-active region interface. The numbers '0', '10' … '30' denote the percentage of the Al content in the claddings and waveguide. Calculations performed by means of the QIP software. (The notation CL/WG/CL represents a system of the $Al_xGa_{1-x}As$ material composition for the consecutive bulk layers: n-type cladding, waveguide, p-type cladding, where x is the varied value. The '0' represents GaAs.)

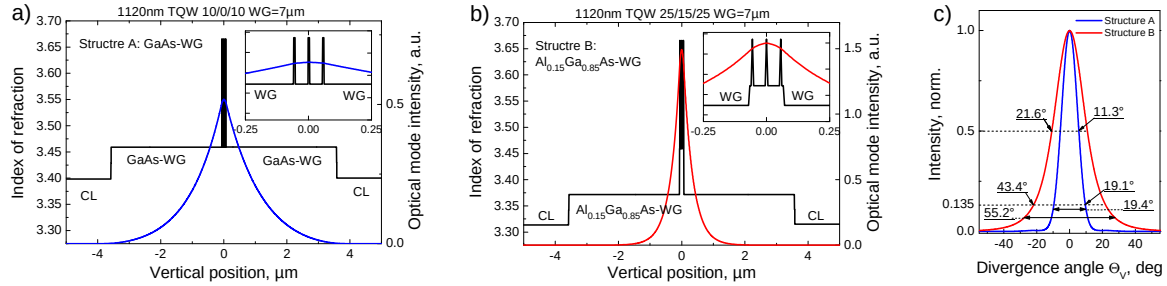

Figure 6.5. (a) Refractive index and optical mode distribution for a structure based on 7 µm thick GaAs waveguide. (b) Refractive index and optical mode distribution for a structure based on 7 µm thick $Al_{0.15}Ga_{0.85}As$-waveguide. (c) Corresponding far-field profiles. The insets of figures (a, b) zooms in on multi-QW active regions utilizing 50 nm-thick GaAs barriers and demonstrate the difference in the designs causing a widening of the divergence angle of the laser beam.

The increment of the Al content in the waveguide correlates with the reduction of the refractive index of that layer (chapter 3.2). Plotting the refractive index distribution of such structures (see the insets of figure 6.5) one can notice that, due to the 'high'-refractive index of the GaAs barriers, the multi-QW active region acts as a 'second waveguide' resulting in a stronger confinement of the optical mode and as a consequence a wider divergence angle of the laser beam. As an example, an increment of the Al content in a 7 µm thick waveguide from 0% (GaAs) up to 15%, while the refractive index step at the cladding-waveguide interface remains the same, leads to an increment of the beam divergence angle at FWHM from Θ_V^{fwhm}=11.3° to Θ_V^{fwhm}=21.6°, and at $1/e^2$ intensity drop from $\Theta_V^{1/e2}$ = 19.1° to $\Theta_V^{1/e2}$ = 43.4° and the angle containing 95% optical power increases from $\Theta_V^{95\%}$ = 19.4 to $\Theta_V^{95\%}$ = 55.2 (illustrated in figure 6.5c).

In the above discussed designs (e.g. the structure presented in figure 6.5b), widening the thickness of the GaAs barrier and increasing the number of QWs or QW thickness leads to stronger mode confinement in the high-refractive active region. As a result, the divergence angle of laser beam becomes wider (see figure 6.6-6.7).

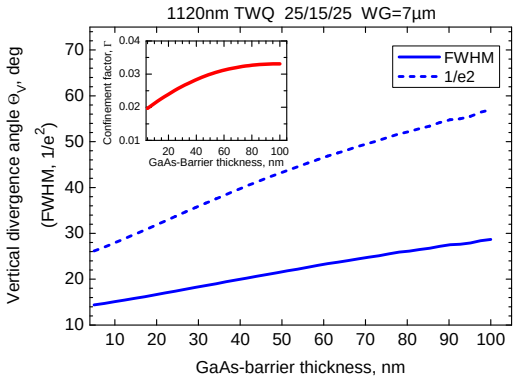

Figure 6.6. Calculated vertical divergence angle of the laser beam versus the thickness of the GaAs-barrier. The inset shows the subsequent changes in confinement factor Γ. (Calculated structure: TQW active region embedded in 7 µm thick $Al_{0.15}Ga_{0.85}As$ waveguide and $Al_{0.25}Ga_{0.75}As$ claddings.)

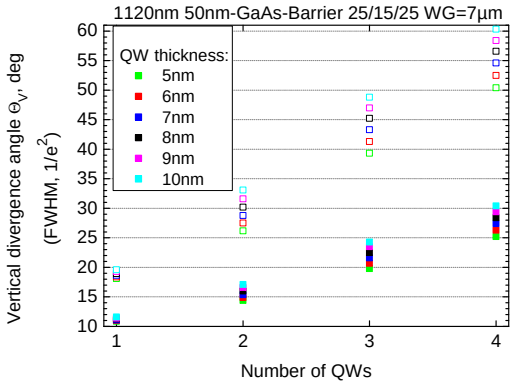

Figure 6.7. Calculated vertical divergence angle of the laser beam as a function of the QW number and QW thickness. Solid symbols represent the angle at FWHM, while open symbols represent the angle at $1/e^2$ intensity drop. (Calculations based on a structure utilizing 50 nm thick GaAs-barrier between QWs, 7 µm thick $Al_{0.15}Ga_{0.85}As$ waveguide and $Al_{0.25}Ga_{0.75}As$ claddings.)

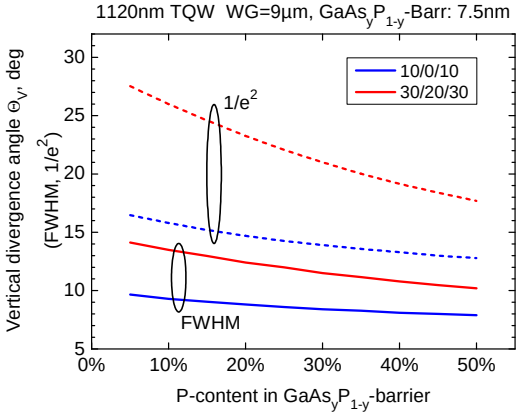

Figure 6.8. Calculated vertical divergence angle of the laser beam as a function of the phosphorus content in the $GaAs_{1-y}P_y$ quantum barriers. Calculations performed for structure based on 9 µm thick GaAs waveguides embedded in $Al_{0.1}Ga_{0.9}As$ claddings (10/0/10) and $Al_{0.2}Ga_{0.8}As$ waveguides embedded in $Al_{0.3}Ga_{0.7}As$ claddings (30/20/30).

For the first time it is presented that the strong optical mode confinement in SLOC structures utilizing multi-QW gain regions can be weakened by using GaAsP quantum barriers instead of GaAs-barriers [1]. The GaAsP material is characterized by a lower refractive index than GaAs (chapter 3.2). The refractive index of the barrier decreases subsequently, with an increasing content of phosphorus atoms in the $GaAs_yP_{1-y}$ layer. Furthermore, the low-index barrier reduces the high average refractive index of the active region♣. As a result, the mode confinement is lower, the mode expands wider in the cavity and the divergence angle of the beam is reduced. Figure 6.8 shows the reduction of the divergence angle of the laser beam with increasing phosphorus content in the $GaAs_{1-y}P_y$ -barriers.

In contrast to structures based on an active region with GaAs barriers, the vertical far-field angle can also be reduced by widening the GaAsP barriers thickness. However, this only happens when the refractive index of the quantum-barriers is lower than the refractive index of the $Al_xGa_{1-x}As$ waveguide layers (figure 6.9).

♣ The MQW-active region can be approximated with an average refractive index when the intensity of the electrical field in the active region is assumed to be constant. The active region is optically homogeneous when the thickness of wells and barriers is much smaller than the laser wavelength.
The averaged refractive index of the MQW active region is calculated as: $\bar{n} = \sqrt{\sum_i n_i^2 \cdot d_i \Big/ \sum_i d_i}$, where n and d are the refractive index and the thickness, respectively, of the i-layer in the active region [2].

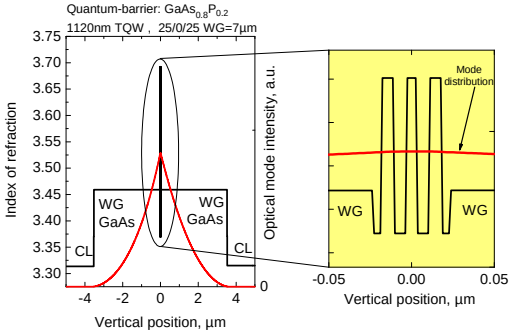

Figure F1. Calculated refractive index and optical mode distribution of a structure where the active region is based on quantum wells and barriers with thicknesses much smaller than the laser wavelength. The graph on the right hand side of the figure zooms in on the multi-QW active region and demonstrates the homogeneous distribution of the electrical field intensity in the active region. (Calculated structure: emission wavelength 1120 nm, TQW active region, QW thickness: 7 nm, $GaAs_{0.8}P_{0.2}$ barrier and spacer thickness: 7.5 nm and 5 nm, respectively. 7 µm thick GaAs-waveguide embedded in $Al_{0.25}Ga_{0.75}As$ claddings.)

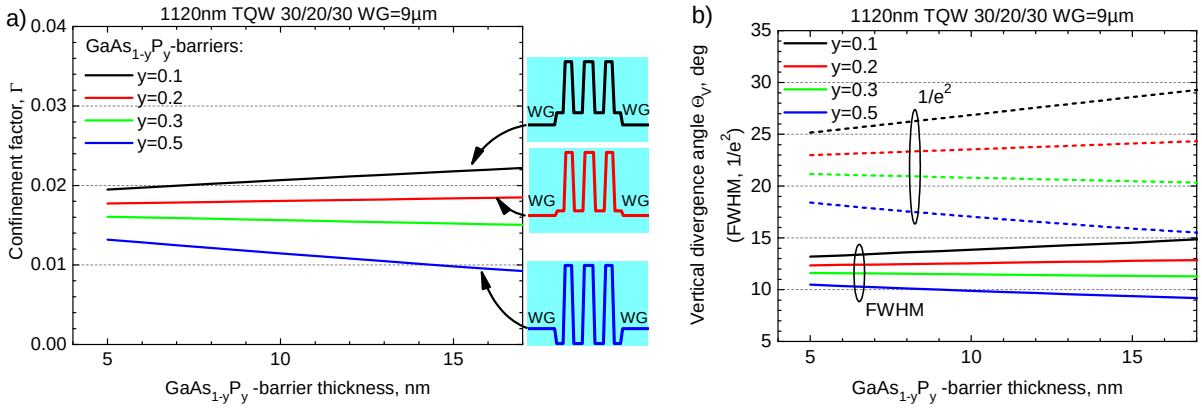

Figure 6.9 (a) Calculated confinement factors Γ and (b) vertical divergence angles of the laser beam as a function of the phosphorus content in the $GaAs_{1-y}P_y$ quantum barriers and the thickness of the quantum barriers. Calculations performed for structure based on 9 µm thick $Al_{0.2}Ga_{0.8}As$ waveguide embedded in $Al_{0.3}Ga_{0.7}As$ claddings (30/20/30). The graphs on the right hand side of figure (a) zoom in on the multi-QW refractive index profile.

Due to the lattice mismatch between GaAs substrate and GaAsP barriers, which increases with increasing content of phosphorus atoms, the thickness of quantum barriers is limited to the so-called critical thickness. Utilizing thicker GaAsP layers with a high phosphorus content leads to crystal defects. The critical thickness of the barrier for the discussed active region varies from 78 nm for 10% phosphorus content to 10 nm for layers containing 50% of phosphorus. However, in practice the thickness is even smaller. The critical thickness is calculated using a double-kink Matthews-Blakeslee relaxation mechanism [2].

6.3. Confinement factor Γ and equivalent vertical spot-size

In the structures with thin waveguides, the optical mode is strongly confined in the active region by the cladding layers. Widening the optical cavity leads to a wider optical mode distribution and its lower overlap with the active region (the electrical field intensity in the active region is reduced, see figure e.g. 10.1). As a result, the confinement factor Γ is reduced.

Structures with a low confinement factor exhibit large equivalent vertical spot-sizes (d/Γ)[♣] - the internal optical power is distributed over a larger area with lower electrical field intensity within the active region. This feature lowers the risk of catastrophic optical damage in the active region as well as the optical load on the facet and results in an increased threshold of the mirror damage (COMD), equation (3.3.29). Figure 6.10 shows the

[♣] Assuming constant electric field amplitude in the quantum well (E_{QW}), one can write the vertical confinement factor (A2.10) in a quantum well in the form:

$$\Gamma = \int_{-dQW/2}^{+dQW/2} |E(x)|^2 dx \Big/ \int_{-\infty}^{+\infty} |E(x)|^2 dx = \left(|E_{QW}|^2 \cdot d_{QW}\right) \Big/ \int_{-\infty}^{+\infty} |E(x)|^2 dx ,$$

where d_{QW}- denotes the QW thickness. Further the equivalent vertical spot-size can be presented as

$$\frac{d_{QW}}{\Gamma} = \frac{\int_{-\infty}^{+\infty} |E(x)|^2 dx}{|E_{QW}|^2}$$

showing the dependence on the electrical field intensity in the active region.

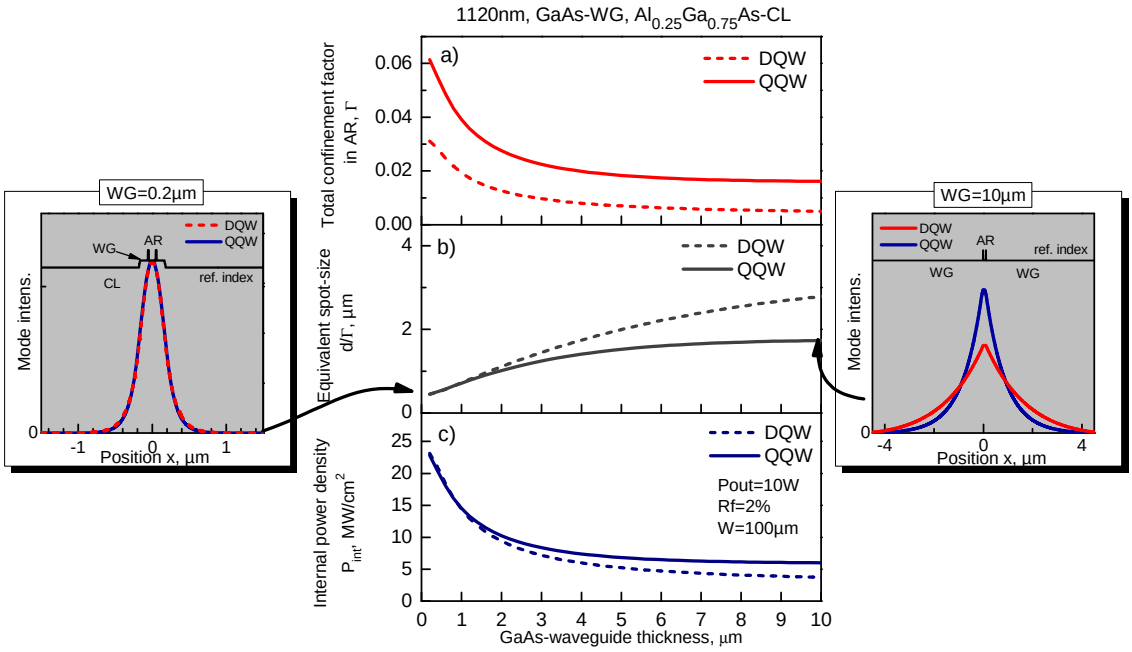

Figure 6.10. (a) The vertical confinement factor, (b) the equivalent vertical spot-size and (c) the internal optical power as a function of the waveguide thickness. The internal power density was calculated for a 100 µm wide laser chip with a front facet coated with reflectivity of 2%, at 10 W output power. The simulated laser structures utilize DQW and QQW active region (emission wavelength 1120nm), GaAs waveguide and $Al_{0.25}Ga_{0.75}As$ cladding layers.

dependence of the confinement factor, corresponding equivalent vertical spot-size and internal optical power on the waveguide thickness.

On the other hand, a low confinement factor leads to low modal gain (see equation (3.3.11)) and as a result the threshold current density is increased (see equation (3.3.19)). In order to raise the modal gain and lower the threshold (per quantum well), a higher number of quantum wells can be utilized (figure 6.10a).

It is interesting to note that for structures based on 'narrow' waveguides (0.2 µm to 2.5 µm), an increment of the quantum well number increases the confinement factor. However, the distribution and intensity of the electrical field remains nearly unchanged and thus the equivalent vertical spot-size is the same size for both structures DQW and QQW (here, the active region does not influence the optical mode profile confined in the optical cavity, theme discussed in chapter 6.2.). On the contrary, in structures based on SLOC-waveguides (thicker than 3 µm) the MQW-active region, due to its waveguiding character, confines the optical mode stronger when the number of QWs is increased – the distribution of the electrical field is changed and the electrical field intensity in the active region is increased (see figure 6.10). Therefore, the spot-size is smaller for QQW structures than for the DQW leading to higher internal optical power in the active region.

Another positive feature of the SLOC design is that in the structures based on wide waveguide layers, a smaller fraction of the fundamental optical mode overlaps with the highly doped cladding layers (figure 6.11). This results in lower free-carrier absorption and further lower modal loss (see equation (3.3.15)).

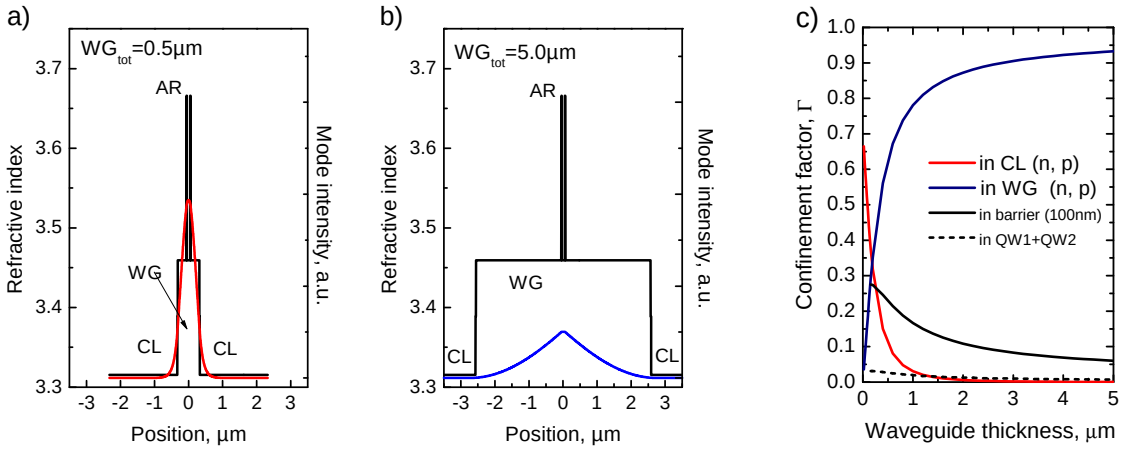

Figure 6.11. (a) The refractive index profile and optical mode distribution for a structure utilizing a 0.5 µm thick waveguide. (b) refractive index profile and optical mode distribution for a structure based on a 5 µm thick waveguide. (The abbreviations CL and AR stand for cladding layers and active region, respectively). (c) The fraction of the optical mode confined in the waveguide and cladding layers versus the vertical optical cavity size.

6.4. The optical cavity size and the number of vertical modes

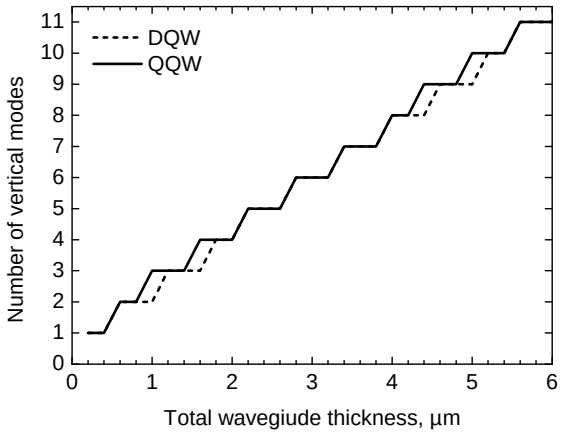

Figure 6.12. Number of guided (TE) modes versus waveguide thickness for a QQW (solid line) and a DQW (dashed line) structure. Calculation performed for 2 µm thick cladding layers. The *real* waveguide equation is solved

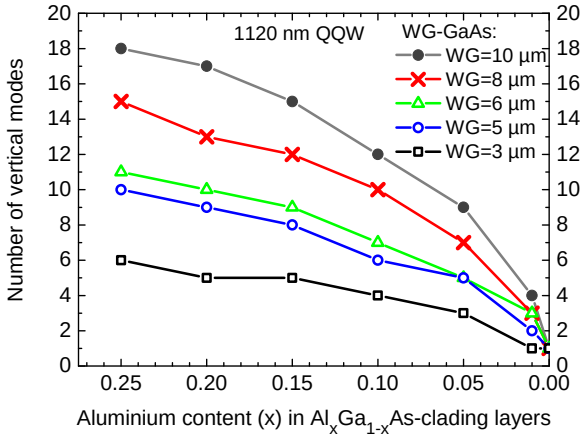

Figure 6.13. The number of excited vertical modes in the GaAs-waveguide versus the Al content in the $Al_xGa_{1-x}As$ claddings (lower Al content lowers the refractive index of the $Al_xGa_{1-x}As$ material). Additionally, the thickness of the GaAs waveguide is varied. (Calculation performed for 2 µm thick cladding layers. The *real* waveguide equation is solved.)

A large optical cavity allows for the existence of higher order vertical modes. Figure 6.12 shows a number of possible TE modes versus waveguide thicknesses (highly compressive strained quantum wells are considered). The number of higher order modes can be reduced by a reduction of the refractive index step at the waveguide-cladding interface correlating with a reduction of Al content in the $Al_xGa_{1-x}As$ material, see figure 6.13. It is sufficient to do that on one side of the waveguide only. During this work symmetric – in Al-mole fraction – $Al_xGa_{1-x}As$ claddings are considered in order to ensure that the maximum intensity of the mode overlaps with the active region for maximum gain.

6.5. Discrimination of higher order modes

The excited higher modes result in a broadening of the laser beam pattern. This effect is disadvantageous because e.g. it reduces the coupling efficiency between the laser and an optical fiber of a small numerical aperture.

The higher order modes in SLOC design can be suppressed in two ways: a) by gain discrimination or b) by loss discrimination.

Gain discrimination of higher order vertical modes.

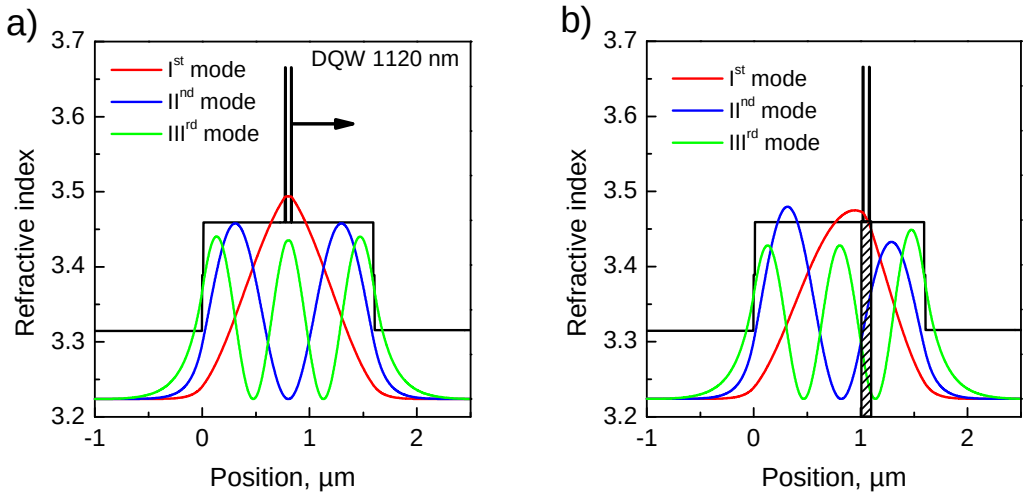

Figure 6.14. The refractive index and the mode profiles of (a) a symmetric and (b) an asymmetric super large optical cavity design.

Each mode starts to propagate in the cavity when the threshold condition for the particular mode is satisfied (see equation (3.3.19). In case of symmetric waveguides (where the active region is placed in the centre of the waveguide), only the even modes are suppressed because they have a node at the active region and do not reach the threshold (figure 6.14a). However, the odd modes have a high confinement factor and their appearance during laser operation is very likely.

By adjusting the quantum well position (shifting it from the centre) within the vertical cavity in a way that only the fundamental mode has a high confinement factor (the smallest threshold) and all other modes overlap much weaker with the active region, the successful discrimination of higher modes can be achieved (figure 6.14b). However, this method becomes challenging when a cavity comprises many modes.

Loss discrimination of higher order vertical modes.

The loss discrimination mechanism applied to the structures discussed in this work is based on the radiation of the waveguide modes into the substrate. Each mode has a particular value of the effective propagation index. The fundamental mode has the highest effective index. The modes with an effective propagation index lower than the refractive index of the substrate layer leaks into the substrate, where it exponentially decays if optical absorption is present. If there is no absorption of the light, the optical mode will propagate sinusoidally, as illustrated in figure 4.16. Changing the thickness of the n-type cladding layer the strength of the propagation loss of a mode is varied. Figure 6.15 illustrates propagation losses of the fundamental and the second order mode versus n-cladding thickness in structure based on

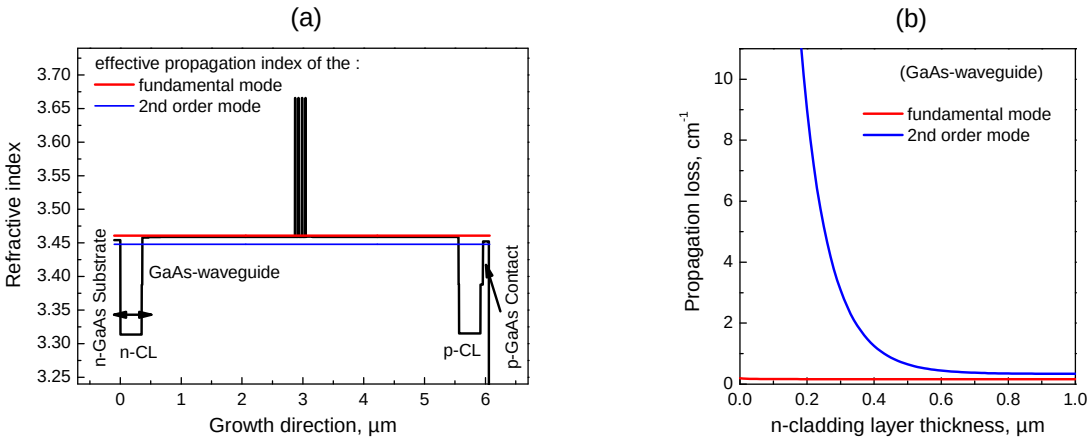

Figure 6.15. (a) The refractive index profile and the effective index of the fundamental and the second order mode. (b) The propagation loss of the fundamental (red line) and the second order mode (blue line). The free-carrier absorption losses depending on the doping are considered. The *complex* waveguide equation is solved. (Simulated structure: 1120 nm QQW, 5 µm thick GaAs waveguide, $Al_{0.25}Ga_{0.75}As$ cladding layers, GaAs substrate and p-contact layer.)

GaAs-waveguide. The radiated modes are called leaky modes or substrate radiation modes and the vertical cavity is called a leaky waveguide. The propagation loss can also be influenced by changing the refractive index of the GaAs substrate. However, the refractive index of the substrate for all designs examined during this work is not varied; its doping level is constant and equals $2 \cdot 10^{18}$ cm^{-3}. In the case of some GaAs waveguide designs (depending on e.g. the wavelength, waveguide thickness and doping profile), the effective propagation index of the fundamental mode is higher than the refractive index of the substrate. In this case, there is no radiation loss for that mode and the propagation loss remains at the level of the absorption loss depending mainly on the doping level in the waveguide (eq. 3.3.15).

According to [1], the n-GaAs ($2 \cdot 10^{18}$ cm^{-3}) substrate is nearly transparent for wavelengths longer than ~950 nm, and the substrate modes only suffer due to free carrier absorption. Thus, the substrate mode is reflected back to the cavity if the cladding layer is not thick enough [2-3]. Such an uncontrolled coupling into the substrate modes deteriorates the vertical far-field profile as well as the power-current characteristic. Figure 6.16 illustrates the calculated and experimentally observed vertical near- and far-field profiles for a structure influenced by the substrate modes (in this case, a cladding layer that is too thin was used).

The mode propagation loss is also adjusted by the thickness of the p-type cladding layer located next to the highly doped ($2 \cdot 10^{19}$ cm^{-3}) GaAs-contact layer. For the GaAs waveguide design, this layer has basically no influence on the fundamental mode propagation loss (a higher doping level leads to a lower refractive index) while providing stronger free-carrier absorption loss for higher order modes (eq. 2.1.6). For designs based on AlGaAs waveguides, one has to choose the p-cladding layer thickness carefully so that there is a minimum loss for the fundamental mode and a high optical loss (radiation and free-carrier absorption loss) for all higher modes.

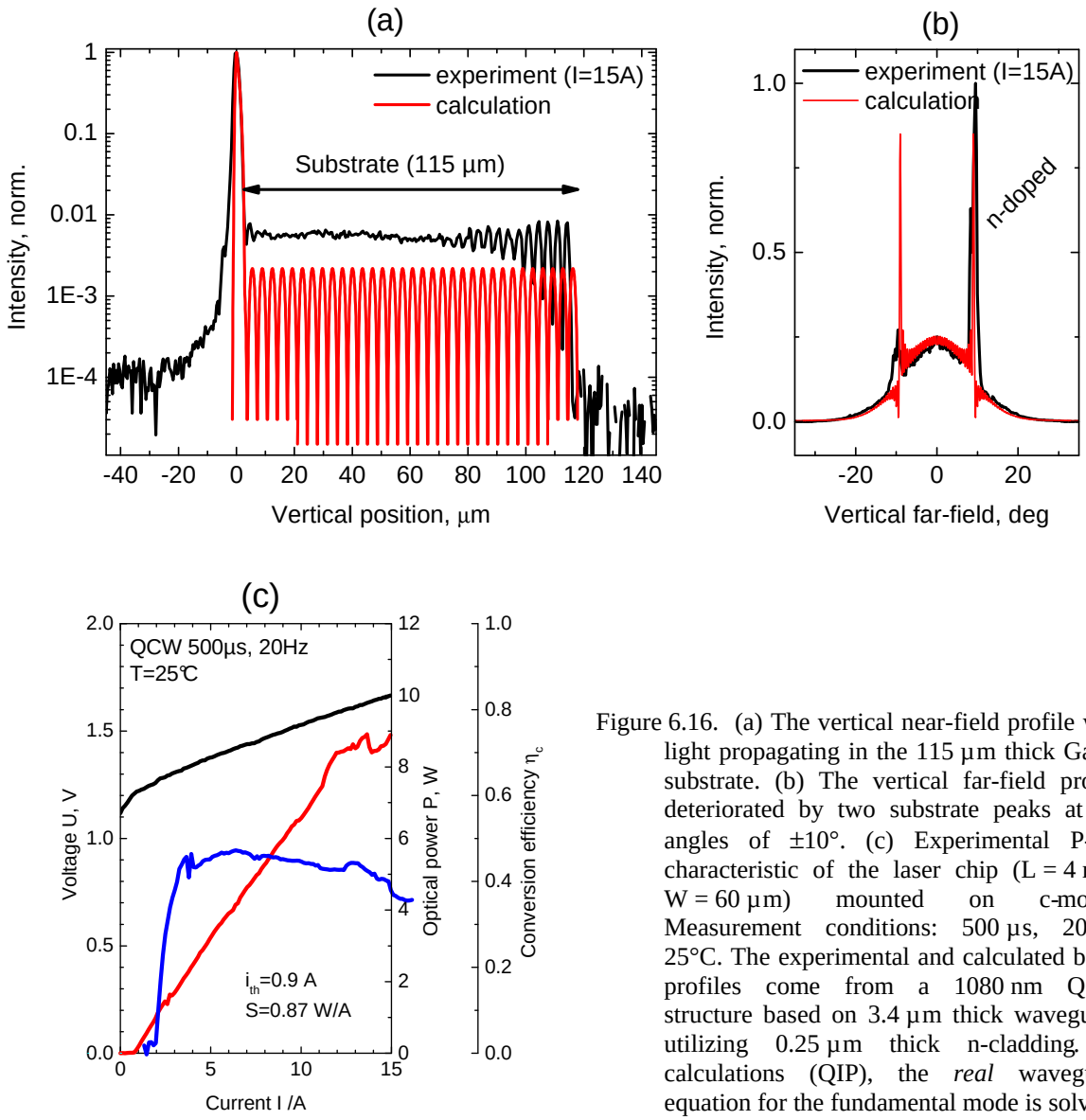

Figure 6.16. (a) The vertical near-field profile with light propagating in the 115 µm thick GaAs-substrate. (b) The vertical far-field profile deteriorated by two substrate peaks at the angles of ±10°. (c) Experimental P-U-I characteristic of the laser chip (L = 4 mm, W = 60 µm) mounted on c-mount. Measurement conditions: 500 µs, 20 Hz, 25°C. The experimental and calculated beam profiles come from a 1080 nm QQW structure based on 3.4 µm thick waveguide, utilizing 0.25 µm thick n-cladding. In calculations (QIP), the *real* waveguide equation for the fundamental mode is solved.

7

Assessment of the limits to the maximum optical power of the 1100 nm SLOC design

7.1. Introduction

Structures utilizing large waveguides (SLOC) have two main positive features. First, light emission is enclosed in a narrow vertical divergence angle. Second, due to the wide optical mode distribution (wide near-field), the facet load is reduced - leading to an increased threshold of the facet damage (COMD). Consequently, the design has the potential to deliver high optical output power before the failure occurs. This chapter is focused on the investigation of factors, other than COMD and device overheating, that limit the maximum output power of the diode lasers based on the 1100 nm multi-QW SLOC design. The studied design utilizes a 3.4 µm thick GaAs waveguide that results in narrow divergence angle of ~ 20° (at FWHM) and ~ 30° (95% power content). It is shown, via simulations and experimentally, that one of the factors reducing the peak optical power is weak carrier confinement in the active region leading to vertical carrier leakage and carrier accumulation in the p-doped waveguide. The reason for the vertical carrier leakage is a low effective barrier between the quantum well and the GaAs-waveguide. It is shown that an increased number of quantum wells strengthens the carrier confinement in the active region and thus a higher maximum optical power can be achieved.

7.2. Investigated SLOC designs

Structure	Number of QWs	GaAs waveguide thickness, µm	Confinement factor, Γ	Vertical divergence angle (measured at I = 10 A)	
				FWHM	95% power content
A1459-3	2	3.4	0.9 %	18.5°	30.0
A1457-3	4	3.4	2.2 %	19.3°	30.5

Table 7.1. The details of epitaxial designs A1459-3 and A1457-3. (Confinement factor calculated with QIP; far-field angles of coated 4 mm x 100 µm laser diodes were measured at 10 A, quasi-CW, 25°C.)

The discussion concerns two SLOC laser diode designs named A1459-3 and A1457-3. The multi-QW active region in both designs is embedded in a symmetric 3.4 µm thick GaAs waveguide that is enclosed in n- and p-doped $Al_{0.25}Ga_{0.75}As$ claddings (each 400 nm thick). The top layer of the epitaxial structures is a 100 nm thick p-GaAs contact layer. The discussed designs differ in the number of $In_xGa_{1-x}As$ quantum wells. Double quantum well (DQW) and

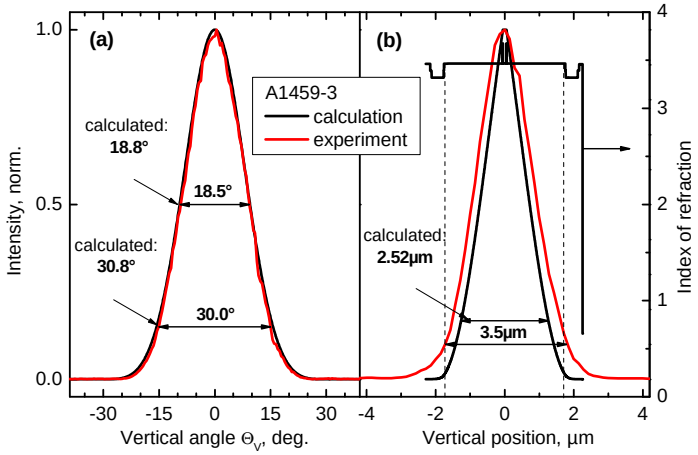

Figure 7.1. The calculated and measured vertical far-field (a) and near-field (b) of a A1459-3 design mounted as 4 mm long, 100 µm wide laser chip on c-mount. The spatial resolution of the near-field measurement is ~1.22 µm, thus the experimental near-field profile is wider than the calculated one. Measurement conditions: I=10 A (500 µs pulse duration, 20 Hz repetition rate) at a temperature of 25°C.

quadruple quantum well (QQW) active regions are utilized by the A1459-3 and the A1457-3 designs, respectively. The thickness and the In composition of the quantum wells are 7 nm and $x = 0.29$, respectively, resulting in a compression strain of ~ -2.1%. The emission wavelength is around 1100 nm. For the DQW structures, a 100 nm thick GaAs barrier was chosen, while in the QQW design, the quantum wells are separated with 50 nm thick GaAs barriers. The main features of both designs are compiled in table 7.1. The energy band profiles and the refractive index distribution of epitaxial structures A1459-3 and A1457-3 are presented in appendix 1.

The discussed structures have been designed to emit light into a vertical far-field angle below 20° at FWHM. The divergence angles of both designs differ slightly, i.e. 18.5° and 19.3° far-field angles were measured for A1459-3 and A1457-3, respectively. The difference in the beam divergence results from the different number of quantum wells utilized as the active region. The optical mode in the structure utilizing the QQW active region is stronger confined resulting in a wider beam divergence. The comparison of the calculated and measured far-fields is presented in figure 7.1.

7.3. Assessment of the limiting factor to the maximum optical power – experimental and simulation results

The power-current characteristic of a 100 µm-wide single emitter with a cavity length of 4 mm from the A1459-3 design was investigated on c-mount under various pulse durations in order to asses the possible maximum optical power. The laser facets have been first passivated in order to increase the mirror damage threshold (COMD) and then the front and the back facets have been coated with reflecivities of 2% and 95%, respectively. The optical power under CW condition was limited to 7 W due to the thermal rollover – overheating of the active region. The temperature rise of the laser crystal occurs upon passing current through a laser chip because of the electrical resistance of the epitaxial layers and the contacts. This heating process leads to thermal carrier re-escape from the active region and an increase of the non-radiative recombination process. This also leads to a higher threshold current and a lower differential efficiency and is observed as ‘rolling’ power-current characteristic. Reducing the time of the current flow through the laser-diode (shorter current-pulse duration) also reduces the transient active layer temperature (figure 6.2) leading to improved laser performance and thus higher maximum optical power (figure 7.2). The

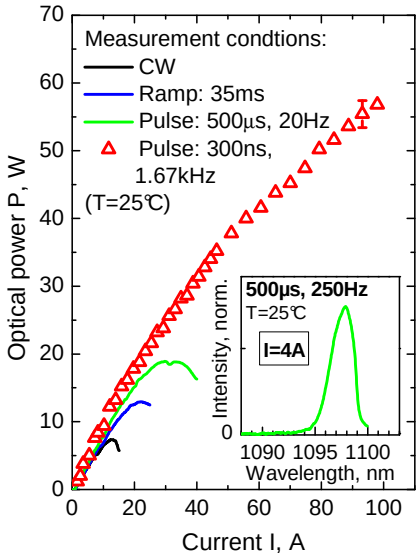

Figure 7.2. The increase of the optical power with the reduction of the current pulse duration from CW to 300 ns at heat-sink temperature of 25°C. The inset presents a spectrum at quasi-CW current of 4 A. Sample A1459-3.

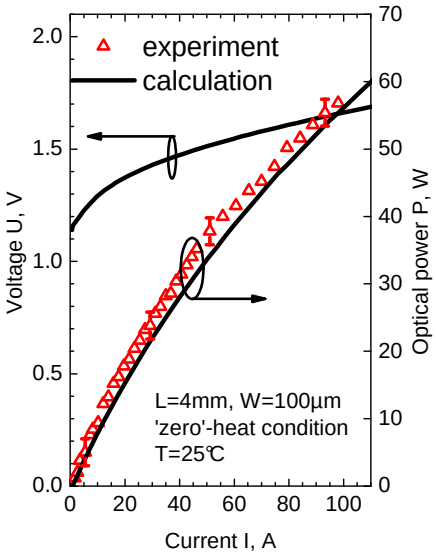

Figure 7.3. The comparison of calculated (solid black line) and measured (red symbols) under 'zero-heat' condition power-current characteristics. The calculated U-I characteristic corresponds to the voltage drop over the epitaxial structure without substrate.

measured thermal resistance of the A1459-3 laser-diode (4 mm x 100 µm) at 300 ns current pulse duration is R_{th} = 0.021 K/W, which corresponds to 5 K active region overheating at 100 A. Under a 300 ns current pulse duration (d-c: 0.05%) test, the maximum optical power of the sample has been increased to 57 W (at 100 A), which corresponds to 38 MW/cm^2 optical density at the laser facet (calculated using eq. (3.3.39)). Nevertheless, despite the strong reduction of the internal heating the diode exhibits non-linearity in the power-current characteristic at high current amplitudes.

By means of the WIAS-TeSCA software (see appendix 4) the simulations of the electro-optical laser performance have been performed without considering thermal effects (fixed temperature at 25°C). The calculated power-current characteristic follows the nonlinearity in the experimental power-current characteristic (figure 7.3). Moreover, the performed calculations of the vertical carrier distribution at various current levels (various applied electrical fields) have shown a vertical carrier leakage and the accumulation of the minority carriers in the p-doped waveguide (figure 7.4.b), indicating the reason of the deterioration of the laser diode performance.

During the electrical pumping of the laser structure, the injected carriers are transported by drift and diffusion via consecutive bulk layers in the direction of the active region where they should be captured and next participate in the stimulated emission process. The drift-diffusion process is initiated by applying an electrical voltage. The energy bands (conduction and valence) bend if an electrical field is applied and the effective barrier (the difference between the electron Fermi level in the active region and the conduction band edge of the waveguide) decreases. The higher the applied electric field, the stronger the reduction in the effective barrier and thus a higher fraction of injected carriers is transmitted through the active region to the waveguide layer, where they are lost to the stimulated photon emission process. The carrier leakage effect is stronger for electrons than for holes because of their lower effective mass and thus their higher mobility. The presence of the minority carriers accumulated in the waveguide was also observed experimentally by detecting a spontaneous emission signal from the waveguide above the threshold (discussed later in the chapter).

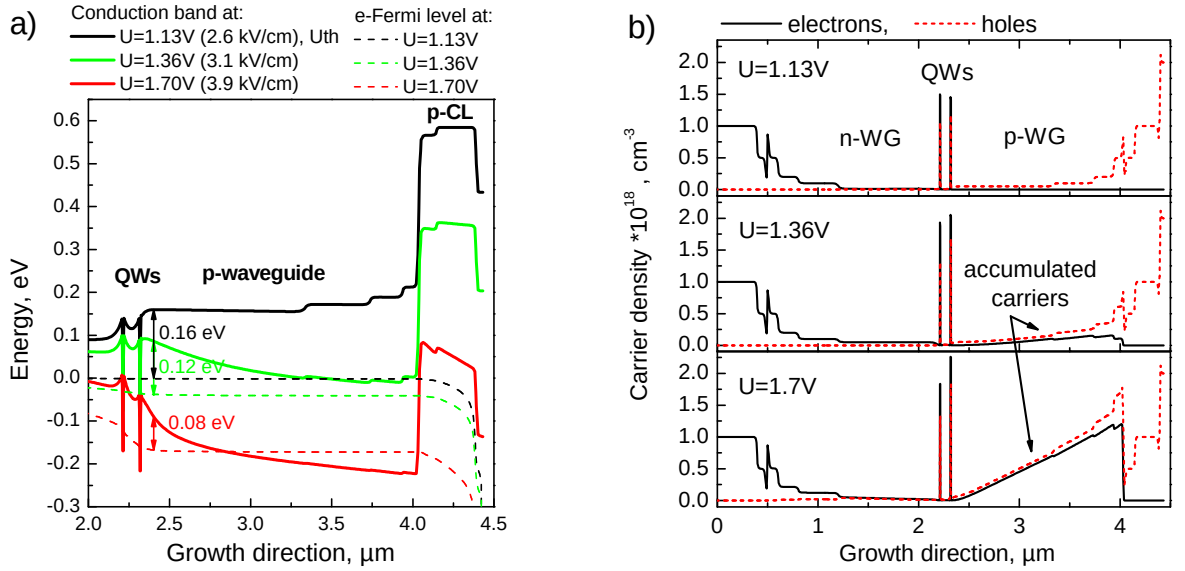

Figure 7.4. (a) The calculated conduction band profiles at the different bias voltages U=1.13 V ('turn-on' voltage), U=1.36 V (corresponding to I=18 A, E=3.1 kV/cm) and U=1.7 V (corresponding to I=110 A, E=3.9 kV/cm). (b) The calculated vertical carrier profiles (electrons – black solid line; and holes – red dashed line) at bias voltages: U=1.13 V, U=1.36 V and U=1.7 V. Simulations performed by means of TeSCA program under 'zero-heat' conditions at 25°C ambient temperature.

D.A. Vinokurov [1] and S.O. Slipchenko [2] discuss another mechanism responsible for the vertical carrier leakage under 'zero-heat' condition, which is a non-equilibrium distribution of the carrier density in the QW due to the finite time of carrier energy relaxation in the quantum well. However, this mechanism is not studied in this work.

7.4. Higher number of quantum wells for vertical carrier leakage reduction

7.4.1. Analytical description of the problem

The analysis of the carrier density in the active region and in the waveguide at threshold is presented as a function of the number of quantum wells. The laser threshold condition can be written as:

$$\frac{M \cdot \gamma_{QW}^{2D}}{W} \cdot \ln \frac{N_{QW}}{N_{tr}} = \alpha, \qquad (7.4.1)$$

where the left side of the above equation represents the modal gain which logarithmically depends on the carrier density in the quantum wells, N_{QW}, with N_{tr} denoting the transparency carrier density and γ_{QW}^{2D} being a dimensionless factor [3]. M is the number of quantum wells and W is the effective mode width. The right side of the equation represents the total losses α, consisting of internal and mirror losses. After simple rearrangement of (7.4.1) the relation between the carrier density in the quantum well and the number of quantum wells can be presented in the form:

$$N_{QW} = N_{tr} \cdot \exp\left(\frac{\alpha \cdot W}{M \cdot \gamma_{QW}^{2D}}\right) \qquad (7.4.2)$$

Furthermore, the drift-diffusion model of carrier transport, as in [4], is considered with the following assumptions:

(1) Charge neutrality in waveguide layers together with the Boltzmann statistic of the electrons in the valance band and holes in the conduction band:

$$n - p - C = 0\,, \tag{7.4.3}$$

where C denotes the density of impurities,

$$n = N_C \cdot \exp\left(\frac{F_n - E_C}{k_B T}\right) \text{ and } p = N_V \cdot \exp\left(\frac{E_V - F_p}{k_B T}\right) \tag{7.4.4}$$

are the densities of electrons and holes, respectively. N_C and N_V represent the density of states in conduction (E_C) and valance (E_V) bands, respectively; F_n and F_p are the quasi-Fermi levels for electrons and holes, respectively. k_B denotes the Boltzmann constant and T the temperature. These assumptions allow writing the quasi-Fermi levels separation V_F (the so-called quasi-Fermi voltage) in the form:

$$V_F = E_g + k_B T \frac{N^2}{N_C N_V} \tag{7.4.5}$$

with E_g representing the effective energy gap (distance of energy levels).

(2) Constant quasi-Fermi levels along the structure:

$$V_F^{QW} = V_F^{WG} \tag{7.4.6}$$

After a few mathematical transformations of the above equations, we obtain the relation between the carrier density in the waveguide and the carrier density in the quantum well:

$$N_{WG} = N_{QW} \cdot \left(\frac{N_C^{WG} N_V^{WG}}{N_C^{QW} N_V^{QW}}\right)^{\frac{1}{2}} \cdot \exp\left(-\frac{E_g^{WG} - E_g^{QW}}{2 k_B T}\right) \tag{7.4.7}$$

With this result, the carrier density in the waveguide is directly proportional to the carrier density in the QWs which in turn depends exponentially on the number of quantum wells according to (7.4.2). Furthermore, the carrier density in the waveguide exponentially depends on the difference between the energy gap of the waveguide and the effective band gap of the QWs ($E_g^{WG} - E_g^{QW}$).

According to this analysis and the results obtained in [5], the implementation of a higher number of quantum wells will decrease the density of carriers in the quantum well (lower quasi-Fermi level) and therefore will lead to a higher effective barrier, resulting in reduced carrier accumulation in the waveguide. This should result in a more linear power–current characteristics and higher maximum optical power.

7.4.2. Experimental results – optical detection of the carrier accumulation in the waveguide at high current injection levels

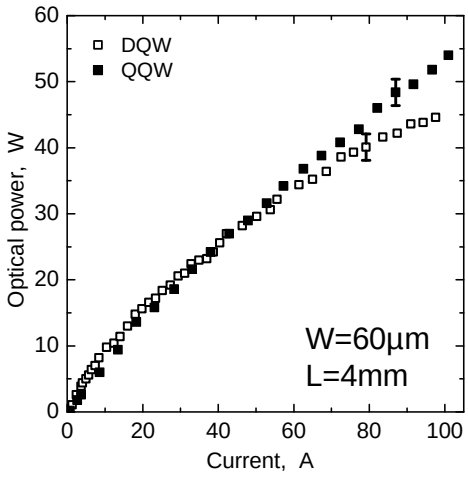

Figure 7.5. Power–current characteristics of the QQW and DQW structures (samples: A1457-3 and A1459-3, respectively) manufactured as 60 μm single emitter devices, measured under 300 ns pulse condition at 25°C ambient temperature.

In the first approach the power-current characteristic of the QQW structure (A1457-3) has been measured and compared to that of the baseline DQW sample (A1459-3). Figure 7.5 shows power-current characteristics under 300 ns pulse condition for 60 µm × 4 mm samples. The threshold current density per quantum well is decreased by about 30% from 110 $A \cdot cm^{-2}$ (DQW design) to 78 $A \cdot cm^{-2}$ (QQW design). The QQW samples show a significantly more linear characteristic and exhibit an increased peak power of 55 W (corresponding to the 74 MW/cm^2 optical density at the facet) whereas the DQW sample delivers only 45 W. Although the power-current curve is more linear, a rollover is still evident, indicating there are still residual carriers accumulated in the waveguide.

In order to directly test the presence of the accumulated carriers in the waveguide, the spontaneous emission in the wavelength range corresponding to the direct GaAs material was measured for both structures. The spontaneous emission component alone and its changes with current were examined. The measurement setup and the method are described in chapter 6.2. Figure 7.6 shows the results of this study. At low currents, no emission below the lasing wavelength is detected. At high currents, a pronounced emission from both structures is observed at a wavelength of 890 nm which relates to the direct band gap of the GaAs waveguide. The relative increase in the spontaneous emission intensity is more rapid (especially at higher currents) for the DQW structure than for the QQW structure, which is consistent with the larger roll-over in the DQW sample (see figure 7.6c). Additionally, for the DQW design a spectral peak at 960 nm is also measured at high carrier densities corresponding to emission coming from a higher transition in the quantum wells. The peak is not observed in the measured spectrum of the QQW design. It can be attributed to the previously mentioned, lower threshold current per quantum well and hence a lower carrier density.

It is interesting to note that the peak wavelength of the spontaneous emission is larger than the corresponding band gap wavelength of GaAs (870 nm). Based on the absorption coefficient for GaAs material presented in figure 7.7 [6], a re-absorption process in the GaAs waveguide that removes the short-wavelength portion of the spectrum might explain this behavior.

The robustness of the QQW design was next demonstrated by Wang et al. in [7]. The 60 µm and 200 µm wide single emitters were driven to an increased current of 240 A. The devices deliver 88 W and 124 W optical power, respectively. The maximum power was limited by the current supply (PicoLAS LDP-V240-100).

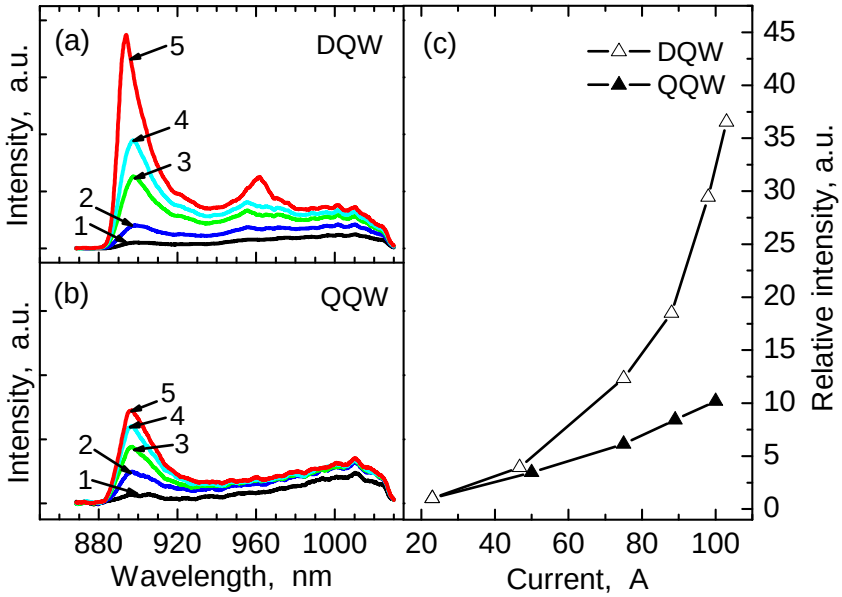

Figure 7.6. Spontaneous emission spectra from the waveguide, of (*a*) DQW and (*b*) QQW structures, at a current pulse duration of 300 ns and amplitudes of (1) 23, (2) 50, (3) 75, (4) 89 and (5) 100 A. (*c*) Increasing spontaneous emission intensity (relative to emission at 23 A) as a function of current as indication for stronger carrier escape in the DQW design (4 mm long with 60 μm stripe samples).

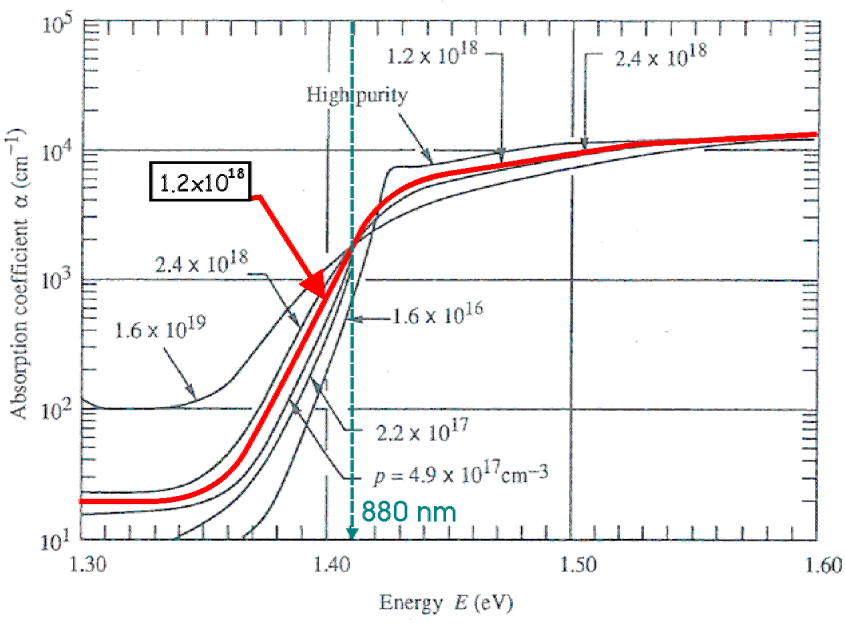

Figure 7.7. Absorption coefficient of p-type GaAs material at 297 K for different doping concentrations (after Schubert [6]).

7.5. Conclusions

In this chapter factors limiting the maximum optical power of diode lasers based on a SLOC design were assessed. The study considered diode lasers based on 1100 nm MQW GaAs-SLOC designs with small divergence angles of ~ 18° - 20° (FWHM). It was found that the peak power under 'zero-heat' conditions is limited by vertical carrier leakage and the minority carrier accumulation in the p-type waveguide. The effect was theoretically predicted and experimentally proven by measurement of the spontaneous emission from the confinement layers.

It was shown, theoretically and experimentally, that the implementation of a higher number of quantum wells strengthens the carrier confinement in the active region. A higher number of quantum wells lowers the threshold carrier density per quantum well, leading to an electron Fermi-level shift towards lower energies and consequently to an increment of the effective barrier heights. It was shown that the density of accumulated electrons in the p-doped waveguide is directly proportional to the carrier density in the quantum wells. It was experimentally proven that utilizing the gain medium with an increased number of quantum wells mitigates the vertical carrier leakage. This results in an increased of the optical output power from 45 W (DQW design) to 55 W (QQW design) at 100 A from a 60 µm wide laser chip. The corresponding optical density at the laser facet reaches 59 MW/cm^2 and 74 MW/cm^2, respectively. Moreover, the QQW-design driven by a current of 240 A delivers 88 W. The single emitter with an increased electrical contact stripe to 200 µm delivers 124 W. The optical power was limited by the current supply.

8

1130 nm-diode lasers with a reduced vertical divergence angle to 13° and maintained high optical power

8.1. Introduction

This chapter deals with diode lasers based on multi-QW SLOC structures emitting light at 1130 nm. High power diode lasers with wavelengths above 1100 nm find application as pump sources for Ho^{3+} and Tm^{3+} doped silica fibers lasers and Raman amplifiers in telecommunications. The aims of the study are as follows. Firstly, the development of a SLOC structure emitting light into a reduced divergence angle below 15° at FWHM (structures discussed in the previous chapter exhibit FWHM far-field angle ~ 20°). Secondly, the high optical output power of the device should be maintained.

In this chapter, it is shown that the vertical divergence angle is reduced from 18° to 13° (FWHM) and from 30° to 21° (95% power content) by increasing the thickness of the GaAs-waveguide from 3.4 µm to 5.0 µm. The second goal of the study – high optical power operation – is achieved by utilizing a higher number of QWs and also by increasing the emission wavelength. Both mechanisms increase the effective barrier between the active region and the waveguide leading to improved carrier confinement in the active region and thus resulting in improved laser operation (this problem is discussed in the previous chapter). A larger equivalent vertical spot-size of the 5 µm thick SLOC structure lowers the optical load at the laser facet and increases the threshold of the COMD. Consequently, a higher optical peak power can be achieved. Additionally, it is presented that processing diode lasers as devices with a large geometry reduces the electric and thermal resistance leading to reduced heating of the device and subsequently results in increased optical output power. The laser diodes are tested under quasi-CW conditions.

8.2. Investigated SLOC designs

Structure	Number of QWs	GaAs-waveguide thickness, µm	Vertical divergence angle (measured at I=17-20 A)	
			FWHM	95% power content
B1110-3	2	3.4	18.0°	29.5°
B1109-3	4	5.0	12.6°	20.6°

Table 8.1. The details of epitaxial designs B1110-3 and B1109-3. (Far-field angles of coated 8 mm x 200 µm laser devices measured at 17 A (B1110-3) and at 20 A (B1109-3), quasi-CW, 25°C).

The two structures that are investigated and discussed are named B1110-3 and B1109-3. Both of them consist of a thick symmetric GaAs waveguide embedded in 400 nm thick (on the p- and n-sides) $Al_{0.25}Ga_{0.75}As$ cladding layers. In both designs, a 100 nm thick p-GaAs contact layer is grown on top of the p-cladding layer. Structure B1110-3 consists of an active region with two quantum wells (DQW). The active region is embedded in the centre of the 3.4 µm thick waveguide, leading to an intended FWHM vertical far-field angle of 18° (measured). Structure B1109-3 consists of an active region with four quantum wells (QQW) and is placed in the middle of a 5.0 µm thick waveguide, resulting in a reduced vertical far-field angle of 13° (measured). The active region of both structures consists of compressively strained (~-2.3%) $In_xGa_{1-x}As$ quantum wells. The thickness and the *In* composition are 7 nm and $x = 0.33$, respectively. The emission wavelength of both structures is around 1130 nm (the optical spectrum is shown in figure 8). The DQW structure utilizes a 100 nm thick GaAs barrier between the quantum wells. In case of the QQW structure, the quantum wells are separated by 50 nm thick GaAs barriers. The main features of both designs are compiled in table 8.1. The energy band profiles and the refractive index distribution of the epitaxial structures B1110-3 and B1109-3 are presented in appendix 1.

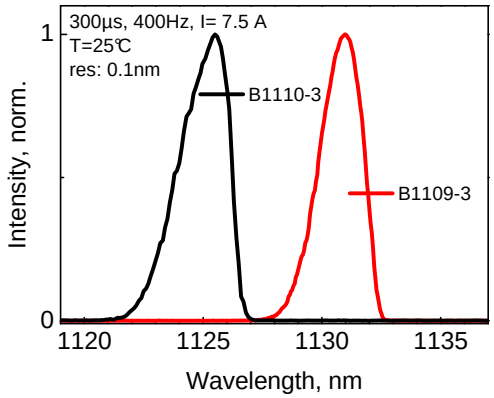

Figure 8. The optical spectrum of laser chips (L = 4 mm, W = 100 µm, mounted on c-mount) based on discussed designs B1110-3 (sold black line) and B1109-3 (solid red line). Measurement conditions: 300 µs, 400 Hz, current amplitude 7.5 A, heat-sink temperature 25°C.

8.3. Parameters of the laser structures – 'Pre-test' results

The first step of the experimental investigation were length dependent measurements of two test structures, t-B1075 for B1110-3 and t-B1059 for B1109-3 (the measurement method is described in chapter 5.1). From these measurements, internal laser parameters like internal efficiency η_i and losses α_i, the transparency current density J_{Tr} and the modal gain ΓG_0 have been determined (table 8.2).

Test structure	**Total waveguide thickness, µm**	**Number of QWs**	**$\Gamma G_{0(total)}$, cm^{-1}**	**η_i, %**	**α_i, cm^{-1}**	**$J_{Tr(total)}$, A/cm^2**	**I_{th}*, mA**	**S*, W/A**	**T_0*, K**	**U*, V**		**Θ_V, deg**	**λ, nm**
										(0.1A)	**(2A)**		
t-B1075	3.0	2	12.9	90	1.06	126.1	319	0.46	85	1.16	1.78	20	1122
t-B1059	4.4	4	22.5	86	1.05	220.1	381	0.44	99	1.20	1.83	15	1128

Table 8.2. Laser parameters determined from measurements in the pulsed operation of uncoated laser chips with 100 µm stripe width (* the slope per facet, the threshold current, the diode voltage and the characteristic temperature T_0 have been determined from a 1 mm long , 100 µm wide device).

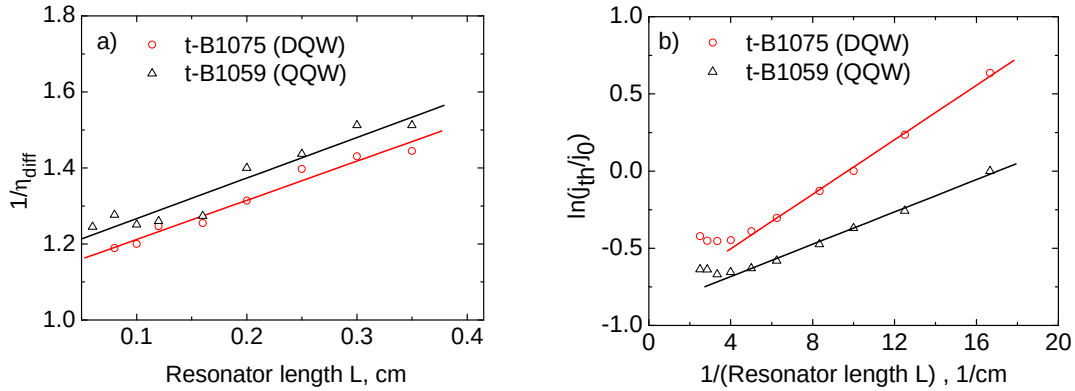

Figure 8.1 The experimental results of the length-dependent measurements of the test structures t-B1075 and t-B1059. (a) The inverse differential efficiency versus resonator length. (b) The logarithmic dependence of the threshold current on the resonator length.

The modal gain, transparency and the threshold current density do not scale linearly with the number of QWs because of the different waveguide thicknesses for both structures. Nevertheless, a slight decrease in the modal gain parameter and the transparency current density per quantum well from structure t-B1075 to structure t-B1059 can still be observed. The characteristic temperature T_0 is higher for the QQW design indicating non-deteriorated carrier confinement in the active region despite the use of much wider waveguides (the number of quantum wells is doubled thus the effective barrier of the active region is increased – this theme is discussed in chapter 7). The internal parameters like η_i and α_i are similar for both structures. This leads to similar slopes (S). The higher diode voltage for structure t-B1059 indicates a higher series resistance of the epitaxial structure due to the thicker waveguide layers and non optimized doping profile of the waveguide and cladding layers.

The waveguide thicknesses of the test structures are by several µm thinner than that of the investigated samples B1110-3 and B1109-3. Therefore, differences in the vertical divergence angles are observed.

8.4. Characterization of mounted devices

The discussed laser structures were processed as 4 mm and 8 mm long devices with stripe widths of 100 µm and 200 µm. The diode laser geometry and the reflectivities of the mirrors are presented in table 8.3. The broad area laser chips were mounted on c-mounts with the junction down for better heat dissipation (figure 3.8). The devices have been characterized at room temperature (25°C) under quasi-CW conditions (500 µs current pulse duration with 20 Hz repetition rate – equivalent to 1% duty-cycle).

Resonator length, L	Electrical stripe width, W	Front mirror reflectivity, Rf	Back mirror reflectivity, Rb
4 mm	100 µm	0.5%	95%
	200 µm	0.5%	95%
8 mm	100 µm	0.1%	95%
	200 µm	0.1%	95%

Table 8.3. Diode laser geometry and reflectivities of the mirrors of mounted devices.

Binary materials, such as GaAs, have a higher electrical and thermal conductivity compared with ternary and quaternary semiconductor materials. For this reason, GaAs is used for the thick waveguide layers. The high carrier mobility of such a material allows for low doping profiles resulting in reduced free-carrier absorption and hence low internal optical losses. This further enabled the construction of powerful devices with extremely long (8 mm) optical cavities. Such a long gain medium allows the use of very low facet reflectivities of the front facet (less than 0.5%). A low reflectivity reduces the optical load on the facet and is expected to lower the risk of the catastrophic optical mirror damage (COMD).

8.4.1. Laser based on 3.4 µm thick GaAs-waveguide

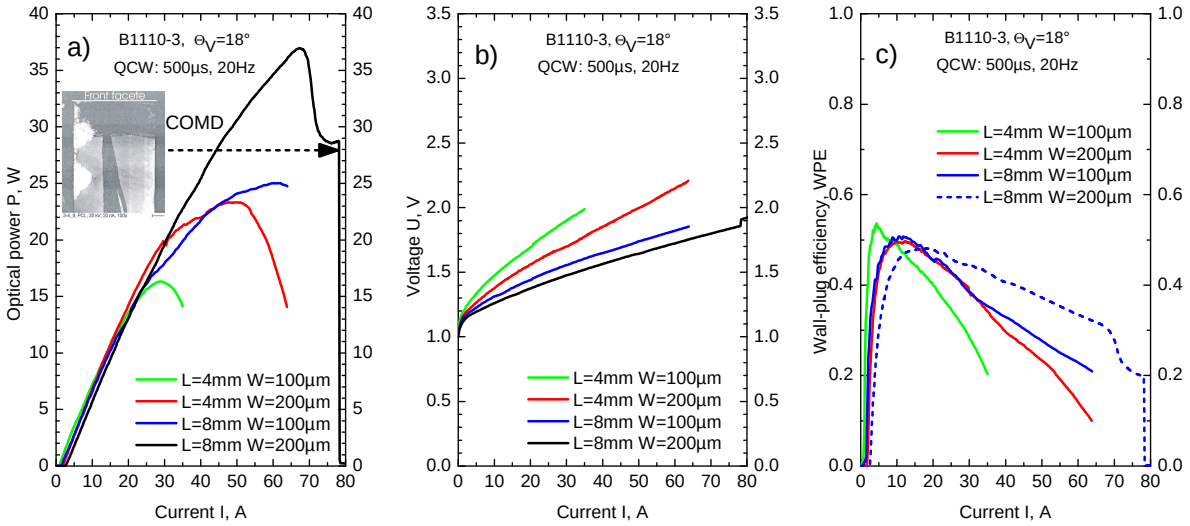

Figure 8.2. The experimental (a) power-current (b) voltage-current and (c) wall-plug efficiency characteristics of the B1110-3 design processed as 4 mm or 8 mm long diode laser with 100 µm or 200 µm electrical stripes mounted junction-down on c-mounts. Measurement conditions: 500 µs, 20 Hz, 25°C heat-sink temperature. The inset of figure (a) - the cathodoluminescence image presenting the COMD damage of the 8 mm x 200 µm laser chip.

Resonator length,	**Mesa stripe**	**I_{th}, A**	**S, W/A at 2xI_{th}**	**S, W/A at 5xI_{th}**	**R_s, mΩ**	**WPE_{max}**	**P, W at rollover**
4 mm	100 µm	0.9	0.87	0.84	40	0.53	16 (29A)
4 mm	200 µm	1.9	0.86	0.84	20	0.49	23 (50A)
8 mm	100 µm	1.5	0.82	0.77	16	0.50	25 (60A)
8 mm	200 µm	2.7	0.80	0.77	12	0.48	37 (67A)

Table 8.4. The electro-optical parameters of the B1110-3 design (DQW, λ = 1130 nm, 3.4 µm-GaAs-WG, Θ_V = 18°) realized as 4 mm and 8 mm long diode laser with 100 µm and 200 µm electrical stripes mounted on c-mount heat-sink. Measurement conditions: 500 µs, 20 Hz, 25°C heat-sink temperature.

The baseline structure B1110-3 mounted as a 4 mm long and 100 µm wide device exhibits 16 W optical power at an injection current of 29 A. Increasing the resonator length and the mesa width results in a lower internal facet load as well as a reduced series and thermal resistance of the device. Consequently, the maximum achievable optical power is increased. Moreover, increasing the optical cavity length reduces the threshold current density leading to improved vertical carrier confinement and thus increased characteristic temperature T_0 [1]. The 4 mm long device with an increased electrical stripe width to 200 µm delivers maximum optical power of 23 W at 50 A. Increasing the resonator length from 4 mm to 8 mm

the optical power was further increased to 37 W at 67 A (200 µm emitter). For three devices, the maximum optical power was limited due to thermal roll-over. Both facet passivation and low modal facet load, due to the SLOC design, reduce the risk of COMD and enable high optical power of 37 W at 67 A corresponding to 24.8 MW/cm^2 of internal power density. However, the 8 mm long and 200 µm wide laser chip, after roll-over, failed at 78 A because of COMD (confirmed by facet inspection and cathodoluminescence imaging [2], illustrated in inset of figure 8.2.a). The electro-optical parameters of the measured devices are compiled in table 8.4. Figure 8.2 shows the power-current and voltage -current characteristics of a baseline structure B1110-3 manufactured as broad area laser for four chip geometries.

8.4.2. Laser based on 5.0 µm thick GaAs-waveguide

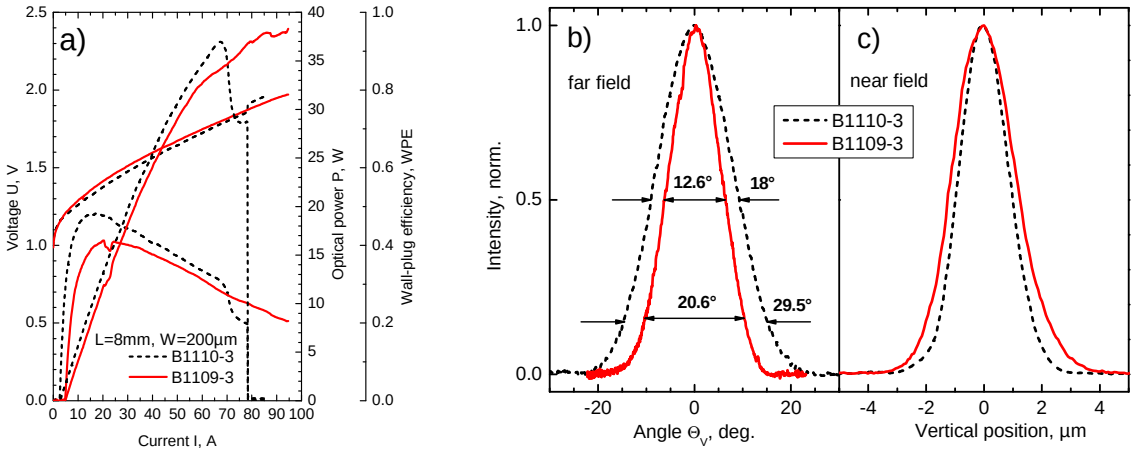

Figure 8.3. The experimental P-U-I characteristic (a) and the vertical beam profiles at 50 A (b,c) of the B1110-3 design (DQW, 3.4 µm-GaAs-WG) and the B1109-3 design (QQW, 5.0 µm-GaAs-WG) realized as 8 mm long, 200 µm wide laser diodes, mounted on c-mount heat-sinks. Measurement conditions: 500 µs, 20 Hz, ambient temperature of 25°C.

Structure	**I_{th}, A**	**S, W/A**	**WPE_{max}**	**P_{max}, W**	**T_0*, K**	**T_1*, K**	**Θ_V, deg (I = 17-20 A)**		**M^2 95%**
							FWHM	**95%**	
B1110-3	2.7	0.80	0.48	37	114 (4)	649 (101)	18.0	29.5	1.3 ±0.3
B1109-3	5.0	0.76	0.40	38	127 (5)	386 (4)	12.6	20.6	1.2 ±0.3

Table 8.5. Experimental parameters of 8 mm long devices with 200 µm stripe width under quasi-CW (500 µs, 20 Hz) operation at 25°C. Parameters T0 and T1 were obtained by short pulse measurements for a temperature range of 15°C – 65°C and 15°C – 45°C, respectively.

Next, the structure B1109-3 with an increased vertical cavity width of 5 µm (resulting in $\Theta_{V,FWHM} = 13°$) and with higher number of quantum wells in the active region (QQW), has been processed as 8 mm long and 200 µm wide single emitters. When tested under quasi-CW conditions, the structure delivers 38 W of the optical power. According to the discussion and results from chapter 7, it can be concluded that the increased number of QWs improves the vertical carrier confinement and thus reduces the minority carrier aggregated in the confinement layers. Despite the wider waveguides, for which an exaggerated negative effect is expected (larger volume where electrons and holes can recombine and be a loss), the design maintains high slope efficiency and high optical power. Moreover, the modal load on the facet is reduced due to the wide vertical near-field. Therefore, the same output power could be

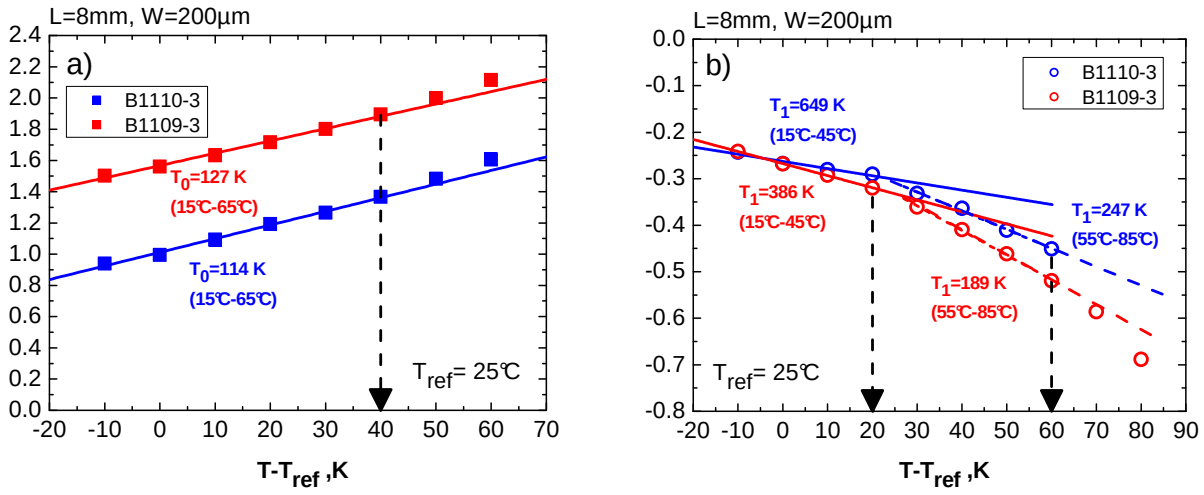

Figure 8.4. Logarithmic dependence of the threshold current (a) and the slope efficiency (b) on the heat-sink temperature for the B1110-3 design (DQW 3.4 µm-GaAs-WG) and the B1109-3 design (QQW 5.0 µm-GaAs-WG). Solid and dashed lines represent the linear fit to the experimental dates (points). Measurements correspond to facet-coated devices with a length of 8 mm and a width of 200 µm.

achieved as compared to B1110-3 (DQW, WG = 3.4 µm, Θ_V = 18°), but without mirror degradation (COMD). The maximum wall-plug efficiency (WPE_{max}) reaches a value of 48% at 11 W for the structure B1110-3 and 40% at 12 W for the structure B1109-3 owing to its higher threshold current. The P-U-I characteristics are illustrated in figure 8.3. The results of the 8 mm long, 200 µm wide laser chips mounted on c-mounts are compiled in table 8.5.

From the temperature dependence of the threshold current and the slope efficiency, the characteristic temperatures T_0 and T_1 were obtained for temperature ranges of 15°C – 65°C and 15°C – 45°C, respectively. The measurements have been carried out under short pulse (300 ns) operation to avoid additional overheating of the active region during its operation (presented in figure 8.4). The T_0 parameter for the structure B1110-3 (114±4 K) is lower than for the B1109-3 sample (127±5 K) despite its lower threshold current density, indicating improved carrier confinement in the active region for the B1109-3 design achieved by an increased number of QWs. However, the T_1 parameter for B1109-3 (386±4 K) is smaller than T_1 for B1110-3 (649±101 K), indicating that there are still high losses - possibly due to carrier accumulation in the thick waveguide layer.

The 8 mm long and 200 µm wide laser devices based on the structure B1110-3 at higher current levels exhibit far-field angles of 18° (FWHM) and 29.5° (95% power content). Of the laser devices, B1109-3 exhibit much lower far-field angles of 12.6° (FWHM) and 20.6° (95% power content). The vertical beam propagation factor M^2, determined from the near- and far-field distributions (95% power content), is equal to 1.3±0.3 and 1.2±0.3 for structures B1110-3 and B1109-3, respectively. The vertical far-field profiles were measured up to a current of 50 A. No changes in the beam profile were observed. The fact that no indication of higher-order vertical modes are visible in the beam profiles and the fact that the beam propagation factor $M^2 \approx 1$ (chapter 5.3), we conclude that these modes are fundamental vertical modes. Figures 8.3.b and c show the vertical far-field distributions of the designed structures at currents corresponding to the maximum efficiency of the laser, i.e. 17 A and 20 A for structures B1110-3 and B1109-3, respectively.

8.5. Conclusions

The 1130 nm MQW SLOC design with the vertical divergence angle reduced to 13° (FWHM) and 21° (95% power content) by widening GaAs waveguide to 5 µm has been characterized. The introduction of a higher number of QWs (four) increased the weak modal gain caused by wide waveguide layers and improved the vertical carrier confinement allowing for high output power operation. The low internal loss design allowed the manufacture of devices with an 8 mm long cavity and with a low front facet reflectivity (0.1%). An optical power of 38 W under quasi-CW operation mode has been demonstrated with an 8 mm long and 200 µm wide single emitter. The optical power was limited by chip overheating. The devices did not suffer from COMD.

9

1060 nm laser design based on extremely large waveguides for small divergence angles of 10°

9.1. Introduction

This chapter focuses on the far-field angle reduction to angles below 15° (FWHM) and 26° (95% power content) for diode lasers emitting at 1060 nm. High power diode lasers emitting near 1060 nm find applications in telecommunications as pump sources for silica-based fiber amplifiers "co-doped" with erbium and ytterbium (for amplification of a 1550 nm optical signals). Furthermore, high power diode lasers emitting at this wavelength are also used for direct material processing. The laser systems usually consist of several single emitters joined together into a laser bar or stack. A lens system is used to combine and shape the asymmetric, widely diverged beams. Often, the optical light of high power laser beams is coupled into and transmitted through optical fibers. In order to increase coupling efficiency (with reduced optical power loss, reduced aberrations) and to ease coupling, diode lasers with narrow vertical divergence are required. Moreover, a narrow far-field angle of the laser beam is advantageous in laser systems with external resonators. The low beam divergence angle results in a higher reflectivity of the volume Bragg grating, which in turn enables building longer resonators. It is shown that for 1060 nm multi-QW designs the GaAs-waveguide does not offer sufficiently high effective barriers to confine the carriers in the active region and, in consequence, the design suffers from strong carrier spill-over. We demonstrate that the effective barrier is sufficiently increased when an AlGaAs-waveguide is utilized. The AlGaAs waveguide, however, results in an increased far-field angle. The influence of the increased Al content in the waveguide on the vertical beam profile is discussed. Finally, a structure with 8.6 µm thick $Al_{0.1}Ga_{0.9}As$ waveguides, is presented resulting in a vertical divergence angle of 10° (FWHM) and a high internal efficiency of 90%.

9.2. Investigated SLOC designs

Three structures are discussed: structure C1357-6 with a 6 µm thick GaAs waveguide, structure C1605-6 with a 6 µm thick $Al_{0.1}Ga_{0.9}As$ waveguide and structure C1625-6 with a very thick, 8.6 µm, $Al_{0.1}Ga_{0.9}As$ waveguide. The active region of the considered designs is placed in the centre of the waveguide and consists of four compressively strained (-1.75%) $In_xGa_{1-x}As$ quantum wells. The thickness and *In* composition are 7 nm and $x = 0.25$, respectively. The quantum wells are separated from each other by tensile strained (~0.73%) $GaAs_{1-y}P_y$ barriers, and separated from the waveguide with a $GaAs_{1-y}P_y$ spacer. The thicknesses and composition are 7.5 nm (barriers), 5 nm (spacers) and $y = 0.8$, respectively.

Structure	Waveguide		Cladding layer	Vertical divergence angle*		Beam propagation parameter* $M^2_{95\%}$
	Material	Thickness, µm	Material	FWHM	95% power content	
B1109-3	*GaAs*	*5.0*	*$Al_{0.25}Ga_{0.75}As$*	*12.6°*	*20.6°*	*1.20 ±0.31*
C1357-6	GaAs	6.2	$Al_{0.1}Ga_{0.9}As$	10.2°	16.6°	1.18 ±0.25
C1605-6	$Al_{0.1}Ga_{0.9}As$	6.0	$Al_{0.2}Ga_{0.8}As$	13.0°	21.6°	1.18 ±0.33
C1625-6	$Al_{0.1}Ga_{0.9}As$	8.6	$Al_{0.2}Ga_{0.8}As$	10.3°	20.3°	1.58 ±0.31

Table 9.1. Details of epitaxial designs C1357-6, C1605-6, C1625-6 and benchmark design B1109-3. *Far-field angles (and the propagation factor M^2) of coated 4 mm x 100 µm laser diodes measured at currents corresponding to the maximum conversion efficiency (~8 A, QCW, 25°C).

The emission wavelength is around 1060 nm. The main features of the designs and the measured vertical beam parameters are compiled in table 9.1. The energy band profiles and the refractive index distribution of each epitaxial structure are presented in appendix 1. The wide optical cavity supports a high number of vertical modes. To reduce the number of guided modes the refractive index of the $Al_xGa_{1-x}As$ cladding layers has been reduced by reducing the Al-content to 10% for the design C1357-6 and to 20% for designs C1605-6 and C1625-6 (the benchmark structure B1109-3 utilizes $Al_{0.25}Ga_{0.75}As$ cladding layers). Moreover, the low Al-content materials feature a lower series resistance.

In previous chapters, laser structures utilizing a MQW active region with thick (50 nm – 100 nm) GaAs-barriers and GaAs-waveguides were discussed. The reference structure B1109-3 utilizing a 5 µm thick waveguide exhibits vertical divergence angles of 13° (FWHM) and 21° (95% power content). Further calculations of the divergence angle dependence on the GaAs-waveguide thickness show an angular reduction to 10° (FWHM) for a waveguide thickness of 7.8 µm (calculations were performed at the emission wavelength of 1060 nm and for $Al_{0.1}Ga_{0.9}As$-claddings). Alternatively, in the SLOC structures, the optical mode profile can be changed by the use of thin GaAsP quantum barriers (7.5 nm) instead of the thick GaAs barriers (50 nm). The optical mode in the structures utilizing thin quantum barriers is less confined in the active region and spreads wider in the optical cavity, (see the inset of Figure 9.1a), resulting in reduced vertical divergence angles (Figure 9.1b). Structures based on an active region with GaAsP quantum barriers have the potential to achieve a vertical far field angle of 10° at FWHM by using a narrower, 6.6 µm thick, waveguide. The grown structure C1357-6, however, utilizes a 6.2 µm thick GaAs-waveguide resulting in a FWHM vertical divergence angle around 10.5°. The measured beam profiles of the mounted laser chips are presented in Figure 9.2. Changing the material and the thickness of the quantum barriers leads to a very small change of the emission wavelength (1-2 nm). The small change of the emission wavelength hardly affects the refractive index of the epitaxial layers and does not influence the far-field angle reduction.

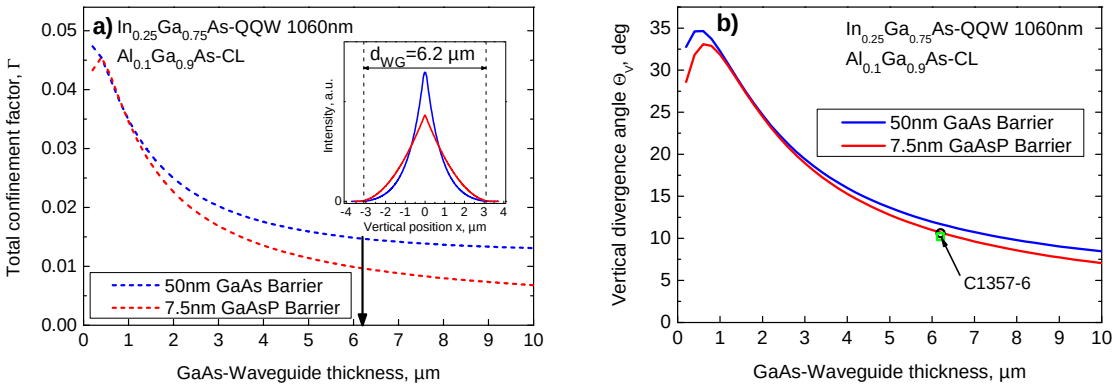

Figure 9.1 (a) Calculated (QIP) confinement factor Γ and (b) the vertical divergence angle of 1060 nm QQW $In_{0.25}Ga_{0.75}As/GaAs/Al_{0.1}Ga_{0.9}As$ structures with different quantum barrier designs versus the waveguide thickness. The inset in figure (a) represents the comparison of the mode distributions of a structure utilizing a 6.2 µm thick GaAs waveguide and two different designs for the quantum barrier.

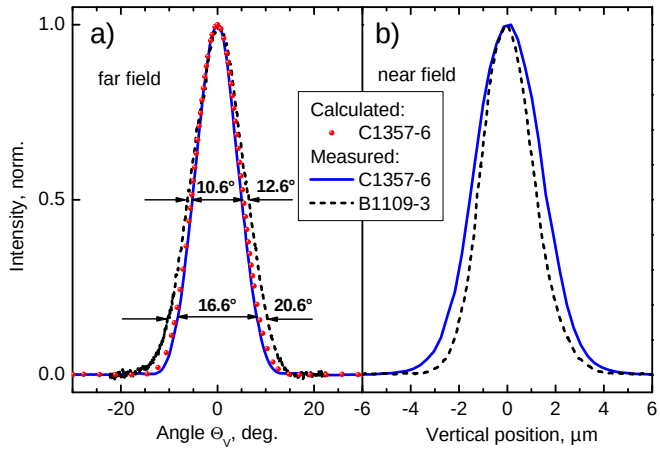

Figure 9.2. Calculated and measured vertical beam profiles (a) far-field and (b) near-field for the C1357-6 design and the benchmark structure B1109-3. Laser geometry: L = 4 mm, W= 100 µm. Measurement conditions: 500 µs, 20 Hz, 25°C at currents corresponding to the maximum conversion efficiencies (8.4 A for C1357-6 and 7.8 A for B1109-3).

The three laser designs, C1357-6, C1605-6 and C1625-6, have been experimentally tested as follows. First, uncoated and unmounted 100 µm wide laser chips with various resonator lengths have been characterized under pulsed operation (1.5 µs, 5 kHz) in order to obtain the internal parameters of the laser structure. In the next step, laser chips were processed as 100 µm wide and 4 mm long single emitters with coated front and back facets resulting in reflectivities of 1.5% and 95%, respectively. The single emitters were mounted junction-down onto c-mounts and tested under quasi-continuous wave (quasi-CW) operation (500 µs, 20 Hz) at a heat sink temperature of 25°C. The internal parameters obtained from length dependent measurements are compiled in table 9.2 and the quasi-CW electro-optical parameters of mounted devices are depicted in table 9.3. The discussion of the laser parameters is presented in the following subchapters. The long-wavelength (1130 nm) structure with a small vertical far-field angle of 13° at FWHM (B1109-3), presented previously in chapter 8, exhibits good internal parameters as well as high optical power when processed as a single broad area emitter. Therefore, it is included here as a benchmark structure for the design optimization of the 1060 nm high power devices with further reduced vertical beam divergence angle.

Structure	$Al_xGa_{1-x}As$ Waveguide		$\Gamma G_{0(total)}$, cm^{-1}	η_i, %	α_i, cm^{-1}	$J_{Tr(total)}$, A/cm^2	I_{th}*, mA	S*, W/A	T_0*, K	U*, V (2A)	λ, nm
	x	Thickness									
t-B1059	*0*	4.4 µm	22.5	86	1.05	220	381	0.44	99	1.83	1128
t-C1357	0	6.2 µm	15.3	54	0.47	336	728	0.34	52	1.51	1060
t-C1605	0.1	6.0 µm	26.4	86	1.06	288	453	0.46	149	1.63	1061
t-C1625	0.1	8.6 µm	22.7	90	1.57	264	467	0.47	143	1.78	1060

Table 9.2. Laser parameters of the discussed SLOC designs obtained from the length-dependent measurements of uncoated chips. The t-B1059 is the benchmark design (25% Al content in claddings results in a higher bias voltage of the diode laser). (* The slope per facet, the threshold current, the bias voltage, as well as the characteristic temperature T_0 have been determined from a 1 mm long, 100 µm wide device.)

Structure	$Al_xGa_{1-x}As$ Waveguide		I_{th}, A	S, W/A at $2xI_{th}$	S, W/A at $5xI_{th}$	WPE_{max}	P, W at 25A	T_0, K 15-65°C	T_1, K	R_{th}, K/W
	x	Thickness								
B1109-3	*0*	*5.0 µm*	*1.53*	*0.80*	*0.74*	*0.41*	*15.6*	*138 ±8*	*386 ±4*	*1.27**
C1357-6	0	6.2 µm	2.03	0.76	0.60	0.38	10.0	85 ±2	95 ±11	0.53
C1605-6	0.1	6.0 µm	1.68	0.80	0.78	0.43	15.0	157 ±6	537 ±45	0.84
C1625-6	0.1	8.6 µm	1.78	0.83	0.81	0.42	14.4	144 ±4	518 ±60	1.26

Table 9.3. Electro-optical parameters of 4 mm long, 100 µm wide single emitters mounted on c-mount. Test conditions: 500 µs, 20 Hz, 25°C. (*The thermal resistance of benchmark structures measured under 300 µs, 400 Hz conditions.). T_0, T_1 parameters have been obtained under 'zero-heat' condition test.

9.3. Low effective barrier in GaAs-waveguide based design resulting in inefficient laser operation

The 1060 nm emission wavelength from sample C1357-6 is obtained from InGaAs quantum wells containing a lower mole fraction of *In* atoms (in comparison to the 1130 nm emission wavelength of the benchmark sample). An $In_xGa_{1-x}As$ material with lower In-content results in a lower affinity energy. This results in higher conduction band edge energy and a lower energy of the valence band edge. When embedded in GaAs-waveguides shallow quantum wells are formed – the effective barriers for both, electrons and holes are reduced. The vertical carrier confinement is weakened and consequently, carrier leakage to the waveguide occurs. (This phenomenon is also shown in simulations and proven experimentally in the further text.) The carrier accumulated in the thick, especially p-doped, waveguide is a loss to the lasing and results in a low internal efficiency η_i = 54% (compared to $\eta_{i,t-B1059}$ = 86%), consequently also a lower external efficiency S = 0.34 W/A (compared to $S_{t\text{-}B1059}$ = 0.44 W/A) and also lower characteristic temperature T_0 = 52 K (compared to $T_{0,t\text{-}B1059}$ = 99 K). The measured internal losses for the t-C1357 design of α_i = 0.47 cm^{-1} are, however, unexpectedly two times smaller than for the benchmark design $\alpha_{i,t\text{-}B1059}$ = 1.05. For laser structures in which strong carrier leakage occurs, the internal losses as well as the internal efficiencies are not independent of the resonator length - especially when short (< 2 mm long) lasers are considered [1]. In shorter lasers, the threshold gain to overcome the mirror losses is higher and thus the threshold current densities are higher. The higher threshold density translates to an increased carrier density in the quantum wells, which leads to increased carrier leakage. This effect is exaggerated in structures characterized with a low confinement factor and thus a low modal gain, as is the case for the C1357 design. Therefore, the α_i and the η_i values obtained in the length dependent measurement are not reliable. Even

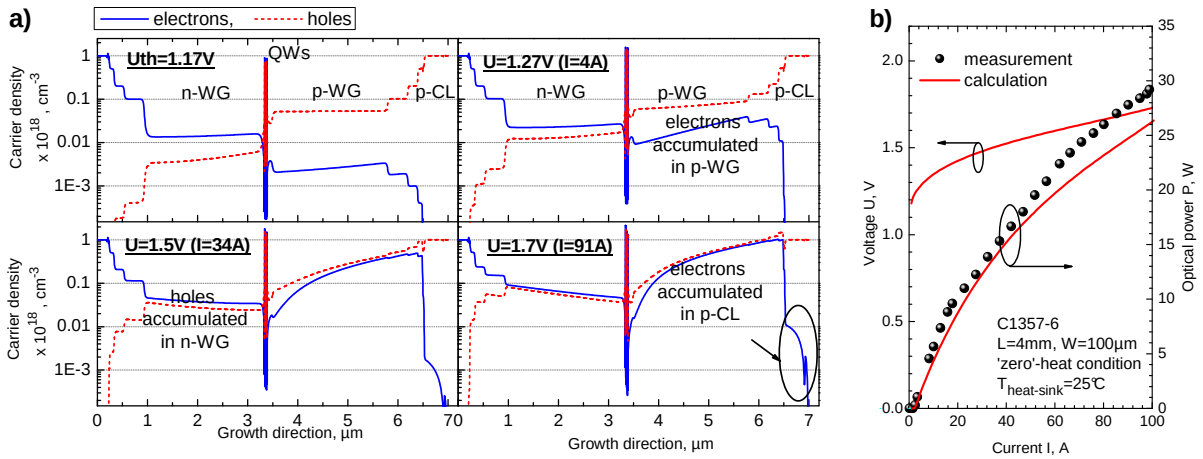

Figure 9.3. (a) The calculated vertical carrier profiles (electrons – black solid line; and holes – red dashed line) at different bias voltages from U=1.17 V ('turn-on' voltage) to U = 1.7 V. (b) Comparison of calculated (solid red line) and measured (black symbols) power-current characteristics for the sample C1357-6 processed as 4 mm long and 100 µm wide laser device. Measurement conditions: short current pulse duration 300 ns, 1 kHz, 25°C heat-sink temperature. Simulations performed by means of WIAS-TeSCA software without self-heating. The calculated U-I characteristic corresponds to the voltage drop over the epitaxial structure without a substrate.

though the η_i value is not quantitatively reliable, it does not contradict the assumption of the carrier leakage in the design. Moreover, the transparency current density obtained from the length dependent measurements depends on α_i. Therefore, its value can only be calculated with an uncertainty. In order to obtain reliable experimental values, the length dependent measurements of lasers with resonator lengths of more than 4 mm have to be performed. However, the thin metallization of the prepared 'pre-test' samples (see chapter 4.2.1) results in an increased inhomogeneous spreading of the injected current. Therefore, the length dependent measurement of longer lasers has not been performed. The increased threshold current for the t-C1357 lasers is caused by a strongly reduced confinement factor, as predicted, and thus a reduced modal gain.

In order to investigate the assumption that the degradation of the slope efficiency for the C1357 design is caused by poor carrier confinement in the active region, the carrier-transport properties and the power-current characteristic of the 4 mm long, 100 µm wide laser device have been simulated. The simulations have been performed with no concern for self-heating. The calculations of the vertical carrier distributions at various applied electrical voltages are presented in figure 9.3a. The calculations indicate carrier escape and its accumulation in both n- and p-doped waveguides - even at low applied electrical fields (U = 1.27 V, E = 1.81 kV/cm, I= 4 A). For an increasing bias voltage, the band bending is stronger, the effective barrier is lower, and the carrier leakage is more severe. At a bias voltage of U = 1.7 V (corresponding to I = 91 A and E = 2.42 kV/cm), the accumulation of the minority carriers can be seen in the p-cladding layers as well... The simulations of the band structure exhibit a reduction of the already low effective barrier for electrons from 0.14 eV at the 'turn-on' voltage to 0.04 eV at U = 1.7 V. The carriers accumulated in the confinement layers are losses to the lasing process resulting in a strongly nonlinear power-current characteristic. In figure 9.3b, the comparison of the simulated and measured power-current characteristics under 'zero-heat' conditions is presented. The simulated power-current characteristic reproduces the roll-over effect, which is seen experimentally as well.

The consequences of the carrier leakage can also be observed in quasi-CW mode operation, where the thermal effects exaggerate the carrier accumulation in the confinement layers. The C1357-6 laser (4 mm long, 100 µm wide) delivers 10 W of quasi-CW optical

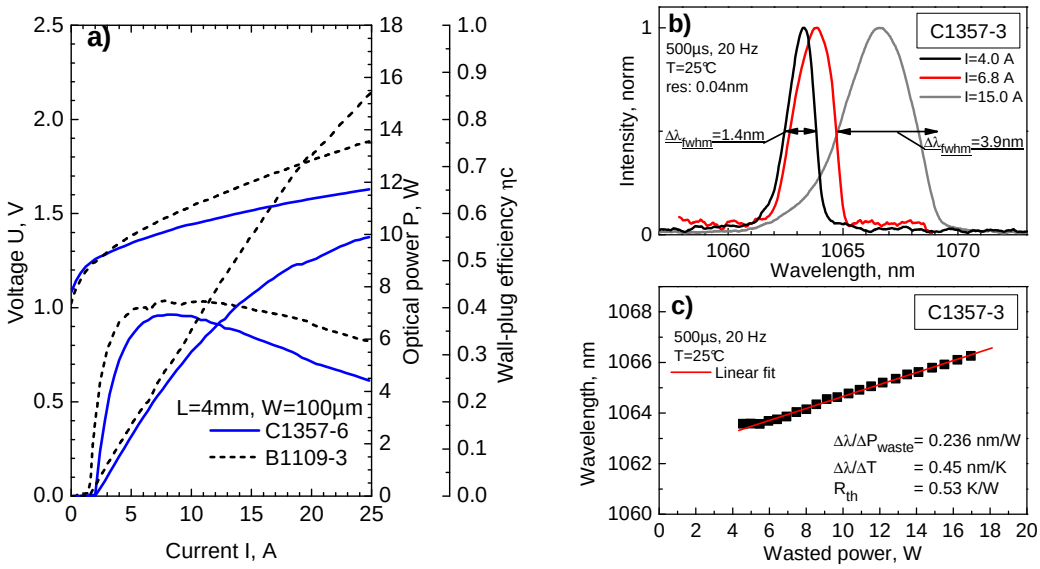

Figure 9.4. (a) Comparison of the experimental P-U-I characteristics between the benchmark structure (B1109-3) and the C1357-6 design. (b) Optical spectrum of the C1357-3 design at 4.0 A, 6.8 A and 15 A. (c) Lasing wavelength of the sample C1357-6 versus wasted power (black symbols) and the linear fit to the experimental data (solid red line). Measured laser devices: 4 mm long, 100 µm wide single emitters mounted on c-mount. Test conditions: 500 µs, 20Hz, heat-sink temperature of 25°C.

power at 25 A. This is 33% less optical power than the benchmark sample (B1109-3, P_{QCW} = 15.6 W). Figure 9.4 shows the comparison of the measured P-U-I characteristics of C1357-6 and B1109-3 lasers.

The C1357-6 lasers feature a lower series resistance than the B1109-3 sample, despite the fact, that it utilizes wider waveguides. The reason for this effect is the lower Al content in the AlGaAs-cladding layers. The low overlap of the optical mode with the active region results in a low modal gain and thus a high threshold current. The high threshold further reduces the maximum value of the conversion efficiency of the laser.

The power-current characteristics of the 4 mm long lasers have been measured under short current pulse operation (300 ns, 1 kHz) at different heat sink temperatures. From the temperature dependence of threshold and slope, the characteristic temperatures T_0 and T_1 have been calculated. The C1357-6 design exhibits much lower characteristic temperatures of T_0 = 85 K and T_1 = 162 K in comparison to the B1109-3 design, characterized with T_0 = 138 K and T_1 = 386 K. Moreover, the temperature dependent laser performance is stable only at low temperatures, namely up to 35-45°C. Above 45°C, the temperature dependence of the threshold current and slope efficiency degrades dramatically – a decrease of more than 50% of the T_0 parameter and a decrease of 70% of the T_1 parameter was observed. The temperature dependencies of threshold and slope efficiency on the heat-sink temperature are presented in Figure 9.5. Considering the low effective barriers of the design (0.14 eV) and the fact that the thermionic emission time depends strongly on the barrier height (~ $\exp(E_{eff}/k_BT)$, [2]), the deterioration of the thermal stability of the laser performance for temperatures above 45°C probably occurs due to thermal carrier spill-over from the active region into the confinement layers.

9.4. AlGaAs-waveguides for good carrier confinement and improved laser operation

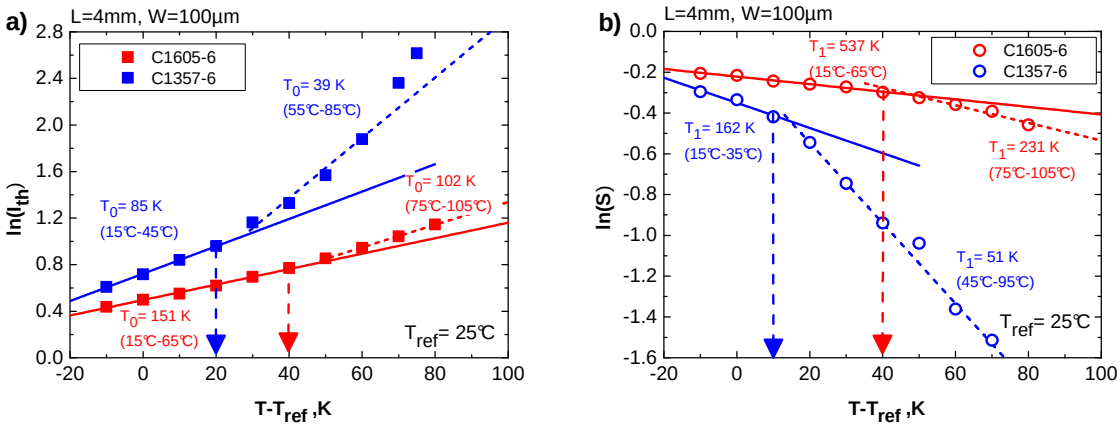

Figure 9.5. Logarithmic dependence of (a) the threshold current and (b) the slope efficiency on the heat-sink temperature for a GaAs waveguide design (C1357-6) and an $Al_{0.1}Ga_{0.9}As$ waveguide design (C1605-6). Solid and dashed lines represent the linear fit to the experimental data (points). (Measurement results correspond to coated 4 mm long, 100 µm wide diode lasers).

(C1357-6), a structure with low aluminum content (10%) in the $Al_xGa_{1-x}As$ waveguides was grown (structure C1605-6). The AlGaAs material features a lower affinity energy in comparison to GaAs. As a result, the conduction band edge (Γ minimum) of the bulk material shifts towards higher energies [3] and the valence band edge shifts toward lower energies. Consequently, the potential barrier (and also the effective barrier) between the quantum well and the waveguide for both electrons and holes, is increased. In this way, the carrier confinement in the active region is strengthened and the carrier leakage is reduced. As a result, the internal efficiency is higher ($\eta_i = 86\%$) and the slope efficiency per facet is increased (S = 0.46 W/A). Moreover, the values are comparable with the benchmark design t-B1059. The introduction of the AlGaAs-waveguide results in higher mode confinement and therefore higher modal gain $\Gamma g_0 = 26.4$ (compared to $\Gamma g_{0,t-C1357} = 15.3$). As a result, a reduction of nearly 40% in threshold current was observed; I_{th} = 453 mA compared to $I_{th,t-C1357}$ = 728 mA.

The measurement of threshold current and slope efficiency deduced from the power-current characteristics at different heat-sink temperatures for 4 mm long, 100 µm wide, facet-coated lasers shows that the design based on $Al_{0.1}Ga_{0.9}As$ waveguide, due to the increased effective barriers for the carriers, is much more temperature stable than the design utilizing a GaAs waveguide. The C1605-6 lasers exhibit high values of the characteristic temperatures T_0 = 151 K and T_1 = 537 K and are temperature stable up to a high heat-sink temperature of around 70°C. The deterioration of the thermal stability of the lasing can still be observed above 75°C (30% drop in T_0 and ~ 50% in T_1 value), however it is still much weaker than for the C1357-6 design. In conclusion, the $Al_{0.1}Ga_{0.9}As$ waveguide strongly improves the carrier confinement in the active region. However, it does not provide barriers that are high enough to eliminate the thermal carrier escape at very high temperatures. Figure 9.5 illustrates the temperature dependence of the threshold and slope efficiency for both designs C1605-6 and C1357-6.

Due to the improved carrier confinement, the C1605-6 lasers work satisfactorily under quasi-CW mode operation. The measured power-current characteristic features a high slope efficiency of 0.77 W/A and a power of 15 W at 25 A. The electro-optical parameters of the laser are comparable to the benchmark device B1109-3. Figure 9.5 shows the measured quasi-CW power-voltage-current characteristics of the C1605-6 laser in comparison to the benchmark device. The reason for the increased electrical and thermal resistance of the

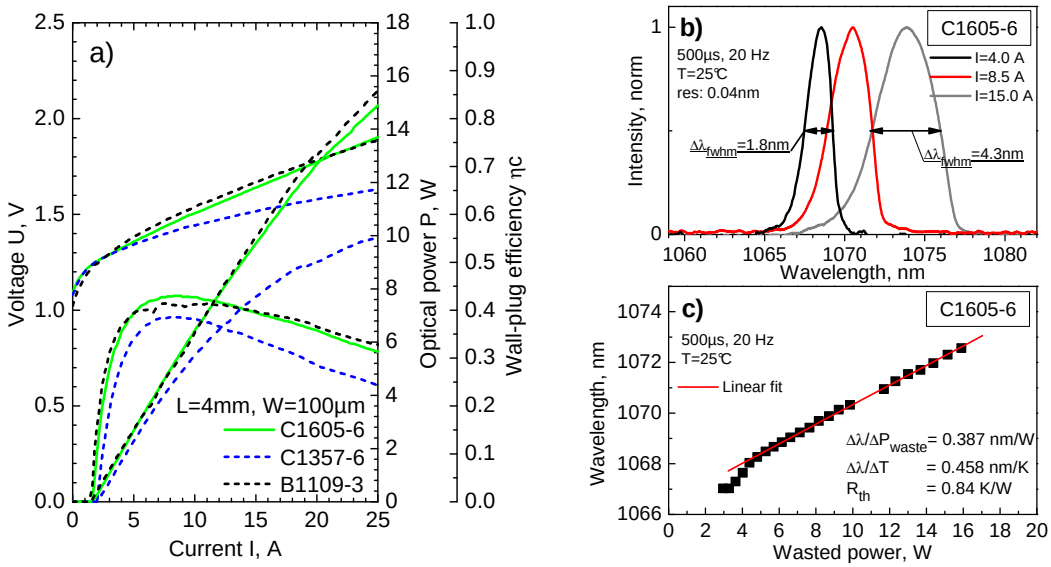

Figure 9.6. (a) The comparison of the experimental P-U-I characteristics between the $Al_{0.1}Ga_{0.9}As$-waveguide design (C1605-6) and the GaAs-waveguide design (C1357-6). B1109-3 is the benchmark sample. (b) Optical spectrum of the C1605-6 design at 4.0 A, 8.5 A and 15 A. (c) The lasing wavelength of the sample C1605-6 versus wasted power (black symbols) and the linear fit to the experimental results (solid red line). Measured lasers: 4 mm long, 100 µm wide single emitters mounted on c-mount. Test conditions: 500 µs, 20Hz, heat-sink temperature of 25°C.

C1605-6 laser is the $Al_xGa_{1-x}As$-material used for the waveguide and the claddings. The AlGaAs material exhibits a lower hole mobility (than GaAs) and thus a reduced electrical and thermal conductivity.

On the other hand, despite the high effective barriers and the good carrier confinement which is provided by the AlGaAs-waveguide in the C1605-6 design, this design pays a penalty for the vertical divergence angle of the laser beam. The increased Al-content in the waveguide lowers its refractive index leading to stronger mode confinement in the active region. Calculations of the vertical mode distributions and the corresponding vertical far-field profiles for various aluminum contents in the waveguide are presented in chapter 6. The structures based on 6.0 µm thick $Al_{0.1}Ga_{0.9}As$ waveguides exhibit a laser beam with divergence angles of 13° (FWHM) and 21.6° (95% power content), whereas the C1357-6 structures utilizing 6.2 µm thick GaAs-waveguides exhibit divergence angles of only 10.6° (FWHM) and 16.6° (95% power content). Figure 9.7 shows the measured beam profiles for the C1605-6 and C1357-6 laser structures.

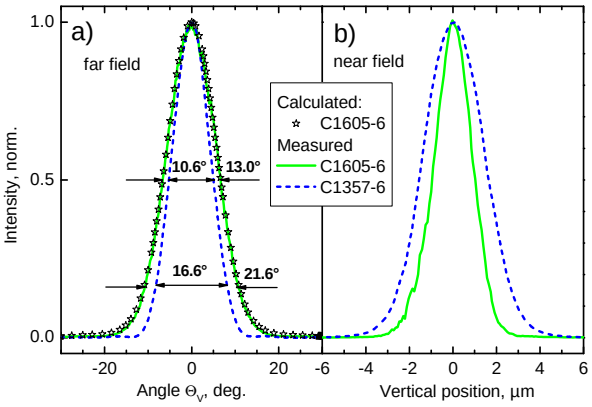

Figure 9.7. The calculated and measured vertical beam profiles, (a) far-field and (b) near-field for the design based on $Al_{0.1}Ga_{0.9}As$-waveguide (C1605-6) and the GaAs-waveguide (C1357-6), measured at currents corresponding to the maximum conversion efficiency under quasi-CW operation mode. Measurement settings: 500 µs, 20 Hz, 25°C heat-sink temperature. Laser diodes (4 mm x 100 µm) mounted on c-mount.

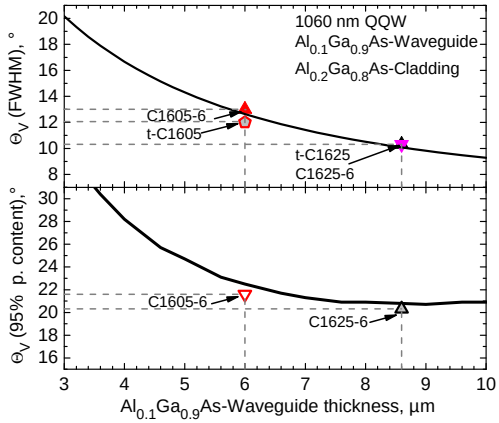

Figure 9.8. Dependence of the vertical divergence angle at FWHM and 95% power content on the $Al_{0.1}Ga_{0.9}As$-waveguide thickness (solid black lines); colour symbols denote measured values.

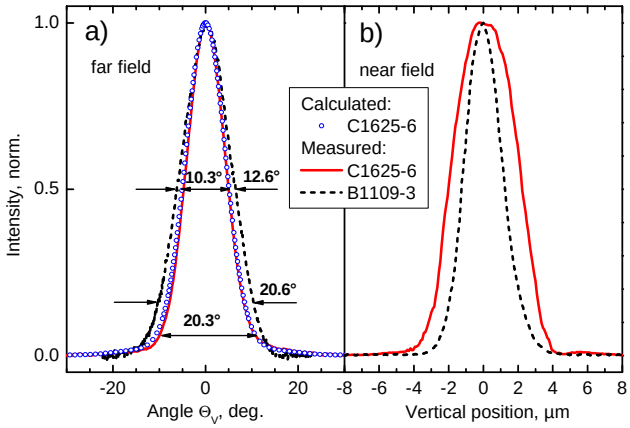

Figure 9.9. Calculated and measured vertical beam profiles (a) far field and (b) near-field of the structure C1625-6 and the benchmark structure B1109-3. Measurement conditions: 500 µs, 20 Hz, 25°C, I = 7.5 A.

In order to reduce the vertical far-field angle to 10°, a structure with a wider waveguide thickness of 8.6 µm waveguide has to be grown (C1625-6 design). Figure 9.8 presents the calculated dependencies of the angle at FWHM and 95% power content on the $Al_{0.1}Ga_{0.9}As$ waveguide thickness. The measured vertical far-field angles of the test samples (t-C1625, t-C1605) and full mounted devices (C1625-6, C1605-6; 4 mm long, 100 µm wide, facet coated) align well with the calculated results. The vertical beam profiles feature angles of 10.3° at FWHM and 20.3° at 95% power content and are stable up to higher current injection levels. Figure 9.9 shows the beam profiles measured under quasi-CW conditions at the current corresponding to the maximum wall-plug efficiency (I = 7.5 A) in comparison the benchmark structure (B1109-3). Despite reduction by 3° of the FWHM angle, the angle containing 95% optical power has only been reduced by 1°, i.e. from $\Theta_{95\%,C1605\text{-}6} = 21.6°$ to $\Theta_{95\%,C1625\text{-}6}$ 20.3°, and compared to the benchmark design only by 0.3° ($\Theta_{95\%,B1109\text{-}3} = 20.6°$). Moreover, further reduction of the angle containing 95% of the optical power by increasing the waveguide thickness only, is not possible for the C1625-6 design (explained in more detail in chapter 10).

The length dependent measurements of the C1625 design show that the widening of the $Al_{0.1}Ga_{0.9}As$ waveguide to 8.6 µm did not deteriorate the internal parameters of the structure. The design features a high internal efficiency of $\eta_i = 90\%$ resulting in a high slope efficiency per facet S = 0.47 W/A. The modal gain is slightly reduced $\Gamma G_0 = 22.7$ cm^{-1} (in comparison to $\Gamma G_{0,t-C1605} = 26.4$ cm^{-1}) due to a small reduction of the confinement factor Γ (presented in figure 9.1) and is comparable to the modal gain of the benchmark design, $\Gamma G_{0,t-B109} = 22.5$ cm^{-1}. The slightly reduced modal gain results in a small increase of the threshold current from $I_{th,t\text{-}C1605} = 453$ mA to $I_{th,t\text{-}C1625} = 467$ mA. The laser parameters obtained from the length-dependent measurements are compiled in table 9.2.

Full mounted devices (4 mm long, 100 µm, facet-coated) tested under short pulse conditions (300 ns, 1.67 Hz) deliver 54 W optical power at 92 A. This is 90% more than the power delivered from the C1357-6 design based on a much thinner, 6.2 µm, GaAs-waveguide. The power-current characteristic, however, still shows a non-linear behavior above 40 A. The non-linearity of the P-I characteristic is probably caused by carrier leakage.

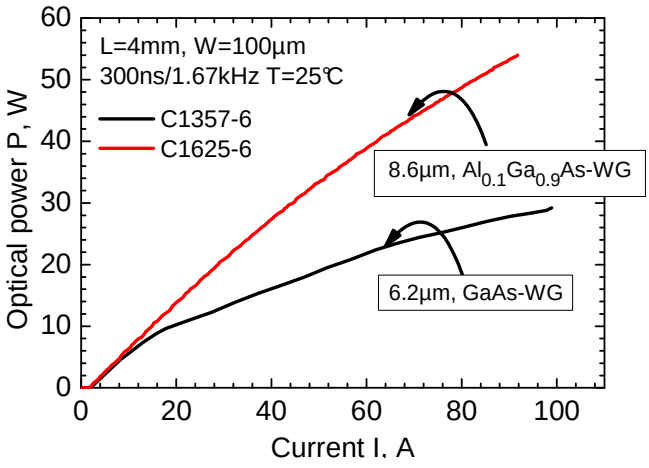

Figure 9.10. Power-current characteristics of laser designs based on 8.6 µm thick $Al_{0.1}Ga_{0.9}As$-waveguide (C1625-6) and 6.2 µm thick GaAs-waveguide (C1357-6), measured under ‚zero-heat' conditions, for a heat-sink temperature of 25°C.

From the dependence of the threshold current and the slope efficiency of the power-current characteristic at different heat-sink temperatures, the characteristic temperatures T_0 and T_1 have been determined. In the temperature range of 15°C to 65°C, the T_0, T_1 values equal 144 K and 518 K, respectively. These are only slightly smaller than the T_0, T_1 values obtained for the C1605-6 design. Above the heat-sink temperature of 65°C, the T_0, T_1 parameters deteriorate for both structures. However, the decrease of the T_1 value for C1625-6 is more significant. The deterioration of the thermal stability of the threshold current and the slope efficiency is likely due to thermal carrier escape from the active region. This can be explained by the strong reduction of the thermionic emission time with increasing temperature [1]. The temperature dependences of the threshold current and the slope efficiency for both designs are presented in figure 9.12.

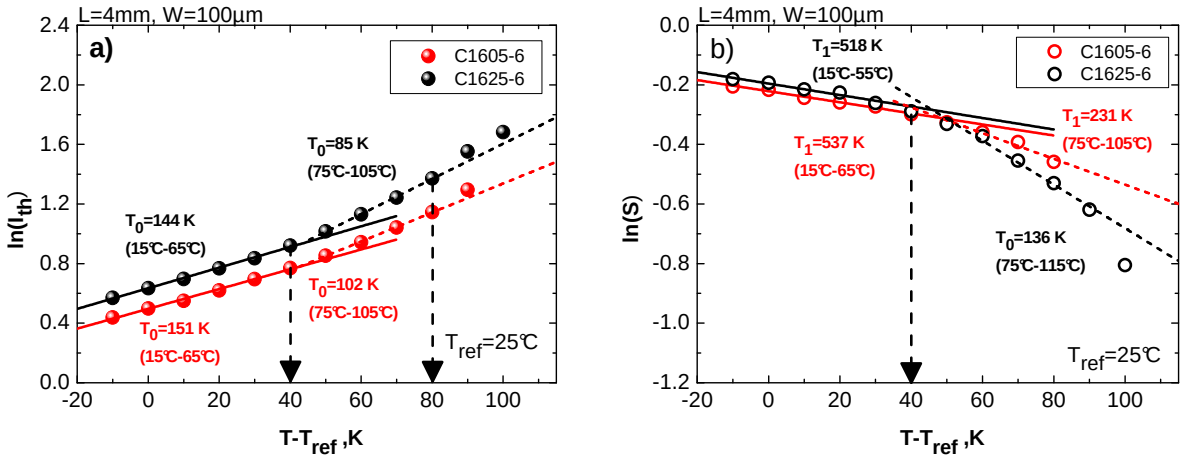

Figure 9.12. Logarithmic dependence of (a) the threshold current and (b) the slope efficiency on the heat-sink temperature for designs utilizing 6.0 µm thick (C1605-6) and 8.6 µm thick (C1625-6) $Al_{0.1}Ga_{0.9}As$ waveguides. Solid and dashed lines represent the linear fit to the experimental dates (points). (Measurement results correspond to facet-coated 4 mm long, 100 µm wide diode lasers).

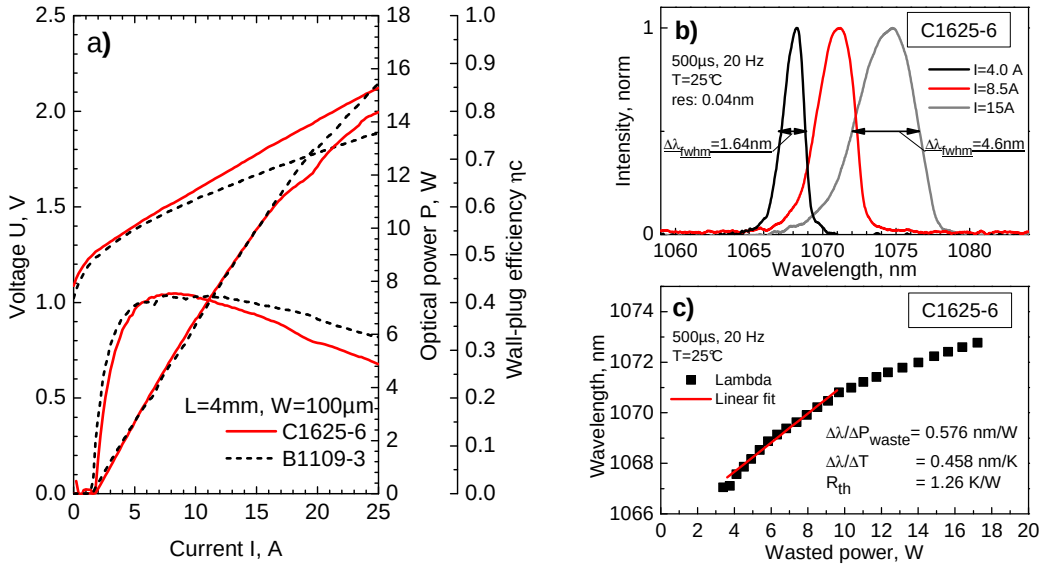

Figure 9.11. (a) Comparison of the experimental P-U-I characteristics between the 8.6 µm thick $Al_{0.1}Ga_{0.9}As$-waveguide design, resulting in a vertical divergence angle of 10.3° (C1625-6) and the benchmark design (B1109-3). (b) Optical spectrum of the C1625-6 design at 4.0 A, 8.5 A and 15 A. (c) The lasing wavelength of the sample C1625-6 versus wasted power (black symbols) and the linear fit to the experimental data (solid red line). Measured laser devices: 4 mm long, 100 µm wide single emitters mounted on c-mount. Test conditions: 500 µs, 20 Hz, heat-sink temperature of 25°C.

Figure 9.11 shows quasi-CW P-U-I characteristics of the 4 mm long, 100 µm wide, facet-coated lasers. Lasers based on the C1625-6 design exhibit a slope efficiency of 0.8 W/A at 10 A and deliver an optical power of 14.4 W at 25 A. The maximum wall-plug efficiencies for the C1625-6 and B1109-3 devices are comparable, while the efficiency for the C1625-6 laser drops at higher applied currents. The maximum of the laser efficiency is maintained due to comparable threshold current and slope efficiency for both of these designs. The very thick $Al_{0.1}Ga_{0.9}As$ waveguide layers feature higher electrical and thermal resistance, than the 5 µm thick GaAs waveguide of the B1109 design, resulting in lower conversion efficiency at higher currents.

9.5. Conclusions

The epitaxial structures for diode lasers emitting at 1060 nm have been optimized with respect to minimum vertical divergence angles in conjunction with high optical output power. It was found that the 1060 nm diode lasers based on 6.2 µm thick GaAs waveguides exhibit narrow divergence angles of 10.6° (FWHM) and 16.6° (95% power content). However, the drawback of this design is the low depth of the quantum wells and thus the weak confinement of both electrons and holes in the active region. The poor carrier confinement in the active region leads to strong vertical carrier leakage and to carrier accumulation in the confinement layers. In consequence, the design suffers from low internal efficiency, strong degradation of the slope efficiency and low optical output power. Additionally, the design exhibits a low confinement factor resulting in a low modal gain and thus a high threshold current. All these factors result in inefficient laser operation.

In the next step, lasers based on $Al_{0.1}Ga_{0.9}As$ waveguides have been tested. The influence of the aluminum content in the waveguides on internal parameters and the laser

beam profile was discussed. It was shown that AlGaAs waveguides increase the effective barrier of the active region, leading to an improved internal efficiency of the laser structure (~ 90%). However, the lower refractive index of the AlGaAs waveguides (in comparison to GaAs) strongly confines the optical mode in the active region and in consequence the vertical far-field angle becomes wider.

Finally, diode lasers based on extremely large, 8.6 µm thick, $Al_{0.1}Ga_{0.9}As$ waveguides were discussed. The design exhibits two desired features: the low divergence angle of 10.3° (FWHM) and 20.3° (95% power content) and the high internal efficiency of ~ 90%. Laser structures processed as 4 mm long, 100 µm wide single emitters deliver an optical power of 54 W under 'zero-heat' conditions. This is 90% more than the power from the design utilizing much thinner, 6.2µm, GaAs-waveguides. Under quasi-CW conditions at a 25°C heat-sink temperature, the devices deliver an optical power of 14.4 W. This power is comparable to the optical power delivered from the benchmark design B1109-3, discussed in Chapter 8.

10

SLOC with low index quantum barriers for small vertical far-fields

10.1. Introduction

The subject of study in this chapter involves the further reduction of the vertical beam divergence of structures based on 8.6 µm thick $Al_{0.1}Ga_{0.9}As$ waveguides. In the previous chapter, it was shown that a reduction of the divergence angle (95% optical power) below 20° was not possible by only increasing the waveguide thickness. In structures based on extremely thick waveguides, the minimum achievable far-field angle is limited by waveguiding of the multi-QW active region itself. In this chapter, it is shown that the use of low refractive index quantum barriers (LIQB) reduces the high average refractive index of the active region and results in a lower divergence angle of the laser beam. The experimental results of the vertical beam profile and electro-optical parameters of diode lasers based on the design with low-index barriers are presented. Furthermore, the limits of the LIQB design are investigated. High power devices delivering 30 W of quasi-CW optical power enclosed in a beam divergence reduced to 8.6° (FWHM) and 15.4° (95% power content) are demonstrated. Moreover, the lateral beam profiles of the LIQB design are presented in comparison to SLOC design.

10.2. Investigated SLOC designs

Design	Quantum well	Quantum barrier	Averaged refractive index of the active region	$Al_{0.1}Ga_{0.9}As$-waveguide thickness	Vertical divergence angle (measured at I= 7.8 A)	
					FWHM	95% power content
C1625-6	$In_{0.25}Ga_{0.75}As$	$GaAs_{0.8}P_{0.2}$	3.511	8.6 µm	10.3°	20.3°
C1690-6	$In_{0.25}Ga_{0.75}As$	$GaAs_{0.65}P_{0.35}$	3.476	8.6 µm	8.6°	15.4°

Table 10.1. Details of epitaxial designs C1625-6 (as reference design) and C1690-6. Refractive index of the quantum barriers is calculated using QIP. Far-field angles of coated 4 mm x 100 µm laser diodes have been measured at currents corresponding to the maximum conversion efficiencies (7.8 A, quasi-CW, 25°C).

Two structures have been investigated: C1625-6 as a reference structure (discussed in chapter 9) and structure C1690-6. Both structures are based on an extremely thick, 8.6 µm, symmetric $Al_{0.1}Ga_{0.9}As$ waveguide. In order to reduce the high number of modes propagating in such a large cavity, the waveguide is embedded in low aluminum content claddings – $Al_{0.2}Ga_{0.8}As$. The thicknesses of the n-doped and p-doped cladding layers are 900 nm and

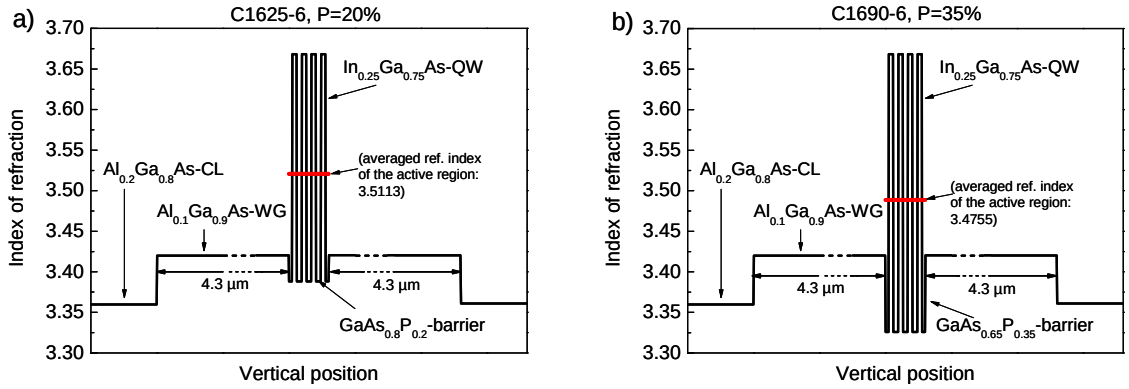

Figure 10.1. The refractive index of (a) the reference design C1625-6 and (b) the design utilizing low index quantum barriers. The red solid line represents the calculated averaged refractive index of the active region.

600 nm, respectively. The chosen thicknesses of the cladding layers provide high losses for the higher order modes due to radiation into the n-GaAs substrate and the p-contact, while the loss of the fundamental mode is minimal. In this way, the higher order modes are discriminated against and single mode operation is ensured. The thick n-cladding layer also prevents uncontrolled mode coupling into the substrate (back reflection of substrate modes into the waveguide, see chapter 6). Both structures utilize four compressively strained $In_xGa_{1-x}As$ quantum wells in the active region. Their thickness and the composition are 7 nm and x = 0.25, respectively. The emission wavelength is ~1060 nm. The first design, C1625-6, utilizes conventional 7.5 nm thick $GaAs_{0.8}P_{0.2}$ quantum barriers to separate the QWs in the active region and 5 nm thick spacers to separate the QWs from the waveguide. The second design, C1690-6, utilizes quantum barriers and spacers with an increased phosphorus content of 0.35 and therefore a reduced refractive index (low index quantum barriers, LIQB). The refractive index profiles of the discussed epitaxial structures are shown in figure 10.1. The tensile strain in the $GaAs_{1-y}P_y$ QB increases from -0.73% to -1.27% with an increase of the phosphorus content from y = 0.2 to y = 0.35. The increased strain may further result in crystal imperfections. Figure 10.2 shows the cathode luminescence (CL) topograms [1] of the complete laser structures. A 975 nm design using $GaAs_{0.65}P_{0.35}$ quantum barriers showed no material degradation and operated with high reliability [2]. The structure based on the epitaxial design C1690-6 also showed no material degradation. For comparison, a structure with too high a phosphorus content ($GaAs_{0.55}P_{0.45}$) resulted in a highly strained crystal and lattice relaxation via misfit dislocations. In [2], it was shown that the increased defect densities in designs with $GaAs_{0.55}P_{0.45}$ barriers lead to increased transparency current density and increased threshold current.

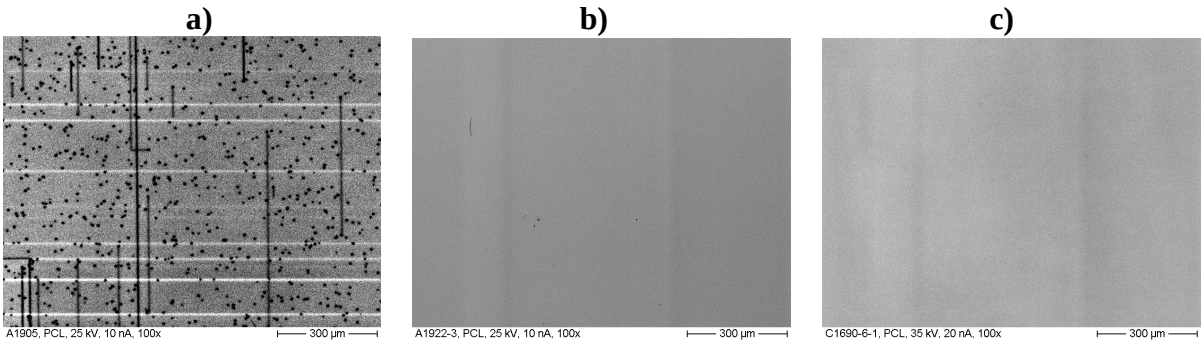

Figure 10.2. Cathodoluminescence image of the complete laser structures: (a) utilizing 8 nm thick $GaAs_{0.55}P_{0.45}$ quantum barriers, (b) utilizing 8 nm thick $GaAs_{0.66}P_{0.34}$ quantum barriers and (c) utilizing 7.5 nm thick $GaAs_{0.65}P_{0.35}$ quantum barriers (C1690-6).

10.3. Optical mode expansion for narrow vertical far-field

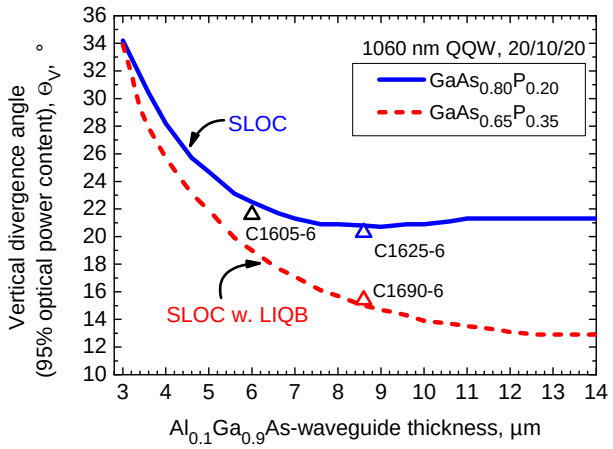

Figure 10.3. Calculated vertical divergence angle containing 95% optical power as a function of $Al_{0.1}Ga_{0.9}As$ waveguide thickness for structures utilizing conventional barriers (blue solid line) and LIQB (red dashed line). Measured far-field angles are shown as symbols.

The SLOC structures require a multi-QW active region to provide sufficient modal gain. The multi-QW active region, however, due to its high average refractive index, contributes significantly to the guiding of the modes. By increasing the thickness of the waveguide layers, the active region acts more and more as a waveguide itself and thus prevents further narrowing of the vertical far-field pattern. In figure 10.3, the calculated dependence of the vertical far-field angle on the $Al_{0.1}Ga_{0.9}As$ waveguide thickness is presented for the 1060 nm reference design that uses conventional barriers (similar to structure C1625-6), labeled SLOC (blue solid line). As the waveguide thickness is increased, the vertical far-field angle containing 95% optical power asymptotically approaches a minimum angle of about $\Theta_{V,\ 95\%} = 20.3°$. The measured values of the far-field angle for structures with 6.0 µm and 8.6 µm wide waveguides are 21.6° and 20.3°, respectively, and correspond well with the simulation results. Increasing the phosphorus content in the $GaAs_{1-y}P_y$ barriers reduces their refractive index and consequently the average refractive index of the multi-QW active region. With the increase of the phosphorus content from 20% to 35%, the average refractive index of the active region, n_{AR}, is reduced from $n_{AR} = 3.511$ to $n_{AR} = 3.476$ and is significantly closer to the refractive index of the waveguide, $n_{WG} = 3.42$. The active region with a lower index confines the optical mode more weakly and the mode expands further in the cavity resulting in a smaller divergence angle [3]. The effect is more significant for structures based on very thick waveguides, for which the claddings play a much smaller role in confining the optical mode (this issue is also discussed in chapter 6). The calculated dependence of the far-field angle on waveguide thickness for an exemplary LIQB-SLOC structure (active region as for structure C1690-6) is shown in figure 10.3 (dashed red line) as well. The measured far-field of a SLOC-LIQB laser with an 8.6 µm thick waveguide (C1690-6) corresponds well to the simulation results. Figure 10.4 shows the calculated profiles of the transversal electric mode intensity and corresponding profiles of the vertical far-field intensity, respectively, for the discussed structures C1625-6 and C1690-6 based on an 8.6 µm thick waveguide. Quantum barriers with an increased phosphorus content of 0.35 lead to a reduction of the confinement factor from $\Gamma_{P=0.20} = 1.48\%$ to $\Gamma_{P=0.35} = 1\%$. The optical mode is broader and as a result the far-field angle containing 95% optical power is reduced from 20.3° to 15°. The measured vertical far-field profile of fully mounted devices (4 mm long, 100 µm broad single emitters, measured at the quasi-CW current I = 7.8 A, corresponding to peak laser efficiency) agrees well with simulation, confirming the benefit of LIQB designs.

Alternatively, the high average refractive index of the active region can be reduced by increasing the thickness of the quantum barriers and/or by decreasing the thickness of the

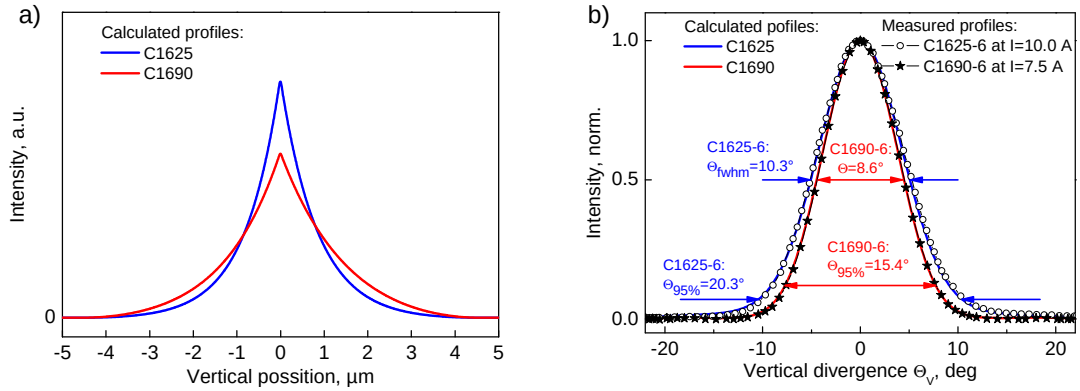

Figure 10.4. (a) Calculated vertical profiles of the mode intensity for structures C1625-6 (with conventional barriers) and C1690-6 (with LIQB). Zero position indicates the position of the active region in the vertical structure. (b) Corresponding, calculated and measured vertical profiles of the far-field. Presented values of far-field angles are measured values.

quantum wells. However, the latter is challenging because the optical gain is decreased due to interface roughness if the quantum wells get too thin [4].

10.4. Internal parameters of the laser design

As will be further shown, the design utilizing LIQB (C1690) suffers from carrier accumulation in the waveguide. As already discussed in the previous chapter, in structures with strong carrier leakage, internal parameters like α_i and η_i are not independent from the resonator length and the values obtained from the length dependent measurement are not reliable. However, the internal parameters of the C1690 design are presented in table 10.2 for reasons of consistency. A small drop in the internal efficiency to 80% (from 90% for the reference structure) has been observed. The slope efficiency of S = 0.44 W/A (per facet) is slightly lower than for the reference structure ($S_{C1625\text{-}6}$ = 0.47 W/A). The theoretically predicted low confinement factor results in a strongly reduced modal gain (from $\Gamma G_{0,C1625}$ = 22.7 cm^{-1} to $\Gamma G_{0,C1690}$ = 13.3 cm^{-1}). The reduced modal gain results in a significant increase of the threshold current density from $I_{th,C1625}$ = 467 A/cm^2 to $I_{th,C1690}$ = 747 A/cm^2.

Structure	**$GaAs_{1-y}P_y$ Barriers**	**$\Gamma G_{0(total)}$, cm^{-1}**	**η_i, %**	**α_i, cm^{-1}**	**$J_{Tr(total)}$, A/cm^2**	**I_{th}*, mA**	**S*, W/A**	**T_0*, K**	**U*, V (2A)**	**λ, nm**
t-C1625	y = 0.20	22.7	90	1.57	264	467	0.47	143	1.78	1060
t-C1690	y = 0.35	13.3	80	0.46	312	747	0.44	164	1.88	1057

Table 10.2. Laser parameters obtained from the 'pre'-test. The t-C1690 design with a higher phosphorus content in the quantum barriers is compared to the reference structure t-C1625. (* The slope per facet, the threshold current, the bias voltage, as well as characteristic temperature T_0 have been determined from a 1 mm-long, 100 µm wide device.)

10.5. Power-current characteristics of mounted lasers

10.5.1. Experimental results

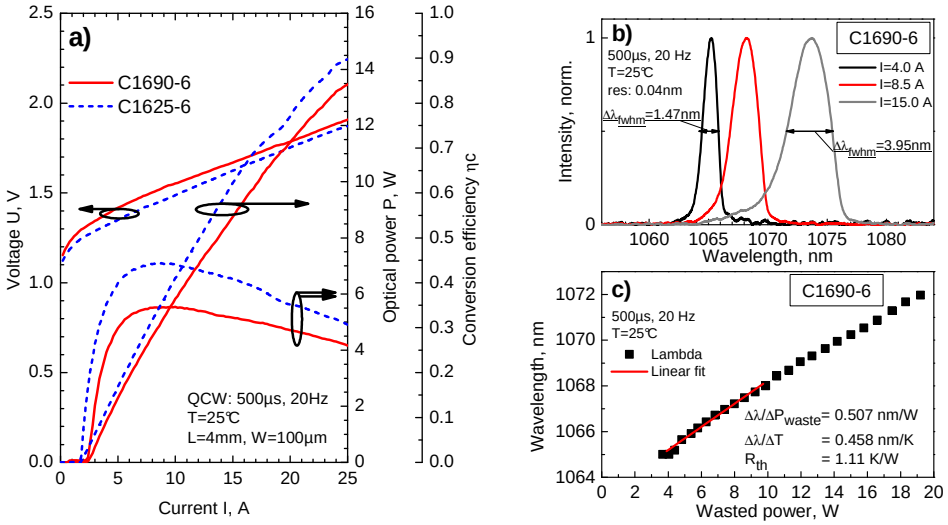

Figure 10.5. (a) Experimental P-U-I characteristics of laser structures: C1690-6 and C1625-6. (b) Optical spectrum of the C1690-6 laser at 4.0 A, 8.5 A and 15 A. (c) The lasing wavelength of the sample C1690-6 versus wasted power (black symbols) and the linear fit to the experimental data (solid red line). Measured laser devices: 4 mm long, 100 µm wide single emitters mounted on c-mount. Test conditions: 500 µs, 20 Hz, heat-sink temperature of 25°C.

Structure	**I_{th}, A**	**S, W/A**	**$\eta_{C,max}$**	**P, W (at 25 A)**	**R_{th}, K/W**	**Θ_V , deg**		**$M^2_{95\%}$**
						FWHM	**95%**	
C1625-6	1.78	0.82	0.44	14.4	1.26	10.3	20.3	1.58 ±0.31
C1690-6	2.45	0.73	0.34	13.8	1.11	8.6	15.4	1.28 ±0.33

Table 10.3. The electro-optical parameters of C1625-6 and C1690-6 designs processed as 4 mm long, 100 µm wide laser chips mounted on c-mount, tested under QCW (500 µm, 20 Hz) at 25°C heat-sink temperature. Thermal resistance was measured under QCW conditions. Far-field angles were measured at currents (7.5 A, 8.0 A) corresponding to the maximum conversion efficiency.

The discussed epitaxial structures C1625-6 and C1690-6 were processed as single emitter broad area lasers with 100 µm stripe width and a cavity length of 4 mm. In this chapter, C1625-6 serves as a reference laser device. The laser facets were passivated with ZnSe. The laser facets were coated in order to obtain mirror reflectivities of 1.5% on the front facet and 95% on the rear facet. The laser chips were mounted junction-side down on CuW submounts and then soldered onto c-mount heat-sinks. The devices were tested under quasi-CW operation with a duty-cycle of 1% (500 µs, 20 Hz) at heat-sink temperature of 25°C. The measured power-voltage-current characteristics of both structures are shown in figure 10.5. The significant reduction of the far-field angle with the LIQB design comes at a price – a slightly deteriorated laser performance. The laser based on design C1690-6 exhibits a higher threshold current of I_{th} = 2.45 A (compared to $I_{th,C1625-6}$ = 1.78 A), a lower slope efficiency of S = 0.73 W/A (compared to S_{C1625} = 0.82 W/A), and an increased roll-over of the P-I characteristic and thus a lower optical power of 13.8 W at 25 A. Moreover, the turn-on voltage for the C1690-6 is increased. The increased threshold is a result of the reduced confinement factor and thus reduced modal gain. The offset in the turn-on voltage, $\Delta U_0 \sim 55$ mV is, however, too high to explained by the ~ 3 nm wavelength difference between these two designs (the electro-optical parameters are compiled in table 10.3). Both, higher threshold and increased voltage lead to a reduction of the maximum power conversion efficiency from 44% for design C1625-6 to 34% for design C1690-6. The non-linearity in the current-voltage characteristic above threshold and the decreased slope efficiency would typically indicate that carrier leakage is occurring [5]. However, the LIQB design leads to a

higher bandgap for the barrier layers, and the interface between the $GaAs_{0.65}P_{0.35}$-barrier and the $Al_{0.1}Ga_{0.9}As$-waveguide results in a higher effective barrier against electron escape. Therefore, electron escape for this structure is not expected. On the other hand, the high barriers may block the hole-injection into the active region, which might explain the higher operating voltage of the design.

10.5.2. Device simulation

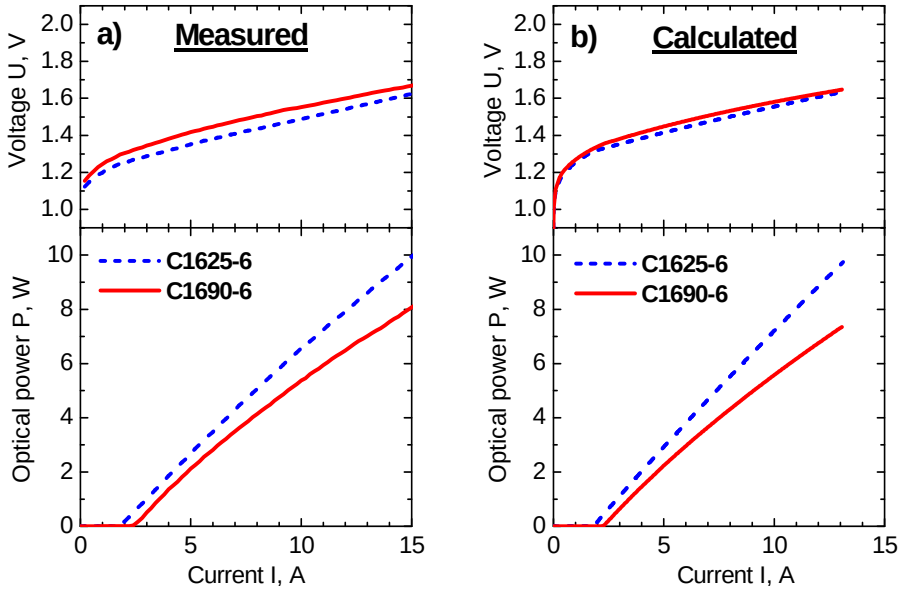

Figure 10.6. (a) Measured and (b) calculated P-U-I characteristics for 4 mm long, 100 µm wide broad area lasers based on epitaxial structure C1625-6 (blue dashed line) and structure C1690-6 (LIQB) (red solid line).

To help diagnose the reason for the unexpected degradation in performance, full finite element device simulations were performed for these two discussed structures. The calculations were carried out by the use of a commercial laser simulation tool, Lastip [6]. The simulations were based on a drift-diffusion model for the carrier transport and performed one dimensionally (vertically) without considering thermal effects (fixed 25°C) or current spreading. The calculated optical output and voltage characteristics are presented in figure 10.6 and reproduce the increased turn-on voltage and the non-linear U-I characteristic, the reduced slope efficiency and the increased threshold current for design C1690-6. The reasons for the degraded performance of the C1690-6 design utilizing LIQB can be clarified by studying the band and carrier profiles in the vicinity of the active region. In figure 10.7, the energy band and carrier density profiles of designs C1625-6 and C1690-6 are shown at threshold. The band-bending at the p-side of the active region in design C1690-6 indicates hole accumulation at the p-edge of the active region. In figure 10.7a, one can see the increase of the valence band discontinuity ($E_{v,WG} - E_{v,lh\text{-}QB}$) for light holes and the conduction band discontinuity ($E_{c,QB} - E_{c,WG}$) at the $GaAs_{1-y}P_y$ barrier /$Al_{0.1}Ga_{0.9}As$ waveguide interface with increasing phosphorus content (y) in the quantum barrier. The valence band discontinuity for design C1625-6 equals 12 meV and increases to 70 meV for design C1690-6, creating a higher barrier hindering the injection of holes into the active region. The holes accumulated at the p-side edge of the active region create a higher local electrical field (-20 kV/cm, for C1690-6). In order to overcome the barrier and inject sufficient holes into the

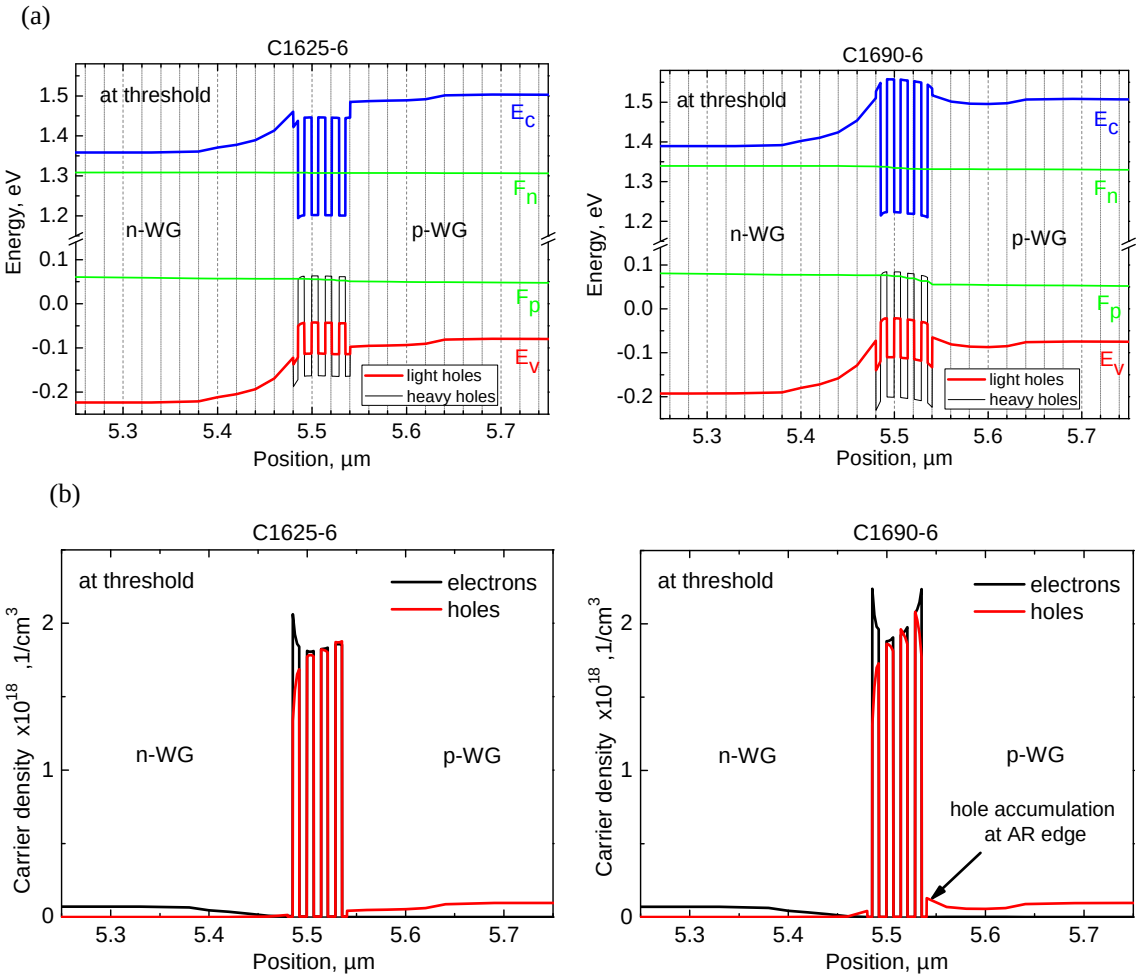

Figure 10.7. (a) The band energy profiles in the vicinity of the active region for design C1625-6 and design C1690-6 at threshold. Notation: E_c and E_v – conduction and valence bands, respectively, Fn, Fp, quasi-Fermi level for electron and holes, respectively. (b) Profiles of electrons (black line) and holes (red line) at threshold.

active region to reach threshold, a higher external bias has to be applied to the structure. Figure 10.6.b illustrates the calculated voltage-current characteristics with increased turn-on voltage for the design with LIQB (C1690-6) correlated with the hole accumulation at the edge of the active region.

The calculated as well as the measured voltage-current characteristics for C1690-6 show a non-linear behavior at higher applied currents. Calculations of the carrier profiles at a higher applied current, I = 13 A, indicate electron leakage, which is stronger for the structure utilizing the LIQB. The energy band and carrier density profiles are illustrated in figure 10.8. The dominant reason for the greater electron accumulation in the p-type waveguide is the presence of a high concentration of accumulated holes at the p-side of the active region. The electric field generated by this hole population attracts the electrons, which can overcome the large energy barrier due to the increased conduction band discontinuity of the quantum barrier [7].

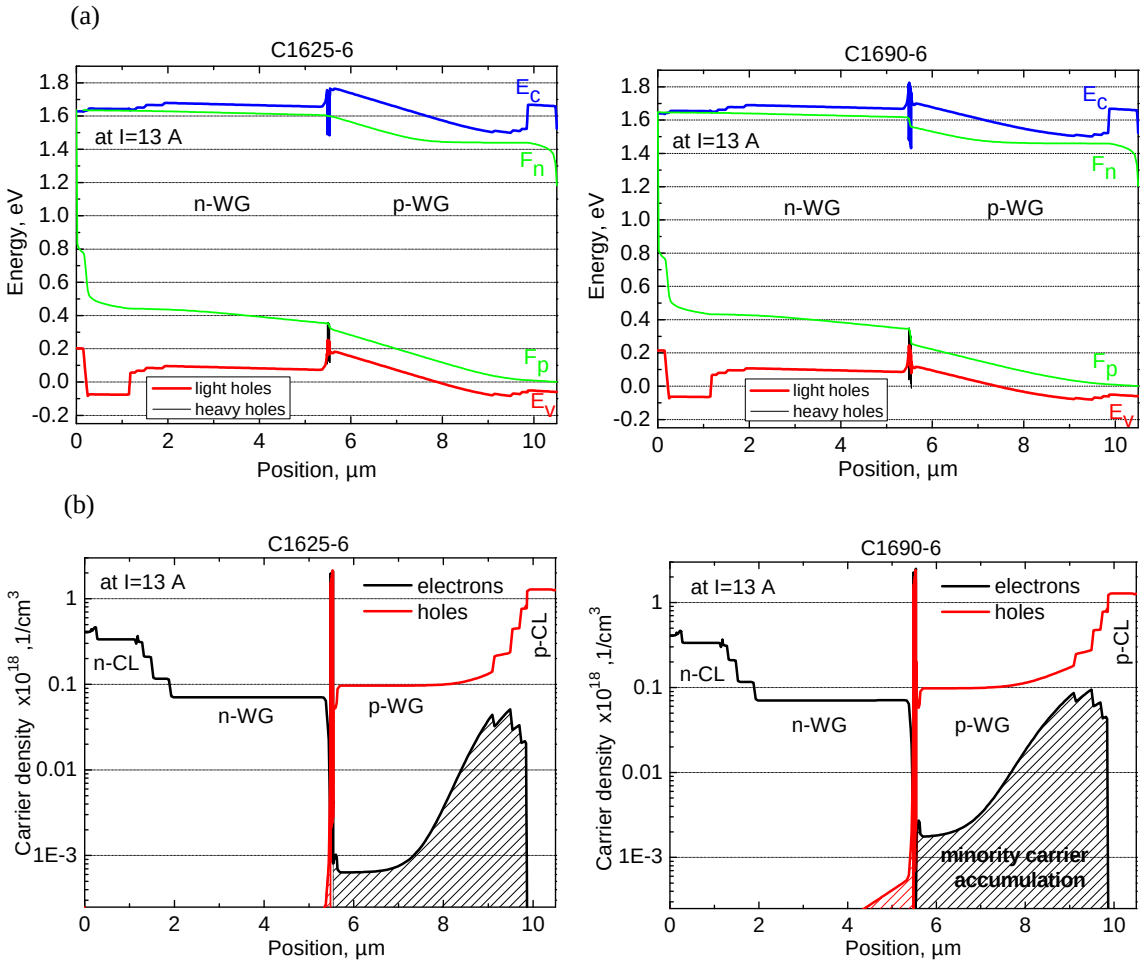

Figure 10.8. (a) The band energy profiles for design C1625-6 and design C1690-6 at current I = 13 A. Notation: E_c and E_v – conduction and valence bands, respectively, Fn, Fp, quasi-Fermi levels for electron and holes, respectively. (b) Profiles of electrons (black line) and holes (red line) at I = 13 A.

The high barrier to hole injection may be reduced by using a lower energy material for the spacer next to the p-waveguide. This can be achieved by lowering the content of phosphorous in the GaAsP spacer. However, different compositions of this spacer and the quantum barriers will create an asymmetric multi-QW active region that could lead to spectral broadening of the modal gain and an increased threshold carrier density. Therefore, further study of the different designs for the barriers and spacers has to be performed.

10.5.3. Thermal stability and the resonator length

The dependence of the threshold current and the slope efficiency on the heat-sink temperature was measured for C1690-6 laser chips with two different resonator lengths, 4 mm and 8 mm. The front facets of the longer lasers were coated with a lower reflectivity of $R_{f,L=8mm} = 0.5\%$. The measurement was performed for a current pulse duration of 300 ns and a repetition rate of 1 kHz. The temperature dependence of the threshold currents and slope efficiencies are presented in figure 10.9. The parameters T_0 and T_1 obtained in the temperature range 15°C-65°C are similar (within the measurement uncertainty) for both resonator lengths: $T_0 = 162\pm9$ K, $T_1 = 373\pm96$ K for a 4 mm long laser and $T_0 = 163\pm8$ K, $T_1 = 346\pm13$ K for an 8 mm long laser. At higher heat-sink temperatures, specifically 75°C – 95°C, the longer lasers feature higher characteristic temperatures T_0 and T_1. The T_0 parameter increases from 90 K to 100 K for an increase of the cavity length from 4 mm to 8 mm, and the

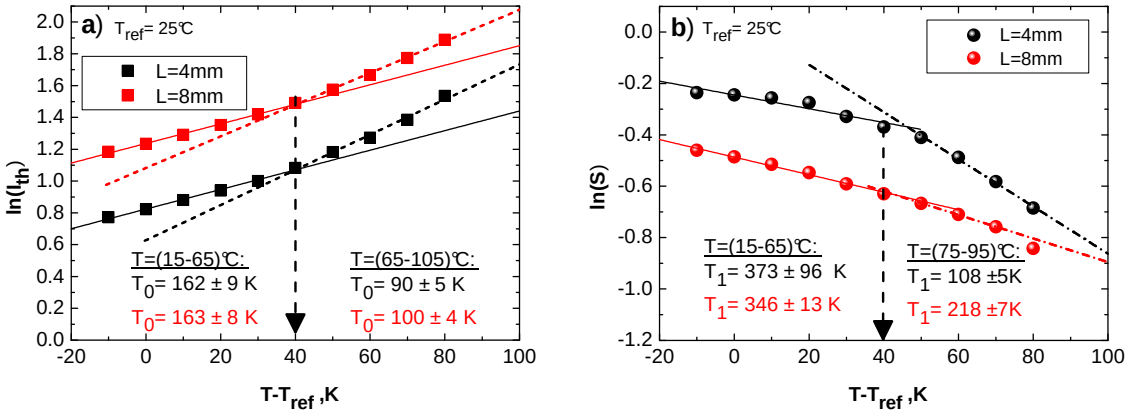

Figure 10.9. The logarithmic dependence of the threshold current (a) and the slope efficiency (b) on the heat-sink temperature for the C1690-6 design processed as 100 µm laser chips with two different resonator lengths, 4 mm and 8 mm. Measurement conditions: 300 ns current pulse duration, 1 kHz, repetition rate, heat-sink temperature range: 15°C – 105°C.

parameter $T_1 = 218$ K for an 8 mm long laser is two times higher than the parameter $T_1 = 108$ K for the shorter, 4 mm long, device. The discontinuity, more significant in the T_1 parameter, might indicate thresholds of additional losses activated at higher temperatures like thermionic carrier escape. The higher values of the characteristic temperatures for lasers with longer resonators are probably attributable to lower carrier densities resulting in lower threshold current densities. Lower carrier densities result in lower carrier leakage in these devices.

10.5.4. High-power laser devices with long resonators

Laser structures based on epitaxial designs C1625-6 and C1690-6 were processed as single emitters with an 8 mm long cavity and 200 µm wide stripes, double that of the 4 mm long devices discussed in previous sections. The long gain medium allows a further reduction of the reflectivity of the front mirror to 0.5% and thus a reduction of the optical load of the facet. The laser chips were mounted junction side down onto CuW submounts and soldered to conduction cooled packages (CCPs). The laser devices were characterized under quasi-CW operation mode, under which the wasted heat produced by the laser is removed by the CuW submount. Therefore, there is almost no difference in the characteristics between the chips that were mounted on a c-mount or on a CCP (in appendix 5 the calculated dependence of the temperature distribution on the heating time for the laser chip mounted junction-down to the heat-sink is presented). The measured quasi-CW light-voltage-current characteristics are presented in figure 10.10. The low confinement factor of the structure reduces the density of the internal optical power and, together with the use of high performance facet passivation, prevents catastrophic device failure due to the internal or mirror damage. As a result, both structures deliver a high output power of 30 W without device degradation. The slope and the roll-over of the quasi-CW power-current characteristics for both designs C1625-6 and C1690-6 are comparable over the whole range of applied currents (up to 80 A). The threshold current of 6.48 A for design C1690-6 is higher than that of design C1625-6 with 5.3 A. The maximum conversion efficiencies are $\eta_{C,\max} = 33\%$ and $\eta_{C,\max} = 30\%$ for design C1625-6 and C1690-6, respectively. Whereas a 10% drop in maximum conversion efficiency was observed

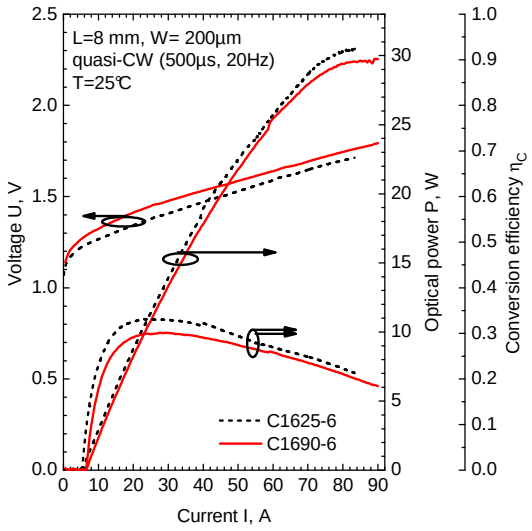

Figure 10.10. Measured quasi-CW light-voltage-current characteristics of 8 mm long, 200 µm wide diode lasers based on epitaxial design C1625-6 (black dashed line) and design C1690-6 (red solid line).

for the 4 mm long devices, the laser with LIQB only exhibited a 3% lower maximum conversion efficiency when processed as an 8 mm long laser. The reason for the much smaller difference in performance is that the increased cavity length leads to a smaller threshold gain and reduced threshold current densities (612.5 A/cm^2 versus 405 A/cm^2). A lower threshold density translates to a reduced carrier density in the quantum wells, which leads to a reduced carrier accumulation in the p-doped waveguide layer. The increased optical roll-over-power from 13.8°W (for a 4 mm long, 100 µm wide laser) to 30 W (for an 8 mm long, 200 µm wide laser) is also due to reduced thermal resistance from R_{th}=1.11 K/W to R_{th}=0.23 K/W, respectively.

10.6. Lateral far-field of laser based on the SLOC-LIQB design

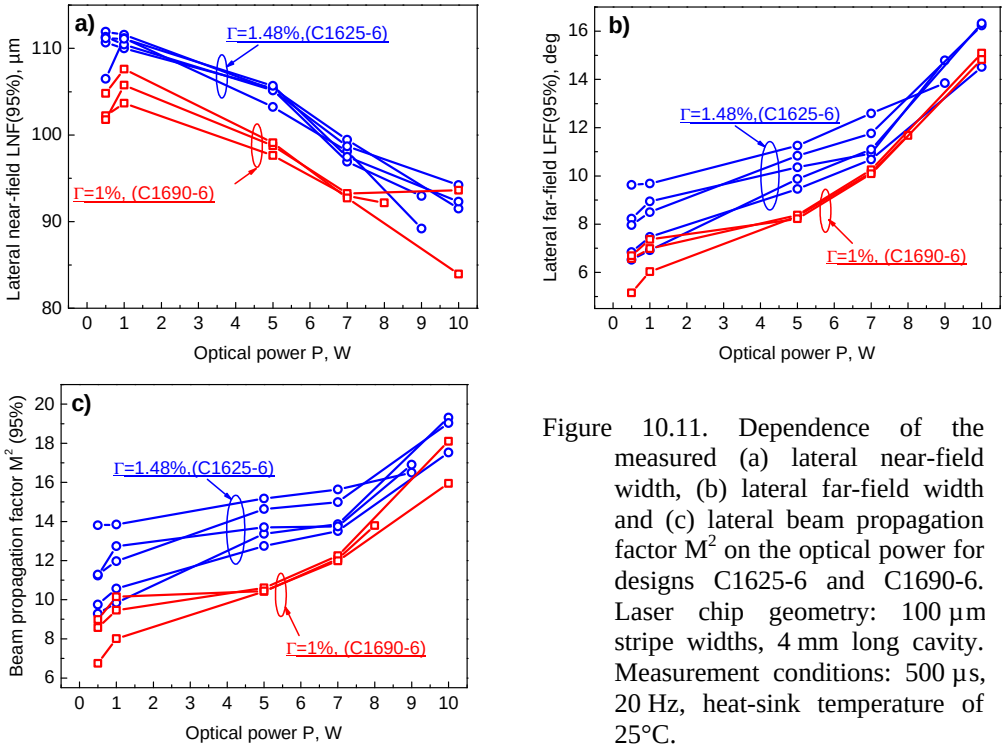

Figure 10.11. Dependence of the measured (a) lateral near-field width, (b) lateral far-field width and (c) lateral beam propagation factor M^2 on the optical power for designs C1625-6 and C1690-6. Laser chip geometry: 100 µm stripe widths, 4 mm long cavity. Measurement conditions: 500 µs, 20 Hz, heat-sink temperature of 25°C.

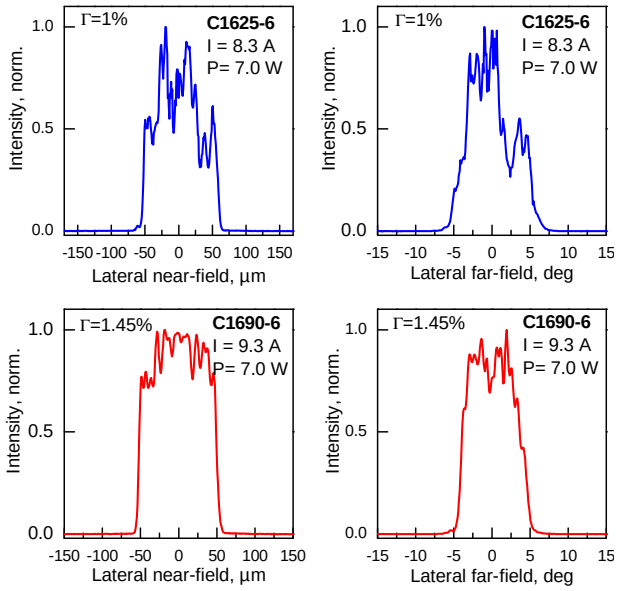

Figure 10.12. Measured lateral beam profiles at an optical power of 7 W from lasers of design C1625-6 and C1690-6. Laser chip geometry: 100 µm stripe widths, 4 mm cavity long. Measurement conditions: 500 µs, 20 Hz, heat-sink temperature of 25°C.

Lateral beam profiles were measured for both designs, C1690-6 utilizing LIQB and C1625-6 using conventional quantum barriers. The structures were processed as 4 mm long, 100 µm wide, facet coated lasers mounted on c-mounts. Figure 10.11 presents values of lateral near-field widths, lateral far-field widths containing 95% optical power and lateral beam propagation factors M^2, measured under quasi-CW operation mode (500 µs, 20 Hz) at different operating powers (from 0.5 W to 10 W). The temperature of the heat-sink was 25°C. The C1690-6 lasers exhibit a less structured lateral near-field pattern even though these lasers have to be driven at higher currents in order to deliver the same optical output power as devices from the design C1625-6. The less structured lateral near-field pattern results in a less structured and narrower lateral far-field pattern and also a lower beam propagation factor, M^2. In figure 10.12, beam profiles measured at 7 W from both designs are presented. The better lateral beam quality of the lasers based on the design using LIQB may be explained as follows. The C1690-6 design features a much lower confinement factor due to the introduced LIQB. Following [8,9], the low confinement factor leads to a lower modal gain and a reduced gain for carrier-induced filaments (like self-focusing in the active region). Consequently, this effect results in improved lateral beam quality.

10.7. Conclusions

Laser structures based on an ultra-wide, 8.6 µm, $Al_{0.1}Ga_{0.9}As$ waveguide with low index quantum barriers (LIQB) have been investigated. The theoretical study of the far-field reduction by introduction of LIQB into the MQW active region was confirmed experimentally. The divergence angle, containing 95% optical power, for the SLOC laser was reduced from 20.3° to 15.4° by the use of the LIQB. The LIQB design in combination with low Al-content waveguides, however, exhibits an increased voltage and reduced laser efficiency. The increased valence band discontinuity of the LIQB was found to be the relevant parameter for the laser performance degradation. The high band discontinuity of the quantum barrier creates a barrier for hole injection and eventually leads to hole accumulation at the p-side edge of the active region, which results in electron leakage. It may be possible to minimize the carrier accumulation effects by utilizing a lower energy p-side spacer. This issue is going to be studied in future work. When using longer cavities, the deterioration of the laser

performance is less severe. The structure processed as device with an 8 mm long resonator and a 200 µm wide stripe delivers a high quasi-CW output power of 30 W. Moreover, it was shown that structures utilizing a LIQB show a less structured lateral near-field patterns resulting in lower lateral far-field angles and lower beam propagation factors, M^2. This effect may be attributed to the low confinement factor of the LIQB design, which further results in smaller carrier induced filaments.

11

Summary and outlook

The aim of this work was to realize diode lasers with extremely narrow vertical beam divergence while simultaneously maintaining a high output power. Structures with narrowed vertical far-field offer easier beam shaping and lower system costs, especially when spectral stabilization with an external volume Bragg grating is necessary. In commercial systems, a narrow far-field emission angle with 95% power content is important in order to avoid unwanted stray light effects such as pumping of the fiber cladding. This work considered diode lasers emitting light in the wavelength range between 1050 nm to 1150 nm, which find application in telecommunications as pump sources for silica based fiber lasers and Raman amplifiers, as well as in direct material processing.

The target of the doctoral thesis was the realization of broad area single emitters, which emit optical power of more than 20 W within an extremely small vertical divergence angle of below 10° defined as full width at half maximum (FWHM). The work included a theoretical study of the waveguiding and carrier-transport properties of the laser structures and an experimental study involving the electro-optical characterization of processed laser devices, intended in part to diagnose what limits their performance.

The structures investigated in this work were based on a vertical Super Large Optical Cavity (SLOC) design. The starting point was a structure with vertical divergence angles of 19° (FWHM) and 30° defined as an angle containing 95% of the optical power. A further reduction of the vertical beam divergence was achieved by two methods. The first method is based on the expansion of the optical mode by further broadening the waveguide. It was noticed that for waveguide thicknesses >> 3 µm the mode profile in the slab waveguide is less influenced by the cladding layers but is strongly influenced by the MQW-active region due to its high average refractive index. This observation was the basis for the second, novel method, for far-field reduction. It was examined, in simulations and experimentally, that the introduction of low-refractive index quantum barriers and spacers reduces the high average refractive index of the MQW-active region, leading to lower mode confinement and significantly reduced vertical far-field angles of both, FWHM and 95% optical power content.

In order to ensure single mode operation, two methods for higher order mode discrimination were used during the laser design, namely gain discrimination and loss discrimination. It was shown that an uncontrolled coupling of the lasing mode into substrate modes may occur in the analyzed structures. This phenomenon deteriorates the vertical beam profile and also results in kinks in the power-current characteristics. This undesirable effect, however, can be suppressed if thick enough cladding layers are utilized.

Based on the simulated designs laser structures were grown and processed as broad area devices with 60 µm to 200 µm wide contact stripes and 4 mm to 8 mm long Fabry-Perot resonators. In the following paragraphs, the experimental results of different laser structures will be summarized.

The first investigated laser structures were based on GaAs waveguides and utilized active regions designed for emission wavelengths from 1100 nm to 1130 nm. Widening the waveguide from 3.4 µm (B1110-3) to 5 µm (B1109-3) resulted in the far-field angle reduction from 19° to 13° (FWHM) and from 30° to 21° (95% power content). In structure B1109-3, the number of quantum wells was increased simultaneously from two to four, which maid it possible to maintain a high optical modal gain despite the wider waveguide. It also strengthened the carrier confinement in the active region, resulting in a high power laser design. Both designs, processed as 8 mm long and 200 µm wide laser chips mounted on a c-mount, delivered 38 W roll-over power in quasi-CW mode.

In the example of a structure based on 3.4 µm thick GaAs-waveguide with a DQW active region and an emission wavelength of 1100 nm (A1459-3), it was shown that the performance of the laser design is limited by carrier spill-over and carrier accumulation in the waveguide - even under pulsed operation, i.e. in the absence of self-heating. It was theoretically shown that increasing the number of quantum wells improves the carrier confinement in the active region. A higher number of quantum wells reduces the carrier density in the QWs at threshold and thus the quasi-Fermi energies of electrons and holes shifts towards lower energies. As a consequence, the effective barrier height between the active region and the waveguide layers is increased and the carrier leakage is diminished. This effect was confirmed experimentally by a measurement of the spontaneous emission spectra emitted from the waveguide. The final result was an increase of the output power from 45 W (A1459-3: two QWs) to 55 W (A1457-3: four QWs) at 100 A from a 60 µm wide and 4 mm long single emitter, measured under 'zero-heat' conditions. The design utilizing a four QW active region, processed as a 200 µm wide chip and driven to an increased current of 240 A, delivered 124 W optical power limited by the current supply.

The efficient long wavelength GaAs-based designs become, however, almost unusable for the commercially important wavelength of 1060 nm, as shown by the example of structure C1357-6. The multi-QW active region designed for a wavelength of 1060 nm results in very low effective barrier heights and thus strong carrier leakage. It was shown that $Al_xGa_{1-x}As$-waveguides are necessary to minimize the carrier leakage deteriorating the laser performance. Even low aluminum content ($x = 0.1$) waveguides build high effective barriers, which significantly improve the carrier confinement and result in high laser efficiency despite the increased electrical resistance of the laser structure. Structures based on $Al_{0.1}Ga_{0.9}As$ waveguides exhibit nearly two-fold higher characteristic temperature T_0 and more than three-fold higher characteristic temperature T_1 ($T_0 = 151$ K, $T_1 = 573$ K) than the structure based on a GaAs waveguide ($T_0 = 85$ K, $T_1 = 162$ K). Moreover, 4 mm long, 100 µm wide laser devices tested under 'zero-heat' conditions delivered 54 W optical power at 92 A (C1605-6). This is 90% more than the power delivered from the device based on a GaAs waveguide (C1357-6). On the other hand, structures based on AlGaAs waveguides exhibit wider divergence angles of the laser beam. The reason is the lower refractive index of the waveguide, which leads to a stronger mode confinement in the active region. Structures based on 6.0 µm thick $Al_{0.1}Ga_{0.9}As$ waveguides (C1605-6) exhibit a laser beam with divergence angles of 13° (FWHM) and 21.6° (95% power content), whereby the structures utilizing GaAs waveguides (6.2 µm thick, C1357-6) exhibit divergence angles of 10.6° (FWHM) and 16.6° (95% power content).

In order to reduce the far-field angles of structures based on AlGaAs waveguides from 13° to 10° (FWHM), it was necessary to widen the waveguide layers from 6.0 µm to 8.6 µm (C1605-6 and C1625-6, respectively). The angle containing 95% optical power was, however,

only reduced by 1°, i.e. from 21.6° to 20.3°. Moreover, the process of further reducing the angle by only increasing the waveguide thickness, was unsuccessful. It was found that in SLOC structures, the MQW-active region, due to its high average refractive index, contributes significantly to the guiding of the modes. By increasing the thickness of the waveguide layers, the active region acts more and more as a waveguide itself and therefore prevents further narrowing of the vertical far-field. It was shown that by the introduction of low-index quantum-barriers (LIQB) in the MQW-active region, its high average refractive index is reduced. In consequence, the mode confinement is reduced resulting in a significant reduction of the divergence angle containing 95% power content. The invention is the subject of the German Patent Application DEA102009024945.

The 8.6 µm waveguide, in combination with the LIQB design, enabled the reduction of the divergence angle containing 95% optical power from 20.3° to 15.3° and the angle at FWHM from 10° to 8.6° (C1625-6 and C1690-6, respectively). However, the LIQB design combined with low Al-content waveguides exhibits increased voltage and reduced laser efficiency. It is shown that the reason for the laser performance degradation is the increased valence band discontinuity of the LIQB. The high band discontinuity of the quantum barrier creates a barrier to hole injection and eventually leads to hole accumulation at the p-side edge of the active region which results in electron leakage. The deterioration of the laser performance is less severe by using longer cavities. The increased cavity length leads to smaller threshold gain and reduced threshold current densities. The lower threshold density translates to reduced carrier density in the QWs, which leads to reduced carrier leakage. The structure processed as a device with an 8 mm long resonator and a 200 mm wide stripe delivers a high roll-over power of 30 W in quasi-CW mode and is only 8 W lower than the initial design based on 3.4 µm GaAs waveguide that exhibits twofold wider divergence angles (B1110-3: 18° (FWHM), 30° (95% power content)).

During this work the realization of laser devices with up to 8 mm long cavities was possible because the designed structures exhibited low internal losses ($\alpha_i \approx 1$ cm^{-1}). The long gain medium allows for low reflectivity at the front facet, so higher output powers can be achieved. Moreover, the large equivalent spot-size of each design and the facet passivation protect the laser mirrors from optical damage. Additionally, the lower thermal resistance of the longer lasers delays the roll-over effect and increases the peak optical power.

Figure 11.1 compares vertical far-field angles and electro-optical parameters (like maximum optical power, usually roll-power, maximum wall-plug efficiency) of all laser designs discussed in the work. It gives an overview of the trend of the far-field reduction together with the maintenance of the high optical output power.

To conclude, this work resulted in the reduction of the vertical divergence angles, of broad area lasers emitting around 1100 nm, from 19° to 8.6° at FWHM and from 30° to 15° defined as the angle containing 95% of the optical power. The laser structure with reduced far-field processed as 8 mm long and 200 µm wide single emitter delivered 30 W optical power in quasi-continuous wave mode.

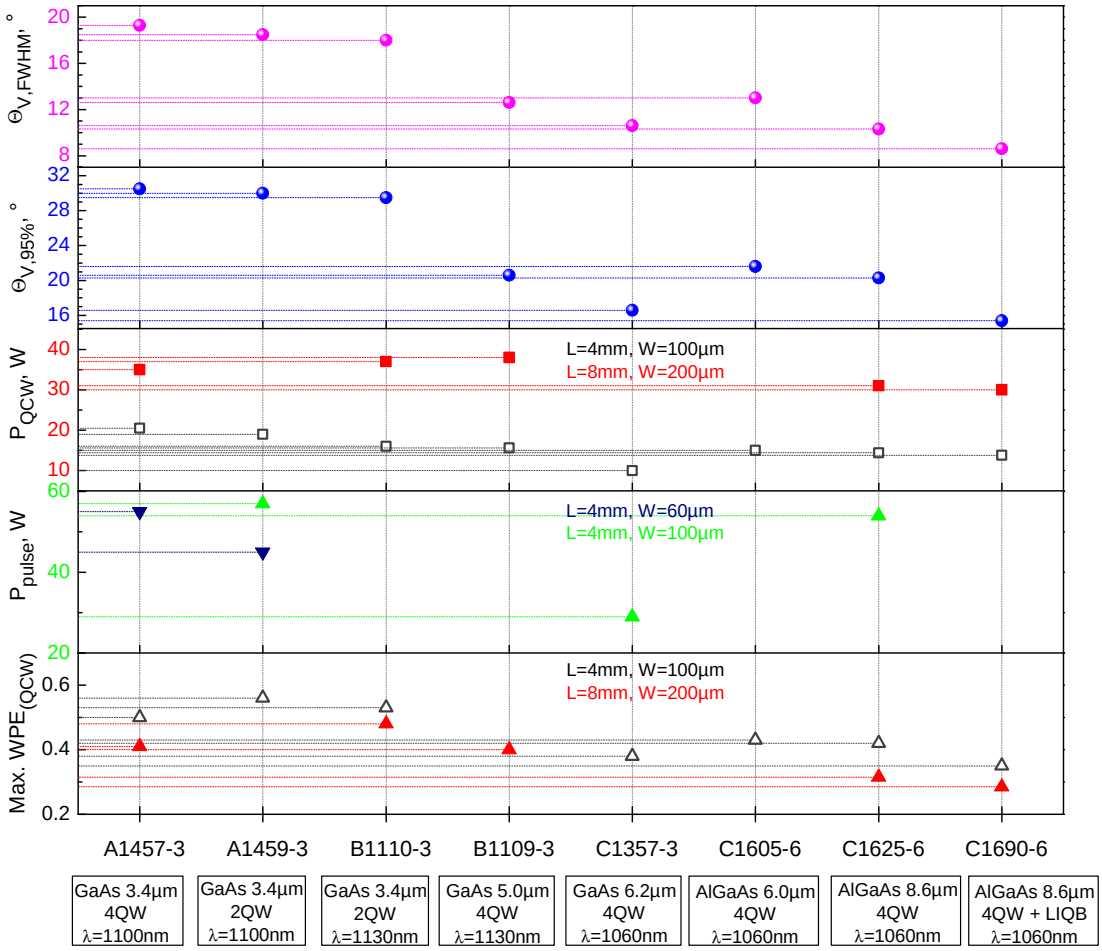

Figure 11.1. The vertical far-field angles corresponding to FWHM ($\Theta_{V,FWHM}$) and 95% power content ($\Theta_{V,95\%}$), maximal wall-plug efficiency (WPE), quasi-CW roll-over power (P_{QCW}) and power at 100 A current under 'zero-heat' condition of laser structures based on SLOC designs presented in the doctoral thesis. Resonator lengths L and stripe widths W are indicated in the figure. The far-field angles are independent of L and W. The boxes under each wafer of the diode laser contain a brief description of the epitaxial structure, i.e. waveguide composition and thickness, number of quantum wells, emission wavelength.

Further work is going to be focused on the improvement of the conversion efficiency of the laser design with an extremely narrow divergence angle. The factor degrading the laser efficiency is the electron accumulation in the p-doped waveguide, where they recombine with holes and are lost to the lasing process. There are two reasons leading to this phenomenon. Firstly, the injected electrons leak to the p-doped waveguide due to low effective barrier of the active region. Secondly, in LIQB design, the increased valence band discontinuity at the GaAsP-spacer and p-AlGaAs-waveguide layer creates a barrier, hindering hole injection into the active region. The holes, gathering at the p-side of the active region, generate an electric field that attracts the injected electrons. The proposed designs for further investigation are structures utilizing asymmetric waveguides with thinner p-doped layers. In such a design, the volume where the electron and holes can recombine is smaller and thus lower optical losses are expected. Moreover, reducing the thickness of the p-waveguide, which is characterized with a higher electrical resistivity, will reduce the electrical resistance of the structure. The influence of the doping of the p-waveguide on the thermal and electrical conductivity of the laser structure should also be investigated. Furthermore, the asymmetric waveguide provides

a broader near-field pattern and thus results in a narrower far-field pattern. The discrimination of higher modes might bechallenging however. Therefore, a single fundamental mode lasing might be more difficult to obtain.
It is planned to investigate how the material composition of the spacer next to the p-waveguide influences the hole accumulation in the vicinity of the active region and the laser efficiency. Reducing the mole fraction of phosphorus in this GaAsP-spacer reduces the valence band discontinuity between the active region and the waveguide, and also diminishes the barrier for hole injection. However, different compositions of this spacer and the quantum barriers will create an asymmetric multi-QW active region that could lead to spectral broadening of the modal gain and an increased threshold carrier density.

Appendix 1

List of grown epitaxial structures.

This Appendix gives an overview of the grown epitaxial structures discussed in the doctoral thesis. The appendix includes a table in which the details of the designs are listed, including: active region design and the emission wavelength, composition and thickness of the waveguide, composition of the claddings, and corresponding vertical far-field angles defined at fwhm and as angle containing 95% optical power. The values of the beam divergence angle are experimental data (Table A1.). Moreover, the Appendix includes figures showing the calculated energy band profiles and refractive index distribution of the discussed designs.

Structure	Wavelength	Active region		Waveguide		Cladding layers	Vertical divergence angle		Chapter
		Quantum well	Barrier (Material; thickness)	Material	Thickness		fwhm	95% power content	
A1459-3	1100 nm	2× $In_{0.29}Ga_{0.71}As$	GaAs; 100 nm	GaAs	3.4 µm	$Al_{0.25}Ga_{0.75}As$	18.5°	30.0°	**7**
A1457-3	1100 nm	4× $In_{0.29}Ga_{0.71}As$	GaAs; 50 nm	GaAs	3.4 µm	$Al_{0.25}Ga_{0.75}As$	19.3°	30.5°	
B1110-3	1125 nm	2× $In_{0.33}Ga_{0.67}As$	GaAs; 100 nm	GaAs	3.4 µm	$Al_{0.25}Ga_{0.75}As$	18.0°	29.5°	**8**
B1109-3	1130 nm	4× $In_{0.33}Ga_{0.67}As$	GaAs; 50 nm	GaAs	5.0 µm	$Al_{0.25}Ga_{0.75}As$	12.6°	20.6°	
C1357-6	1060 nm	4× $In_{0.25}Ga_{0.75}As$	$GaAs_{0.8}P_{0.2}$; 7.5 nm	GaAs	6.2 µm	$Al_{0.1}Ga_{0.9}As$	10.6°	16.6°	**9**
C1605-6	1061 nm	4× $In_{0.25}Ga_{0.75}As$	$GaAs_{0.8}P_{0.2}$; 7.5 nm	$Al_{0.1}Ga_{0.9}As$	6.0 µm	$Al_{0.2}Ga_{0.8}As$	13.0°	21.6°	
C1625-6	1060 nm	4× $In_{0.25}Ga_{0.75}As$	$GaAs_{0.8}P_{0.2}$; 7.5 nm	$Al_{0.1}Ga_{0.9}As$	8.6 µm	$Al_{0.2}Ga_{0.8}As$	10.3°	20.3°	**9, 10**
C1690-6	1057 nm	4× $In_{0.25}Ga_{0.75}As$	$GaAs_{0.65}P_{0.35}$; 7.5nm	$Al_{0.1}Ga_{0.9}As$	8.6 µm	$Al_{0.2}Ga_{0.8}As$	8.6°	15.4°	**10**

Table A1. The epitaxial structures grown and discussed in the doctoral thesis. The wavelength and the values of the vertical far-field angle are experimental data, measured at currents corresponding to the maximum of the conversion efficiency of each laser. The tested laser devices are 100 µm broad single emitters with 4 mm long cavity, mounted on c-mount. The measurement conditions: 500 µs current pulse duration, 20 Hz repetition rate, 25°C heat-sink temperature.

The energy band profiles calculated with QIP software and the refractive index distributions of the epitaxial structures discussed at the this work are presented below. (Γ and X denote the Γ and X conduction band edges; $hh\,Ev$ and $lh\,Ev$ represent the heavy and light hole valence band edge, respectively; $1st\ hh\ level$, $1st\ lh\ level$ denote the first energy level

of the heavy and light hole, respectively). The insets of the graphs present enlarged image of the active region.

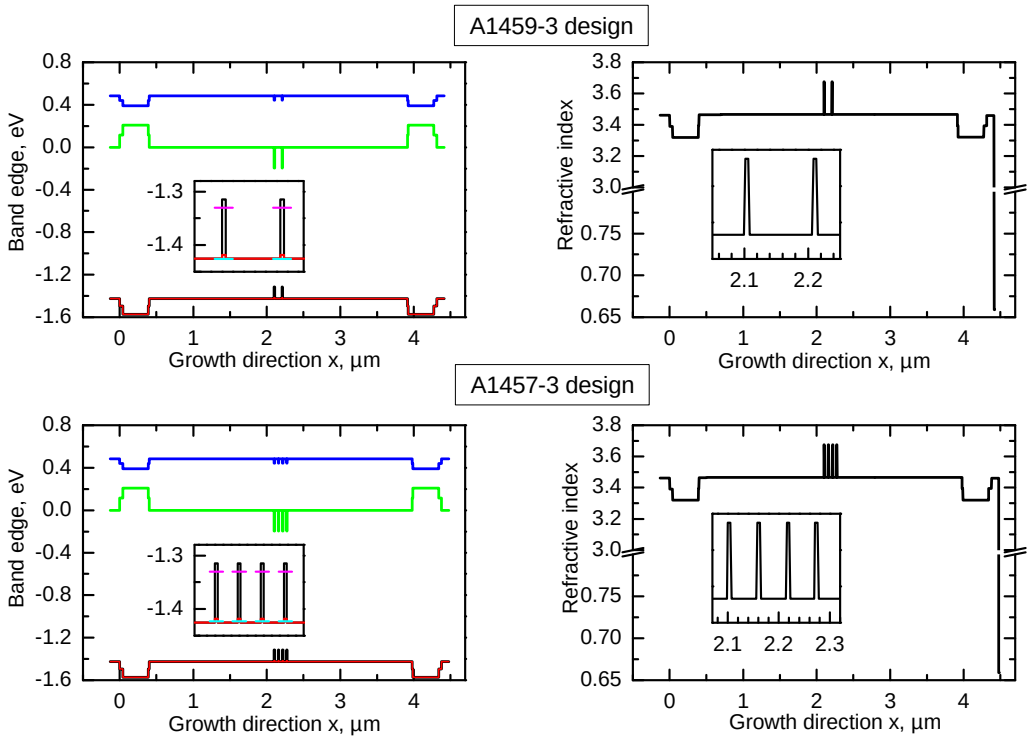

Figure A1.1. Energy band profiles and refractive index distribution of structures based on 3.4 µm thick GaAs-waveguide, utilizing active region with two QWs (A1459-3) and four QWs (A1457-3) designed for emission wavelength of 1100 nm.

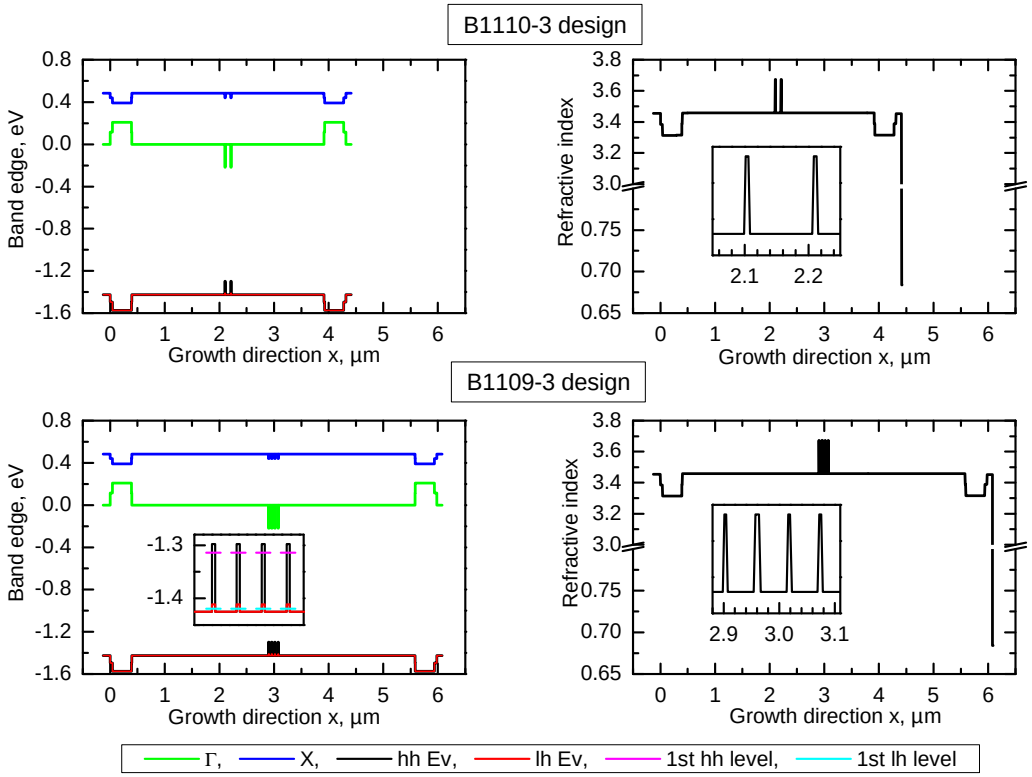

Figure A1.2. Energy band profiles and refractive index distribution of a structure based on 3.4 µm thick GaAs-waveguide, utilizing two QWs active region (B1110-3) and a structure based on 5 µm thick GaAs-waveguide and active region with four QWs (B1109-3). Emission wavelength: 1130 nm.

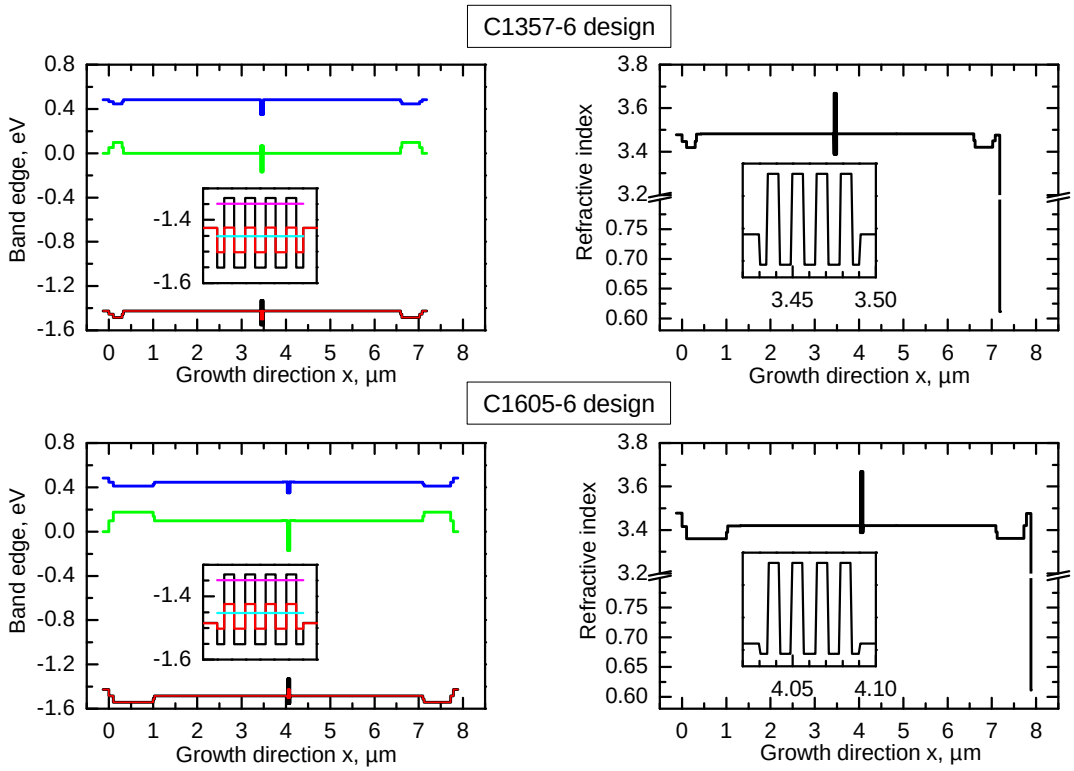

Figure A1.3. Energy band profiles and refractive index distribution of a structure based on 6.2 µm thick GaAs-waveguide (C1357-6) and a structure based on 6.0 µm thick $Al_{0.1}Ga_{0.9}As$-waveguide (C1605-6). Both structures utilize active region with four QWs designed for emission wavelength of 1060 nm.

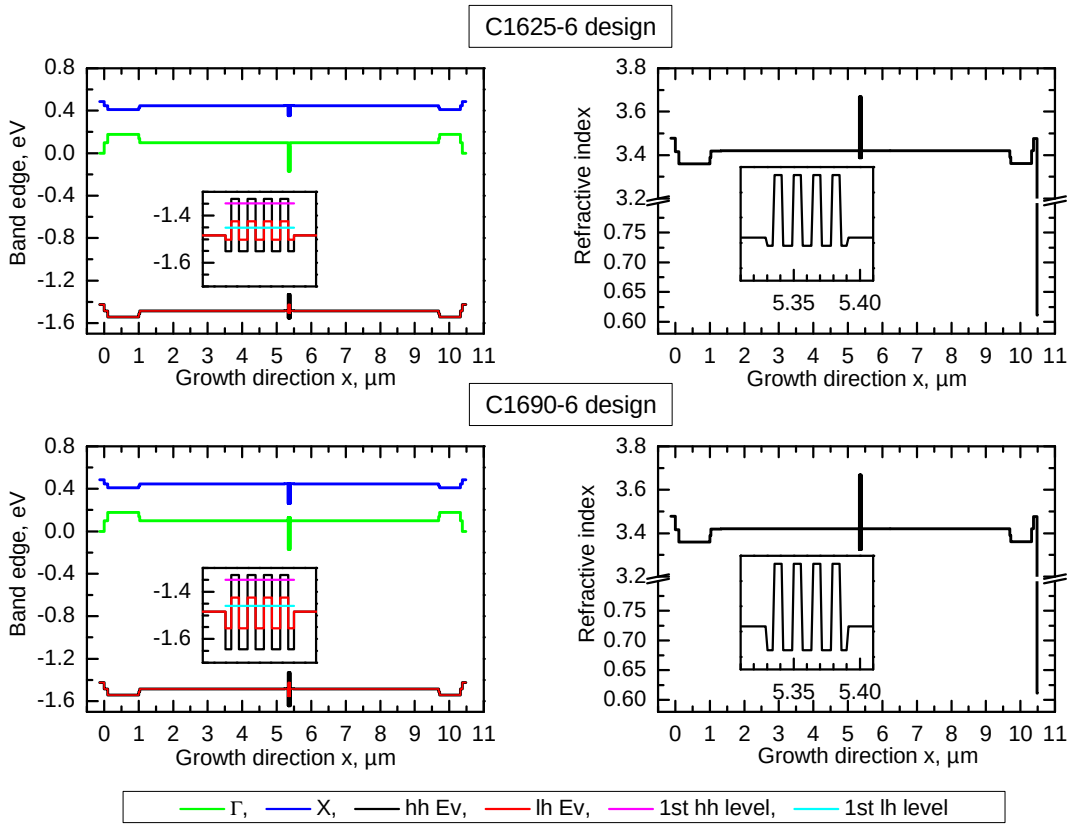

Figure A1.4. Energy band profiles and refractive index distribution of structures based on 8.6 µm thick $Al_{0.1}Ga_{0.9}As$-waveguide, utilizing active region with four QWs. Structure C1625-6 utilizes conventional QBs and structure C1690-6 utilizes LIQB. Emission wavelength: 1060 nm.

Appendix 2

Stimulated emission recombination rate and the power of the guided mode.

The stimulated emission recombination term in the eq. 3.3.1 can be written as [1]:

$$R_{Stim} = \frac{\varepsilon_0 \cdot c \cdot n_r \cdot g_m}{2\hbar\omega} \cdot \left|\vec{E}\right|^2, \qquad \text{(A2.1)}$$

where E is the electric field, g_m denotes the material gain that is approximated with a linear dependency on the carrier density N [1]:

$$g_m = g'\left(N - N_{Tr}\right), \qquad \text{(A2.2)}$$

where g' denotes the differential gain and N_{Tr} is the transparency carrier density, for which the material loss is compensated by the optical gain and the material become optically transparent.

Following [2] the total guided power by TE modes ($H_x = -\frac{\beta}{\omega\mu_0} \cdot E_y$, β - propagation constant in the z-direction) can be written as:

$$\overline{P} = \frac{1}{2}\frac{\beta}{\omega\mu_0}\int_{-\infty}^{+\infty}\int_{-\infty}^{+\infty}\left|E_y(x)\right|^2 dxdy\,. \qquad \text{(A2.3)}$$

The electric field of a mode propagating in the z-direction can be expressed as:

$$\vec{E}(x,y,z) = \frac{\vec{E}_y(x,y)}{\sqrt{\frac{1}{2}\frac{\beta}{\omega\mu_0}\int_{-\infty}^{+\infty}\int_{-\infty}^{+\infty}\left|E_y(x)\right|^2 dxdy}} \cdot \sqrt{\overline{P}(z)}\,. \qquad \text{(A2.4)}$$

Substituting the square of $\vec{E}(x,y,z)$ from eq. (A2.4) into eq. (A2.1) and considering basic relations like $\varepsilon_0\mu_0 = \frac{1}{c^2}$ and $\beta = \frac{\omega}{c} \cdot n_{eff}$ yields:

$$R_{Stim}(x,y,z)=\frac{n\cdot g_m(x,y)}{n_{eff}\cdot\hbar\omega}\cdot\frac{\left|E_y(x)\right|^2}{\int_{-\infty}^{+\infty}\int_{-\infty}^{+\infty}\left|E_y(x)\right|^2 dxdy}\cdot\overline{P}(z) \qquad \text{(A2.5)}$$

Since

$$g_m=\begin{cases} g_m=const, & x=d_{AZ},\ y=W \\ 0 & |x|>d_{AZ},|y|>W \end{cases} \qquad \text{(A2.6)}$$

we average R_{Stim} over the active region (W - the lateral active width, d_{AZ} - the vertical active region thickness) and the averaged stimulated emission recombination term can be written as:

$$\overline{R}_{Stim}=\frac{1}{d_{AZ}\cdot W}\frac{n_{AZ}\cdot g_m}{n_{eff}\cdot\hbar\omega}\cdot\frac{\int_{-d_{AZ}/2}^{d_{AZ}/2}\int_{-W/2}^{W/2}\left|E_y(x)\right|^2 dxdy}{\int_{-\infty}^{+\infty}\int_{-\infty}^{+\infty}\left|E_y(x)\right|^2 dxdy}\cdot\overline{P}(z). \qquad \text{(A2.8)}$$

Since

$$g_{\mathrm{mod}al}=\frac{n_{AZ}}{n_{eff}}\cdot\frac{\int_{-d_{AZ}/2}^{d_{AZ}/2}\int_{-W/2}^{W/2}\left|E_y(x)\right|^2 dxdy}{\int_{-\infty}^{+\infty}\int_{-\infty}^{+\infty}\left|E_y(x)\right|^2 dxdy}\cdot g_m \qquad \text{(A2.9)}$$

and

$$\Gamma=\frac{\int_{-d_{AZ}/2}^{d_{AZ}/2}\int_{-W/2}^{W/2}\left|E_y(x)\right|^2 dxdy}{\int_{-\infty}^{+\infty}\int_{-\infty}^{+\infty}\left|E_y(x)\right|^2 dx} \qquad \text{(A2.10)}$$

is the confinement factor, the finale expression for the stimulated emission recombination rate represented by the optical power of the guided mode takes the form:

$$R_{Stim}=\frac{g_{\mathrm{mod}al}}{d_{AZ}\cdot W}\cdot\frac{\overline{P}(z)}{\hbar\omega} \qquad \text{(A2.11)}$$

Appendix 3

Mirror losses and laser threshold condition.

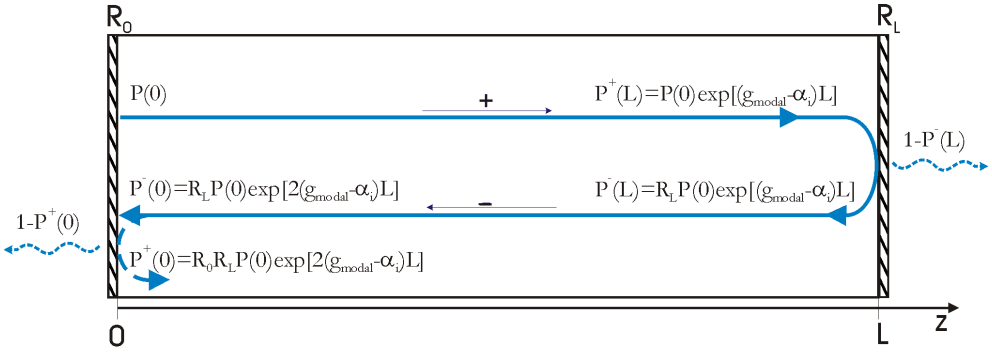

Figure A3.1. The internal optical power carried by a planar wave during a roundtrip in a Fabry-Perot optical resonator with R_0, R_L mirror reflectivities and cavity length L. '+', '-' indicate the direction of the wave propagation.

An optical wave travelling forth $E^+ \sim E_0 \exp(+i\beta z)$ and back $E^- \sim E_0 \exp(-i\beta z)$ along a gain medium on z direction between two mirrors R_0 and R_L ($0 < R_0, R_L < 1$) in an optical resonator of length L is considered. The optical power the wave carries is $P \sim P_0 \exp(2\,\mathrm{Im}\,\beta \cdot z)$, where $2\,\mathrm{Im}\,\beta$ denotes the modal gain. The optical wave travelling in the optical resonator, however, also experiences optical loss α_i.

The internal optical power P at the starting point ($z = 0$) is defined as $P(0)$.
Passing forwards $z = L$, from the left-hand side to the right-hand side of the resonator, the optical power takes the form:

$$P^+(L) = P(0) \cdot \exp[(g_{modal} - \alpha_i) \cdot L]. \qquad \text{(A3.1)}$$

The reflected power at the facet R_L, $P^+(L)$, equals:

$$\begin{aligned} P^-(L) &= R_L P^+(L) \\ &= R_L \cdot P(0) \cdot \exp[(g_{modal} - \alpha_i) \cdot L] \end{aligned} \qquad \text{(A3.2)}$$

Furthermore, the optical power carried by the wave after passing backwards from the right-hand side to the left-hand side of the resonator to $z = 0$ takes the form:

$$\begin{aligned} P^-(0) &= P^-(L) \cdot \exp[(g_{modal} - \alpha_i) \cdot L] \\ &= R_L \cdot P(0) \cdot \exp[2 \cdot (g_{modal} - \alpha_i) \cdot L]. \end{aligned} \qquad \text{(A3.3)}$$

Finally, considering the power loss at the mirror R_0, the internal power after one full round trip equals now:

$$\begin{aligned} P^+(0) &= R_0 P^-(0) \\ &= R_0 R_L P(0) \cdot \exp\left[2 \cdot \left(g_{\mathrm{mod}\,al} - \alpha_i\right) \cdot L\right]. \end{aligned} \tag{A3.4}$$

In order that the optical power carried by the optical mode after the round trip has again its initial value $P^+(0) = P(0)$, the following condition has to be fulfilled:

$$1 = R_0 R_L \cdot \exp\left[2 \cdot \left(g_{\mathrm{mod}\,al} - \alpha_i\right) \cdot L\right]. \tag{A3.5}$$

Equation (A3.5) also provides the laser threshold condition:

$$g_{\mathrm{mod}\,al,th} = \alpha_i + \frac{1}{2L} \cdot \ln \frac{1}{R_0 R_L} = \alpha_i + \alpha_m \ . \tag{A3.6}$$

The modal gain at the laser threshold equals the total optical losses: the free-carrier absorption loss α_i and the mirror loss α_m.

Appendix 4

The WIAS-TeSCA Software.

The simulator WIAS-TeSCA has been used to simulate the vertical electrical carrier transport in the semiconductor laser as well as the power-voltage-current characteristics without self-heating effects.

The lasers considered are wide stripe devices, so the calculations were done only quasi-one-dimensional. This means, that the simulation area is taken as a slice with a vertical extension according to the layer structure and a lateral width of 10 nm for numerical reasons. At the lateral boundaries, the derivatives of the optical field and electro-chemical potentials are set to zero (homogeneous Neumann conditions). This implies that there are no lateral variations of all quantities. The calculated parameters like output power and current are then rescaled to the considered stripe width of the device. This approach does not take into account e.g. the lateral current spreading effect which by real broad-area devices is typically less than 10%. The second assumption is the homogeneity of the optical power distribution in the longitudinal dimension. This longitudinal power averaging is approximately correct for Fabry-Perot lasers. However, this approach does not take into account the longitudinal spatial hole-burning phenomenon.

TeSCA software works properly for bulk materials. There are no quantisation effects implemented. Therefore, the band-structure of the strained multi quantum well active region is separately simulated by $eight-band\ \ k\cdot p$ calculations. The results of this calculation are entered the WIAS-TeSCA simulator in terms of net coefficients. Consequently, the quantum wells are treated as a classic material with a specific material parameters.

A4.2.1. Calculation of the power-voltage-current characteristic.

In order to simulate a power-voltage-current characteristic of a laser, the WIAS TeSCA simulator solves the coupled system of partial differential equations for the charged carriers and the optical field. These equations are listed below [1].

a) The Poisson equation in the transverse direction is solved to find the electrostatic potential:

$$-\varepsilon\frac{d^2\varphi}{dx^2} = C + p - n\,. \qquad \text{(A4.1)}$$

ε is the static dielectric constant, φ denotes the electrostatic potential, n, p are the electron and hole densities, respectively, and C is the charged impurity density.

b) The continuity equations for electrons and holes are solved to simulate the carrier transport:

$$\frac{dn}{dt} - \frac{dj_n}{dx} = -R \quad and \quad \frac{dp}{dt} + \frac{dj_p}{dx} = -R \quad . \qquad \text{(A4.2)}$$

j_n, j_p denotes the current densities of electrons and holes, respectively. The recombination rate R involves the nonradiative recombination processes like:
- the Shockley-Read-Hall recombination rate. The general expression can be found in [Piprek]. Here three special cases are presented:

$$R_{SRH} \approx \frac{N}{\tau_n^{SRH} + \tau_p^{SRH}} \text{ for } n = p = N \text{ and } N >> n_0, p_0, \text{ (active region)} \qquad \text{(A4.3.a)}$$

$$R_{SRH} \approx \frac{p}{\tau_p^{SRH}} \qquad \text{for } n >> p, \qquad \text{(n-doped layer)} \qquad \text{(A4.3.b)}$$

$$R_{SRH} \approx \frac{n}{\tau_n^{SRH}} \qquad \text{for } p >> n. \qquad \text{(p-doped layer)} \qquad \text{(A4.3.c)}$$

The electron and hole lifetimes τ^{SRH} are structure dependent and are within an order of magnitude of 10^{-9} s.
- the Auger recombination rate:

$$R_{Aug} = (C_n n + C_p p)(np - n_0 p_0), \qquad \text{(A4.4)}$$

with Auger coefficients C_n, C_p within the order of magnitude of 10^{-30} $cm^6 s^{-1}$.
Included are also the spontaneous radiative recombination rate:

$$R_{spon} = B(np - n_0 p_0), \qquad \text{(A4.5)}$$

with material coefficient B of the order of magnitude of 10^{-10} $cm^3 s^{-1}$; and the stimulated recombination rate described with eq. A2.5.

The carrier transport and the optical waveguiding are coupled via the stimulated recombination rate.

The quasi-Fermi energies F_n and F_p are linked with the carrier densities n and p by means of the Fermi-Dirac statistics.

As a consequence of the above equations, the current conservation equation is inferred:

$$j = -\varepsilon \nabla \frac{d\varphi}{dt} + j_n + j_p. \qquad \text{(A4.7)}$$

c) The optical field distribution is determined by solving the waveguide equation:

$$\frac{d^2 E}{dx^2} + \left(\frac{\omega^2}{c^2} \tilde{\varepsilon}(\omega, x) - \tilde{\beta}^2 \right) E(x) = 0, \qquad \text{(A4.8)}$$

where ω represents the optical circular frequency of the lasing mode. The complex dielectric function $\tilde{\varepsilon}(\omega, x)$ is a function of the gain, the background absorption and the refractive index. Thus, it depends on almost all properties of the operating device. As a consequence, the propagation constant and the eigenfunction E depend parametrically on the carrier density distribution and on the temperature profile.

The above equations are supplemented by boundary conditions as well as matching conditions at the heterointerfaces. The waveguide equation is solved by inverse vector iteration using the homogeneous Dirichlet or Neumann conditions. At the heterointerfaces, the continuity of the quasi-Fermi energies is assumed. The details are presented in [1].

Additionally, in order to consider the longitudinal dimension of the laser, the rate equation for the optical power is self-consistently solved with the other equations.

$$\frac{dP}{dt} = \frac{c}{n_g}\left[2\,\mathrm{Im}\,\tilde{\beta} - \alpha + \frac{1}{2L}\ln\frac{1}{R(0)R(L)}\right]P + R_{spont}\,. \qquad \text{(A4.9)}$$

$2\,\mathrm{Im}\,\tilde{\beta}$ represents the modal gain; α denotes the free-carrier absorption and scattering losses; R_{spont} is the rate of photons spontaneously emitted into the lasing mode; L and R represents the laser length and facet reflectivity, respectively. In the stationary solution, eq. (A4.9) takes the form:

$$P = \frac{R_{spont}}{g_{\mathrm{mod}\,al} - \alpha + \frac{1}{2L}\ln\frac{1}{R(0)R(L)}}\,. \qquad \text{(A4.10)}$$

In all calculations with the TeSCA software, only the lasing mode is considered and the power carried by all other modes is neglected.

A4.2.2. Simulated structures

The power-voltage-current characteristics and the vertical carrier profiles (calculated by means of the WIAS-TeSCA simulator) in the work are presented for two samples: A1459-3 and C1357-6. The results are presented in chapter 7 in figure 7.3 and in chapter 9 in figure 9.2, respectively. tables A4.1 and A4.2 present the parameters used for the simulations of samples A1459-3 and C1357-6, respectively.

Entered parameter	Value	Unit	Comments
Gain coefficient	12.1×10^3	cm^{-1}	Considered only for the QWs
Carrier lifetime (Shockley-Read-Hall recombination)	$\tau_n = 2.8$ $\tau_p = 2.8$	ns	Equal for each epitaxial layer i.e. QWs, waveguide and claddings
Radiative rate coefficient	$B = 2.7 \times 10^{-10}$	cm^3s^{-1}	
Auger recombination rate coefficient	$C_n = 2 \times 10^{-30}$ $C_p = 2 \times 10^{-30}$	cm^6s^{-1}	
Absorption cross sections for free electrons and free holes	$\sigma_n = 3 \times 10^{-18}$ $\sigma_p = 7 \times 10^{-18}$	cm^2	
Scattering loss	0.6	cm^{-1}	

Table A4.1. Parameters entered the simulation software during calculations of power-current characteristic and vertical carrier distribution under 'zero-heat' condition for sample A1459-3, discussed in chapter 7. The simulation results are presented in figures 7.3 and 7.4.

Entered parameter	Value	Unit	Comments
Gain coefficient	6×10^3	cm^{-1}	Considered only for the QWs
Carrier lifetime (Shockley-Read-Hall recombination),	$\tau_n = 2.3$ $\tau_p = 2.3$	ns	Equal for each epitaxial layer i.e. QWs, waveguide and claddings
Radiative rate coefficient	$B = 8.6 \times 10^{-10}$	cm^3s^{-1}	
Auger recombination rate coefficient	$C_n = 2 \times 10^{-30}$ $C_p = 2 \times 10^{-30}$	cm^6s^{-1}	
Absorption cross sections for free electrons and free holes	$\sigma_n = 4 \times 10^{-18}$ $\sigma_p = 12 \times 10^{-18}$	cm^2	
Scattering loss	0.3	cm^{-1}	

Table A4.2. Parameters entered the simulation software during calculations of power-current characteristic and vertical carrier distribution under 'zero-heat' condition for sample C1357-6, discussed in chapter 9. The simulation results are presented in figure 9.3

Appendix 5

Simulations of temperature distribution in the transverse cross section of the laser diode.

This doctoral thesis deals with high power diode lasers with several Watts of output power. One of the main factors limiting the laser performance is the internal heating. the mounting process of the laser chip plays a significant role here. In order to reduce the thermal resistance and thus the bulk junction temperature the laser chips tested during the work were mounted junction-down. This mounting configuration (in contrary to the junction-up mounting) prevents the heat generated during laser operation, from spreading through the thick substrate. Thus the internal heating of the laser crystal is reduced. To support this argument, the temperature distributions and the temperature rise of the active region were calculated for junction-up and junction-down bonded laser chips as a function of the heating time. The results are presented in chapter 3 in figure 3.8. The simulation software is discussed in the text below.

The laser chips discussed in this work are mounted on a CuW submount that is soldered to a C-mount heat-sink and tested under short pulse and quasi-CW operation modes. Some of the diode-lasers discussed in chapter 10, however, were mounted to an another type of heat-sink, i.e. CCP. In order to show that P-I characteristics of the lasers mounted on two different types of the heat-sink but tested at the same quasi-CW operation mode are comparable, the temperature distributions and their dependence on the heating time were simulated. From the calculations presented in Appendix 5 in figure A5.1, one can see that the heat-sink type only has an influence on the laser performance when tested under CW conditions.

The simulations of the two-dimensional temperature distribution in the transverse cross section of the laser diode (mounted on CuW/C-mount) were done with the help of the MSC Patran/Nastran software package by Dr. F. Schnieder at the FBH institute. The software solves the time-dependent linear heat equation. During simulations, the heat fluxes in the epitaxial layer structure, in the submount and in the heat-sink were accounted for. The temperature at the bottom of the Cu heat-sink was kept constant and at all other boundaries, zero heat flux was assumed (no heat exchange between the laser and the surrounding air). All material parameters [1] of the simulated structures were assumed to be temperature independent. The temperature distribution versus time was initially calculated for an arbitrary loss power.

A5.1 Simulations of the temperature distribution in the transverse cross section of the laser diode mounted junction -up and junction-down to c-mount.

The different layers of the simulated laser structure, together with their respective geometries and material parameters, are listed in table A5.1 (junction-up mounting) and table A5.2 (junction-down mounting). During simulation, the complete heat source (10 W) was placed in the plane of the active region (thickness of about 30 nm - neglected in the simulation). The heat-sink temperature was set to 300 K [2]. The simulated temperature distributions versus heating time (0.1 µs to 500 µs) are graphically presented in figure 3.8 for a laser geometry 100 µm wide and 4 mm long.

Layer	Material	Thickness, mm	Width, mm	Half width, mm	Thermal conductivity, W/Kmm	Heat capacity, J/gK	Density, g/mm^3
Gold	Au	0.003	0.4	0.2	0.32	0.129	0.019
p-metal	(Ti/Pt/Au)	0.0001	0.4	0.2	0.1	0.38	0.012
p-epitaxy	AlGaAs	0.0013	0.4	0.2	0.012	0.366	0.00485
Active region - Heat source		0	0.1	0.05			
n-epitaxy	AlGaAs	0.0045	0.4	0.2	0.012	0.366	0.00485
n-substrate	GaAs	0.12	0.4	0.2	0.044	0.327	0.00532
n-metal	(Ni/Au/Ge+ Ti/Pt/Au)	0.00055	0.4	0.2	0.1	0.38	0.012
Solder	AuSn	0.006	0.4	0.2	0.057	0.17	0.0145
Submout	CuW	0.53	2	1	0.2	0.175	0.0161
Solder	$Pb_{0.4}Sn_{0.6}$	0.02	2	1	0.050	0.27	0.0089
Heatsink	Cu	5	6.4	3.3	0.384	0.383	0.0089

Table A5.1. Geometrical and material data for the time-dependent simulation of a Broad Area asymmetric-SLOC structure mounted junction-up to CuW/C-mount.

Layer	Material	Thickness, mm	Width, mm	Half width, mm	Thermal conductivity, W/Kmm	Heat capacity, J/gK	Density, g/mm^3
n-metal	(Ni/Au/Ge+ Ti/Pt/Au)	0.00055	0.4	0.2	0.1	0.38	0.012
n-substrate	GaAs	0.12	0.4	0.2	0.044	0.327	0.00532
n-epitaxy	AlGaAs	0.0045	0.4	0.2	0.012	0.366	0.00485
Active region - Heat source		0	0.1	0.05			
p-epitaxy	AlGaAs	0.0013	0.4	0.2	0.012	0.366	0.00485
p-metal	(Ti/Pt/Au)	0.0001	0.4	0.2	0.1	0.38	0.012
Gold	Au	0.003	0.4	0.2	0.32	0.129	0.019
Solder	AuSn	0.006	0.4	0.2	0.057	0.17	0.0145
Submout	CuW	0.53	2	1	0.2	0.175	0.0161
Solder	$Pb_{0.4}Sn_{0.6}$	0.02	2	1	0.050	0.27	0.0089
Heatsink	Cu	5	6.4	3.3	0.384	0.383	0.0089

Table A5.2. Geometrical and material data for the time-dependent simulation of a Broad Area asymmetric-SLOC structure mounted junction-down to CuW/C-mount.

A5.2 Simulations of the temperature distribution in the transverse cross section of the laser diode at steady state conditions (CW) and quasi-CW heating conditions.

The different layers of the simulated laser structure, together with their respective geometries and material parameters, are listed in table A3. During simulation, the complete heat source (10 W) was placed in the plane of the p-doped waveguide and cladding layer. The epi-down mounting and laser geometry 400 µm × 1 mm (width × length) were considered. The heat-sink temperature was set to 300 K. The simulated temperature distributions versus time heating (0.1 µs to CW) rescaled for 20 W heat source and a 200 µm × 4 mm laser device geometry are graphically presented in figure A5.1. Moreover, the simulated temperature rise of the active region, rescaled for 70 W heat source, is presented in figure 6.2as a function of the heating time.

Layer	Material	Thickness, mm	Width, mm	Half width, mm	Thermal conductivity, W/Kmm	Heat capacity, J/gK	Density, g/mm^3
n-metal	(Ni/Au/Ge+ Ti/Pt/Au)	0.00055	0.6	0.3	0.1	0.38	0.012
n-substrate	GaAs	0.12	0.6	0.3	0.044	0.327	0.00532
n-epitaxy	AlGaAs	0.0027	0.6	0.3	0.012	0.366	0.00485
p-epitaxy	AlGaAs	0.0014	0.6	0.3	0.012	0.366	0.00485
p-metal	(Ti/Pt/Au)	0.0001	0.6	0.3	0.1	0.38	0.012
Gold	Au	0.003	0.6	0.3	0.32	0.129	0.019
Solder	AuSn	0.006	0.6	0.3	0.057	0.17	0.0145
Submout	CuW	0.53	2	1	0.2	0.175	0.0161
Solder	Pb0.4Sn0.6	0.02	2	1	0.050	0.27	0.0089
Heatsink	Cu	5	6.4	3.3	0.384	0.383	0.0089

Table A5.3. Geometrical and material data for time-dependent simulation of an array (20×100 µm stripe) asymmetric-SLOC structure mounted junction-down to CuW/C-mount.

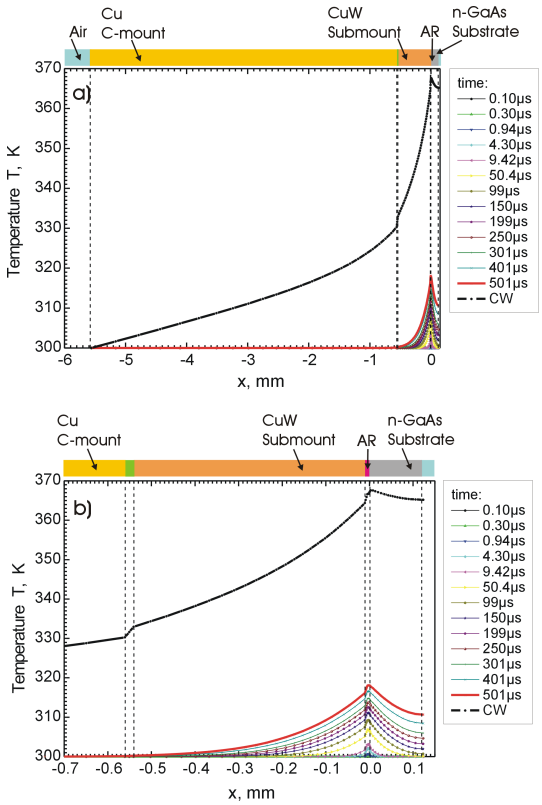

Figure A5.1. Temperature distribution in vertical plain of the laser diode in dependence on the heat time (0.1 µs to stead-state condition). Laser mounted junction-down to the C-mount heat-sink. In figure (b) zoom to the CuW submount.

Bibliography

Chapter 1:

[1] ‘High Reliable, High Brightness, 915 nm Laser Diodes for Fiber Laser Applications’, Z. Xu, et al. Proc. of SPIE Vol. 6909, 2008.

[2] ‘High d/gamma Values in Diode Laser Structures for Very High Power’, I. Petrescu-Prahova, P. Modak, E. Goutain, D. Silan, D. Bambrick, J. Riordan, T. Moritz, S. D. McDougall, B. Qiu, J. H. Marsh, Proc. of SPIE Vol. 7198, 2009.

[3] ‘Limitations to Peak Continuous Wave Power in High Power Broad Area Single Emitter 980 nm Diode Lasers’, P. Crump, C. Roder, R. Staske, A. Pietrzak, W. Pittroff, A. Ginolas, J. Fricke, K. Paschke, F. Bugge, P. Ressel, H. Wenzel, and G. Erbert, Tech. Digest CLEO Europe/EQEQ, Paper CB-P33-TUE, 2009.

[4] ‘Advances in Spatial and Spectral Brightness in 800-1100 nm GaAs-Based High Power Broad Area Lasers’, P. Crump, H. Wenzel, G. Erbert, and G. Tränkle, Proc. SPIE Europe Security-Defence, 2009.

[5] ‘16W Continuous-Wave Output Power From 100 μm-Aperture Laser with Quantum Well Asymmetric Heterostructure’, N. A. Pikhtin, S. O. Slipchenko, Z. N. Sokolova, A. L. Stankevich, D A. Vinokurov, I. S. Tarasov, and Zh. I. Alferov, Electron. Lett. Vol. 40, p. 1413, 2004.

[6] ‘High-Power High-Efficiency 1150-nm Quantum-Well Laser’, G. Erbert, F. Bugge, J. Fricke, P. Ressel, R. Staske, B. Sumpf, H. Wenzel, M. Weyers, and G. Tränkle, J. Sel. Top. Quant. Electron. Vol. 11, p. 1217, 2005.

[7] ‘High Brightness Diode Lasers with Very Narrow Vertical Divergence’, G. Erbert, F. Bugge, B. Eppich, J. Fricke, K-H. Hasler, K. Paschke, A. Pietrzak, H. Wenzel, and G. Tränkle, Proc. of SPIE Vol. 6909, 2008.

[8] ‘High-Power Laser Diodes Emitting Light Above 1100 nm with a Small Vertical Divergence Angle of 13°’, A. Pietrzak, H. Wenzel, G. Erbert, and G. Tränkle, Opt. Lett. Vol. 33, p. 2188, 2008.

Chapter 2:

[1] ‘Beam Divergence of the Emission From Double-Hetrostructure Injection Lasers’, H. C. Casey, M. B. Panish, J. L. Merz, J- Appl. Phys. Vol. 44, No. 12, pp.5470-75, 1973.

[2] ‘A Very Narrow-Beam AlGaAs Laser with a Thin Tapered Thickness Active Layer (T3 Laser)’, T. Murakami, K. Ohtaki, H. Matsubara, T. Yamawaki, H. Saito, K. Isshiki, Y. Kokubo, A. Shima, H. Kumabe and W. Susaki, J. Quant. Electron., Vol. 23, No. 6, 1987.

[3] ‘Tapered Thickness MQW Waveguide BH MQW Lasers’, H. Kobayashi, Photon. Tech. Lett., Vol. 6, No. 9, p.1080, 1994.

[4] ‘Extremely Small Vertical Far-Field Angle of InGaAs-A1GaAs Quantum-Well Lasers with Specially Designed Cladding Structure’, G. Lin, S.T. Yen, C.P. Lee, and D.C. Liu, Photon. Tech. Lett., Vol. 8, No. 12, 1996.
[5] ‘Theoretical Investigation on Quantum Well Lasers With Extremely Low Vertical Beam Divergence and Low Threshold Current’, G. W. Yang, J. Y. Xu, Z. T. Xu, J. M. Zhang, L. H. Chen, and Q. M. Wang, J. Appl. Phys. Vol. 83, No. pp.8-14, 1998.
[6] ‘A Novel Cladding Structure for Semiconductor Quantum-Well Lasers With Small Beam Divergence and Low Threshold Current’, S.T. Yen, and Ch.P. Lee, J. Quant. Electron. Vol. 32, No. 9., pp.1588-95, 1996.
[7] ‘Design of High-Power Strained InGaAs/AlGaAs Quantum-Well Lasers With a Vertical Divergence Angle of 18°’, J. Temmyo, and M. Sugo, Electron. Lett. Vol. 31, No. 8, pp 642-44, 1995.
[8] ‘High-Power Low Vertical Beam Divergence 800-nm-Band Double-Barrier-SCH GaAsP-(AlGa)As Laser Diodes’, A. Malag, A. Jasik, M. Teodorczyk, A. Jagoda, and A. Kozlowska, Photon. Tech. Lett. Vol. 18, No. 15, pp. 1582-84, 2006.
[9] ‘Low Divergence Angle, 808 nm, GaAlAs/GaAs Laser Diode Using Asymmetric-Cladding Structure’, Z. Xu, W. Gao, B. Siskavich, A. Nelson, L. Cheng, K. Luo, H. Kim, Z. Wang, A. Chin, Proc. SPIE Vol. 5365, pp 142-145, 2004.
[10] ‘Vertical beam divergence of double-barrier multiquantum well (DBMQW) (AlGa)As heterostructure lasers’, A. Malag, B. Mroziewicz, J. of Light and Tech. 14, No.6, p.1514, 1996.
[11] ‘Design and Fabrication of Low Beam Divergence and High Kink-Free Power Lasers, B. Qiu, S.D. McDougall, X. Liu, G. Bacchin, J. Marsh, J. Quant. Electron., Vol. 41, No. 9, pp. 1124-30, 2005.
[12] ‘650-nm Laser With Narrow Far-Field Divergence With Integrated Optical Mode Expansion Layers’, P.M. Smowton, G.M. Lewis, H.D. Summers, G. Berry, and C.C. Button, J. Sel. Top. Quant. Electron., Vol. 5, No. 3, pp. 735-39, 1999.
[13] ‘Semiconductor Lasers with Unconventional Cladding Structures for Small Beam Divergence and Low Threshold Current’, S. T. Yen, and C. P. Lee, Opt. Quant. Electron., Vol. 28, pp. 1229-38, 1996.
[14] ‘980 nm Spread Index Laser with Strain Compensated InGaAs/GaAsP/InGaP and 90% Fibre Coupling Efficiency’, D. Vakhshoori, Electron. Lett., Vol. 32, No. 11, p.1007, 1996.
[15] ‘Single-Quantum-Well Laser with 11.2 Degree Transverse Beam Divergence’, Y. C. Chen, Electron. Lett., Vol. 26, No.17, p.1349, 1990.
[16] ‘A Periodic Index Separate Confinement Heterostructure Quantum Well Laser’, M. C. Wu, Appl. Phys. Lett., Vol. 59, No.9, p.1046, 1991.
[17] ‘Antiresonant Reflecting Optical Waveguides in SiO_2-Si Multilayer Structures’, M. A. Duguay, Y. Kokubun, L. Pfeiffer, and T.L. Koch, Appl. Phys. Lett., Vol. 49, p.13, 1986.
[18] ‘High-Power Diode Lasers with Small Vertical Beam Divergence Emitting at 808 nm’, H. Wenzel, F. Bugge, G. Erbert, R. Hülsewede, R. Staske, and G. Tränkle, Electron. Lett., Vol. 37, No. 16, 2001.
[19] ‘Diode Lasers and Photonic Integrated Circutes’. L.A. Coldren, S.W. Corzine, Inc. John Wiley & Sons, New York, 1995. p. 333.
[20] ‘Nanostrukturen für die Optoelektronik. Bericht zur Machbarkeitsstudie: Herstellung von *Photonic-Bandgap-Crystal*-Lasern mit Niedriger Schwellstromdichte TESAG’, Berlin 2006.
[21] ‘High-Power one-, two-, and three-Dimensional Photonic Crystal Edge Emitting Laser Diodes for Ultrahigh Brightness Applications’, N.Y. Gordeev, M.V. Maximova, Y.M. Shernyakov, I.I. Novikov, L.Y. Karachinsky, V.A. Shchukin, T. Kettler, K. Posilovic, N. N. Ledentsov, D. Bimberg, R. Duboc, A. Sharon, D.B. Arbiv, U. Ben-Ami, Proc. of SPIE Vol. 6889, p. 68890W, 2008.

[22] ‘High Brilliance Photonic Band Crystal Lasers’ V.A. Shchukin, N.N. Ledentsov, N.Y. Gordeev, L.Y. Karachinsky, N.V. Kryzhanovskaya, S.M. Kuznetsov, M.B. Lifshits, M.V. Maximov, I.I. Novikov, Y.M. Shernyakov, T. Kettler, K. Poslovic, and D. Bimberg, Proc of SPIE Vol. 6350 p. 635005-1, 2006.
[23] ‘Wavelength-Stabilized Tilted Wave Lasers with a Narrow Vertical Beam Divergence’, I.I. Novikov, Y.M. Shernyakov, M.V. Maximov, N.Y. Gordeev, N.A. Kaluzhniy, S.A. Mintairov, V.M. Lantratov, A.S. Payusov, V.A. Shchukin, and N.N. Ledentsov, Semicond. Sci. Technol. Vol. 23, p. 075043, 2008.
[24] ‘High-Power Laser Diodes Emitting Light above 1100 nm with a Small Vertical Divergence Angle of 13°’, A. Pietrzak, H. Wenzel, G. Erbert, G. Tränkle, Opt. Lett. Vol. 33, No.19, p. 2188, 2008.
[25] ‘High Power 1060 nm Ridge Waveguide Lasers with Low-Index Quantum Barriers for Narrow Divergence Angle’, A. Pietrzak, P. Crump, H. Wenzel, F. Bugge, G. Erbert, G. Tränkle, Tech. Digest CLEO/QELS, CWE2, 2010.

Chapter 3:

[1] ‘Semiconductor Laser Fundamentals’, T. Suhara, Marcel Dekker, Inc. New York, 2004.
[2] ‘Physics of Optoelectronic Devices’, S. L. Chuang, John Wiley & Sons, Inc., Canada, 1995.
[3] ‘High Power Diode Lasers: Technology and Applications’, ed. F. Bachmann, P. Loosen, R. Poprawe, Springer Series in Optical Sciences, 2007.
[4] ‘Semiconductor Optoelectronic Devices: Introduction to Physics and Simulation’, J. Piprek, Academic Press, 2003.
[5] ‘High-Power Diode Lasers: Fundamentals, Technology, Applications’, edited by R. Diehl, Springer, New York, 2000.
[6] ‘Beam Divergence of the Emission From Double-Hetrostructure Injection Lasers’, H. C. Casey, M. B. Panish, J. L. Merz, J- Appl. Phys. Vol. 44, No. 12, pp.5470-75, 1973.
[7] ‘Refractive Index Of $Ga_{1-x}Al_xAs$’, M.A. Afromowitz, Sol. Stat. Communications Vol. 15, pp. 59-63, 1974.
[8] ‘Phase and Group Indices For Double Heterostructure Lasers’, J. Buss, and M.J. Adams, Sol. Stat. Electron. Devices Vol. 3, No.6, pp. 189-195, 1979.
[9] ‘Refractive Index Dispersion in Group IV and Binary III-V Semiconductors: Comparison of calculated and experimental values’, D. Campi, and C. Papuzza, J. Appl. Phys. Vol.57, No. 4, pp. 1305-10, 1985.
[10] ‘Optical Wave Science and Technology, Vol. 1: Optical Waveguide Concepts’ ,Ch. Vassallo, Elsevier 1991.
[11] ‘Semiconductor Lasers and Heterojunction LEDs’, H. Kressel, J. Butler, Principles and Applications, Quantum Electronics, ACADEMIC PRESS 1977, Chapter 5.
[12] ‘Diode Lasers and Photonic Integrated Circuits’, L.A. Coldren and S.W. Corzine, Wiley, New York 1995.
[13] ‘Internal Optical Loss in Semiconductor Lasers’ N.A. Pikhtin, S.O. Slipchenko, Z.N. Sokolova, and I.S. Tarasov, Semiconductors, Vol. 38, No. 3, pp.360-367, 2004.
[14] ‘The Differential Efficiency of Quantum-Well Lasers’ P. Smowton and P. Blood, J. of Sel. Top. Quant. Electron., Vol. 3, NO. 2, pp.491-98, 1997.
[15] ‘The Temperature Dependence of 1.3- and 1.5- μm Compressively Strained InGaAs(P) MQW Semiconductor Lasers’, A. F. Phillips, S. J. Sweeney, A. R. Adams, and P. J. A. Thijs, J. Sel. Top. Quantum Electron., Vol. 5, No. 3, pp. 401-412, 1999.

[16] ‘Comprehensive Modeling of the Electro-Optical-Thermal Behaviour of (AlGaIn)(AsSb) -Based 2.0 µm Diode Lasers’, M. Rattunde, C. Mermelstein, J. Schmitz, R. Kiefer, W. Pletschen, M. Walther, and J. Wagner, Appl. Phys. Lett. Vol. 80, No. 22, 2002.
[17] ‘Design Considerations and Analytical Approximations for High Continuous-Wave Power, Broad-Waveguide Diode Lasers’, D. Botez, Appl. Phys. Lett. Vol. 74, No. 21, 1999.

Chapter 4:

[1] ‘High-Power Diode Lasers: Fundamental, Technology, Applications’ Ed. R.Diehl, Springer 2000.
[2] ‘MOVPE Growth Optimization for Laser Diodes with Highly Strained InGaAs MQWs’, F. Bugge, U. Zeimer, R. Staske, B. Sumpf, G. Erbert, and M. Weyers, J. Cryst. Growth Vol. 298, pp. 652–57, 2007.
[3] ‘Effect of Growth Conditions and Strain Compensation 0n Indium Incorporation for Diode Lasers Emitting above 1050 nm’, F. Bugge, U. Zeimer, S. Gramlich, I. Rechenberg, J. Sebastian, G. Erbert, and M. Weyers, J. Cryst. Growth. Vol. 221, pp. 469-502, 2000.
[4] ‘Highly Strained Very High-Power Laser Diodes with InGaAs QWs’, F. Bugge, M. Zorn, U. Zeimer, T. Sharma, H. Kissel, R. H.ulsewede, G. Erbert, and M. Weyers, J. Cryst. Growth, Vol. 248, pp. 354–58, 2003.
[5] ‘MOVPE Growth Of InGaAs/GaAsP-MQWs For High-Power Laser Diodes Studied by Reflectance Anisotropy Spectroscopy’, F. Bugge, M. Zorn, U. Zeimer, A. Pietrzak, G. Erbert, and M. Weyers, J. Cryst. Growth, Vol. 311, pp. 1065–69, 2009.
[6] ‘Effect of GaAsP Barrier Layers on the Parameters of InGaAs/AlGaAs Laser Diodes Emitting in the 1050-1100 nm Spectral Range’, V. Duraev, A. Marmalyuk, A. Padalitsa, A. Petrovskii, Yu. Ryaboshtan, M. Sumarokov, and A. Sukharev, Quant. Electron. Vol. 35, No. 10, pp. 909-11, 2005.
[7] ‘Interdiffusion in Highly Strained InGaAs-QWs for High Power Laser Diode Applications’, F. Bugge, U. Zeimer, H. Wenzel, G. Erbert, and M. Weyers, J. Cryst. Growth Vol. 272, pp. 531–37, 2004.
[8] ‘Doping in III-V Semiconductors. Cambridge Studies in Semiconductor Physics and Microelectronic Engineering’, E.F. Schubert ed. A. Haroon, Cambridge University Press, 1993 p.189.
[9] ‘Influence of Current Spreading on The Transparency Current Density of Quantum-Well Lasers’, H. Wenzel, G. Erbert, A. Knauer, A. Oster, K. Vogel, and G. Tränkle, Semicond. Sci. Technol. Vol. 15, pp. 557–60, 2000.
[10] P. Ressel and G. Erbert, European Patent No. EP 1 514 335 B1/16.03.2005
[11] ‘Novel Passivation Process for the Mirror Facets Of Al-Free Active-Region High-Power Semiconductor Diode Lasers’, P. Ressel, G. Erbert, U. Zeimer, K. Häusler, G. Beister, B. Sumpf, A. Klehr, and G. Tränkle, Phot. Tech. Lett., Vol. 17, No. 5, pp. 962-64, 2005.
[12] ‘Thermal Management Strategies for High Power Semiconductor Pump Lasers’, X. Liu, M.H. Hu, C. G. Caneau, R. Bhat, C. Zah, Trans. Comp. Pack. Tech. Vol.29, No.2, pp.268-76, 2006.
[13] ‘Mounting of High Power Laser Diodes on Boron Nitride Heat Sinks Using an Optimized Au/Sn Metallurgy’, W. Pittroff, G. Erbert, G. Beister, F. Bugge, A. Klein, A. Knauer, J. Maege, P. Ressel, J. Sebastian, R.Staske, and G. Traenkle, IEEE Trans. Advanc. Pack., vol. 24, no. 4, pp 434-41, 2001.
[14] ‘Einfluss des Lötverfahrens auf die Eigenschaften von Hochleistungslaserdioden’, I. Hoffmann, Diplomarbeit, Fachhochschule für Technik und Wirtschaft and Ferdinand-Braun-Institut für Höchstfrequenztechnik, Berlin, 2003.

[15] ‘Thermal properties of diamond/copper composite material’, K. Yoshida, and H. Morigami, Microelectronics Reliability Vol. 44, pp. 303-8, 2004.

Chapter 5:

[1] ‘Physics of Optoelectronic Devices’, S. L. Chuang, John Wiley & Sons, Inc., Canada, 1995.
[2] ‘Semiconductor Optoelectronic Devices: Introduction to Physics and Simulation’, J. Piprek, Academic Press, 2003.
[3] ‘Temperature Dependence of the Photoluminescence Properties and Band Gap Energy of $In_xGa_{1-x}As/GaAs$ Quantum Wells, J.R Botha, and A.W.R. Leitch, J. Electron. Mat., Vol. 29, No. 12, pp.1362-71, 2000.
[4] ISO 11146-2:2005 Lasers and Laser-related Equipment - Test Methods for Laser Beam Widths, Divergence Angles and Beam Propagation Ratios - Part 2: General Astigmatic Beams.
[5] ‘Laser And Gaussian Beam Propagation and Transformation, J. Alda, Encyclopaedia of Optical Engineering, Publisher: Marcel Dekker, Inc., New York 2003.
[6] ‘Principles of Optics’, M. Born and E. Wolf, Pergamon Press 1993.

Chapter 6:

[1] German Patent Application DEA102009024945 P.Crump, G.Erbert, A.Pietrzak, H.Wenzel: ‘Optoelektronisches Halbleiterbauelement und Verfahren zu dessen Herstellung’, 2009.
[2] ‘A Model for the Calculation of the Threshold Current of SCH-MQW-SAS Lasers’, H. Wenzel and H. Wünsche, Phys. Stat. Sol (a). Vol. 120, pp.661-73, 1990.
[3] ‘Doping In III-V Semiconductors. Cambridge Studies in Semiconductor Physics and Microelectronic Engineering’, E.F. Schubert ed. A. Haroon, Cambridge University Press, 1993.
[4] ‘Analysis Of Beam Quality Factor For Semiconductor Lasers”, Gen-Ichi Hatakoshi, Opt. Rev. Vol. 10, No. 4, pp. 307-14, 2003.
[5] ‘Substrate Modes Of (Al,In)GaN Semiconductor Laser Diodes On SiN and GaN substrates’, V. Laino, F. Roemer, B. Witzigmann, C. Lauterbach, U. Schwarz, C. Rumbolz, M. Schillgalies, M. Furitsch, A. Lell, and V. Härle, J. Quant. Electron., Vol. 43, No. 1, pp. 16-24, 2007.

Chapter 7:

[1] ‘Saturation Of Light–Current Characteristics Of High-Power Laser Diodes (λ= 1.0–1.8 µm) Under Pulse Operation’, D.A. Vinokurov, V.A. Kapitonov, A.V. Lyutetskii, N.A. Pikhtin, S.O. Slipchenko, Z.N. Sokolova, A.L. Stankevich, M.A. Khomylev, V.V. Shamakhov, K.S. Borshchev, I.N. Arsent’ev, and I.S. Tarasov, Semiconductors Vol. 41, No. 8, pp. 984–990, 2007.
[2] ‘Finite Time Of Carrier Energy Relaxation as a Cause Of Optical-Power Limitation In Semiconductor Lasers’, S.O. Slipchenko, Z.N. Sokolova, N.A. Pikhtin, K.S. Borschev, D.A. Vinokurov, and I.S. Tarasov, Semiconductors, Vol. 40, No. 8, pp. 990–95, 2006.

[3] ‘On The Dimensionality Of Optical Absorption, Gain, And Recombination In Quantum Confined Structures’, P. Blood, J. Quantum Electron. Vol. 36, No. 3, pp. 354–62, 2000.
[4] ‘A Model for Calculation of the Threshold Current of SCH-MQW-SAS Lasers’, H. Wenzel, and H. Wünsche, Phys. Status. Solidi. A Vol. 120, pp. 661–73 (1990).
[5] ‘Effect of Carrier Loss Through Waveguide Layer Recombination on the Internal Quantum Efficiency in Large-Optical-Cavity Laser Diodes’, B.S. Ryvkin, and E.A. Avrutin, J. Appl. Phys. 97, p. 113106, 2005.
[6] ‘Doping in III-V Semiconductors. Cambridge Studies in Semiconductor Physics and Microelectronic Engineering’, E.F. Schubert ed. A. Haroon, Cambridge University Press, 1993, pp 39, 52.
[7] ‘Root-Cause Analysis of Peak Power Saturation in Pulse-Pumped 1100 nm Broad Area Single Emitter Diode Lasers’, X. Wang, P. Crump, H. Wenzel, A. Liero, T. Hoffmann, A. Pietrzak, C.M. Schultz, A. Klehr, A. Ginolas, S. Einfeldt, F. Bugge, G. Erbert, and G. Tränkle, J. Quant. Electron. 46, No. 5, pp. 658-66, 2010.

Chapter 8:

[1] ‘Properties of Wide-Mesastripe InGaAsP/InP Lasers’, E. G. Golikova, V. A. Kureshov, A. Yu. Leshko, A. V. Lyutetski, N. A. Pikhtin, Yu. A. Ryaboshtan, G. A. Skrynnikov, I. S. Tarasov, and Zh. I. Alferov, Semiconductors, Vol. 34, No. 7, pp. 853–856, 2000.
[2] Catastrophic Damage of $Al_xGa_{1-x}As$ Double Heterostructure Laser Material, C.H Henry, P.M. Petroff, R.A. Logan, and F.R. Merritt, J. Appl. Phys., Vol. 50, No. 5, pp. 3721-32, 1978.

Chapter 9:

[1] ‘Semiconductor Optoelectronic Devices: Introduction to Physics and Simulation’, J. Piprek, Academic Press, Ch. 7.3., pp. 161-2, 2003.
[2] ‘Semiconductor Lasers I: Fundamentals’, ed. E. Kapon, Academic Press San Diego 1999, p. 198.
[3] ‘The Conduction Band Structure and Deep Levels in $Ga_{l-x}Al_xAs$ Alloys from a High-Pressure Experiment”, A.K. Saxenat, J. Phys. C: Solid St. Phys., Vol. 13, pp. 4323-34, 1980.

Chapter 10:

[1] Catastrophic Damage of $Al_xGa_{1-x}As$ Double Heterostructure Laser Material, C.H Henry, P.M. Petroff, R.A. Logan, and F.R. Merritt, J. Appl. Phys., Vol. 50, No. 5, pp. 3721-32, 1978.
[2] ‘975 nm High Power Diode Lasers with High Efficiency and Narrow Vertical Far Field Enabled by Low Index Quantum Barriers’, P. Crump, A. Pietrzak, F. Bugge, H. Wenzel, G. Erbert, and G. Tränkle, Appl. Phys. Lett. Vol. 96, pp. 131110-1-3, 2010.
[3] German Patent Application DEA102009024945, P.Crump, G.Erbert, A.Pietrzak, and H.Wenzel/Ferdinand-Braun Institut fuer Hoechstefrequenztechnik: ‘Optoelektronisches Halbleiterbauelement und Verfahren zu dessen Herstellung’, 2009.
[4] ‘Material Issues in AlGaInP Red-Emitting Laser Diodes’, P. Blood, Mater. Sci. Eng., B, Vol. 66, pp. 174-180, 1999.

[5] ‘55W Peak Power from 1100 nm Wavelength 60 μm Broad-Area Laser Diodes Enabled by Reduced Carrier Accumulation in the Waveguide’, A. Pietrzak, P. Crump, H. Wenzel, R. Staske, G. Erbert, and G. Tränkle, Semicond. Sci. Technol. Vol. 24, p. 035020, 2009.
[6] Lastip by Crosslight Inc.
[7] B. Ryvkin and E. Avrutin, “Effect of Carrier Loss Through Waveguide Layer Recombination on the Internal Quantum Efficiency in Large-Optical-Cavity Laser Diodes”, *J. App. Phys*., vol. 97, pp.113106, 2005
[8] ‘Low Confinement Factors for Suppressed Filaments in Semiconductor Lasers’, G. Dente J. Quant. Electron, Vol. 37, No. 12, pp. 1650-53, 2001.
[9] ‘Self-stabilized Nonlinear Lateral Modes of Broad Area Lasers’, D. Mehuys, R.J. Lang, M. Mittelstein, J. Salzman, and A. Yariv, J. Quant. Electron.,Vol. 23, No. 11, pp. 1909-20, 1987.

Appendix 2:

[1] ‘Semiconductor Laser Fundamentals’, T. Suhara, Marcel Dekker, Inc. New York, 2004.
[2] ‘Physics of Optoelectronic Devices’, S. L. Chuang, John Wiley & Sons, Inc., Canada, 1995.

Appendix 4:

[1] ‘Optoelectronic Devices: Advanced Simulation and Analysis. Springer California 2005, Ed. J. Piprek, Chapter 3: U. Bandelow, H. Gajewski, and R. Hünlich: Fabry-Perot lasers: Thermodynamics-Based Modeling.

Appendix 5:

[1]. ‘Dynamics of Thermo-Optical Properties of Semiconductor Lasers’, E. Kowalczyk, L. Ornoch, Z. Gniazdowski, B. Mroziewicz, Proc. SPIE, Vol. 6456, p. 64561G-1, 2007.
[2] ‘Experimental Determination of The Thermal Lens pParameters in a Broad Area Semiconductor Laser Amplifier’, A.I. Bawamia, B. Eppich, K. Paschke, H.Wenzel, F. Schnieder, G. Erbert, G. Tränkle, Appl. Phys. B Vol. 97, pp. 95–101, 2009.